Search for the Higgs boson decaying to tau leptons in the associated production mode at ATLAS

Curtis William Black

A thesis submitted in fulfilment of the requirements
for the degree of Doctor of Philosophy
School of Physics
University of Sydney
2016

Abstract

This thesis presents the results of the search for the Standard Model Higgs boson, decaying to tau leptons, and produced in association with a leptonically decaying vector boson. Using the ATLAS detector at the LHC, the analysis is performed on $20.3\,\mathrm{fb}^{-1}$ of proton-proton collisions recorded in 2012 at $\sqrt{s} = 8\,\mathrm{TeV}$ centre-of-mass energy. The analysis is made robust through the development of a background estimation method which uses Monte-Carlo simulation for the irreducible backgrounds and a data-driven estimation for the reducible backgrounds. No significant excess of events is observed. For a Higgs boson mass of $m_H = 125\,\mathrm{GeV}$, the 95% confidence level upper limit on the observed cross-section is 5.6 times the Standard Model prediction. The measured signal strength, normalized to the Standard Model expectation, is $\hat{\mu} = 2.3 \pm 1.6$. This excess corresponds to a 1.4σ upward fluctuation of the background-only expectation but is consistent with the Standard Model expectation.

Acknowledgements

A lot of effort goes into completing a physics analysis and writing a thesis. The people listed here were all generous in sharing their time and effort towards helping me complete this work.

Firstly, I would like to thank my supervisor Kevin Varvell, for inspiring me to pursue particle physics with his undergraduate lecture courses and for his valuable guidance towards completing this thesis. To Aldo Saavedra, thank you for getting me started in particle physics analysis during my honours year, and for the continued help and support in completing my service work. I'd also like to thank all the members of the Sydney Particle Physics group for the many pieces of valuable advice over the years.

To Geng-yuan Jeng and Sarah Demers, thank you both for being great conveners of the VH analysis, in particular for the huge amounts of feedback you both provided and for the great deal of effort involved in getting the analysis through to publication.

To my friends whom I shared an office with over the many years, Mark, Ian, Nik, Cameron, and The Chuz, I want to thank all of you for the help and advice when things just didn't seem to work, I hope I was able to do the same for you in return. In addition, I want to thank you all for the many coffees and drinks which provided some level of distraction throughout this journey.

To my family and friends, Nicola, Clancy, and Nathan, thank you all for your support and encouragement, and for always being available to distract me with fun and interesting conversations. Finally, I want to give a special thank you to my parents, Kate and Danny, for the love and support you have always given me.

Preface

The work presented in this thesis describes the author's contribution to a Higgs boson search which has since been published in reference [1]. This work builds upon the many decades of research by thousands of physicists working on the LHC and ATLAS experiment. Chapter 2 provides an overview of the theoretical motivation and Chapter 3 describes the experimental setup. Due to the scale and complexity of physics analyses with the ATLAS experiment, it is necessary to collaborate closely. The analysis presented here draws from the expertise of a small group of people within the ATLAS collaboration, of which the author was involved. In some cases the results presented here were produced solely by, or in collaboration with, fellow analysis members but are included here to provide a complete description of the analysis. Section 5.5 presents the results of work done entirely by others. Sections 6.3, 6.4, and 6.5 describe the event selection criteria determined by others. These selection criteria were used by the author to produce the combined results for the analysis. The work presented in Section 4.3 is the result of a collaborative effort between the author and fellow analysers. The author was involved in implementing this into the analysis framework software package used by the analysis group. All other work presented here was performed by the author unless explicitly referenced.

Contents

Chapter 1

Introduction

The Standard Model of particle physics has long stood as the most successful description of subatomic particles and their interactions. While many believe that it is not a complete description of particle physics, for example it does not include dark matter or gravity, it is nonetheless an excellent effective theory of particle phenomena observed at low energies. The Standard Model has been tested in many high-precision experiments, however for a long time the final missing piece of the theory, the Higgs boson, has remained unconfirmed.

On the 4th of July 2012, a milestone in the more than 50 year quest for the understanding of the origin of electroweak symmetry breaking was achieved. The discovery of a Higgs boson, with a mass near 125 GeV, by the ATLAS [2] and CMS [3] experiments at the LHC, provided evidence for the Higgs mechanism in the Standard Model. Following these experimental observations, the Nobel Prize in Physics was awarded to François Englert and Peter Higgs in 2013 for the theoretical discovery of a mechanism that contributes to our understanding of the origin of mass of subatomic particles.

Subsequent measurements of the couplings and production rates [4], and spin-parity quantum numbers [5] of the discovered particle are all consistent with the predictions for the Standard Model Higgs boson. These measurements, as well as the discovery itself, have been mainly performed on the bosonic decay modes of the Higgs boson, in particular the $H \to \gamma\gamma$, and $H \to ZZ^{(*)} \to 4\ell$ decay modes. Of particular interest is the status of the fermionic decay modes. Fermions are predicted to acquire mass through so-called Yukawa couplings to the Higgs field. Observation of fermionic decay modes would provide strong evidence for these couplings. In particular, the $H \to \tau\tau$ decay mode is one of the most promising opportunities to provide such evidence. The $H \to \tau\tau$ decay mode has been studied at ATLAS in the vector boson fusion and gluon-gluon fusion production

channels [6]. While an excess has been seen, the results are not significant enough to claim observation. For this reason, analysis of all Higgs boson production channels is necessary, in particular the WH and ZH associated production channels may provide additional sensitivity.

This thesis presents a direct search for the associated production of a Higgs boson with a vector boson (referred to as VH, where $V = W/Z$), where the Higgs boson decays to a pair of tau leptons, and the vector boson decays leptonically. These additional leptons can be used to efficiently trigger on the signal and reduce the backgrounds. The analysis is performed on $20.3\,\mathrm{fb}^{-1}$ of proton-proton collisions recorded by the ATLAS detector in 2012 at $\sqrt{s} = 8\,\mathrm{TeV}$ centre-of-mass energy. The structure of this thesis is as follows.

In Chapter 2, the Standard Model of particle physics is reviewed, covering the structure of the theory, the constituent fundamental particles, and their interactions. This is done in the Lagrangian formalism, describing the gauge quantum field theory framework of the theory. Of particular importance is the theory's mechanism for electroweak symmetry breaking, which predicts the existence of the Higgs boson. An overview of previous Higgs boson searches is given, as well as measurements of its properties, such as its spin-parity quantum numbers, its mass, and production and decay rates in different channels. Lastly, the associated production channel studied in this analysis is described.

In Chapter 3, an overview of the LHC is given, followed by a more detailed description of the ATLAS experiment. Each of the detector subsystems is described, as well as their role in reconstructing, identifying, and measuring properties of particles. The event reconstruction procedure is described, along with an overview of the algorithms used to reconstruct events for this analysis. The specific requirements made by this analysis are described in the next chapter.

In Chapter 4, the analysis strategy is presented. The event reconstruction procedure described in the previous chapter is used to select events with a topology matching the VH signal. After events are selected, they are divided into different categories for separate analysis in the following chapters. Also described in this chapter are the background processes which look sufficiently signal-like that they may pass through the event selection procedure and therefore must be estimated.

In Chapter 5, the development of the background estimation procedure used in this analysis is presented. The backgrounds are estimated from a combination of: Monte-Carlo for the irreducible backgrounds, and a data-driven component for the reducible

backgrounds. The method framework is derived in its most general form, followed by the specific application to this analysis. The method relies on measurements of the rates of particle misidentification. The procedure used to perform these measurements is presented here, along with the results. Lastly, the performance of the background estimation method is shown.

In Chapter 6, the analysis of the VH channels is presented. A sensitive mass variable is constructed from the available kinematic information of the signal topology which is used to discriminate signal from background. The event requirements for each channel are refined to further discriminate against the background processes. All of the systematic uncertainties which affect the analysis are described. The fitting procedure used to extract the final results is described, along with a description of the statistical tests used to present the results. Lastly, the results of the search are presented in the form of an upper limit on the observed cross-section and a measurement of the significance of any observed excess. This is done for each of the VH categories separately, as well as for the combination of all channels combined. The fitted signal strength is shown.

In Chapter 7, the work presented in this thesis is summarised and final remarks are presented.

Chapter 2

The Standard Model and the Higgs Boson

Particle physics is the study of elementary particles and the fundamental forces that govern their interactions. The Standard Model (SM) of particle physics is currently the most successful attempt to describe these particles and interactions.

In particle physics literature (including this work) it is common to use *natural units*. In this system, the speed of light, the reduced Planck constant, and the Boltzmann constant are each normalised to unity, that is $c = \hbar = k_B = 1$. Mass, energy and momentum are all measured in units of electron volts (eV) and electric charge is measured in units of the magnitude of the charge of an electron.

The Einstein summation convention is used throughout this work. Greek letters are used for the four Minkowski space-time indices $\{0, 1, 2, 3\}$

$$A_\mu A^\mu = \eta_{\mu\nu} A^\mu A^\nu = A_0^2 - A_1^2 - A_2^2 - A_3^2 \tag{2.1}$$

Roman letters are used for indices in Euclidean dimensions $[1, n]$

$$A_i A^i = \delta_{ij} A^i A^j = A_1^2 + A_2^2 + ... + A_n^2 \tag{2.2}$$

		Particle	Symbol		Charge	Spin	Mass
Fermions	Leptons	electron neutrino	$\cdots\cdots\cdots$	ν_e	0	$1/2$	$\lesssim 2\,\text{eV}$
		muon neutrino	$\cdots\cdots\cdots$	ν_μ	0	$1/2$	$\lesssim 2\,\text{eV}$
		tau neutrino	$\cdots\cdots\cdots$	ν_τ	0	$1/2$	$\lesssim 2\,\text{eV}$
		electron	————	e^-	-1	$1/2$	$511\,\text{keV}$
		muon	————	μ^-	-1	$1/2$	$106\,\text{MeV}$
		tau	————	τ^-	-1	$1/2$	$1.777\,\text{GeV}$
	Quarks	up	————	u	$+2/3$	$1/2$	$2.3^{+0.7}_{-0.5}\,\text{MeV}$
		charm	————	c	$+2/3$	$1/2$	$1.275 \pm 0.025\,\text{GeV}$
		top	————	t	$+2/3$	$1/2$	$173.21 \pm 0.87\,\text{GeV}$
		down	————	d	$-1/3$	$1/2$	$4.8^{+0.5}_{-0.3}\,\text{MeV}$
		strange	————	s	$-1/3$	$1/2$	$95 \pm 5\,\text{MeV}$
		bottom	————	b	$-1/3$	$1/2$	$4.18 \pm 0.03\,\text{GeV}$
Bosons		photon	$\sim\sim\sim$	γ	0	1	0
		W boson	$\sim\sim\sim$	$W^\pm$	±1	1	$80.385 \pm 0.015\,\text{GeV}$
		Z boson	$\sim\sim\sim$	Z	0	1	$91.188 \pm 0.002\,\text{GeV}$
		gluon	$\mathcal{QQQQ}$	g	0	1	0
		Higgs boson	$- - - - -$	H	0	0	$125.09 \pm 0.24\,\text{GeV}$

Table 2.1: Standard Model particles and their properties [7]. The lines shown for each symbol are the pictorial representations of particles used when drawing Feynman diagrams. Charges are given in units of the absolute value of the charge of an electron. Masses of neutrinos are small but measured to be non-zero. The very small uncertainties on the masses of the charged leptons are not shown.

2.1 The Standard Model

All of the elementary particles in the SM can be categorised as either *fermions* (spin $1/2$) or *bosons* (integer spin). Table 2.1 lists the particles of the SM with a few of their properties.

Fermions are the *matter* particles in the SM which can be further categorised as either *quarks* or *leptons*. There are three electrically charged leptons, they are, in increasing order of mass, the *electron* (e^-), *muon* (μ^-) and *tau* (τ^-). Each of these particles has a

corresponding neutrally charged neutrino partner, these being the *electron neutrino* (ν_e), *muon neutrino* (ν_μ) and *tau neutrino* (ν_τ) respectively. There are six *flavours* of quarks, they are the *up* (u), *charm* (c) and *top* (t) which are referred to as the *up-type* quarks and the *down* (d), *strange* (s) and *bottom* (b) which are referred to as the *down-type* quarks. Each fermion in the SM has a corresponding antiparticle with opposite electric charge. Quarks are never observed as individual free particles but are bound together as composite particles called *hadrons*. Combinations of three quarks (qqq) or three antiquarks ($\bar{q}\bar{q}\bar{q}$) are called *baryons*, combinations of quark antiquark pairs ($q\bar{q}$) are called *mesons*.

The mathematical framework of the SM is a gauge quantum field theory where the fields are representations of the internal symmetry groups $SU(3)_C \times SU(2)_L \times U(1)_Y$. According to Noether's theorem [8], every local[1] symmetry produces a conserved current. The $SU(3)_C$ symmetry group describes the *strong interaction* which is mediated by eight *gluons* (g) and conserves *colour charge* (C). $SU(2)_L \times U(1)_Y$ describes the unified *electroweak interaction* which is mediated by four massless vector (spin 1) fields $W^{1,2,3}$ and B, which conserve *weak isospin* (I) and *weak hypercharge* (Y) respectively. Particles in the SM gain mass though interactions with a scalar (spin 0) Higgs field which spontaneously breaks the electroweak symmetry. The introduction of this breaking mechanism is required to account for experimental observation the massive $W^\pm$ and Z bosons and requires the existence of a massive spin 0 Higgs boson. After electroweak symmetry breaking takes place the $SU(2)_L \times U(1)_Y$ symmetry is broken into $U(1)_{EM}$ and four physical vector bosons $W^\pm$, Z and the photon (γ) which are linear combinations of the $W^{1,2,3}$ and B fields. The $W^\pm$ and Z mediate the *weak interaction* and the $U(1)_{EM}$ symmetry group describes the *electromagnetic interaction* which is mediated by the photon and conserves *electric charge* (Q).

The framework of the SM is the unified combination of the theories of the strong and electroweak interactions with the addition of the Higgs sector. The SM is represented by a Lorentz invariant scalar Lagrangian density $\mathcal{L}$ which describes the dynamics of the system. The Lagrangian density of the SM is

$$\mathcal{L}_{\text{SM}} = \mathcal{L}_{\text{strong}} + \mathcal{L}_{\text{electroweak}} + \mathcal{L}_{\text{Higgs}} \tag{2.3}$$

---

[1]A symmetry is said to be local if the system is invariant under transformations which may act differently at different points in space-time. To be compared with global symmetries which have the same transformation at all points in space-time.

In the following sections the electromagnetic, strong, and weak interactions as well as the Higgs mechanism are each derived using the Lagrangian formalism.

2.1.1 Electromagnetic Interaction

The Dirac equation describes the free propagation of a fermion with mass m.

$$(i\gamma^\mu \partial_\mu - m)\psi = 0 \tag{2.4}$$

ψ is the four-component spinor representing the fermionic field and γ^μ are the Dirac matrices. Each component of ψ is a function of the space-time coordinate $x^\mu = (t,\ x,\ y,\ z)$, where $\mu \in \{0, 1, 2, 3\}$ is the index of the four space-time components. The corresponding Lagrangian density of the Dirac equation is given by

$$\mathcal{L} = \bar{\psi}(i\gamma^\mu \partial_\mu - m)\psi \tag{2.5}$$

where $\bar{\psi} = \psi^\dagger \gamma^0$ is the adjoint spinor. This Lagrangian density is invariant under a global phase transformation of the type

$$\psi \rightarrow e^{iq\alpha}\psi \tag{2.6}$$

where $\alpha \in \mathbb{R}$ and q is the electric charge of the fermion. Transformations of this type build up the $U(1)$ symmetry group. The SM is also required to be locally invariant under transformations of the type

$$\psi \rightarrow e^{iq\alpha(x)}\psi \tag{2.7}$$

where the phase $\alpha(x)$ is an arbitrary function of the space-time point x^μ. The free Dirac equation as given in equation (2.4) is not invariant under these types local phase transformations. To preserve the invariance, the derivative ∂_μ in equation (2.4) must be replaced by a new covariant derivative

$$\mathcal{D}_\mu = \partial_\mu - iqA_\mu \tag{2.8}$$

This derivative introduces a new vector field A_μ, the electromagnetic field, which is required to transform as

$$A_\mu \to A_\mu - \partial_\mu \alpha(x) \tag{2.9}$$

Following Noether's theorem, this local invariance leads to the conservation of electric current

$$J^\mu = q\bar{\psi}\gamma^\mu\psi \tag{2.10}$$

With this new set of locally invariant transformations, equation (2.5) can be rewritten as

$$\mathcal{L} = \bar{\psi}(i\gamma^\mu\mathcal{D}_\mu - m)\psi \tag{2.11}$$
$$= \bar{\psi}i\gamma^\mu\partial_\mu\psi - m\bar{\psi}\psi - q\bar{\psi}\gamma^\mu A_\mu\psi \tag{2.12}$$

The Lagrangian density used to derive Maxwell's equation is

$$\mathcal{L} = -\frac{1}{4}F_{\mu\nu}F^{\mu\nu} - J^\mu A_\mu \tag{2.13}$$

where $F^{\mu\nu} = \partial^\mu A^\nu - \partial^\nu A^\mu$ is the electromagnetic field strength tensor. The first term in equation (2.13) describes the kinetic energy of the electromagnetic field. This term is required to complete the Lagrangian density of the electromagnetic interaction, which is given by

$$\mathcal{L}_{\text{EM}} = \underbrace{\bar{\psi}i\gamma^\mu\partial_\mu\psi}_{\text{fermion kinetic term}} - \underbrace{m\bar{\psi}\psi}_{\text{fermion mass term}} - \underbrace{\frac{1}{4}F^{\mu\nu}F_{\mu\nu}}_{\text{field kinetic term}} - \underbrace{q\bar{\psi}\gamma^\mu A_\mu\psi}_{\text{interaction term}} \tag{2.14}$$

The interaction term describes the interaction between a fermion and a photon with a coupling strength given by the electric charge q of the fermion. Electromagnetism is an *abelian* gauge theory, meaning the result of applying multiple transformations of the type in equation (2.7) does not depend on the order in which they are applied. A consequence of the abelian nature of electromagnetism is that photons are not able to interact with themselves, thus no photon self-interaction terms are present in the above Lagrangian density. It is not possible to introduce a mass term for the photon of the form $m^2 A^\mu A_\mu$ since it is not gauge invariant. The theory requires the photon to be massless as is observed experimentally.

2.1.2 Strong Interaction

The strong interaction is described by Quantum Chromodynamics (QCD), which is a non-abelian gauge theory [9, 10]. QCD introduces the $SU(3)_C$ symmetry group which conserves colour charge. There are three colour quantum numbers: r, g, and b, however this is just the naming convention and they have no relation to the visual concept of colour we experience. Similarly to how electrons have negative electric charge while positrons have positive electric charge, quarks carry colour charge while antiquarks carry anticolour charge ($\bar{r}$, $\bar{g}$, or $\bar{b}$). Gluons can be interpreted as having one unit of colour and one unit of anticolour. Leptons and bosons (other than the gluon) do not carry colour charge and therefore do not participate in the strong interaction.

The Lagrangian density for the gluon field is analogous to that for electromagnetic field, in place of the electromagnetic field strength tensor $F^{\mu\nu}$ there is the gluon field strength tensor $G_a^{\mu\nu} = \partial^\mu G_a^\nu - \partial^\nu G_a^\mu - g_3 f_{abc} G_b^\mu G_c^\nu$ where G_a^μ are the eight gluon vector fields ($a, b, c \in [1, 8]$), one for each of the eight combinations of colour and anticolour. By analogy to q in the electromagnetic interaction, g_3 will defined the coupling strength of the strong interaction. The coefficients f_{abc} are the structure constants. The Lagrangian density of the gluon field is

$$\mathcal{L}_{\text{gluons}} = -\frac{1}{4} G_a^{\mu\nu} G_{a\mu\nu} \tag{2.15}$$

The presence of trilinear and quartic terms here allow for gluon self-interactions with vertices connecting three or four gluons, this is a consequence of the non-abelian nature of QCD. The interaction between quarks and gluons comes about by the replacement of the derivative ∂_μ in the Dirac equation with the new covariant derivative

$$\mathcal{D}_\mu = \partial_\mu - ig_3 T_a G_{a\mu} \tag{2.16}$$

where T_a are the eight generators of the $SU(3)_C$ symmetry group which satisfy the commutation relations $[T_a, T_b] = if_{abc}T_c$. The Lagrangian density for quarks is

$$\mathcal{L}_{\text{quarks}} = \bar{\psi}_f(i\gamma^\mu \mathcal{D}_\mu - m)\psi_f \tag{2.17}$$

$$= \bar{\psi}_f i\gamma^\mu \partial_\mu \psi_f - g_3 \bar{\psi}_f \gamma^\mu T_a G_{a\mu} \psi_f - m\bar{\psi}_f \psi_f \tag{2.18}$$

where the summation over the six quark flavours $f \in [1, 6]$ is implied. The Lagrangian density of the strong interaction is then given by

$$\mathcal{L}_{\text{strong}} = \mathcal{L}_{\text{gluons}} + \mathcal{L}_{\text{quarks}} \tag{2.19}$$

$$= - \underbrace{\frac{1}{4}G_a^{\mu\nu}G_{a\mu\nu}}_{\text{field kinetic term}} + \underbrace{\bar{\psi}_f i\gamma^\mu\partial_\mu\psi_f}_{\text{quark kinetic term}} - \underbrace{g_3\bar{\psi}_f\gamma^\mu T_a G_{a\mu}\psi_f}_{\text{interaction term}} - \underbrace{m\bar{\psi}_f\psi_f}_{\text{quark mass term}} \tag{2.20}$$

2.1.3 Weak Interaction and Electroweak Unification

The weak interaction is described by the $SU(2)_L$ symmetry group which conserves the 3rd component of the weak isospin (I_3). L is used to represent the left-handed fermions as the weak interaction does not couple to right-handed fermions. The left-handed fermions are ordered into doublets of weak isospin

$$\psi_L = \begin{pmatrix} \nu_e \\ e \end{pmatrix}_L, \ \begin{pmatrix} \nu_\mu \\ \mu \end{pmatrix}_L, \ \begin{pmatrix} \nu_\tau \\ \tau \end{pmatrix}_L, \ \begin{pmatrix} u \\ d' \end{pmatrix}_L, \ \begin{pmatrix} c \\ s' \end{pmatrix}_L, \ \begin{pmatrix} t \\ b' \end{pmatrix}_L \tag{2.21}$$

Where d', s' and b' are the weak eigenstates of the physical quark states of definite mass d, s and b given by the mixing terms in the Cabibbo-Kobayashi-Maskawa (CKM) matrix

$$\begin{pmatrix} d' \\ s' \\ b' \end{pmatrix} = \begin{pmatrix} V_{ud} & V_{us} & V_{ub} \\ V_{cd} & V_{cs} & V_{cb} \\ V_{td} & V_{ts} & V_{tb} \end{pmatrix} \begin{pmatrix} d \\ s \\ b \end{pmatrix} \tag{2.22}$$

The elements of the CKM matrix represent the probability that a specific up-type quark couples to a specific down-type quark when interacting with a $W^\pm$ boson. The values of these matrix elements are not predicted by the SM. However the requirement that the matrix be unitary (probabilities sum to one) allows the matrix to be parametrised by three mixing angles and a phase.

By analogy to equation (2.5) for the electromagnetic interaction, the Lagrangian density of the weak interaction for a pair of massless left-handed fermions is given by

$$\mathcal{L} = \bar{\psi}_L(i\gamma^\mu\partial_\mu)\psi_L \tag{2.23}$$

The local gauge transformations will be of the type

$$\psi_L \rightarrow e^{i\frac{g_2}{2}\alpha^a(x)\sigma^a}\psi_L \qquad (2.24)$$

where σ^a are the three Pauli matrices

$$\sigma^1 = \begin{pmatrix} 0 & 1 \\ 1 & 0 \end{pmatrix}, \quad \sigma^2 = \begin{pmatrix} 0 & -i \\ i & 0 \end{pmatrix}, \quad \sigma^3 = \begin{pmatrix} 1 & 0 \\ 0 & -1 \end{pmatrix} \qquad (2.25)$$

and $\alpha^a(x)$ are the three arbitrary space-time dependent functions. By analogy to the charge q in the electromagnetic interaction, g_2 will define the coupling strength of the interaction. To preserve the invariance of the Lagrangian density under local $SU(2)_L$ transformations, the derivative ∂_μ in equation (2.23) is replaced by a new covariant derivative

$$\mathcal{D}_\mu = \partial_\mu - i\frac{g_2}{2}\sigma^a W_\mu^a \qquad (2.26)$$

This new derivative introduces three new massless vector fields W_μ^a ($a = 1, 2, 3$) which are required to transform as

$$W_\mu^a \rightarrow \partial_\mu\alpha^a(x) - g_2\epsilon^{abc}\alpha^b(x)W_\mu^c \qquad (2.27)$$

where ϵ^{abc} is the Levi-Civita tensor. By analogy to equation (2.13) for the electromagnetic interaction, the kinetic energy of these new gauge fields is given by $\frac{1}{4}W^{a\mu\nu}W_{\mu\nu}^a$ where $W_{\mu\nu}^a = \partial_\mu W_\nu^a - \partial_\nu W_\mu^a - g_2\epsilon^{abc}W_\mu^b W_\nu^c$ is the field strength tensor. The complete Lagrangian density of $SU(2)_L$ is given by

$$\mathcal{L}_L = \underbrace{\bar{\psi}_L i\gamma^\mu\partial_\mu\psi_L}_{\text{fermion kinetic term}} - \underbrace{\frac{1}{4}W^{a\mu\nu}W_{\mu\nu}^a}_{\text{field kinetic and self-interaction term}} - \underbrace{\frac{g_2}{2}\bar{\psi}_L\gamma^\mu\sigma^a W_\mu^a\psi_L}_{\text{interaction term}} \qquad (2.28)$$

The derivation of the Lagrangian density for $U(1)_Y$ is almost identical to that of the electromagnetic interaction. Unlike $SU(2)_L$, $U(1)_Y$ couples to both the left-handed isospin doublets and the right-handed isospin singlets

$$\psi_R = e_R, \ \mu_R, \ \tau_R, \ u_R, \ d_R, \ c_R, \ s_R, \ t_R, \ b_R \qquad (2.29)$$

The local gauge transformations are of the type

$$\psi \rightarrow e^{i\frac{g_1}{2}\alpha(x)}\psi \tag{2.30}$$

where g_1 is the coupling strength of the interaction and again $\alpha(x)$ is an arbitrary space-time dependent function. The covariant derivative used to preserve local gauge invariance is given by

$$\mathcal{D}_\mu = \partial_\mu + i\frac{g_1}{2}B_\mu \tag{2.31}$$

which introduces the new vector field B_μ. The field strength tensor is then defined as $B_{\mu\nu} = \partial_\mu B_\nu - \partial_\nu B_\mu$. The complete Lagrangian density of $U(1)_Y$ is given by

$$\mathcal{L}_Y = \underbrace{\bar{\psi}i\gamma^\mu\partial_\mu\psi}_{\text{fermion kinetic term}} - \underbrace{\frac{1}{4}B^{\mu\nu}B_{\mu\nu}}_{\text{field kinetic term}} + \underbrace{\frac{g_1}{2}\bar{\psi}\gamma^\mu B_\mu\psi}_{\text{interaction term}} \tag{2.32}$$

Electroweak unification [11–13] requires local gauge invariance of the Lagrangian density of the combined $SU(2)_L \times U(1)_Y$ symmetry. The electroweak covariant derivative is the combination of equation (2.26) and equation (2.31), given by

$$\mathcal{D}_\mu = \partial_\mu + i\frac{g_2}{2}\sigma^a W_\mu^a + i\frac{g_1}{2}B_\mu \tag{2.33}$$

The complete Lagrangian density of the electroweak interaction is given by

$$\mathcal{L}_{\text{electroweak}} = \underbrace{\bar{\psi}_L i\gamma^\mu\partial_\mu\psi_L}_{\text{left-handed fermion kinetic term}} + \underbrace{\bar{\psi}_R i\gamma^\mu\partial_\mu\psi_R}_{\text{right-handed fermion kinetic term}}$$

$$- \underbrace{\frac{g_2}{2}\bar{\psi}_L\gamma^\mu\sigma^a W_\mu^a\psi_L - \frac{g_1}{2}\bar{\psi}_L\gamma^\mu\sigma^0 B_\mu\psi_L}_{\text{left-handed interaction terms}} - \underbrace{\frac{g_1}{2}\bar{\psi}_R\gamma^\mu B_\mu\psi_R}_{\text{right-handed interaction term}}$$

$$- \underbrace{\frac{1}{4}W^{a\mu\nu}W_{\mu\nu}^a - \frac{1}{4}B^{\mu\nu}B_{\mu\nu}}_{\text{field kinetic and self-interaction terms}} \tag{2.34}$$

where σ^0 is the 2×2 unit matrix

$$\sigma^0 = \begin{pmatrix} 1 & 0 \\ 0 & 1 \end{pmatrix} \tag{2.35}$$

To relate these four vector fields to the physically observed gauge bosons responsible for mediating the charged and neutral currents of the electroweak interaction, a basis change of the fields is performed. The fields W_μ^1 and W_μ^2 mix to produce the charged $W^\pm$ bosons

$$W_\mu^\pm = \frac{1}{\sqrt{2}}(W_\mu^1 \mp iW_\mu^2) \tag{2.36}$$

The fields W_μ^3 and B_μ mix to produce the neutral Z boson and the photon

$$\begin{pmatrix} Z_\mu \\ A_\mu \end{pmatrix} = \begin{pmatrix} \cos\theta_W & -\sin\theta_W \\ \sin\theta_W & \cos\theta_W \end{pmatrix} \begin{pmatrix} W_\mu^3 \\ B_\mu \end{pmatrix} \tag{2.37}$$

which corresponds to a rotation by the Weinberg angle θ_W where

$$\cos\theta_W = \frac{g_2}{\sqrt{g_1^2 + g_2^2}} \quad \text{and} \quad \sin\theta_W = \frac{g_1}{\sqrt{g_1^2 + g_2^2}} \tag{2.38}$$

The non-abelian nature of the electroweak interaction gives rise to the presence of trilinear and quartic terms in the electroweak Lagrangian density which allow for $W^\pm$ and Z self-interactions with vertices connecting three or four $W^\pm$ or Z bosons.

2.1.4 The Higgs Mechanism and Spontaneous Symmetry Breaking

The Lagrangian density developed in the previous section describes all properties of the electroweak interaction with the exception of particle masses. The requirement of local gauge invariance requires massless particles and would no longer hold if mass terms were inserted into the electroweak Lagrangian density by hand. This contradicts experimental evidence of massive fermions and $W^\pm$ and Z bosons. This problem is solved through the use of *spontaneous symmetry breaking* where the electroweak symmetry is broken by the intrinsic features of the fields rather than the explicit introduction of symmetry breaking mass terms into the Lagrangian density[2]. Electroweak symmetry breaking in the SM is achieved by the Higgs mechanism [14–19]. The Higgs mechanism introduces a new

---

[2]In the previous sections the Lagrangian densities, derived from the Dirac equation, included mass terms explicitly. For this reason, the Lagrangian densities in these sections describe the theories after electroweak symmetry breaking has taken place.

(a) $\mu^2 > 0, \ \lambda > 0$ **(b)** $\mu^2 < 0, \ \lambda > 0$
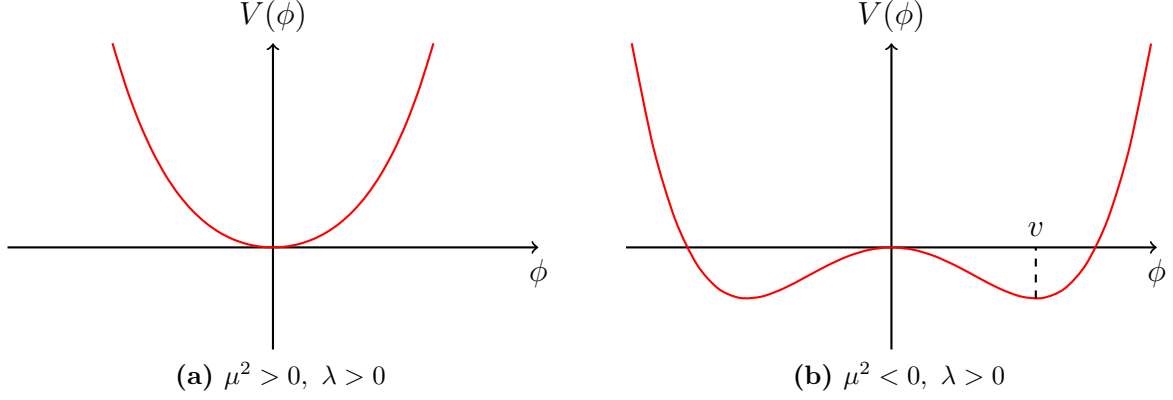
Figure 2.1: The symmetric quartic Higgs potential, $V(\phi) = \mu^2\phi^2 + \lambda\phi^4$, of a scalar field ϕ.

$SU(2)_L$ doublet of complex scalar fields

$$\Phi = \frac{1}{\sqrt{2}}\begin{pmatrix} \phi_1 + i\phi_2 \\ \phi_3 + i\phi_4 \end{pmatrix} \tag{2.39}$$

where ϕ_i are the four real scalar fields. The Lagrangian density of this scalar doublet contains a kinetic term and a potential term, given by

$$\mathcal{L}_{\text{Higgs}} = (\mathcal{D}^\mu\Phi)^\dagger(\mathcal{D}_\mu\Phi) - V(\Phi^\dagger\Phi) \tag{2.40}$$

where $\mathcal{D}_\mu$ is the electroweak covariant derivative from equation (2.33) and $V(\Phi^\dagger\Phi)$ is the potential term which is chosen to be

$$V(\Phi^\dagger\Phi) = \mu^2\Phi^\dagger\Phi + \lambda(\Phi^\dagger\Phi)^2 \tag{2.41}$$

where μ^2 and λ are real parameters. To ensure the existence of a global minimum, the parameter λ is required to be positive. Positive values of μ^2 (Figure 2.1a) will give a single global minimum at $\Phi^\dagger\Phi = 0$, however for the case where $\mu^2 < 0$ (Figure 2.1b), the global minimum is non-zero and occurs at

$$(\Phi^\dagger\Phi)_{\text{min}} = (\phi_1^2 + \phi_2^2 + \phi_3^2 + \phi_4^2)_{\text{min}} = -\frac{\mu^2}{2\lambda} \tag{2.42}$$

This minimum of the potential, the vacuum ground state, has infinitely many solutions on a four-dimensional hypersphere. For this reason we are free to choose any point on

this hypersphere to be the vacuum state without loss of generality. The point chosen is

$$\phi^2_{1,\text{min}} = \phi^2_{2,\text{min}} = \phi^2_{4,\text{min}} = 0 \tag{2.43}$$

$$\phi^2_{3,\text{min}} = -\frac{\mu^2}{2\lambda} = v^2 \tag{2.44}$$

where v is the vacuum expectation value of the field ϕ_3. The choice of this minimum spontaneously breaks the $SU(2)$ rotational symmetry. The vacuum expectation value of the complex scalar doublet is

$$\langle 0|\Phi|0\rangle = \frac{1}{\sqrt{2}} \begin{pmatrix} 0 \\ v \end{pmatrix} \tag{2.45}$$

The physical interpretation is found by expanding the Lagrangian density around the vacuum expectation value. There are three massless degrees of freedom at this point which allow the potential to remain at a minimum. Expansion about the potential in the direction away from the minimum is associated with one massive scalar field, the Higgs field H. Expanding the kinetic term of the Lagrangian density around this minimum

$$\Phi = \frac{1}{\sqrt{2}} \begin{pmatrix} 0 \\ v + H \end{pmatrix} \tag{2.46}$$

gives

$$(\mathcal{D}^\mu\Phi)^\dagger(\mathcal{D}_\mu\Phi) = \frac{1}{2}\partial^\mu H\partial_\mu H + \frac{1}{4}g_2^2 W_\mu^- W^{+\mu}(v+H)^2 + \frac{1}{4}(g_1^2 + g_2^2)Z_\mu Z^\mu(v+H)^2 \tag{2.47}$$

The first term can be interpreted as the kinetic energy of the Higgs field, the other terms which contain H are the interaction terms, lastly, the masses of the gauge bosons can be read off from the bilinear terms as:

$$m_W = \frac{1}{2}vg_2, \qquad m_Z = \frac{1}{2}v\sqrt{g_1^2 + g_2^2}, \qquad m_A = 0 \tag{2.48}$$

The Higgs kinetic term, $\frac{1}{2}\partial^\mu H\partial_\mu H$, implies the existence of a new particle in the theory, the spin 0 Higgs boson. The mass of the Higgs boson can be found by expansion of the potential around the ground state

$$V = \frac{1}{2}\mu^2(v+H)^2 + \frac{1}{4}\lambda(v+H)^4 \tag{2.49}$$

The bilinear term in this expansion is $\frac{1}{2}\lambda v^2 H^2$, which gives the mass of the Higgs boson to be $m_H = \sqrt{\lambda}v$. The vacuum expectation value of the Higgs field is known to be

$v \approx 246$ GeV. However the value of the parameter λ is not predicted by the theory. For this reason, the mass of the Higgs boson is also a free parameter of the theory as it cannot be directly predicted by other parameters of the SM. In summary, the introduction of this doublet of complex scalar fields, along with a symmetric potential, breaks the $SU(2)_L \times U(1)_Y$ symmetry which results in the existence of a massive spin 0 Higgs boson and produces masses for the weak gauge bosons while leaving the photon massless.

2.1.5 Fermion Masses

Explicitly adding mass terms for the fermions would break local gauge invariance, as was the case for the gauge bosons. However additional terms can be added to the SM Lagrangian which couple the Higgs field to the fermions, these terms are called Yukawa couplings and are of the form

$$\mathcal{L}_{\text{Yukawa}}^f = -\lambda_f \bar{\psi}_L \Phi \psi_R - \lambda_f \bar{\psi}_R \Phi \psi_L \tag{2.50}$$

These Yukawa coupling terms are added to the SM Lagrangian once for each fermion f, except for neutrinos where Yukawa couplings are not possible since both ψ_R^ν and $\bar{\psi}_L^\nu$ are zero. Again, expansion about the ground state yields

$$\mathcal{L}_{\text{Yukawa}}^f = -\frac{\lambda_f}{\sqrt{2}}(v + H)\bar{\psi}_L \psi_R - \frac{\lambda_f}{\sqrt{2}}(v + H)\bar{\psi}_R \psi_L \tag{2.51}$$

$$= -\underbrace{\frac{\lambda_f v}{\sqrt{2}}(\bar{\psi}_L \psi_R + \bar{\psi}_R \psi_L)}_{\text{fermion mass term}} - \underbrace{\frac{\lambda_f}{\sqrt{2}}H(\bar{\psi}_L \psi_R + \bar{\psi}_R \psi_L)}_{\text{interaction term}} \tag{2.52}$$

The first term gives mass to each of the fermions, given by

$$m_f = \frac{\lambda_f v}{\sqrt{2}} \tag{2.53}$$

which means that mass is not an intrinsic property that fermions possess, but rather is generated through their coupling to the Higgs field. The second term corresponds to interactions between a Higgs boson and fermions with a coupling coefficient given by

$$g_{Hff} = i\frac{m_f}{v} \tag{2.54}$$

This essentially states that the strength of the coupling between fermions and the Higgs boson is proportional to the mass of the fermion. The introduction of Yukawa couplings

to the SM is not required by the theory, however a description of fermion masses is required to account for experimental observation. For this reason it is of particular interest to study the Higgs boson coupling to the different fermions.

2.2 The Higgs Boson

Proposed in 1964, the Higgs mechanism is expected to give mass to the other fundamental particles. For many years the Higgs boson has remained the last missing piece required to complete the SM. This section reviews the phenomenology of the Higgs boson, experimental searches including the discovery of a Higgs like particle at CERN, as well as measurements of the properties of this newly discovered particle.

2.2.1 Higgs Boson Searches

The search for the Higgs boson has been one of the most important and challenging endeavours in particle physics over the past decades. Experimental searches for the Higgs boson and limits on its mass are of two kinds: direct searches at colliders like the Large Electron Positron Collider (LEP), the Large Hadron Collider (LHC) and the Tevatron, and indirect limits from precision measurements of the electroweak parameters of the SM.

Searches at LEP

The LEP machine was an electron-positron collider at CERN which operated from 1989 to 2000. The search for the Higgs boson at LEP was done with collisions at centre-of-mass energies up to $\sqrt{s} = 209\,\text{GeV}$. The main Higgs boson production mode at LEP was the so-called *associated production* (VH) of a Higgs and vector boson, where the Higgs boson is radiated from a virtual Z boson as shown in Figure 2.2. The LEP machine provided data to four detector experiments: ALEPH, DELPHI, L3 and OPAL. In the Higgs boson mass range available to LEP the dominant decay modes of the Higgs boson are $H \rightarrow bb$ ($\approx$74%) and $H \rightarrow \tau\tau$ ($\approx$7%) as show in Figure 2.3. The combined result from the experiments, shown in Figure 2.4, showed no significant excess. The result is
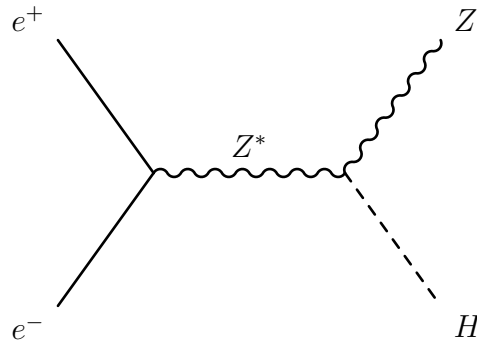
Figure 2.2: Feynman diagram of the associated production mode of the Higgs boson at LEP.
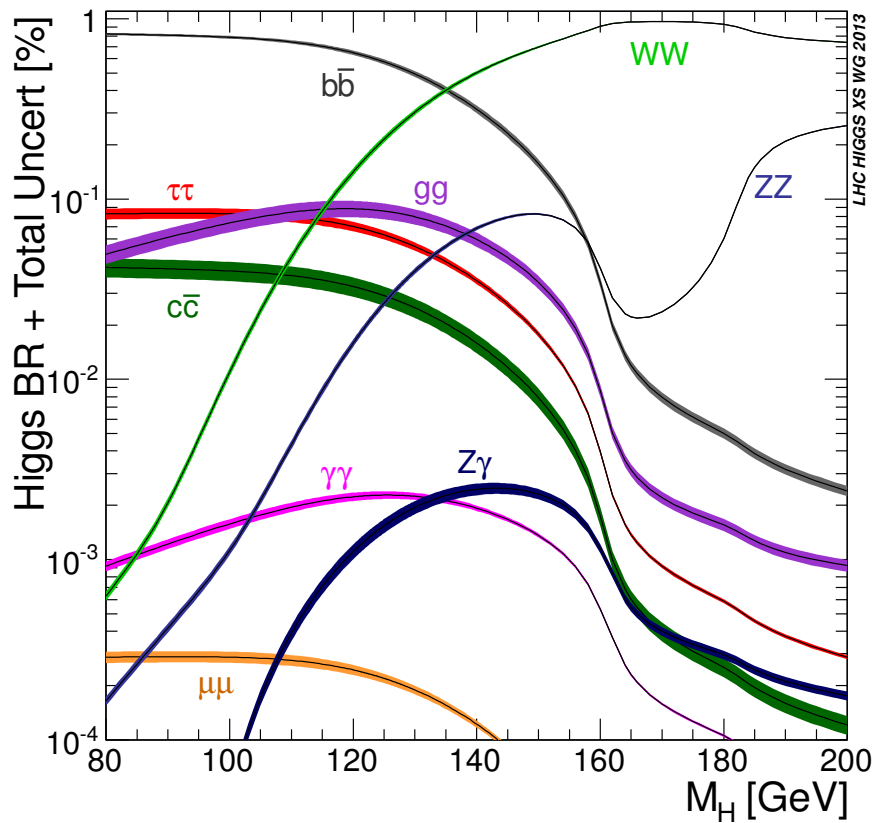
Figure 2.3: Higgs boson decay branching fractions as a function of the Higgs boson mass. The coloured bands show the total theoretical uncertainty on the prediction [20].

expressed in terms of the likelihood ratio

$$Q = \frac{\mathcal{L}_{S+B}}{\mathcal{L}_B} \tag{2.55}$$

where $\mathcal{L}_{S+B}$ and $\mathcal{L}_B$ are the likelihood of the signal-plus-background and background-only hypothesis respectively. A lower limit on the Higgs boson mass is placed at 114.4 GeV, at
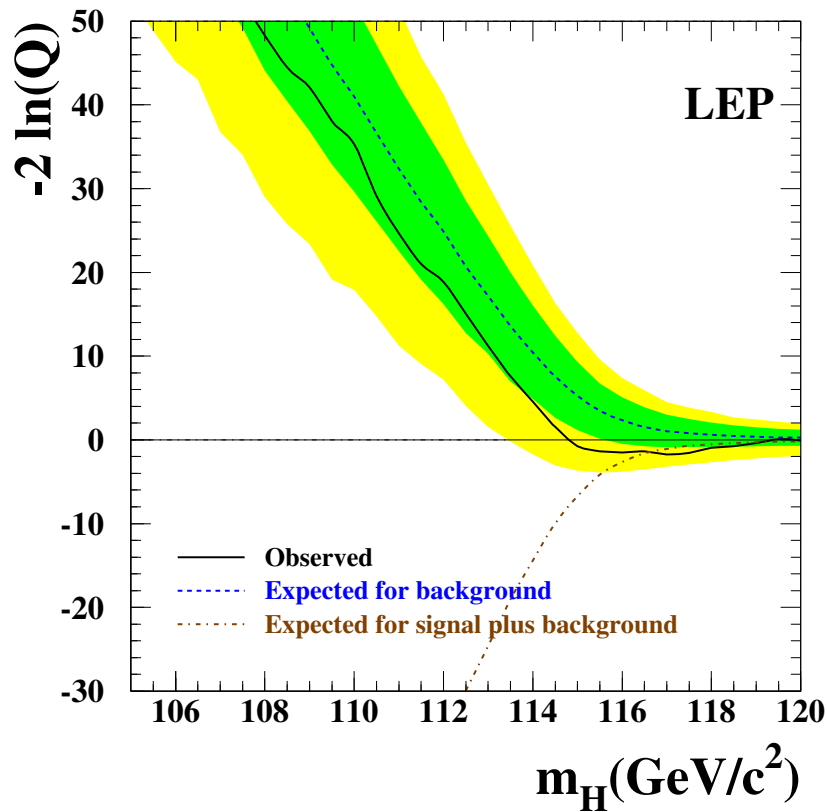
Figure 2.4: Combined results of the direct search for the SM Higgs boson by the four LEP experiments. The observed and expected behaviour of the test statistic $-2\ln Q$ is shown as a function of the Higgs boson mass hypothesis. The green and yellow bands show the 68% and 95% probability bands around the median background-only expectation [21].

the 95% confidence level, given that the observed data is consistent with the background-only hypothesis in this mass range.

Searches at the Tevatron

The Tevatron was a proton-antiproton collider at Fermilab which achieved first collisions in 1985 and operated until 2011, reaching a maximum centre-of-mass energy of $\sqrt{s} = 1.96$ TeV. The Tevatron machine delivered data to the two detector experiments: CDF [22] and D0 [23]. The main Higgs boson production modes at the Tevatron were: the associated production mode which includes both the WH and ZH channels as shown in Figure 2.5c, the *gluon-gluon fusion* (ggF) mode shown in Figure 2.5a, and the *vector*
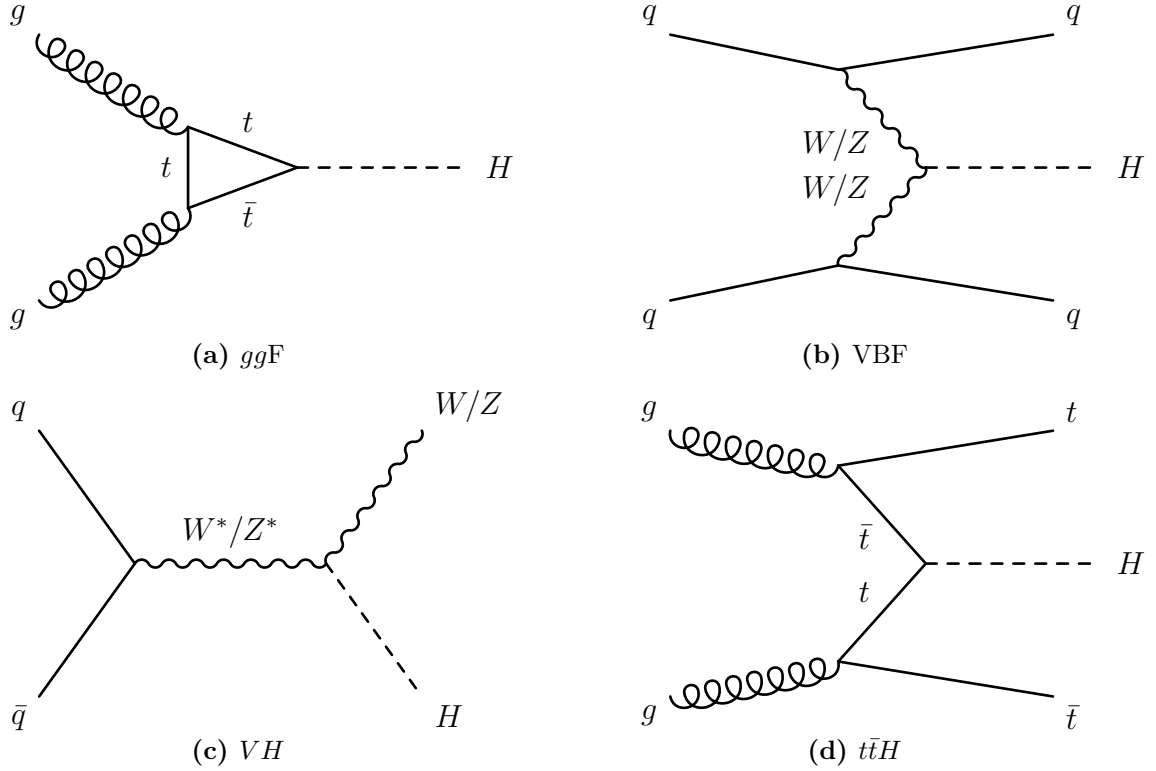
Figure 2.5: Feynman diagrams of the dominant SM Higgs boson production modes at the LHC and Tevatron: gluon-gluon fusion (a), vector boson fusion (b), associated production (c) and $t\bar{t}H$ (d).

boson fusion (VBF) channel shown in Figure 2.5b. The Higgs boson decay modes studied were: $H \to bb$, $H \to WW^{(*)}$, $H \to ZZ^{(*)}$, $H \to \tau\tau$, and $H \to \gamma\gamma$ where the branching fractions are given in Figure 2.3. The $H \to WW^{(*)}$ and $H \to ZZ^{(*)}$ decay modes become dominant at larger values of the Higgs boson mass which were inaccessible at LEP. The results of the combined searches by CDF and D0 are shown in Figure 2.6. The results are expressed as the upper limit on the ratio of the cross-section of the Higgs boson to the SM prediction, given at the 95% confidence level. The CDF and D0 experiments were able to exclude the Higgs boson mass range $147 < m_H < 180$ GeV at the 95% confidence level.

Searches at the LHC

The LHC is a proton-proton collider at CERN which began operation in 2009. In 2010 and 2011 collisions were recorded at $\sqrt{s} = 7$ TeV centre-of-mass energy, this was increased to $\sqrt{s} = 8$ TeV in 2012. ATLAS and CMS are two detector experiments at the

Figure 2.6: Combined results of the direct search for the SM Higgs boson by the CDF and D0 collaborations. The observed and expected limits at the 95% confidence level on the cross-section are shown as a function of the Higgs boson mass hypothesis. The mass ranges excluded by different experiments are also shown [24].
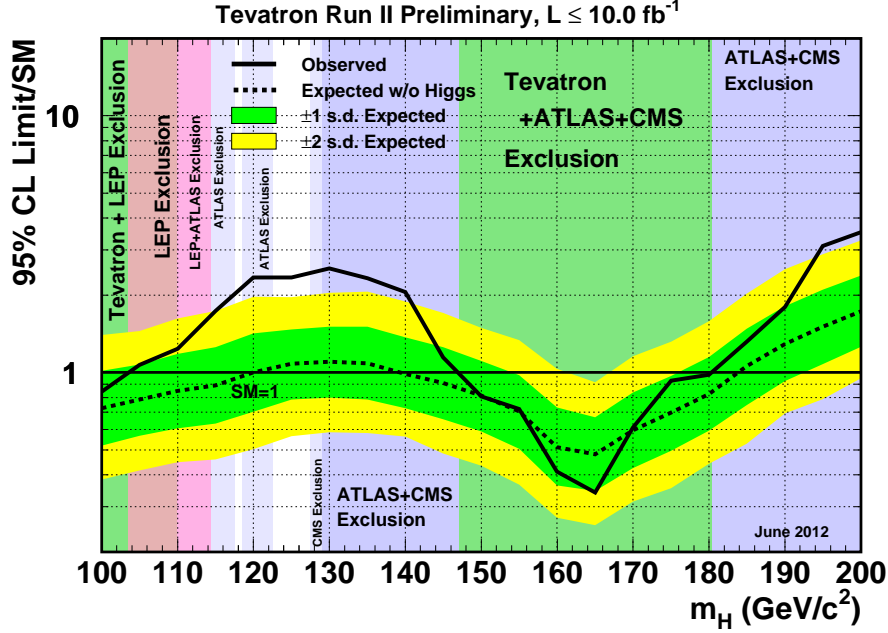
LHC which perform direct Higgs boson searches. Further details about the LHC and its detector experiments will be given in Chapter 3, the remainder of this section will outline the Higgs boson searches at the LHC. The main production modes of the Higgs boson at the LHC are shown in Figure 2.5, they are, in decreasing order of cross-section: ggF, VBF, WH, ZH and $t\bar{t}H$. Figure 2.7 shows the cross-sections of each of these processes as a function of the mass of the Higgs boson, the values of these cross-sections at $m_H = 125\,\text{GeV}$ are shown in Table 2.2.

In July of 2012, both ATLAS [2] and CMS [3] announced the observation of a new particle, with a mass near 125 GeV, consistent with the SM Higgs boson. The ATLAS result was made using the full 2011 dataset ($4.6 - 4.8\,\text{fb}^{-1}$ at $\sqrt{s} = 7\,\text{TeV}$) and a portion of the 2012 dataset ($5.8 - 5.9\,\text{fb}^{-1}$ at $\sqrt{s} = 8\,\text{TeV}$) and combined the analysis of many Higgs decay modes, in particular the $H \to \gamma\gamma$, $H \to ZZ^{(*)} \to 4\ell$, and $H \to WW^{(*)} \to \ell\nu\ell\nu$ decay modes provided most of the sensitivity. The invariant mass distributions of the $H \to \gamma\gamma$ and $H \to ZZ^{(*)} \to 4\ell$ channels are shown in Figure 2.8, which shows an excess of observed events above the expected background yield at 125 GeV. The local significance of the excess was observed to be 5.9σ, corresponding to the probability of $p_0 = 1.7 \times 10^{-9}$,

Figure 2.7: Cross-sections of the five dominant Higgs boson production modes in proton-proton collisions at the LHC at $\sqrt{s} = 8$ TeV centre-of-mass energy [20].

Production Mode	Cross-section [pb]	Fraction of Total [%]
$pp \rightarrow H$ (ggF)	$19.27 \pm 10.4\%$	87.2
$pp \rightarrow qqH$ (VBF)	$1.578^{+2.6\%}_{-2.8\%}$	7.1
$pp \rightarrow WH$	$0.7046 \pm 3.4\%$	3.2
$pp \rightarrow ZH$	$0.4153 \pm 5.6\%$	1.9
$pp \rightarrow t\bar{t}H$	$0.1293^{+8.9\%}_{-12.3\%}$	0.6

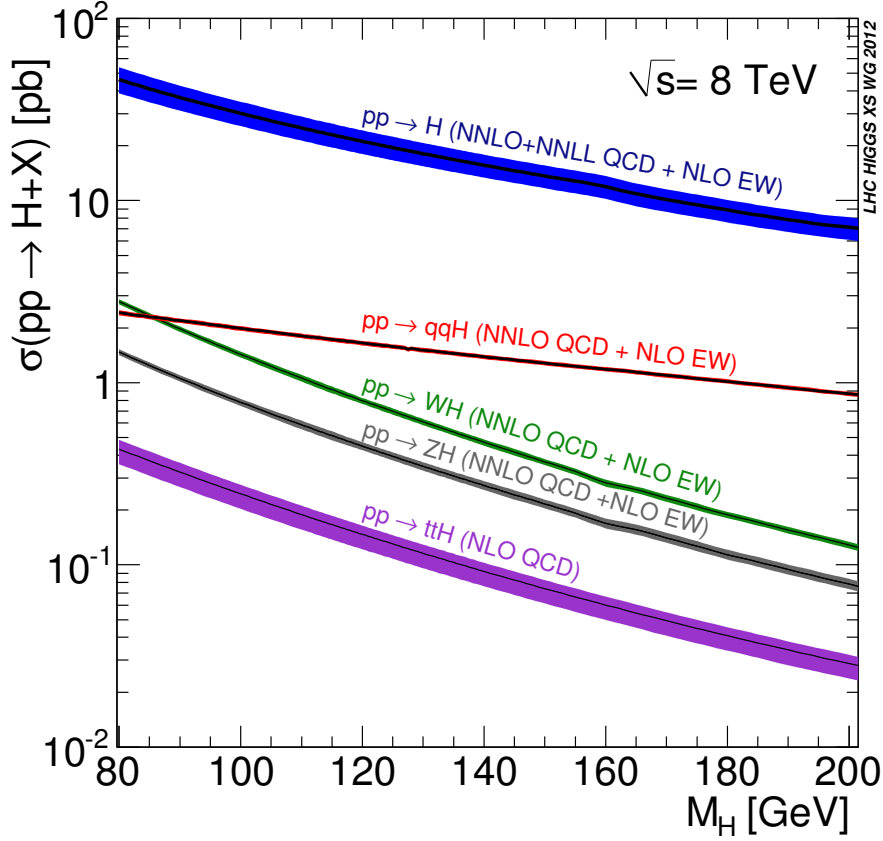**Table 2.2:** Cross-sections of the five dominant Higgs boson production modes in proton-proton collisions at the LHC at $\sqrt{s} = 8$ TeV centre-of-mass energy for a Higgs boson mass of $m_H = 125$ GeV [20].

that the background can produce a fluctuation at least as large as the observed excess in data. The local significance as a function of the Higgs boson mass hypothesis is shown in Figure 2.9.
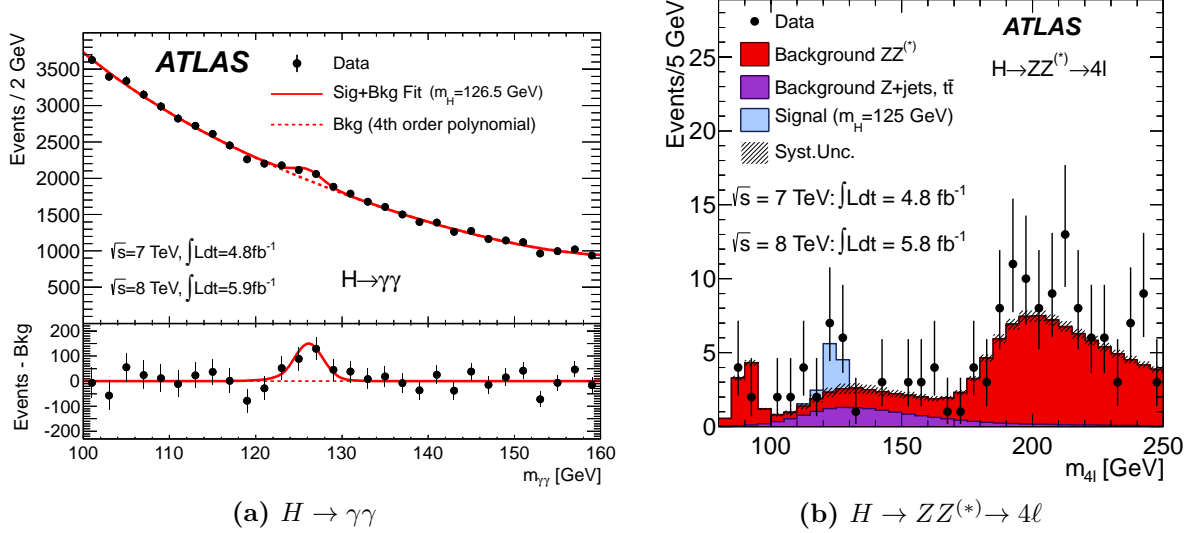
Figure 2.8: Invariant mass distributions of: the di-photon system in the $H \to \gamma\gamma$ search (a), and the four-lepton system in the $H \to ZZ^{(*)} \to 4\ell$ search (b) at ATLAS [2].

After the completion of the 2012 data taking period, each of these three analysis channels was provided with enough statistics to each separately claim observation [25–27]. In particle physics searches, it is a convention to claim an excess above 5σ an *observation*, and an excess above 3σ as *evidence*. These observations of Higgs boson couplings to the $W^\pm$ and Z bosons provide strong evidence for the nature of gauge boson masses predicted by the SM as described in Section 2.1.4.

2.2.2 Measurements of Higgs Boson Properties

Since the discovery of a new particle consistent with the Higgs boson, its nature has been investigated further to strengthen the hypothesis that this new particle is indeed the SM Higgs boson. Its properties, including mass, production and decay rates, spin, and parity, have been measured by ATLAS and CMS using the full 2011 and 2012 dataset.

A mass measurement is made based on the combined data samples of the ATLAS and CMS experiments in the $H \to \gamma\gamma$ and $H \to ZZ^{(*)} \to 4\ell$ decay channels, which have the best mass resolution [28]. The results are obtained from a simultaneous fit to the reconstructed invariant mass peaks in the two channels and for the two experiments. The measured masses from the individual channels and the two experiments are found to be
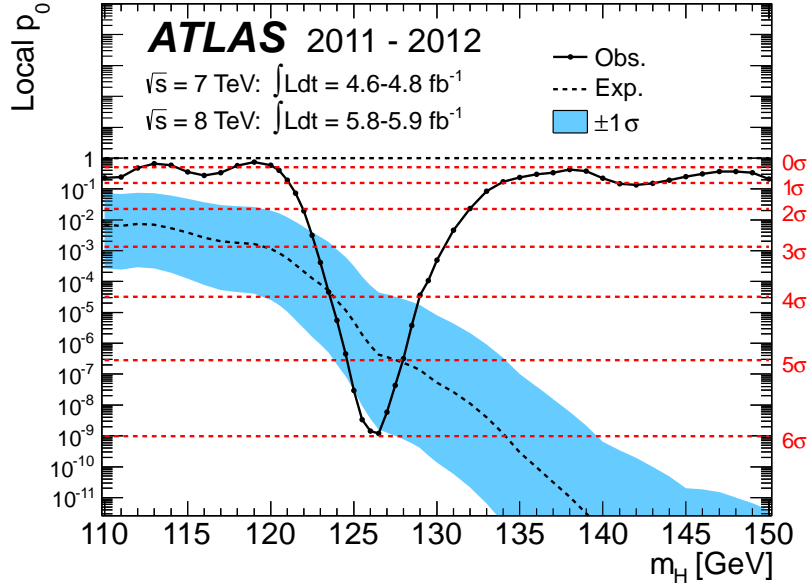
Figure 2.9: The observed (solid) local p_0 as a function of the Higgs boson mass hypothesis m_H. The dashed curve shows the expected local p_0 under the hypothesis of a SM Higgs boson signal at that mass with its $\pm 1\sigma$ band. The horizontal dashed lines indicate the p-values corresponding to significances of 1 to 6 σ. The result is from the combination of the $H \to \gamma\gamma$, $H \to ZZ^{(*)} \to 4\ell$, and $H \to WW^{(*)} \to \ell\nu\ell\nu$ channels studied at ATLAS [2].

consistent among themselves within 2σ, as seen in Figure 2.10. The combined measured mass of the Higgs boson is $m_H = 125.09 \pm 0.21(\text{stat.}) \pm 0.11(\text{syst.})$ GeV [28].

The relative contribution to each Higgs decay channel is determined with a corresponding signal strength parameter μ, which is the ratio of the observed rate to that predicted by the SM. Any significant deviation from the SM expectation of $\mu = 1$ would be a sign of new physics. Figure 2.11 shows the measurements of the signal strength parameter μ from a simultaneous fit to all decay channels studied at ATLAS [4]. Combining all measurements results in a global signal strength value of $\mu = 1.18^{+0.15}_{-0.14} = 1.18 \pm 0.10(\text{stat.}) \pm 0.07(\text{expt.})^{+0.08}_{-0.07}(\text{theo.})$, consistent with the SM expectation with a p-value of 18%. Each of the channel measurements are consistent and compatible with the combined value with a p-value of 76%.

In addition to the signal strengths of different decay channels, the signal strengths of different production modes are determined, exploiting the sensitivity offered by the use of event categories in the analyses of all channels. The Higgs boson production processes can be categorised into two groups according to the Higgs boson couplings to
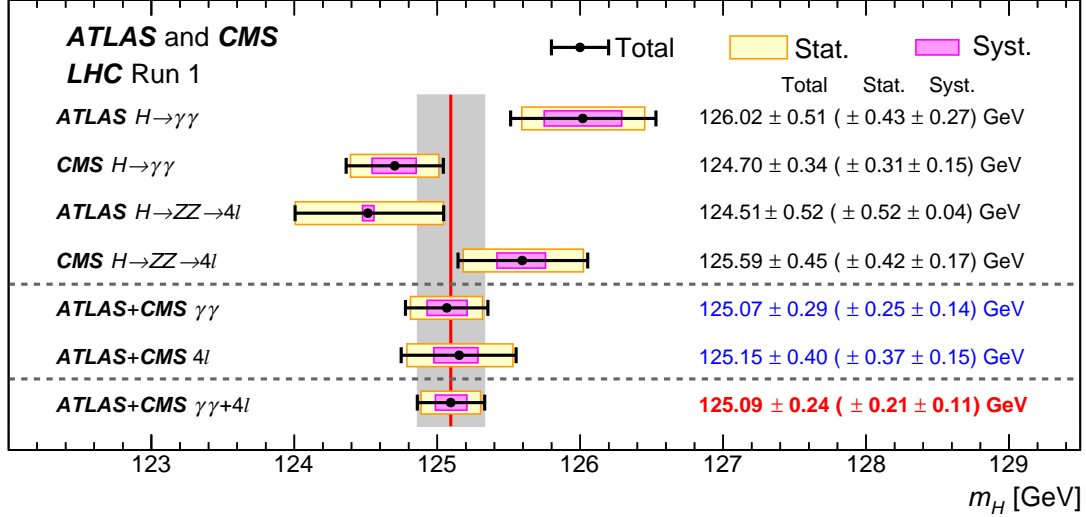
Figure 2.10: Summary of Higgs boson mass measurements from the individual analyses of ATLAS and CMS and the combination. The systematic (narrower, magenta-shaded bands), statistical (wider, yellow-shaded bands), and total (black error bars) uncertainties are indicated. The (red) vertical line and corresponding (grey) shaded column indicate the central value and the total uncertainty of the combined measurement, respectively [28].

fermions (ggF and $t\bar{t}H$) or vector bosons (VBF and VH). Potential deviations from the SM can be tested with two signal strength parameters, $\mu_{ggF+t\bar{t}H} \equiv (\mu_{ggF} = \mu_{t\bar{t}H})$ and $\mu_{VBF+VH} \equiv (\mu_{VBF} = \mu_{VH})$ for each decay channel. The 68% and 95% confidence level two-dimensional contours of $\mu_{ggF+t\bar{t}H}$ and μ_{VBF+VH} of the five main decay channels are shown in Figure 2.12. The SM expectation of $\mu_{ggF+t\bar{t}H} = 1$ and $\mu_{VBF+VH} = 1$ is within the 68% confidence level contour of most of these measurements [4].

The SM predicts the Higgs boson to be spin 0 and even parity, $J^P = 0^+$. This hypothesis has been tested against alternative hypotheses: $J^P = 0^-$, 1^+, 1^-, and 2^+ [5]. The observation of the $H \to \gamma\gamma$ decay channel excludes the possibility of the spin 1 hypothesis, as the decay of a massive spin 1 particle into a pair of identical massless spin 1 particles is forbidden by the Landau-Yang theorem [29, 30]. The 2^+ hypothesis is tested in fractional variations of gg- and $q\bar{q}$-initiated production processes, using the $H \to \gamma\gamma$, $H \to ZZ^{(*)} \to 4\ell$, and $H \to WW^{(*)} \to \ell\nu\ell\nu$ decay channels, and is excluded at a confidence level of more than 99.9%. The 0^- hypothesis is tested using kinematic distributions in the $H \to ZZ^{(*)} \to 4\ell$ decay channel, and is rejected at the 97.8% confidence level. The SM prediction is strongly favoured compared to these alternate hypotheses.
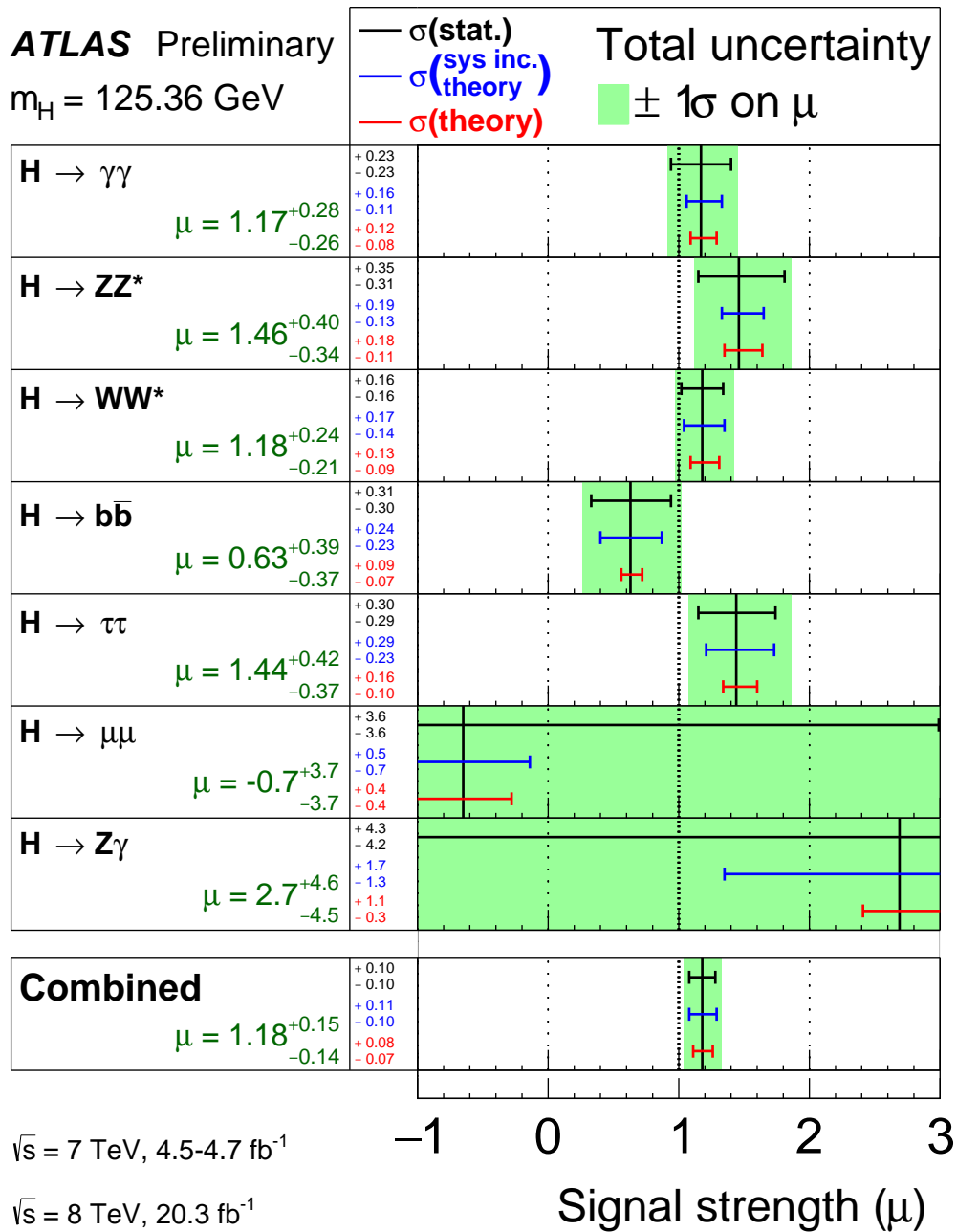
Figure 2.11: The observed signal strengths and uncertainties for different Higgs boson decay channels and their combination measured at ATLAS. The best-fit values are shown by the solid vertical lines. The total $\pm 1\sigma$ uncertainty is indicated by green shaded bands, with the individual contributions from the statistical uncertainty (top), the total (experimental and theoretical) systematic uncertainty (middle), and the theory systematic uncertainty (bottom) on the signal strength shown as horizontal error bars [4].
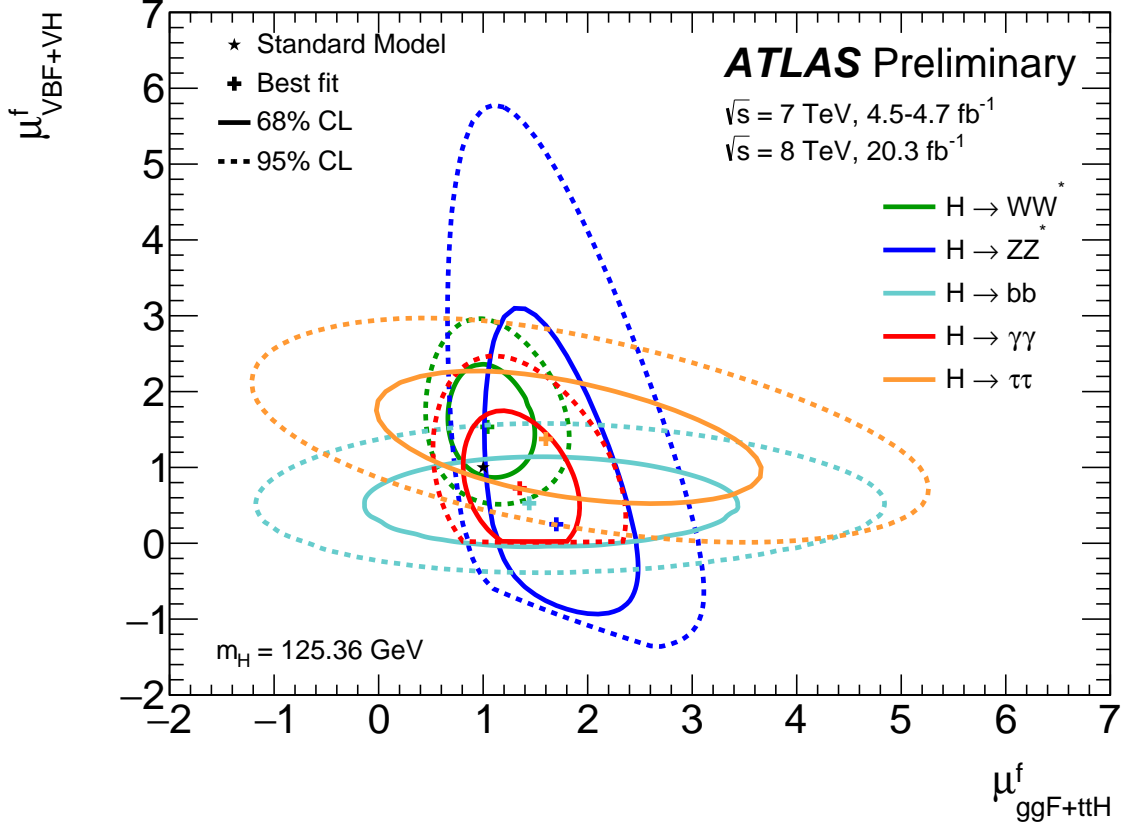
Figure 2.12: Likelihood contours in the ($\mu_{ggF+t\bar{t}H}$, μ_{VBF+VH}) plane, measured separately for $H \rightarrow WW^{(*)}$, $H \rightarrow ZZ^{(*)}$, $H \rightarrow bb$, $H \rightarrow \gamma\gamma$, and $H \rightarrow \tau\tau$ decays at ATLAS. The best-fit values to the data (+) and the 68% (full) and 95% (dashed) confidence level contours are indicated, as well as the SM expectation ($\star$) [4].

2.2.3 Fermionic Decay Modes

To date, observation of Higgs boson decays to fermionic final states is not conclusive, while the data show evidence for the presence of fermionic decays, the results are not significant enough to claim observation. It is necessary to study fermionic final states to determine if the new observed particle is consistent with the SM prediction. The observation of fermionic decay modes would provide strong evidence that fermions also acquire mass through the Higgs mechanism as described in Section 2.1.5. In particular, analysis of the $H \rightarrow \tau\tau$ decay mode, having the second largest branching fraction of all fermionic decay modes at $m_H = 125$ GeV, is one of the most promising opportunities to provide such evidence. To date, the $H \rightarrow \tau\tau$ decay mode has been studied at ATLAS using the full 2011 and 2012 dataset in the VBF and ggF production channels [6]. Two exclusive analysis categories are defined to exploit signal sensitive event topologies. The

VBF category targets Higgs bosons produced via VBF, these events are characterised by the presence of two jets with large transverse momenta and a large pseudorapidity separation. The *boosted* category targets events produced via ggF where the Higgs boson has a large transverse momentum. While an excess has been seen in these channels, shown in Figure 2.13, the results are not significant enough to claim observation. For this reason, analysis of all production channels is necessary, in particular the WH and ZH associated production channels may provide additional sensitivity.

2.3 The Associated Higgs Production Channel

The associated production channel (denoted VH, where $V = W/Z$) of a Higgs boson with a W or Z boson has a small cross-section compared to other production modes such as ggF and VBF, as shown in Figure 2.7. For this reason, previous searches for the Higgs boson in the $H \to \tau\tau$ decay mode at ATLAS have focused their attention on the ggF and VBF production modes. The VH production modes can contain additional light leptons, which have a high reconstruction efficiency. For this reason, the VH production modes offer an additional opportunity to study Higgs boson properties. While the $W(\to \ell\nu)H(\to \tau\tau)$ and $Z(\to \ell\ell)H(\to \tau\tau)$ production modes have not previously been studied at ATLAS, they have been studied at CMS [31].

2.3.1 Production and Decay Channels

There are six different VH event topologies where the W/Z boson decays leptonically and the Higgs boson decays to taus, shown in Figure 2.14. Taus can decay leptonically ($\tau \to \ell\nu_\ell\nu_\tau$), denoted τ_ℓ, or hadronically ($\tau \to$ hadrons ν_τ), denoted τ_h. Here and throughout this work, ℓ is used to denote the light leptons: e, and μ. This set of six channels is made from the combinations of two production modes (WH or ZH) and three Higgs decay modes ($\tau_\ell\tau_\ell$, $\tau_\ell\tau_h$, or $\tau_h\tau_h$). These channels can be differentiated by the number of light leptons and hadronic taus reconstructed in their final state. A summary of each channel is given below:

- $W(\to \ell\nu)H(\to \tau_\ell\tau_\ell)$ (Figure 2.14a): This channel contains three light leptons. The light leptons may be either flavour. Two of the light leptons will have opposite charge, the third light lepton may have either charge. A total of five neutrinos will be produced from the W and τ decays.
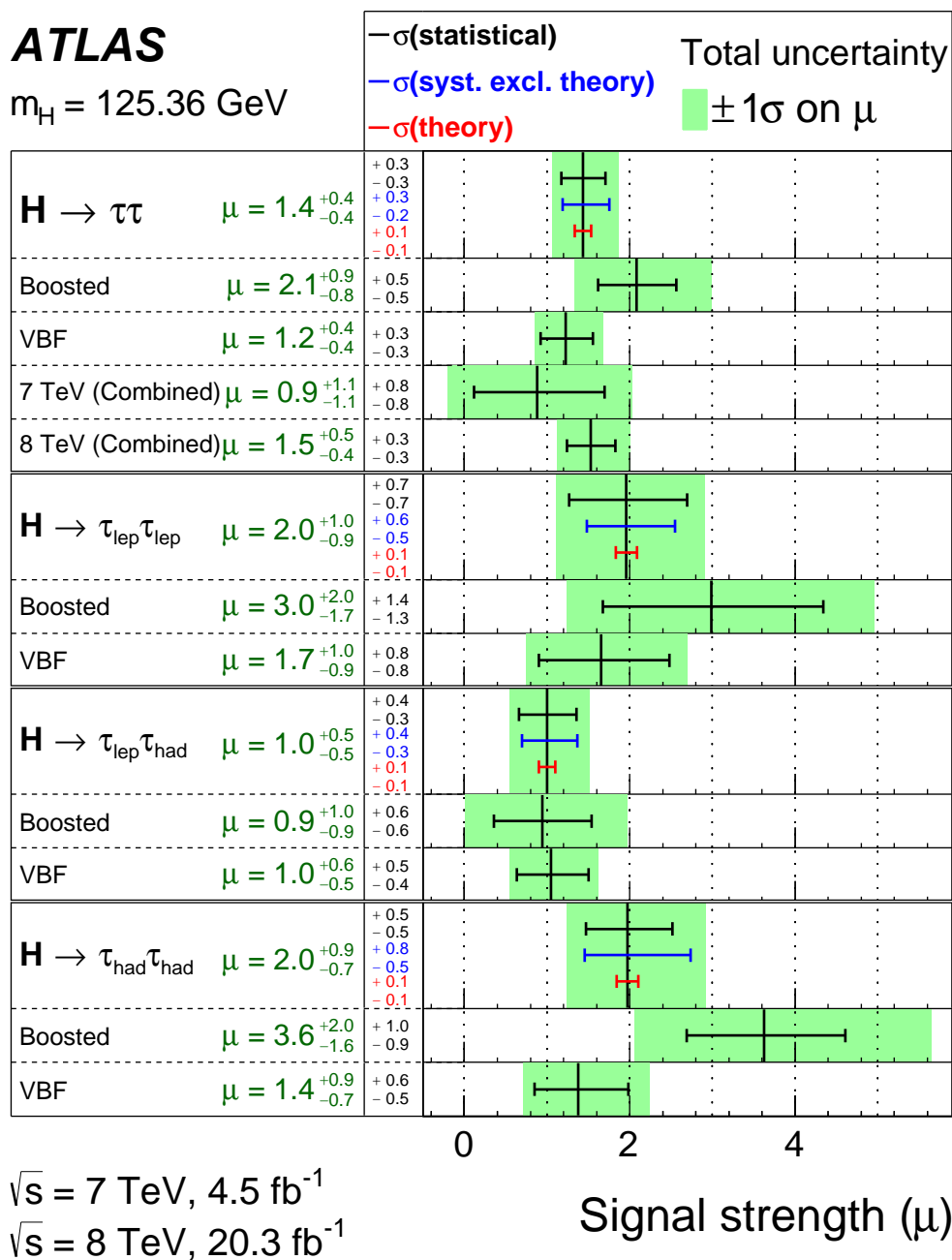
Figure 2.13: The observed signal strengths and uncertainties for different $H \rightarrow \tau\tau$ decay channels and their combination measured at ATLAS. The total $\pm 1\sigma$ uncertainty is indicated by the shaded green band, with the individual contributions from the statistical uncertainty (top, black), the experimental systematic uncertainty (middle, blue), and the theory uncertainty (bottom, red) on the signal cross-section (from QCD scale, PDF, and branching ratios) shown by the error bars and printed in the central column [6].

- $W(\to \ell\nu)H(\to \tau_\ell\tau_h)$ (Figure 2.14b): This channel contains two light leptons and one hadronic tau. The light leptons may be either flavour and either charge. One of the light leptons will be opposite charge to the tau, the other light lepton may have either charge. A total of four neutrinos will be produced from the W and τ decays.

- $W(\to \ell\nu)H(\to \tau_h\tau_h)$ (Figure 2.14c): This channel contains two hadronic taus and one light lepton. The two hadronic taus will be opposite charge. A total of three neutrinos will be produced from the W and τ decays.

- $Z(\to \ell\ell)H(\to \tau_\ell\tau_\ell)$ (Figure 2.14d): This channel contains four light leptons. One pair of light leptons will be the same flavour and opposite charge. The other pair will be opposite charge but each can be either flavour. Four neutrinos will be produced from the τ decays.

- $Z(\to \ell\ell)H(\to \tau_\ell\tau_h)$ (Figure 2.14e): This channel contains three light leptons and one hadronic tau. Two of the light leptons will have the same flavour and opposite charge. The other light lepton may have either flavour and will have opposite charge to the hadronic tau. Three neutrinos will be produced from the τ decays.

- $Z(\to \ell\ell)H(\to \tau_h\tau_h)$ (Figure 2.14f): This channel contains two light leptons and two hadronic taus. Two of the light leptons will have the same flavour and opposite charge. The two hadronic taus will have opposite charge. Two neutrinos will be produced from the τ decays.

The production cross-section of the WH channel is larger than that of the ZH channel. Of all the $H \to \tau\tau$ decay modes, the $\tau_\ell\tau_h$ channel has the highest branching fraction (45.5%), followed by the $\tau_h\tau_h$ channel (42.25%), and the $\tau_\ell\tau_\ell$ channel (12.25%). The cross-section times branching fraction ($\sigma \times BF$) for each channel is shown in Figure 2.15 as a function of the Higgs mass. The total $pp \to VH$ cross-section decreases smoothly towards higher Higgs masses due to the increase in energy required to produce the Higgs. The branching fraction decreases with higher Higgs mass and has a distinct drop-off at around 160 GeV ($\approx 2m_W$) where other decay modes such as $H \to WW$ and $H \to ZZ$ become available. At the measured Higgs mass value of 125 GeV, the $H \to \tau\tau$ decay branching fraction is 6.3% [20]. The $W(\to \ell\nu)H(\to \tau_\ell\tau_h)$ and $W(\to \ell\nu)H(\to \tau_h\tau_h)$ channels have the largest production rate of all channels. Given that light lepton reconstruction is more efficient than hadronic tau reconstruction, the $W(\to \ell\nu)H(\to \tau_\ell\tau_h)$ channel provides the best search opportunity.

(a) $W(\to \ell\nu)H(\to \tau_\ell\tau_\ell)$

(b) $W(\to \ell\nu)H(\to \tau_\ell\tau_h)$

(c) $W(\to \ell\nu)H(\to \tau_h\tau_h)$

(d) $Z(\to \ell\ell)H(\to \tau_\ell\tau_\ell)$

(e) $Z(\to \ell\ell)H(\to \tau_\ell\tau_h)$

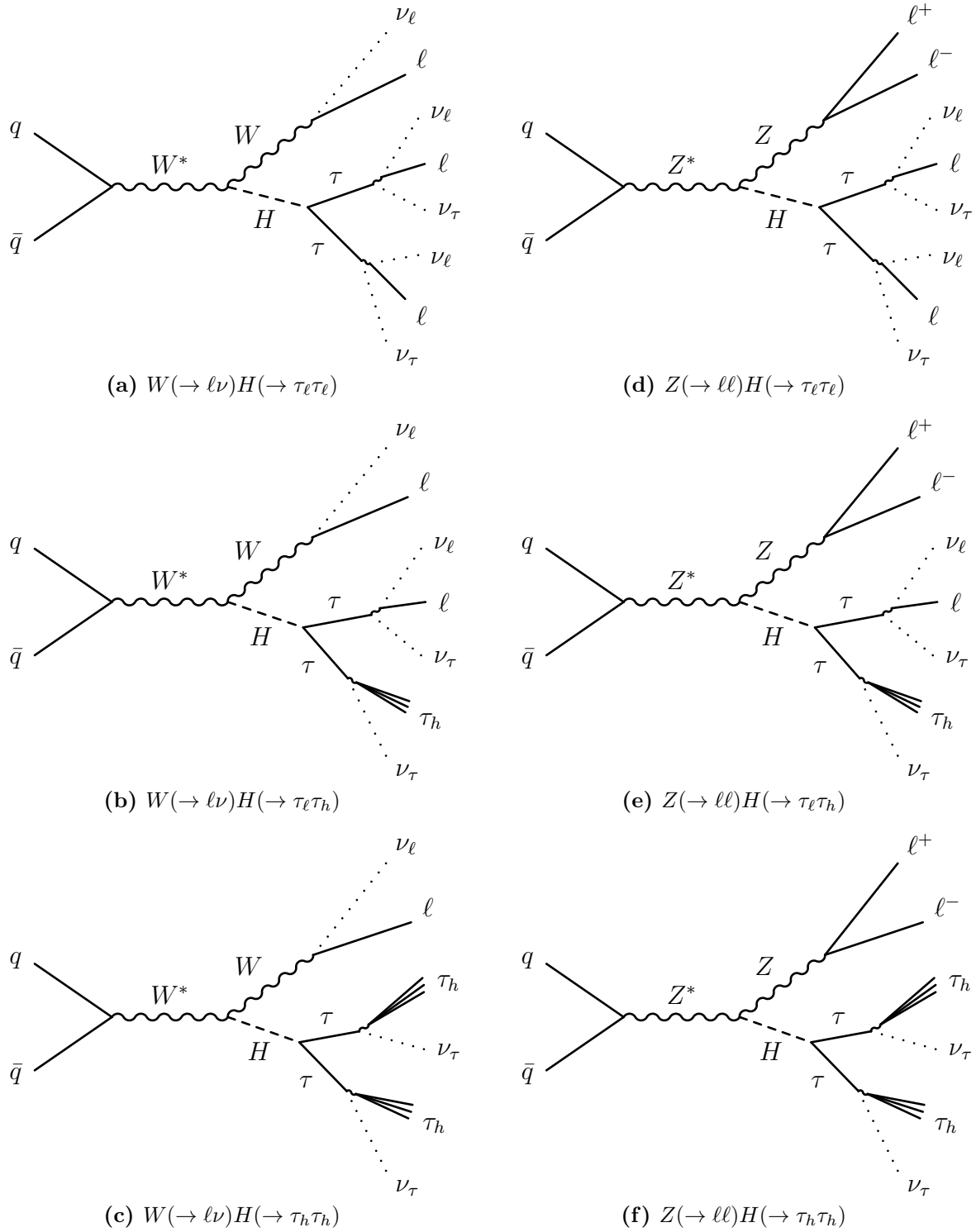**(f)** $Z(\to \ell\ell)H(\to \tau_h\tau_h)$

Figure 2.14: Feynman diagram of the production and decay of a Higgs boson in association with a vector boson where the Higgs boson decays to a tau pair.
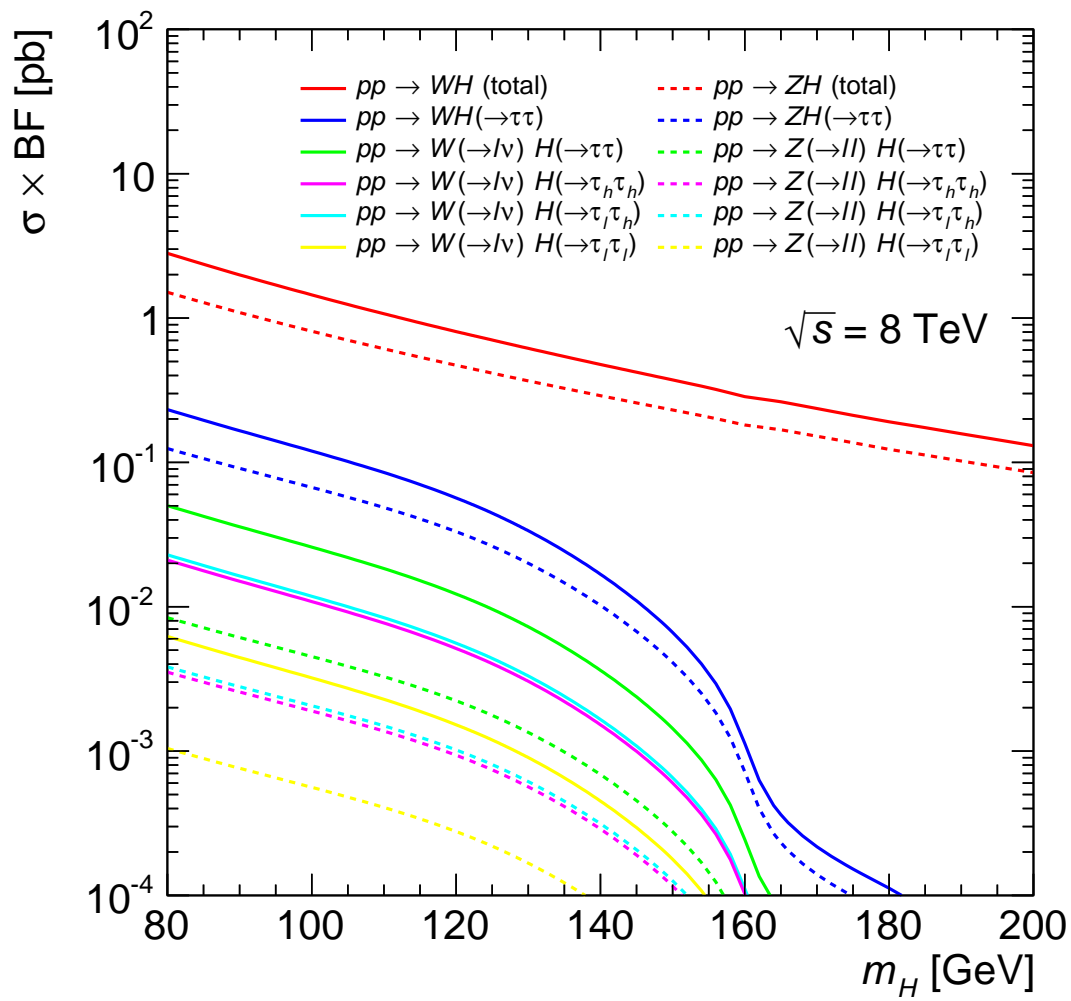
Figure 2.15: Production cross-section times decay branching fraction for each of the VH channels as a function of the Higgs mass [20].

Chapter 3

The ATLAS Experiment at the Large Hadron Collider

Founded in 1954, the European Organisation for Nuclear Research (CERN), located outside Geneva, Switzerland, is one of the largest scientific research institutes in the world. CERN operates a network of particle accelerators, the Large Hadron Collider (LHC) is the most recent and is the most powerful particle collider in existence today.

The LHC accelerates two beams of protons or heavy ions in opposite directions. These beams are made to collide at four locations on the ring where detector experiments are installed. The ATLAS (A Toroidal LHC Apparatus) [32] and CMS (Compact Muon Solenoid) [33] experiments are general purpose detectors whose core physics program is to understand the nature of the Higgs boson predicted by the SM. The LHCb [34] experiment is designed for making precision measurements of the rare decays of B mesons. The ALICE (A Large Ion Collider Experiment) [35] experiment is designed to study the nature of the strong interaction in the quark-gluon plasma.

3.1 The Large Hadron Collider

The LHC is housed in the tunnel formerly used for the Large Electron Positron Collider (LEP) which is roughly circular with a 26.7 km circumference, consisting of eight straight sections and eight arcs. It lies between 45 and 170 m underground. The layout of the LHC machine is shown in Figure 3.1. Each of the eight straight sections serve as sites for experiments or machine utilities and are numbered 1-8 in the clockwise direction.
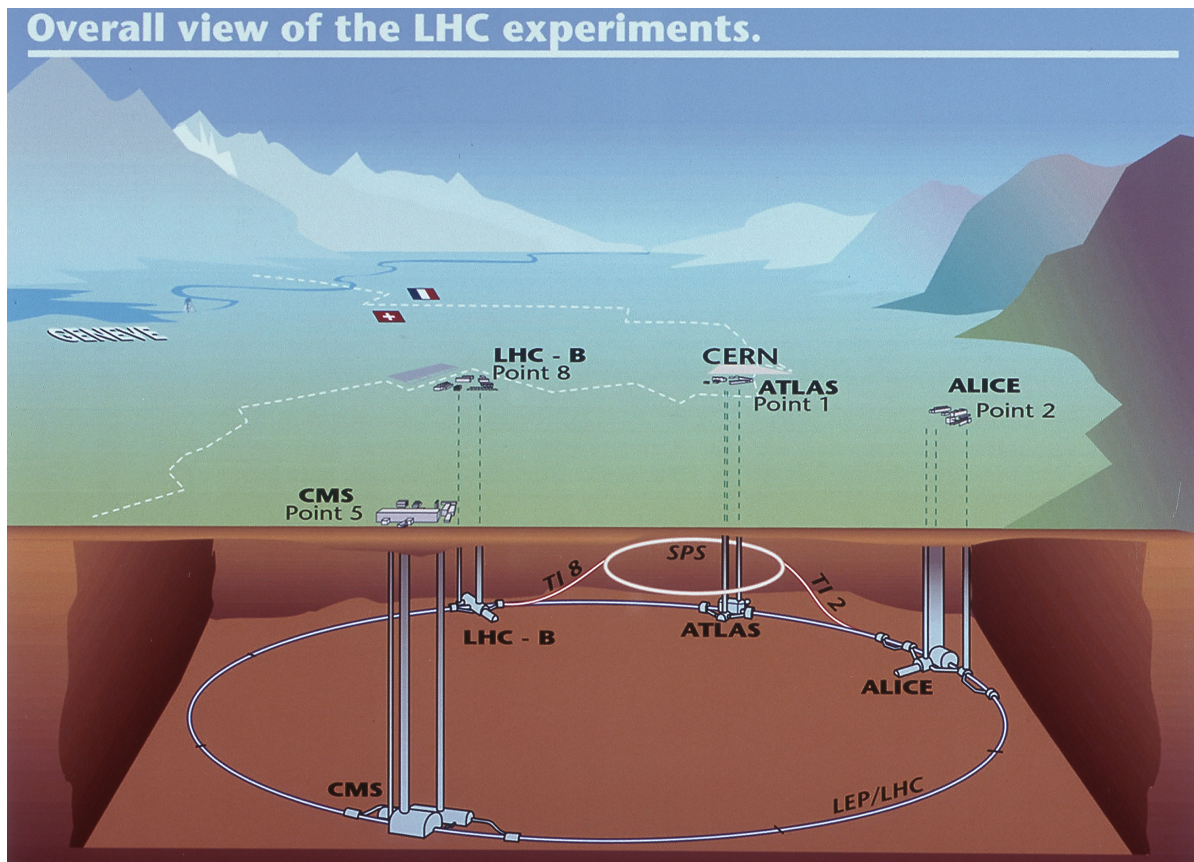
Figure 3.1: Schematic of the LHC showing the four main experiments [36].

The four main detector experiments: ATLAS, CMS, ALICE, and LHCb, are located on the straight sections at Points: 1, 5, 2, and 8, respectively. The two proton beams are injected into the LHC at Points 2 and 8 with an energy of 450 GeV by a series of smaller accelerator facilities. The two proton beams are then further accelerated by two independent radio-frequency systems at Point 4. Each system contains 8 superconducting radio-frequency cavities which produce an oscillating potential difference. The eight arc sections contain a total of 1232 superconducting dipole magnets which provide the 8.3 T magnetic field required to bend the protons trajectory. The superconducting systems are cooled to a temperature of 1.9 K by a liquid helium based cryogenic system.

In March of 2010 the first proton-proton collisions took place at 7 TeV centre-of-mass energy. In 2011 proton-proton collisions were recorded at 7 TeV, and in 2012 the centre-of-mass energy was increased to 8 TeV. After a roughly two-year long shutdown period, proton-proton collisions at 13 TeV began in June of 2015. By the end of 2015, an integrated luminosity of 4.3 fb^{-1} was recorded.

Parameter	2010	2011	2012	Nominal
centre-of-mass energy [TeV]	7	7	8	14
N_p [10^{11}]	1.2	1.5	1.6	1.15
n_b	348	1380	1380	2808
ϵ_n [μm]	2.4-4	1.9-2.4	2.2-2.5	3.75
β^* [m]	3.5	1.5→1	0.6	0.55
crossing angle [μrad]	200	240	290	285
bunch spacing [ns]	150	75→50	50	25
L [10^{34} cm^{-2}s^{-1}]	0.02	0.4	0.76	1

Table 3.1: Summary of the LHC proton-proton beam parameters for the 2010, 2011 and 2012 data taking periods as well as the nominal design configuration.

The event rate of a process with a cross-section[1] σ, is given by

$$\frac{dN}{dt} = L\sigma \tag{3.1}$$

where L is the *instantaneous luminosity* of the proton-proton collisions which is determined by the beam parameters according to

$$L = \frac{N_p^2 n_b f \gamma F}{4\pi\epsilon_n\beta^*} \tag{3.2}$$

where N_p is the number of protons in each bunch, n_b is the number of bunches per beam, f is the revolution frequency, γ is the relativistic gamma factor of the protons, ϵ_n is the normalised transverse beam emittance, which is a measure of the spread of the beam, β^* is a measure of how much the beam is squeezed toward the interaction point, and F is the geometric luminosity reduction factor due to the crossing angle at the interaction point. The operational and nominal design values of these parameters for proton-proton collisions are shown in Table 3.1.

The integral of the instantaneous luminosity over time gives the *integrated luminosity*, expressed in units of inverse cross-section, given by

$$\mathcal{L} = \int L dt \tag{3.3}$$

---

[1]Cross-sections are measured in units of area, typically expressed in *barns*, where $1b = 10^{-28}$ m^2.

(a) Integrated luminosity recorded in 2011

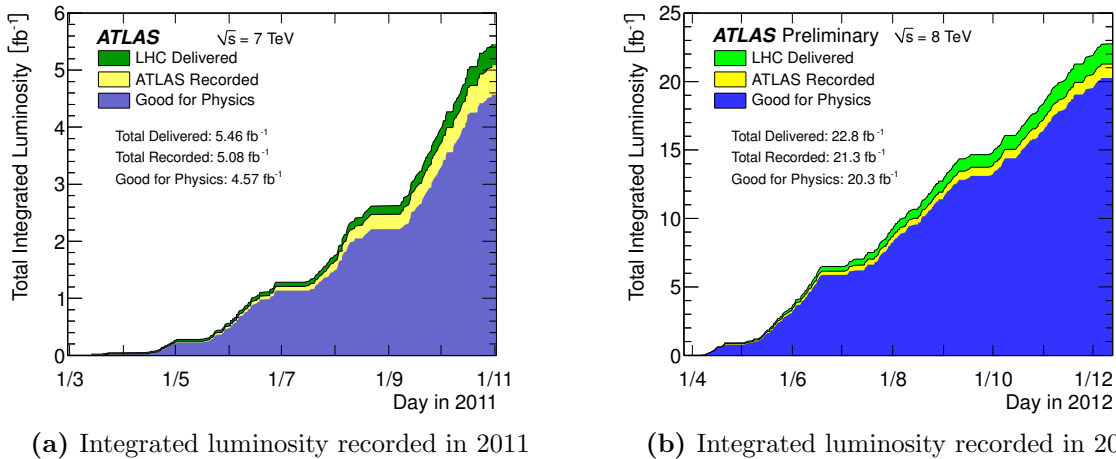**(b)** Integrated luminosity recorded in 2012

Figure 3.2: Cumulative luminosity versus time delivered by the LHC (green), recorded by ATLAS (yellow), and certified to be good quality data (blue) in 2011 (a) and 2012 (b) [37].

The number of expected events of a process with cross-section σ in this time period is

$$N = \mathcal{L}\sigma \tag{3.4}$$

Figure 3.2 shows the integrated luminosity delivered to ATLAS during the 2011 and 2012 data taking periods. In 2012, for example, it can be seen that the LHC delivered $22.8\,\mathrm{fb}^{-1}$ of data to ATLAS of which $20.3\,\mathrm{fb}^{-1}$ are certified as quality data to be used for physics analysis.

3.2 The ATLAS Detector

The ATLAS detector [32] is a general purpose detector located at Point 1 on the LHC beam line. The layout of the entire detector is shown in Figure 3.3 which shows its dimensions and labels most of its main components. The ATLAS detector has a cylindrical geometry centred at the interaction point on the beam line with a length of 44 m, a diameter of 25 m, and a weight of 7000 t. It contains multiple concentric sub-detector systems which measure different properties of particles produced in proton-proton collisions. The remainder of this section will outline these sub-detector systems.
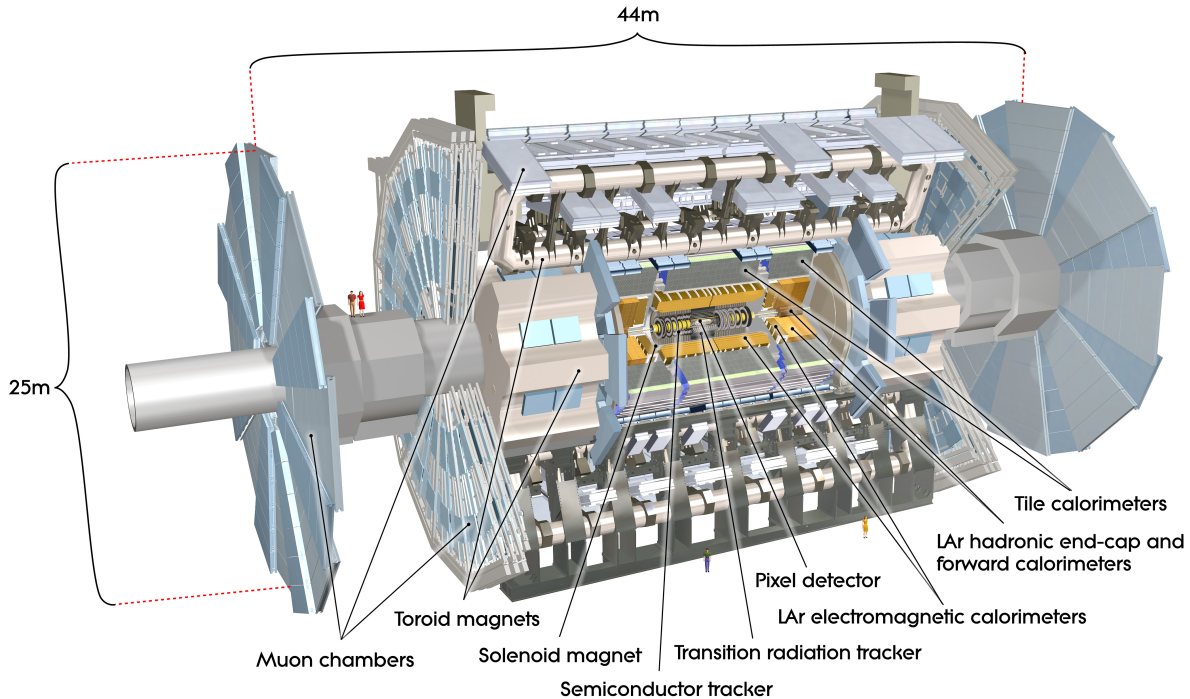
Figure 3.3: Schematic of the entire ATLAS detector [36].

3.2.1 Coordinate System

The coordinate system of the ATLAS detector is as follows. The origin is the nominal interaction point at the centre of the detector. The positive x direction points toward the centre of the LHC ring, the positive y direction points upward and the z direction points along beam line. The $x - y$ plane is the transverse plane. In addition to the cartesian coordinate system, it is more convenient to also define the azimuthal angle ϕ around the beam line in the transverse plane. The polar angle θ is the angle from the beam axis. The *pseudorapidity* is defined as $\eta \equiv \ln \tan \frac{\theta}{2}$. $\eta = 0$ is on the transverse plane, and $\eta = \pm\infty$ are the directions forward and backward along the beam line. It is common practice to define a variable, $\Delta R \equiv \sqrt{(\Delta\phi)^2 + (\Delta\eta)^2}$, which is a measure of the angular separation between two objects in the detector (particles, jets, tracks, etc). One would expect the maximum value of ΔR to be π when objects are back-to-back as ϕ is in the range $\pm\pi$, however η is in the range $\pm\infty$ so ΔR can be greater than π if the particles are back-to-back with large $|\eta|$.

Most proton-proton interactions of interest only involve one *parton* (quark or gluon) from each proton. Although the total energy of each proton is known, each parton can

carry any fraction of the total momentum of the proton, as such the initial *longitudinal* momentum of the colliding partons is not known. It is however known that the initial *transverse* momenta of the colliding partons is close to zero, since the protons are being collided head on. For this reason, most quantities are measured in the transverse plane. The *transverse momentum* two-vector $\vec{p}_{\mathrm{T}} = (p_x, \ p_y)$ is a quantity derived primarily from tracking information. It is common to use the magnitude of this vector, defined as $p_{\mathrm{T}} = |\vec{p}_{\mathrm{T}}| = |\vec{p}| \sin\theta$, for analysis requirements. The *transverse energy* two-vector $\vec{E}_{\mathrm{T}} = (E_x, \ E_y)$ is a quantity derived from energy deposits in the calorimeters and the direction of the deposits relative to the interaction point. The magnitude of this vector is denoted as $E_{\mathrm{T}} = |\vec{E}_{\mathrm{T}}| = E \sin\theta$. Although energy is normally known as a scalar quantity, the transverse energy vector is a useful quantity since it is equivalent to transverse momentum for massless particles and is a good approximation for relativistic particles which have a large momentum compared to their mass. Neutrinos produced in the proton-proton interactions will leave the detector without a recorded response, however their presence can be inferred by a momentum imbalance in the transverse plane. The *missing transverse energy* two-vector $\vec{E}_{\mathrm{T}}^{\mathrm{miss}} = (E_x^{\mathrm{miss}}, \ E_y^{\mathrm{miss}})$ is a quantity derived primarily from calorimeter information which will be described in Section 3.4.5. The magnitude of this vector, defined as $E_{\mathrm{T}}^{\mathrm{miss}} = |\vec{E}_{\mathrm{T}}^{\mathrm{miss}}|$, is useful for analysis requirements.

3.2.2 Inner Detector

The ATLAS Inner Detector (ID), shown in Figure 3.4, is the first sub-detector system surrounding the interaction point. It is 6.2 m long and 2.1 m in diameter, covering the region $|\eta| < 2.5$. The aim of the ID is to measure the tracks of charged particles and their properties such as p_{T}, η, and ϕ. The ID sits inside a 2 T magnetic field generated by a solenoidal magnet which, due to the Lorentz force, curves the path of charged particles in the transverse plane and allows the inner detector to measure their charge and momentum. To accomplish this, three sub-detector systems are used. Each contains a barrel section surrounding the interaction point and an end-cap section on each end of the barrel section.

Pixel Detector

The silicon Pixel Detector (PD) [38] consists of three barrel layers with average radii of 5 cm, 9 cm, and 12 cm, and three end-cap disks on each end. It consists of 1744 modules,
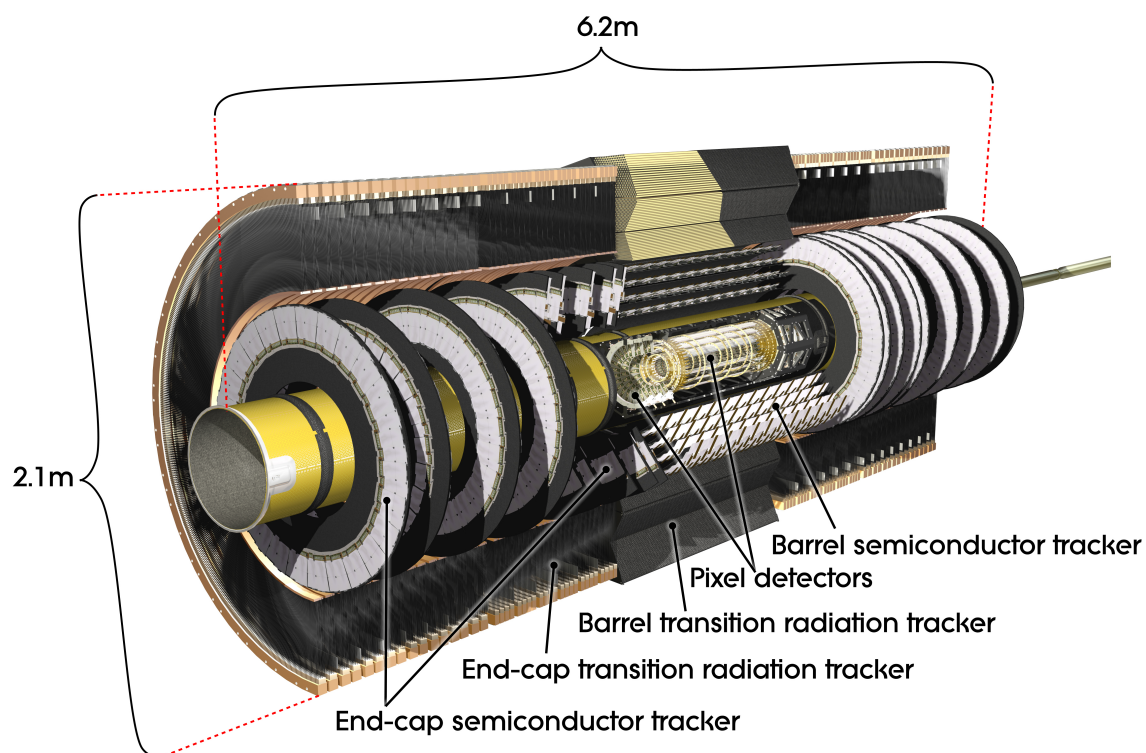
Figure 3.4: Schematic of the ATLAS inner detector [36].

each with a size of 19 mm×63 mm. Each module contains 47232 silicon pixels with a size of 50 μm×400 μm in the $\phi \times z$ directions. The spatial resolution of a single hit in the PD is about 14 μm×115 μm in the $\phi \times z$ directions. A typical track will pass through three pixel layers.

Semiconductor Tracker

Surrounding the PD is the Semiconductor Tracker (SCT) [39] which consists of four barrel layers with average radii of 30 cm, 37 cm, 44 cm, and 51 cm, and nine end-cap discs on each end. It consists of 4088 double-sided modules, each side of each module containing two silicon microstrip sensors. The two sides are placed back-to-back with an angle offset of 40 mrad to provide measurements in both spatial directions of the plane. The spatial resolution of a single hit in the SCT is about 17 μm×580 μm in the $\phi \times z$ directions. A typical track will pass through four SCT modules providing eight track measurements.

Transition Radiation Tracker

Surrounding the SCT is the Transition Radiation Tracker (TRT) [40, 41] which consists of approximately 351000 gaseous cylindrical straw drift tubes interleaved with transition radiation material. The straw tubes are 4 mm in diameter. There are 73 straw layers in the barrel region between radii of 55 cm and 108 cm, they run parallel to the beam line and are 144 cm in length. There are 160 planes of 768 straws in the end-cap region arranged radially between distances of 85 cm and 2.7 m from the interaction point, each straw being 37 cm in length. The combined barrel and end-cap units provide coverage up to $|\eta| < 2$. The spatial resolution of a single hit in the TRT is approximately 130 μm per straw. A typical track will pass through 36 straws in the barrel or 22 in the end-cap.

Each straw is filled with a gas mixture of 70% Xe for good x-ray absorption and 27% CO_2 and 3% O_2 to increase the electron drift velocity. The straw anodes are gold-plated tungsten wires at ground potential and the straw cathodes are typically operated at 1530 V. When a charged particle passes through a TRT straw it ionises the gas inside. The electric field between the straw cathode and the central wire anode induces an ionisation cascade. The electrons produced in the cascade are collected on the central wire which produces a signal proportional to the energy of the original charged particle.

In addition to track measurements, the TRT also has the ability to distinguish electrons from charged hadrons by detecting transition radiation photons. Interleaved between the straws are foils and fibres which form the transition radiation material. A charged particle traversing this material will emit transition radiation photons, the energy of these photons is proportional to the energy of the emitting particle divided by its mass. The signal response to these photons will be larger for electrons than it will be for more massive charged hadrons.

3.2.3 Calorimetry

Surrounding the ID sits the calorimetry system, shown in Figure 3.5, designed to measure the energy of the outgoing particles. Two different systems are employed to do this, the Electromagnetic Calorimeter (ECAL) surrounds the ID (both in the barrel and end cap region) and is used to measure the energy of photons and electrons. The ECAL contains lead absorber plates as well as active layers of liquid argon (LAr). Incident electrons and photons interact with the lead plates, loosing energy through bremsstrahlung and pair creation processes, and produce cascades of photons and electrons (an *electromagnetic*
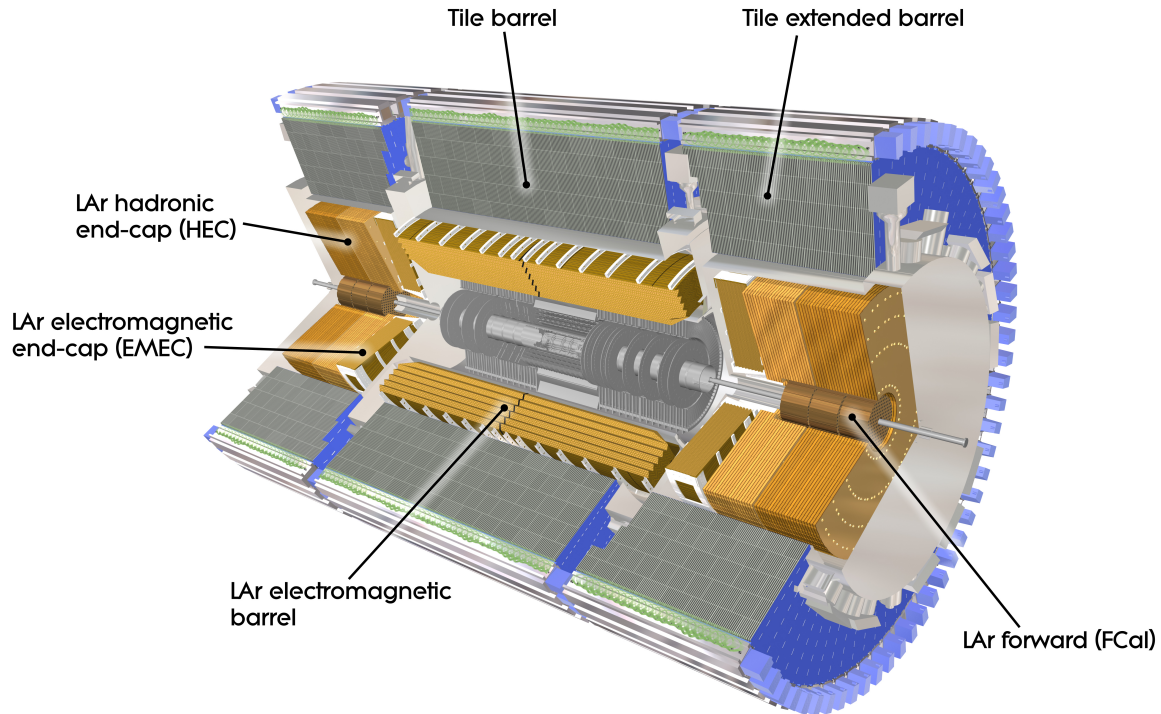
Figure 3.5: Schematic of the ATLAS calorimetry systems [36].

shower) which causes ionisation in the LAr layers. Since the ECAL is a *sampling* calorimeter, the measured ionisation energy is proportional to the particles total energy. The total energy of the particle can be determined through knowledge of the detector geometry and the particle interaction lengths. The sampling calorimeter design has a key advantage over homogeneous calorimeters, these calorimeters contain absorbing layers and active layers. The latter is capable of supplying particle tracking information. Since neutral particles are not detected by the tracking systems, the calorimeters provide the only means of tracking these particles. The ECAL lead and LAr strips are arranged in an accordion shaped geometry. This ensures there are no cracks and allows for complete ϕ coverage.

Although hadrons will interact with the ECAL to some extent, they are much more massive than electrons, so they mostly lose energy through strong nuclear inelastic scattering processes. To measure hadron energies a different system is employed, the Hadronic Calorimeter (HCAL), which surrounds the ECAL and is also a sampling calorimeter. The HCAL system is further divided into three sections. The *tile calorimeter* surrounds the ECAL in the barrel region, it uses steel as the absorber and scintillating

tiles as the detecting material. In the end cap regions sit the LAr Hadronic End Cap (HEC) and LAr Forward Calorimeter (FCAL). The combined HCAL system extends out to $|\eta| < 4.9$ which provides almost complete hermetic coverage (the so-called 4π solid angle). Providing complete coverage around the interaction point is crucial for making accurate measurements of $E_{\mathrm{T}}^{\mathrm{miss}}$.

3.2.4 Muon Spectrometer

While most particles produced in events are absorbed by the calorimeters, muons produced at the LHC are in the minimum ionizing regime and therefore are able to pass through, typically depositing a few GeV of energy in the calorimeters. For this reason, the Muon Spectrometer (MS), shown in Figure 3.6, occupies the outermost region of the detector, surrounding the calorimetry system. In the barrel region three concentric cylindrical tracking layers track muon trajectories and a large toroidal magnet provides the bending power to deflect their paths due to the Lorentz force, allowing measurements of the muon's charge and momentum to be made. Each of the end cap regions also contains a toroidal magnet system and three tracking discs aligned in the plane transverse to the beam line to ensure almost complete hermetic coverage.

3.2.5 Triggers and Data Acquisition

At full luminosity, proton bunches will collide every 25 ns. Detector information can not be stored for all of these events due to limitations in data transfer bandwidth and computational processing speeds. In ATLAS, an event *trigger* is used to record only events which could potentially contain interesting physics, such as events with large $E_{\mathrm{T}}^{\mathrm{miss}}$ or high-p_{T} leptons or jets. This allows most events to be discarded and reduces the rate at which events are written to permanent storage. The trigger system consists of three levels, shown in Figure 3.7, which progressively refine the decision to accept or reject events using an increasing level of data analysis complexity and sophistication.

Level 1 Trigger

The Level 1 (L1) trigger is a completely hardware-based system which uses only information from the calorimeters and muon spectrometer. It makes a decision to accept or reject every single bunch crossing event based on the presence or absence of high-p_{T}
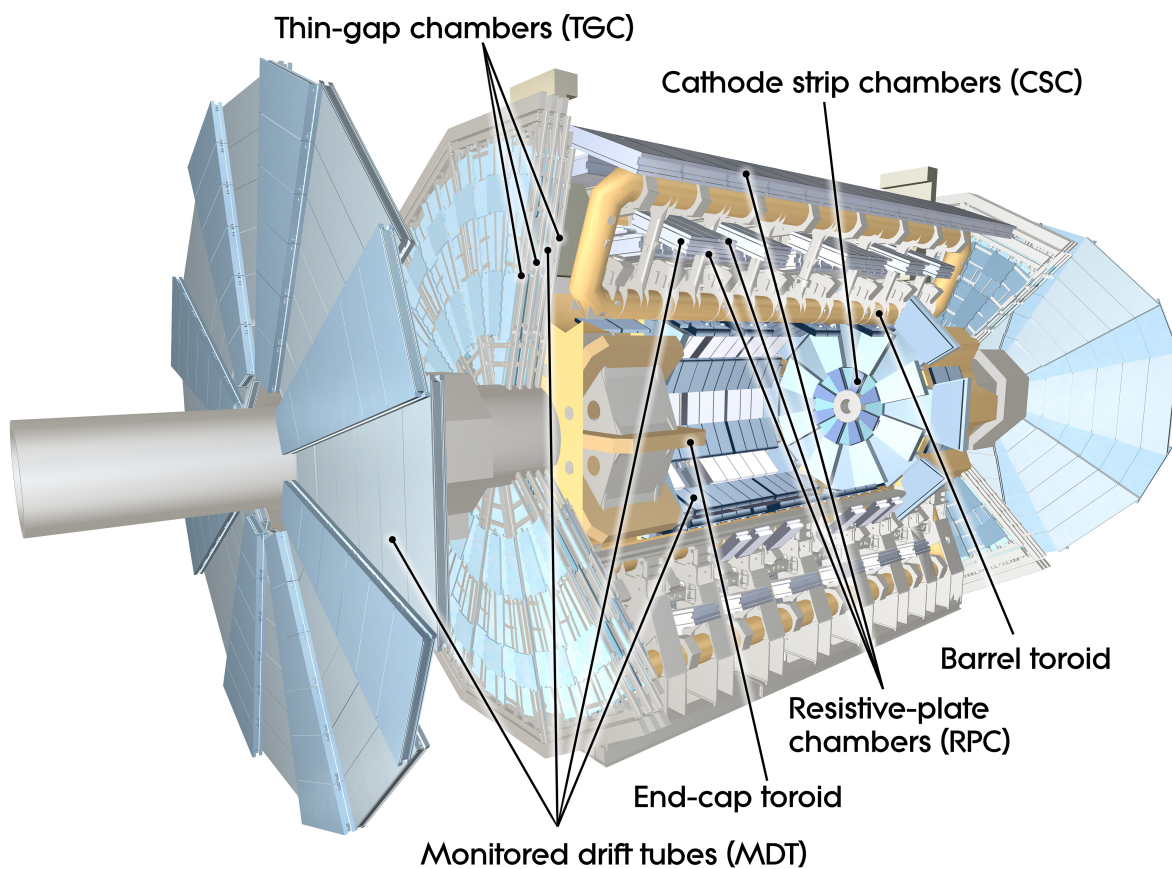
Thin-gap chambers (TGC)

Cathode strip chambers (CSC)

Barrel toroid

Resistive-plate chambers (RPC)

End-cap toroid

Monitored drift tubes (MDT)

Figure 3.6: Schematic of the ATLAS muon system [36].

photons, electrons, muons, hadronic taus, and jets, as well as large missing and total transverse energy. To do this, a *sliding window* algorithm [42] is used to find regions of the calorimeter which contain deposits of energy larger than preset thresholds. The L1 trigger defines a Region of Interest (RoI) specifying the (η, ϕ) location of each of the selected calorimeter clusters and muon hits. The results of the L1 trigger are sent to the Central Trigger Processor (CTP) which computes the decision to accept or reject the event. If the decision is made to accept the event, the data recorded by all detector systems, as well as the information of each discovered RoI, is transmitted through the readout systems to be processed further. This reduces the event rate to about 75 kHz.

Level 2 Trigger

The Level 2 (L2) trigger is a software-based system, running on some 500 computing nodes, which further refines the decision made at L1. Event fragments (about 2% of the
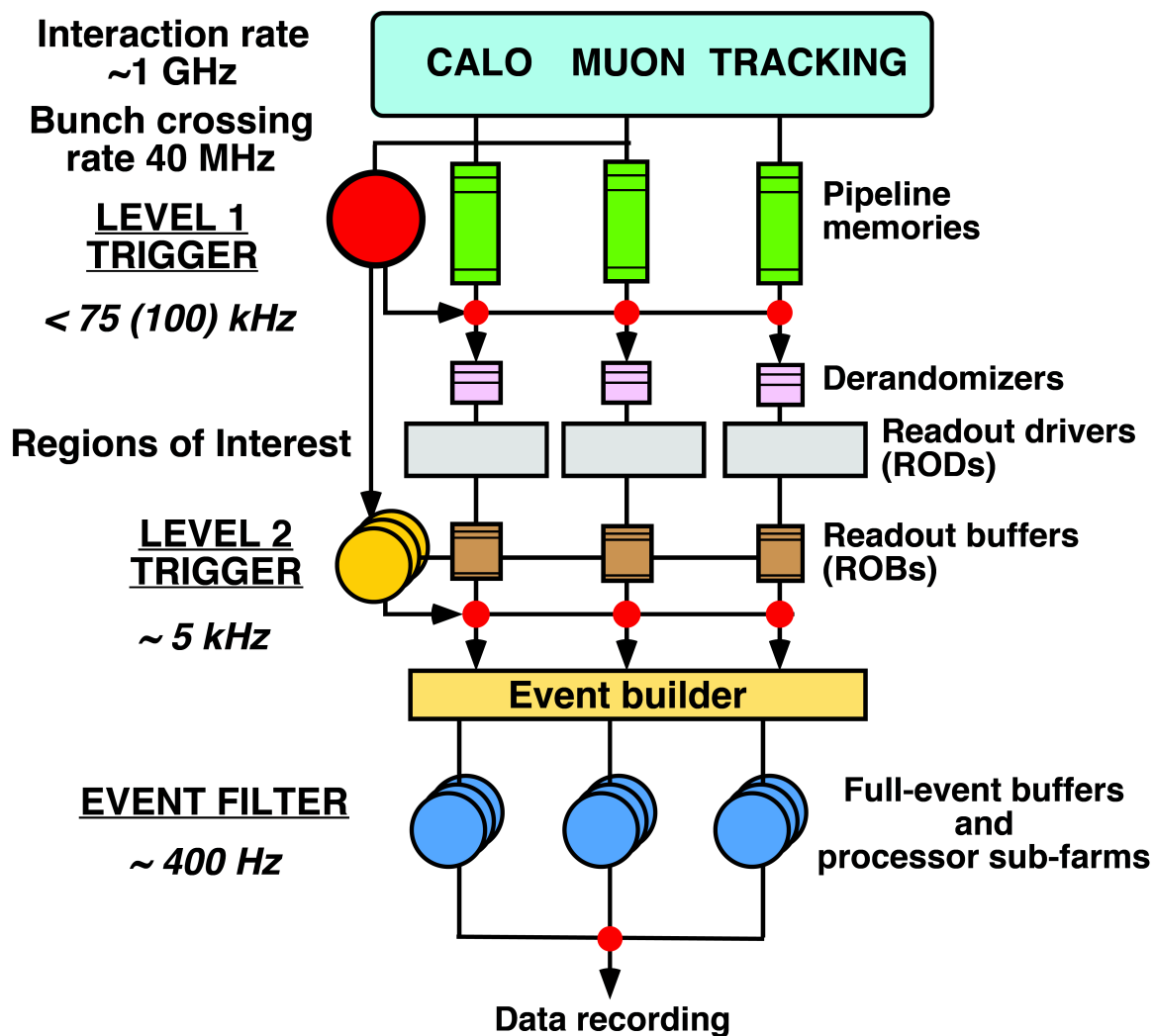
Figure 3.7: Schematic of the ATLAS trigger system [36].

total event data) are reconstructed within each RoI using the full detector granularity, including the response of the ID tracking systems. The additional information and accuracy allows for tighter and more sophisticated selections, such as track-cluster matching and requirements on shower shape information. The nominal output rate of the L2 trigger is approximately 5 kHz, however in 2012 an output rate of approximately 6.5 kHz was achieved.

Event Filter Trigger

The Event Filter (EF) trigger performs the final decision of whether or not the event will be written to permanent storage. Each event is fully reconstructed, using the full detector response, on some 1800 computing nodes. This stage of reconstruction uses more sophisticated selection requirements and energy calibrations, which are almost identical to those used in offline event reconstruction (Section 3.4) for physics analyses. The output rate in which events are written to storage is about 400 Hz.

The events written to data also include boolean flags indicating which triggers fired in each particular event. An offline analysis can then filter events based on these flags to find only events of interest to the particular analysis. The specific triggers used in this analysis will be mentioned in Section 4.3.1 however the general naming scheme of EF triggers will be described here for reference. EF trigger names begin with the prefix `EF_`, followed by the type of object the trigger matches against, for example `e`, `mu`, or `tau`. Next is the number representing the p_T threshold for the object. If the object has any additional quality criteria imposed, these are mention next. The `T` flag, if present, indicates that the p_T threshold of the corresponding L1 trigger item is higher than those without the `T` flag. The `vh` flag, if present, indicates that a veto on energy in the HCAL at L1 greater than 1 GeV is imposed. The `i` flag, if present, indicates that an isolation requirement is imposed which requires the sum of the p_T of additional tracks in a cone of $\Delta R < 0.2$ around the lepton to be less than a set fraction of the lepton p_T. This threshold is 10% for electrons and 12% for muons. Lastly the trigger name is ended with the identification requirement imposed on the object to reject fakes, these values can be `loose`, `medium`, or `tight`. For some trigger items the identification requirements have changed over time, in these cases the identification threshold is suffixed with a number representing the version of the identification requirement used. Some triggers require multiple objects to be present in an event, these can be denoted in two different ways: by repeating all of the previous information again for the second object, or by prefixing the object type with the number of objects required, for example `2mu`. The `EFFS` tag, if present, indicates that the full scan algorithm was used to find the trigger objects.

3.3 Event Simulation

Monte-Carlo (MC) simulation of the proton-proton interactions and outgoing propagation of particles through the detector is used extensively in ATLAS physics analyses. This procedure allows an analyser to investigate the features of the expected signal and background in order to develop and compare analysis strategies. Event simulation consists of two stages: MC event generation, and detector simulation. Event generation uses the MC method to generate proton-proton collisions which includes the production and decay of all outgoing particles, such as hadronised partons. These generated events are then passed though detector simulation where the propagation of outgoing particles through the detector is recorded by the detector systems. After this, the simulated events are passed though event reconstruction (Section 3.4) in the same manner that is done for real collision data.

3.3.1 Event Generation

Event generation is itself a multi-stage process. The first stage is the *hard event* which generates the hard partonic interaction, calculated by sampling the relevant matrix element of the process and weighted by the Parton Distribution Function (PDF) of the input partons. In addition, the *underlying event* simulates the interactions of the partons not actively involved in the hard event. The output partons of the hard event are passed to the *parton shower* stage which models additional radiation. The final stage hadronises all output partons to produce the set of final state particles of the proton-proton interaction.

Due to the large number of protons in each bunch (Table 3.1), each bunch crossing produces many proton-proton interactions. Figure 3.8 shows the distribution of the number of proton-proton interactions per bunch crossing in 2011 and 2012 data. In 2012, for example, the mean number of interactions per bunch crossing was 20.7. In many cases these interactions contain no hard collision, but only soft inelastic collisions. These are called *pileup* collisions as they can contribute additional final state particles to an event with a hard collision. These pileup collisions are added to the simulation such that the distribution matches that which is observed in data.

A variety of MC generators exist, some provide a full proton-proton collision while others provide only specific parts of the complete MC generation procedure. The MC
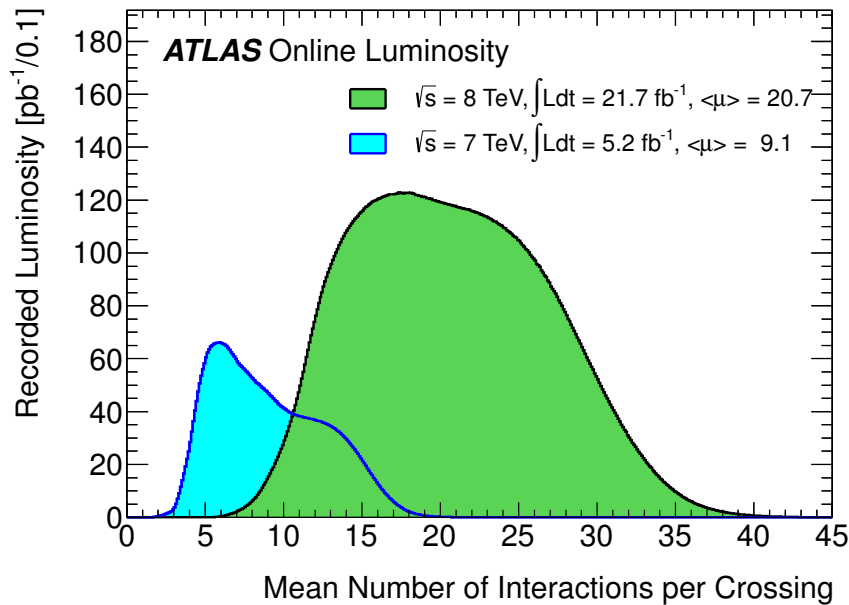
Figure 3.8: The luminosity-weighted distribution of the mean number of interactions per bunch crossing for the 2011 and 2012 data [37].

programs used in this analysis are: PYTHIA [43], HERWIG [44], JIMMY [45], POWHEG [46], ALPGEN [47], MC@NLO [48], and ACERMC [49].

3.3.2 Detector Simulation

The final state particles from generated events are passed through detector simulation [50] to model their interactions with the material and magnetic field of the ATLAS detector. GEANT4 [51] is the standard detector simulator program used by the ATLAS collaboration. The GEANT4 program contains a geometric description of the complete ATLAS detector, with each sub-detector system represented by material volumes. The event generation output particles are propagated through these detector volumes to simulate the many different material interactions which provide the simulated detector response in each of these volumes. The output of the detector simulation stage is a file containing the location and magnitude of all measured interactions, which is in the same format as the actual detector output. These output files are passed though the same full reconstruction algorithm that is applied to actual recorded data.

3.4 Event Reconstruction

The detector output data, either real (Section 3.2.5) or simulated (Section 3.3.2), of a collision event is a digitised record of the signals from the sensitive detector systems. Offline event reconstruction is the process of converting these records into quantities useful for a physics analysis. The reconstruction and identification of the final state particles produced in a collision event is determined by their interactions with the different detector volumes, shown in Figure 3.9. Particle reconstruction is the procedure of finding and building particle candidates from the recorded detector information. Each reconstructed particle candidate is described by a number of calibrated quantities which measure its properties. Particle identification is the procedure of using these measured properties to distinguish real particles against backgrounds which may mimic their signature. This section outlines the procedure used to reconstruct and identify the final state particles used in this analysis.

3.4.1 Electron Reconstruction

Electrons are charged particles which leave tracks in the ID and deposit energy in the ECAL. Reconstruction and identification of electrons is challenging due to the large backgrounds from misidentified hadronic jets, secondary electrons from photon conversions, and electrons from hadron decays. The following procedure has been employed to provide good discrimination against these backgrounds [52].

The reconstruction procedure begins by finding deposits of energy larger than 2.5 GeV in the ECAL within a region of size $\Delta\eta \times \Delta\phi = 0.025 \times 0.025$ using a sliding window algorithm [42]. Tracks reconstructed in the ID are extrapolated to the ECAL. If the extrapolated track is sufficiently close[2] to the barycentre of the energy cluster, an electron candidate is formed. If there are multiple tracks matched to a single cluster, those with hits in the PD are preferred and the track which is closest in ΔR is chosen. The four-vector of the electron candidate is constructed from the η and ϕ parameters of the matched track at the interaction point and the energy of the cluster.

These electron candidates have further selection requirements imposed to reject the cases where the detector signatures were not caused by a real electron. Electron

---

[2]$\Delta\eta < 0.05$, $\Delta\phi < 0.1$ if the track is bending away from the cluster, $\Delta\phi < 0.05$ if the track is bending toward the cluster.
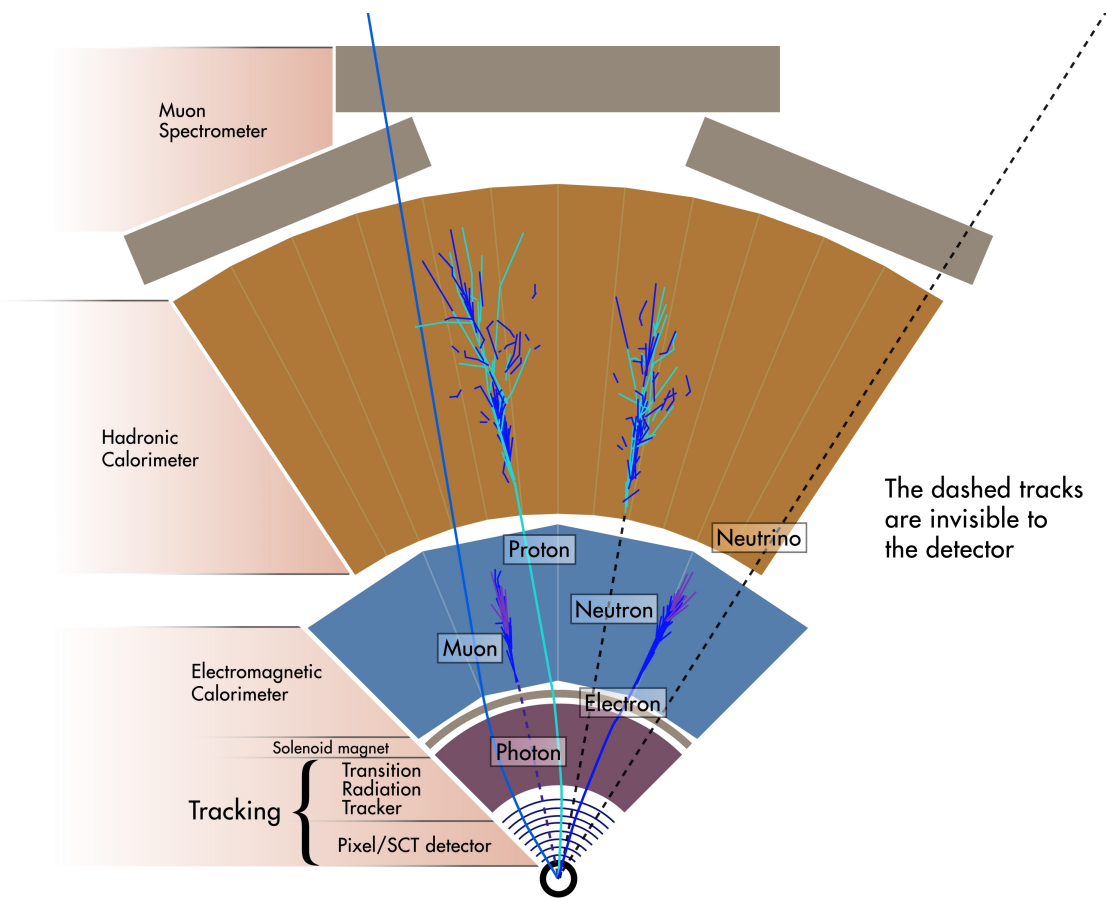
Figure 3.9: Cross-section view of the ATLAS detector illustrating how different particles interact with the detector volumes [36].

identification is the process of discriminating real electrons from hadronic jets using cuts on variables constructed from the track and cluster information. Three identification working points are defined: `loose++`, `medium++`, and `tight++`, which place increasingly tighter cuts on these variables to achieve larger background rejection rates, at the cost of decreased signal efficiency.

3.4.2 Muon Reconstruction

Muons are charged particles which leave a track in the MS. The reconstruction of muon candidates begins by separately reconstructing tracks in both the MS and ID [53]. Tracks reconstructed in the MS are extrapolated toward the interaction point where a matching track in the ID is searched for. When an ID track is found, the track is refit using the parameters of both the ID and MS to form the *combined* muon. This combination

provides good rejection against muons from decays of in-flight hadronic jets and muons from secondary interactions.

Additional quality criteria are applied to the ID track as follows. At least one hit in the PD is required, if the track passes through a region with dead pixels these are also counted as expected hits. At least five hits in the SCT are required, if the track passes through a region with dead SCT sensors these are also counted as expected hits. At least one hit in the b-layer is required if the track passes through a region where a hit is expected. In some cases a track passes through a functional part of the sensor but no hit is recorded, these are referred to as holes. A maximum of three holes are allowed in the PD and SCT combined. The TRT quality criteria imposed depend on the $|\eta|$ region. In the region $0.1 < |\eta| < 0.9$ there must be at least six hits (including outliers), and the number of outlier hits must be less than 90% of the total number of hits. In the remaining $|\eta|$ region there is no requirement on the number of hits, however if the number of hits is six or more, then the number of outlier hits must be less than 90% of the total number of hits.

3.4.3 Jet Reconstruction

Jets are a collimated spray of hadrons which come from the hadronisation of outgoing partons. Jets are composed of a variety of hadrons such as protons, neutrons, and pions. The charged hadrons will leave tracks in the ID. Jets produce a complex response in the calorimeters, most hadrons will produce showers in the HCAL, however some hadrons, such as the neutral pion, will decay into a pair of photons which produce closely spaced clusters in the ECAL.

Jets are reconstructed using the anti-k_{T} topological clustering algorithm [54]. This algorithm groups neighbouring calorimeter cells which recorded significant energy deposits into a single cluster per particle. Electromagnetic and hadronic showers produce different responses in the detector, photons and electrons tend to produce a single cluster whereas hadronic jets tend to produce a number of fragmented clusters. The energy of the jet is measured as sum of the energies of the individual calorimeter cells in the cluster, the direction is the energy-weighted average of the directions of the cells. Jet reconstruction is performed over the entire range, $|\eta| < 4.9$, of the calorimeter. For jets reconstructed in the range $|\eta| < 2.5$, tracks reconstructed in the ID are associated to a jet cluster if they lie within a radius of $\Delta R < 0.4$ of the cluster barycentre.

It is important to know whether a jet originates from a hard collision or from pileup collisions. The Primary Vertex (PV) is the interaction point which produced the largest amount of transverse activity of all interactions in that event. For any given jet, a quantity known as the Jet Vertex Fraction (JVF) is calculated as

$$\mathrm{JVF} = \frac{\sum\limits_{\text{jet tracks from PV}} p_{\mathrm{T}}^{\text{track}}}{\sum\limits_{\text{all jet tracks}} p_{\mathrm{T}}^{\text{track}}} \tag{3.5}$$

If a jet has no associated tracks, it is the convention to set $\mathrm{JVF} = -1$. Jets with a larger JVF are deemed more likely to have originated from partons produced in the primary interaction.

Jet reconstruction is particularly sensitive to the effects of pileup due to the fact that the area of a reconstructed jet can often overlap with particles from pileup interactions. This can degrade the jet energy resolution and shift the jet energy scale. The pileup correction to the jet calibration [55] is a subtraction technique which uses an estimate for the amount of pileup contained in each jet. This is based on the assumption that pileup can be treated as a uniform, diffuse background, adding signal to jets. The jet area is a measure of the susceptibility of a jet to pileup, and is measured per jet. The diffuse background is characterised by measuring the pileup energy density in the calorimeter per event. The pileup energy density times jet area gives the amount of pileup inside the jet which allows for a correction to the reconstructed four-momentum of the jet.

It is useful to discriminate jets containing b-quarks from those containing light quarks. This is possible due to the relatively long lifetime of B-hadrons which results in a flight time long enough for its decay products to be identified as originating from a secondary vertex or from a large displacement from the PV. This displacement is quantified by two *impact parameters*, which are the distance of a tracks closest approach to the PV, d_0 is the impact parameter in the transverse plane, z_0 is the impact parameter along the beam axis. In the range $|\eta| < 2.5$, the `MV1` algorithm [56] is used to tag b-jets. The algorithm combines the information of the PV, secondary vertex, and impact parameters into a single discriminant using a neural network. The working point used in this analysis has a b-tagging efficiency of 70% for b-jets with $p_{\mathrm{T}} > 15\,\mathrm{GeV}$. This corresponds to a light quark jet misidentification efficiency of approximately 0.1%.

Decay Type	Decay Mode	Branching Fraction [%]
leptonic	$\tau^{\pm} \to e^{\pm}\nu_e\nu_{\tau}$	17.8
	$\tau^{\pm} \to \mu^{\pm}\nu_{\mu}\nu_{\tau}$	17.4
1-prong hadronic	$\tau^{\pm} \to \pi^{\pm}\nu_{\tau}$	10.9
	$\tau^{\pm} \to \pi^{\pm}\pi^0\nu_{\tau}$	25.5
	$\tau^{\pm} \to \pi^{\pm}\pi^0\pi^0\nu_{\tau}$	9.3
	$\tau^{\pm} \to \pi^{\pm}\pi^0\pi^0\pi^0\nu_{\tau}$	1.0
3-prong hadronic	$\tau^{\pm} \to \pi^{\pm}\pi^{\mp}\pi^{\pm}\nu_{\tau}$	9.3
	$\tau^{\pm} \to \pi^{\pm}\pi^{\mp}\pi^{\pm}\pi^0\nu_{\tau}$	4.6

Table 3.2: The dominant tau decay modes and their branching fractions [7].

3.4.4 Hadronic Tau Reconstruction

Tau leptons are the heaviest of the charged leptons and are the only lepton with enough mass to be able to decay into hadrons. Tau leptons have a mean lifetime of $(290.3 \pm 0.5) \times 10^{-15}$ s [7]. A relativistic tau will have a mean decay length of 87.03 μm, which means that taus will decay inside the beam pipe, very close to the interaction point in which they were produced. The ATLAS detector will not directly detect the tau lepton itself, only the tau decay products can be detected. The origin of the decay products is, for the most part, indistinguishable from the interaction point which produced the tau. For this reason, light leptons produced from tau decays are very difficult to distinguish from those produced at the primary interaction point. The identification of tau leptons at ATLAS therefore focuses on the hadronic tau decay modes.

The most common hadronic tau decay modes produce one charged pion, zero or more neutral pions, and a tau neutrino, shown in Table 3.2. These decay modes are referred to as *1-prong* decay modes, since they produce one charged hadron which will leave a track in the ID. A smaller fraction of the time, taus can decay to three charged pions, zero or more neutral pions, and a tau neutrino, these are called *3-prong* decay modes.

Hadronic tau reconstruction [57] begins by first reconstructing a jet, as previously discussed. The origin of the hadronic tau is the *tau vertex*, which is chosen as the vertex with the largest JVF calculated for the reconstructed jet. The four-vector is constructed from the η and ϕ parameters of the barycentre of the reconstructed topological cluster

relative to the tau vertex. The energy is calculated as the sum of the energy deposits in the cells of the calorimeters which lie within a radius of $\Delta R < 0.2$ around the cluster barycentre.

Any reconstructed hadronic jet with $E_T > 10\,\text{GeV}$ in the range $|\eta| < 2.5$ becomes a reconstructed hadronic tau candidate. Tracks reconstructed in the ID are added to the hadronic tau candidate if they have $p_T > 1\,\text{GeV}$ and lie within a radius of $\Delta R < 0.2$ around the cluster barycentre. In addition, the tracks must pass a set of quality criteria, requiring at least two hits in the PD, and at least seven hits combined in the PD and SCT. Lastly, the impact parameters of the track from the tau vertex must satisfy $|d_0| < 1.0\,\text{mm}$, and $|z_0 \sin \theta| < 1.5\,\text{mm}$. The charge of the hadronic tau is reconstructed as the sum of the charges of the associated tracks.

The main background to hadronic tau reconstruction is jets originating from parton scattering or QCD radiation, both are produced far more frequently than taus. Hadronic tau decays tend to produce a more collimated spray of hadrons compared to those from QCD jets, as shown in Figure 3.10. In addition, hadronic taus tend to produce a smaller number (usually one or three) of charged particle tracks in the ID. A variety of variables are calculated, based on the tracks and clusters, which are combined into a Boosted Decision Tree (BDT) which is trained using simulated tau decays as the signal and QCD jets from data as the background. Hadronic tau identification used in this analysis discriminates hadronic tau decays from QCD jets using requirements on the BDT score. Three identification working points are defined: `loose`, `medium`, and `tight`, which correspond to signal selection efficiencies of 70%, 60%, and 40% for 1-prong candidates, and 65%, 55%, and 35% for 3-prong candidates. The background rejection rates for these working points depend on the kinematics of the candidates considered. Generally they are around 10-40 for the `loose` working point, ranging up to 500 for the `tight` working point.

Electrons are the second largest background to hadronic tau reconstruction, especially for 1-prong candidates. A BDT is trained on simulated tau decays as the signal and simulated electrons as the background. The variables used in this BDT describe the transition radiation surrounding the tau candidate recorded in the TRT. An electron veto is constructed from requirements on the BDT score. Three progressively tighter working points are defined: `loose`, `medium`, and `tight`, which correspond to signal selection efficiencies of 95%, 85%, and 75% respectively.

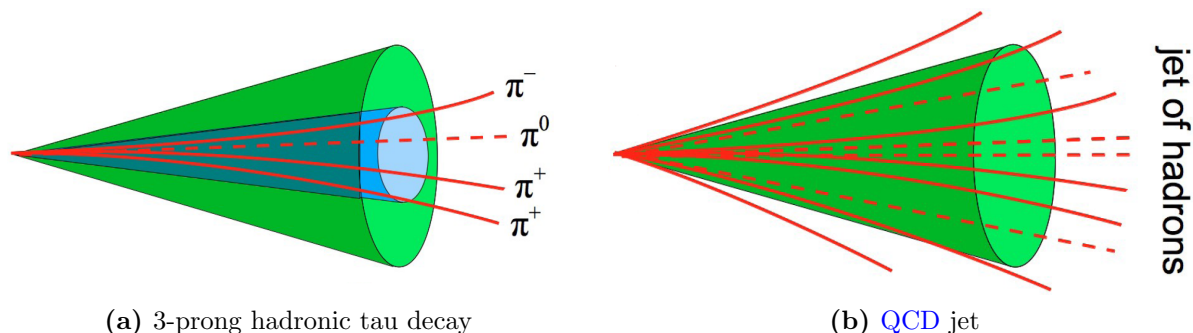**(a)** 3-prong hadronic tau decay   **(b)** QCD jet

Figure 3.10: Cartoon diagrams showing the different signatures of (a) a hadronic tau decay, and (b) a QCD jet.

Although it is quite rare, muons may sometimes be misidentified as a hadronic tau decay and at the same time fail to be reconstructed as a muon. There are three main scenarios where this may occur. The muon may pass though an inefficient region of the MS and not be detected. The muon may deposit an abnormally large amount of energy in the calorimeters, altering its trajectory enough such that track reconstruction in the MS fails. Finally, the muon may have had a small amount of energy and was stopped by the calorimeters. In each of these scenarios, muons will leave a track in the ID and may deposit a small amount of energy in the calorimeters, mimicking the signature of a hadronic tau decay. To discriminate against these scenarios, a muon veto is constructed from variables based on the relative amounts of energy deposited in the ECAL and HCAL, as well as the momentum of the track in the ID. Requirements are placed on these variables to define a single working point which is more than 96% efficient while reducing the amount of muon fakes by about 40%.

3.4.5 $E_{\mathrm{T}}^{\mathrm{miss}}$ Reconstruction

Missing transverse energy quantifies the momentum imbalance in the transverse plane and is a sign that particles have left the detector without leaving a response. The calculation of $E_{\mathrm{T}}^{\mathrm{miss}}$ uses all fully reconstructed and energy calibrated photons, electrons, muons, hadronic taus, and jets, discussed in the previous sections. In addition, a *soft* term is included which is composed of topological clusters and tracks not associated to any high-level reconstructed objects. $E_{\mathrm{T}}^{\mathrm{miss}}$ is calculated as the negative vector sum of

the transverse energy contributions from each of these terms [58], given by

$$\vec{E}_{\mathrm{T}}^{\mathrm{miss}} = -(\vec{E}_{\mathrm{T}}^{\gamma} + \vec{E}_{\mathrm{T}}^{e} + \vec{E}_{\mathrm{T}}^{\mu} + \vec{E}_{\mathrm{T}}^{\tau_h} + \vec{E}_{\mathrm{T}}^{\mathrm{jets}} + \vec{E}_{\mathrm{T}}^{\mathrm{soft}}) \tag{3.6}$$

Again, the magnitude of this vector $E_{\mathrm{T}}^{\mathrm{miss}} = |\vec{E}_{\mathrm{T}}^{\mathrm{miss}}|$ is the quantity which generally gets used for analysis requirements. In some cases it is useful to know the direction of $E_{\mathrm{T}}^{\mathrm{miss}}$ in the transverse plane, this is calculated as $\phi^{\mathrm{miss}} = \arctan(E_y^{\mathrm{miss}}, E_x^{\mathrm{miss}})$. The typical resolution on $E_{\mathrm{T}}^{\mathrm{miss}}$ can be described by the relation $\sigma = k\sqrt{\sum E_{\mathrm{T}}}$ where $\sum E_{\mathrm{T}}$ is the scalar sum of the transverse energies of all the reconstructed objects and k is a parameter determined to be about $0.5\,\mathrm{GeV}^{1/2}$ [58].

Chapter 4

Analysis Strategy

As described in Section 2.2, the main production modes of the Higgs boson at the LHC are the ggF, VBF, and VH processes. Although the cross-section of the VH processes are an order of magnitude smaller than that of the ggF and VBF processes, the presence of additional leptons from the decays of the associated vector boson allows for analysis selections which can increase the signal-to-background ratio significantly. This chapter describes the strategy used to select $VH(\rightarrow \tau\tau)$ signal events, as well as the main backgrounds which can mimic the signal topology.

The strategy used in this analysis is similar to other Higgs searches. Firstly, the minimal set of particle reconstruction requirements is established which matches the expected signal events, this is called *event selection*. After this, events are categorised according to their final state event topologies in order to perform a separate dedicated analysis for each signal channel, this is called *event categorisation*. Both of these steps are outlined in Section 4.3.

In each signal channel the nature of the signal features and expected background processes is investigated. A background model is developed in Chapter 5 and its performance is studied in the $W(\rightarrow \ell\nu)H(\rightarrow \tau_\ell\tau_h)$ channel in Section 6.2. The features of the signal which discriminate signal from background are identified and used to construct further event selection requirements.

To discriminate the signal events from background events further, a mass variable is developed in Section 6.1 which exploits the distinct properties of the signal topology. To identify or exclude the presence of the signal, a series of statistical tests are performed in Section 6.7.

4.1 Data

The data used in this analysis was collected by the ATLAS detector in 2012. Proton-proton collisions were recorded at a centre-of-mass energy $\sqrt{s} = 8\,\text{TeV}$. The data collection process is divided into many *luminosity blocks* which last for roughly 2 minutes with a fixed set of running conditions. For a given luminosity block to be considered good for physics, all detector subsystems must be running optimally during this time. A list of good luminosity blocks is stored in the Good Run List (GRL) maintained by the experiment. All data used in this analysis is required to be included in the GRL and corresponds to a total integrated luminosity of $20.3\,\text{fb}^{-1}$ as shown in Figure 3.2b.

4.2 Blinding Strategy

It is common practice in analyses searching for new physics phenomena to remain *blinded* until the point where the analysis strategy, background models, control regions, and systematics are all deemed to be well understood and free of bias. This decision is made, following a peer-review system, by an internal committee within the ATLAS collaboration whose members are composed of experts not actively participating in the analysis. This unblinding approval must be granted before analysers are allowed to look at experimental data in regions where the signal is expected to be significant. It is however a requirement that analysers must validate background models, and this is done in regions where the signal is not expected to be significant. The events which pass the categorisation requirements described in Section 4.3 are deemed not signal sensitive as the expected background will be large in this region. Within each signal category, further requirements are made to isolate specific background processes to create control regions, this is done in Section 5.7. These are constructed to be orthogonal to the signal regions so are also unblinded in order to validate the background models.

4.3 Event Selection and Categorisation

Event Selection is the set of common base event requirements used by all of the different signal channels. Events which pass these requirements are then separated into different categories which match each of the VH signal topologies. A further dedicated analy-

Trigger Name	Trigger Threshold [GeV]		Offline Threshold [GeV]	
`EF_e24vhi_medium1`	$p_\mathrm{T}(e) > 24$		$p_\mathrm{T}(e) > 26$	
`EF_e60_medium1`	$p_\mathrm{T}(e) > 60$		$p_\mathrm{T}(e) > 60$	
`EF_mu24i_tight`	$p_\mathrm{T}(\mu) > 24$		$p_\mathrm{T}(\mu) > 26$	
`EF_mu36_tight`	$p_\mathrm{T}(\mu) > 36$		$p_\mathrm{T}(\mu) > 38$	
`EF_mu18_tight_mu8_EFFS`	$p_\mathrm{T}(\mu_1) > 18$	$p_\mathrm{T}(\mu_2) > 8$	$p_\mathrm{T}(\mu_1) > 20$	$p_\mathrm{T}(\mu_2) > 10$
`EF_2mu13`	$p_\mathrm{T}(\mu_1) > 13$	$p_\mathrm{T}(\mu_2) > 13$	$p_\mathrm{T}(\mu_1) > 15$	$p_\mathrm{T}(\mu_2) > 15$
`EF_e12Tvh_medium1_mu8`	$p_\mathrm{T}(e) > 12$	$p_\mathrm{T}(\mu) > 8$	$p_\mathrm{T}(e) > 14$	$p_\mathrm{T}(\mu) > 10$
`EF_e12Tvh_medium1_mu6_topo_medium`	$p_\mathrm{T}(e) > 12$	$p_\mathrm{T}(\mu) > 6$	$p_\mathrm{T}(e) > 14$	$p_\mathrm{T}(\mu) > 8$
`EF_e24vh_medium1_e7_medium1`	$p_\mathrm{T}(e_1) > 24$	$p_\mathrm{T}(e_2) > 7$	$p_\mathrm{T}(\mu) > 26$	$p_\mathrm{T}(\mu) > 9$
`EF_2e12Tvh_loose1`	$p_\mathrm{T}(e_1) > 12$	$p_\mathrm{T}(e_2) > 12$	$p_\mathrm{T}(e_1) > 14$	$p_\mathrm{T}(e_2) > 14$

Table 4.1: All triggers used in the various channels, along with the corresponding trigger and offline p_T thresholds on the reconstructed objects. The EF trigger naming convention is described in Section 3.2.5.

sis is performed in each channel which refines these selection requirements to further discriminate against backgrounds, this will be described in Chapter 6.

4.3.1 Trigger Requirements

The first step of event selection is to choose which triggers will be used to collect the data used in the analysis. Since all VH events contain at least one light lepton, the triggers used in this analysis are all based on the requirement of one or more light leptons. The list of un-prescaled light lepton triggers available is shown in Table 4.1. Each trigger has a p_T requirement on the triggered lepton(s). Triggers generally have a p_T region where they fire with maximum efficiency, this is generally a few GeV above the trigger threshold. This region is also where the trigger performance is most well understood and modelled correctly by MC. For these reasons, if a trigger fires, an additional requirement on the p_T of the corresponding reconstructed particles is made to ensure that events are collected in this region.

Each VH channel contains a different set of final state light leptons, therefore not all triggers are applicable to every channel. Table 4.2 shows which triggers are used in each channel. Only one trigger is assigned to each event, triggers higher in the list are preferred over those below. Each trigger is tested for each event in the order listed, if

Trigger Name	$W(\to \ell\nu)H(\to \tau_\ell\tau_h)$ $Z(\to \ell\ell)H(\to \tau_\ell\tau_h)$	$W(\to \ell\nu)H(\to \tau_h\tau_h)$ $Z(\to \ell\ell)H(\to \tau_h\tau_h)$
EF_mu24i_tight or EF_mu36_tight	○	○
EF_e24vhi_medium1 or EF_e60_medium1	○	○
EF_mu18_tight_mu8_EFFS	○	
EF_2mu13	○	
EF_e12Tvh_medium1_mu8	○	
EF_e12Tvh_medium1_mu6_topo_medium	○	
EF_e24vh_medium1_e7_medium1	○	
EF_2e12Tvh_loose1	○	

Table 4.2: A summary of which triggers are used in each channel. Only one trigger is associated to any event, with the triggers higher on this list preferred over those below. The EF trigger naming convention is described in Section 3.2.5.

a trigger fires and the corresponding reconstructed particles satisfy the the thresholds shown in Table 4.1 the event is kept, otherwise it is no longer considered for analysis.

4.3.2 Particle Reconstruction Requirements

For the most part, the particle reconstruction requirements used in this analysis are chosen to be consistent with other ATLAS Higgs boson searches. These requirements are described here, they build upon the existing requirements described in Section 3.4.

Electrons

Electron candidates are required to be identified as `loose++`, have $p_\mathrm{T} > 10$ GeV, and be in the region $|\eta| < 2.47$. Electron candidates falling in the *crack region*, $1.37 < |\eta| < 1.52$, are ignored as there is insufficient calorimeter information. Furthermore, selected candidates are required to have $|z_0| < 10$ mm and to pass additional quality criteria which require no recorded cluster problems. Lastly, tracking and calorimeter isolation criteria are applied. Track isolation requires the sum of the p_T of additional tracks in a cone of $\Delta R < 0.4$ around the electron to be less than 20% of the electron p_T. Calorimeter isolation requires the sum of energies of additional calorimeter clusters in a cone of $\Delta R < 0.2$ around the electron to be less than 20% of the electron p_T.

Muons

Muon candidates must be reconstructed from the combination of tracks in the ID and MS, have $p_T > 6 \, \text{GeV}$, be in the region $|\eta| < 2.5$, and have $|z_0| < 10 \, \text{mm}$. Lastly, tracking and calorimeter isolation criteria are applied. Track isolation requires the sum of the p_T of additional tracks in a cone of $\Delta R < 0.4$ around the muon to be less than 8% of the muon p_T. Calorimeter isolation requires the sum of energies of additional calorimeter clusters in a cone of $\Delta R < 0.2$ around the muon to be less than 8% of the muon p_T.

Hadronic Taus

Hadronically decaying tau candidates are reconstructed from clusters in the ECAL and HCAL as described in Section 3.4.4. Tau candidates are are required to have: $p_T > 20 \, \text{GeV}$, charge equal to ± 1, and either 1 or 3 tracks in a cone of radius $\Delta R < 0.2$. Tau candidates must pass `medium` criteria of the BDT identification algorithm, which corresponds to approximately 55-60% signal efficiency. The highest p_T track of 1-prong tau candidates is required to be in the range $|\eta| < 2.47$, for 3-prong tau candidates the required range is $|\eta| < 2.5$. An electron veto is applied, which requires all 1-prong tau candidates to pass the `loose` criteria of the BDT electron veto algorithm.

Jets

While this analysis does not require the presence of jets they are used to suppress backgrounds in some channels, in particular, the presence of b-tagged jets is a useful discriminator against the $t\bar{t}$ background. Jets are required to have $p_T > 30 \, \text{GeV}$ and be in the range $|\eta| < 4.5$. To suppress contributions from pileup, jets in the range $|\eta| < 2.4$ are required to have $|\text{JVF}| > 0.5$.

4.3.3 Overlap Removal

If different particles are reconstructed which overlap with each other geometrically (within $\Delta R < 0.2$) only one is considered for further analysis. Overlap resolution is handled by an order of priority: muons are considered over electrons which are considered over hadronic taus which are considered over jets. This procedure ensures that any particle in an event cannot be reconstructed as two separate particles in the final state of that event.

4.3.4 Event Categorisation

After all event and particle reconstruction requirements, events are classified into different categories to match the signal channels described in Section 2.3.1. Since each signal category has a distinct number of final state light leptons, N_ℓ, and hadronic taus, N_{τ_h}, the categorisation process is based on these numbers. Some category definitions have further requirements in addition to number of final state particles. The categorisation process is as follows:

- $N_\ell = 4$, $N_{\tau_h} = 0$: The event is classified as $Z(\to \ell\ell)H(\to \tau_\ell\tau_\ell)$ if two of the light leptons are the same flavour and opposite charge.

- $N_\ell = 3$, $N_{\tau_h} = 1$: The event is classified as $Z(\to \ell\ell)H(\to \tau_\ell\tau_h)$ if two of the light leptons are the same flavour and opposite charge.

- $N_\ell = 2$, $N_{\tau_h} = 2$: The event is classified as $Z(\to \ell\ell)H(\to \tau_h\tau_h)$ if the light lepton pair are the same flavour and opposite charge.

- $N_\ell = 3$, $N_{\tau_h} = 0$: The event is classified as $W(\to \ell\nu)H(\to \tau_\ell\tau_\ell)$ if two of the light leptons are opposite charge.

- $N_\ell = 2$, $N_{\tau_h} = 1$: The event is classified as $W(\to \ell\nu)H(\to \tau_\ell\tau_h)$ if at least one of the light leptons is opposite charge to the tau.

- $N_\ell = 1$, $N_{\tau_h} = 2$: The event is classified as $W(\to \ell\nu)H(\to \tau_h\tau_h)$.

Any event which does not match any of these criteria is not considered any further.

4.3.5 Lepton Association

In signal channels which contain multiple light leptons, an important requirement is the ability to designate a lepton as originating from either the decay of a W/Z boson or from the decay of a tau from a Higgs boson. The process of associating light leptons to either the W/Z or the H boson is the following:

- In the $Z(\to \ell\ell)H(\to \tau_\ell\tau_\ell)$ channel: The pair of same flavour and opposite charge light leptons which has an invariant mass closest to the Z mass is assigned to the Z. The remaining two leptons are assigned to the H.

- In the $Z(\to \ell\ell)H(\to \tau_\ell\tau_h)$ channel: If the event contains an opposite sign, same flavour pair of light leptons as well as another light lepton of different flavour, the pair is assigned to the Z and the other lepton to the H. If the event contains three light leptons of the same flavour, the pair whose invariant mass is closest to the Z mass is assigned to the Z, the other to the H.

- In the $W(\to \ell\nu)H(\to \tau_\ell\tau_h)$ channel: If the event contains two light leptons of opposite charge, the lepton whose charge is opposite to the hadronic tau charge is assigned to the H, the other lepton is assigned to the W. If both leptons have the same charge (which must be opposite to the hadronic tau charge), the highest p_{T} lepton is assigned to the W, the lower p_{T} lepton to the H. This assumption is correct approximately 75% of the time as the lepton from the W originates higher up in the decay chain where the W decay can impart the lepton with a large momentum. The lepton on the Higgs side of the decay originates further down the decay chain where large amounts of momentum are taken away by neutrinos from the tau decay.

- In the $W(\to \ell\nu)H(\to \tau_\ell\tau_\ell)$ channel: Two of the light leptons in this channel will have the same charge, the higher p_{T} lepton is assigned to the W, the lower p_{T} lepton and the remaining lepton are both assigned to the H.

4.4 Background Contributions

The main backgrounds which mimic the VH signal topology are events containing a mixture of real, fake, and non-prompt reconstructed particles. Hadronic taus considered in the fake background originate primarily from jets which are suitably tau-like to pass tau identification. Electrons considered in the fake background originate from multiple sources. Jets may be misidentified as electrons. Photons passing through material can pair create real non-prompt electrons and positrons, either may pass object selection. Jets may contain real electrons from non-prompt decays of light mesons or heavy flavour hadrons. From here onward, the reducible fake background collectively refers to all three of these fake and non-prompt sources. The irreducible real electron background originate from prompt decays of taus, or W or Z bosons.

4.4.1 W+Jets

This process contributes to the background in cases where the W decays leptonically and additional partons produce jets which mimic the signature of electrons or hadronic taus. The branching fraction of the decay $W \to \ell\nu$ is approximately 11% [7] for each of the lepton flavours. In these cases the final state contains only one real lepton and two fake leptons. Figure 4.1 shows two examples of events which could contribute to the background. The neutrino from the W decay will produce large $E_\mathrm{T}^\mathrm{miss}$, which is also an expected feature of the WH signal. The probability of misidentifying two jets as leptons is low, this process is not expected to contribute significantly to the total background but is included for completeness.
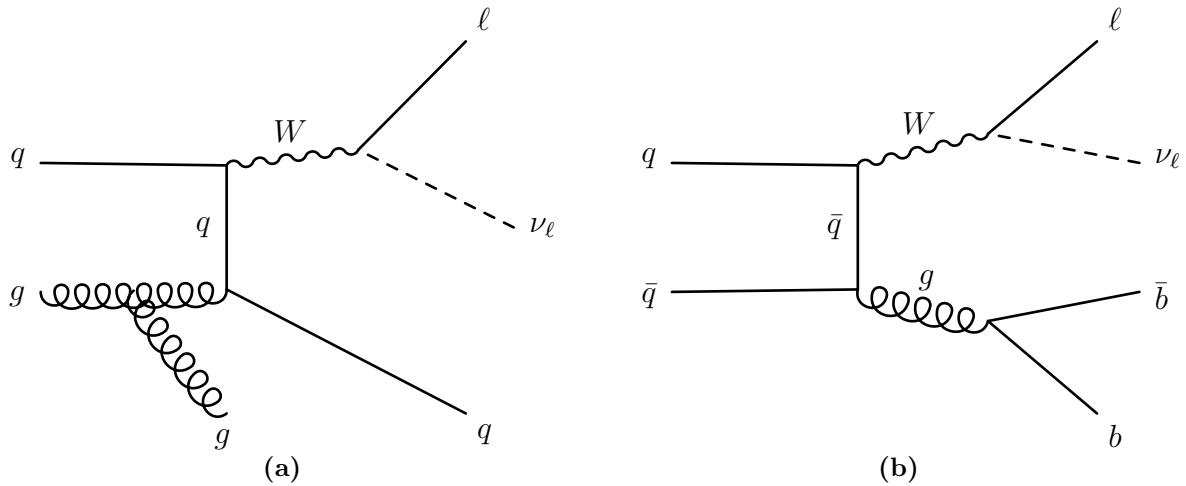
Figure 4.1: Example Feynman diagrams of the W+jets background.

4.4.2 Z/γ^*+Jets

Similar to the W+jets processes, the Z/γ^*+jets processes contribute to the background in cases where the Z/γ^* decays leptonically and is produced with additional photons or jets capable of being reconstructed as electrons or hadronic taus. This process is expected to be a large contributor to the background as it produces two real leptons, an additional lepton can be misidentified from one of the additional photons or jets. In practice however, events where the Z/γ^* decays to a light lepton pair can be largely removed by requiring the two leptons to have the same charge. In a small fraction of events, one of the leptons may have its charge misidentified, in these cases it is possible

to remove these events by requiring the invariant mass of the two light leptons be away from the Z mass. Events where the Z/γ^* decays to a tau pair are expected to contribute to the background, especially in cases where the two taus decay differently. For example, events where one tau decays to an electron and the other to a muon, and an additional jet can mimic a hadronic tau. Alternatively, one tau can decay hadronically, the other leptonically, and an additional electron is present in the event. In cases where the Z decays to light leptons, the event is expected to have low $E_{\mathrm{T}}^{\mathrm{miss}}$, this can be used to separate it from signal, however when the Z decays to taus $E_{\mathrm{T}}^{\mathrm{miss}}$ is expected due to the neutrinos from tau decays. Figure 4.2 shows two examples of events which could contribute to the background.
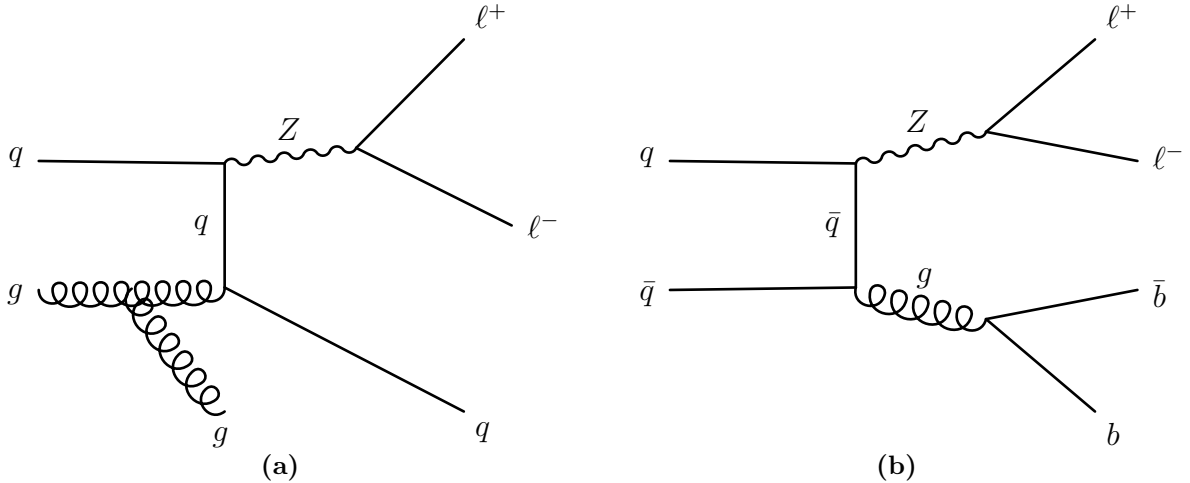
Figure 4.2: Example Feynman diagrams of the Z+jets background.

4.4.3 $t\bar{t}$+Jets

Physics processes containing top quarks produce a high multiplicity of final state particles. Top quarks decay dominantly to a W boson and a b quark [7]. The large mass of the top quark allows W to be produced on-shell, providing a source of high momentum leptons. Additional leptons can be produced from decays of b quarks, any jet in the event can mimic a hadronic tau decay. $t\bar{t}$ events with leptonic W decays will contain neutrinos which can produce large $E_{\mathrm{T}}^{\mathrm{miss}}$ as expected in the WH signal. For these reasons, there is a large number of ways the $t\bar{t}$ background can resemble the VH signal. The dominant $t\bar{t}$ backgrounds to the VH analysis are shown in Figure 4.3.

(a) $t\bar{t}$ (semi-leptonic)   **(b)** $t\bar{t}$ (fully-leptonic)
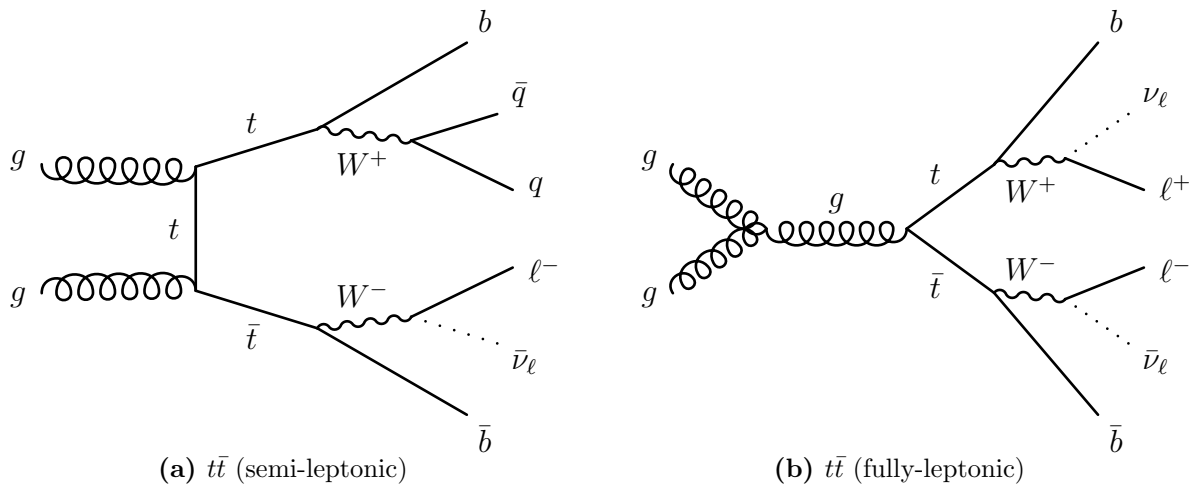
Figure 4.3: Feynman diagrams of the dominant $t\bar{t}$ production processes at the LHC [59].

4.4.4 t+Jets

Single top events usually produce at least one real lepton and two or more jets, which may originate from b quarks. This process is expected to contribute to the background in cases where one or more of the b jets decay leptonically, producing non-prompt leptons. Theses events can then mimic the signal if additional photons or jets are reconstructed as electrons or taus. Since the dominant top quark decay channel contains a W boson, which may decay leptonically, large $E_{\mathrm{T}}^{\mathrm{miss}}$ can be expected in single top events. The dominant single top backgrounds to the VH analysis are shown in Figure 4.4.

(a) single top t-channel   **(b)** single top s-channel   **(c)** single top Wt-channel
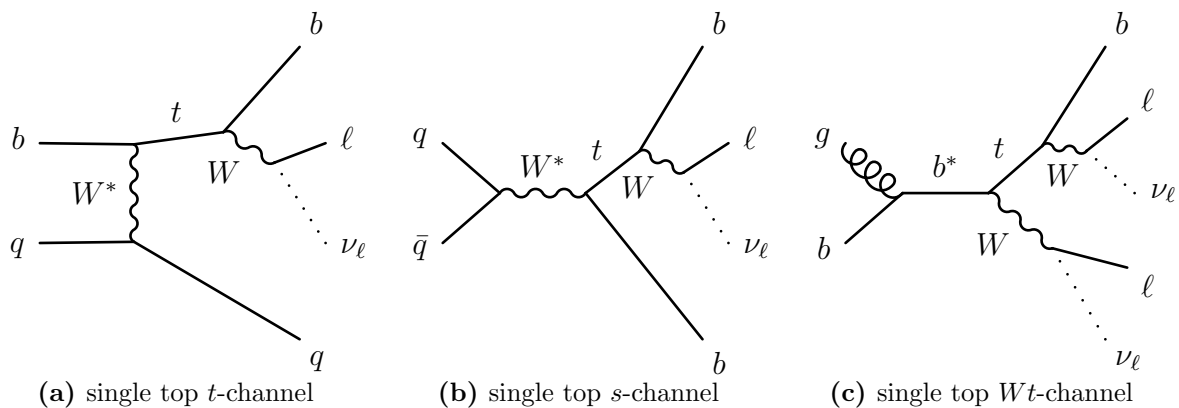
Figure 4.4: Example Feynman diagrams of the single top background.

4.4.5 WW

The WW process is expected to be a contributor to the background in cases where both W's decay leptonically and additional photons or jets in the event are reconstructed as electrons or taus. The dominant WW backgrounds to the VH analysis are shown in Figure 4.5.

(a) WW s-channel   **(b)** WW t-channel
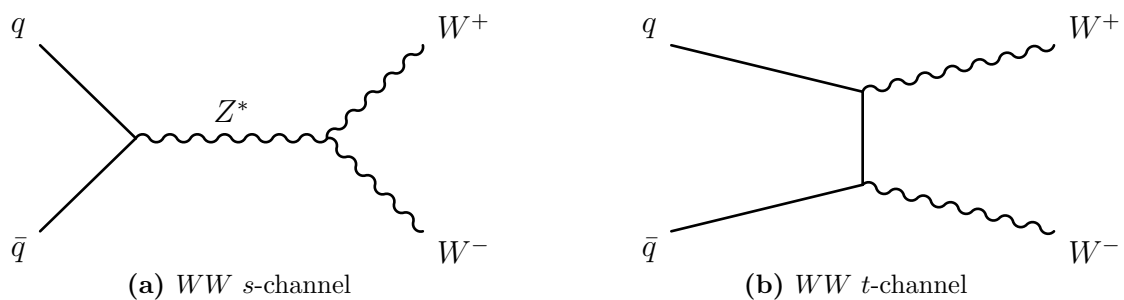
Figure 4.5: Example Feynman diagrams of the WW background.

4.4.6 WZ

The WZ process is the main irreducible background to the WH signal. WZ events can contain the same final state particles as WH events. In most cases, WZ events mimic WH events when the W decays to light leptons and the Z decays to a tau pair. The dominant WZ backgrounds to the VH analysis are shown in Figure 4.6.

(a) WZ s-channel   **(b)** WZ t-channel
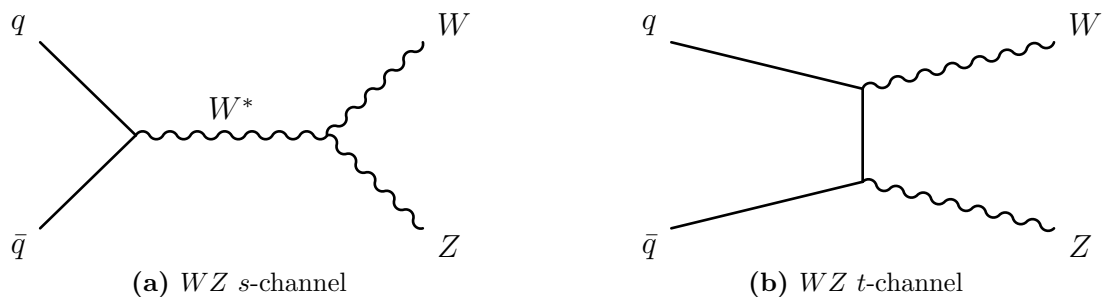
Figure 4.6: Example Feynman diagrams of the WZ background.

4.4.7 ZZ

The ZZ process is the main irreducible background to the ZH signal. ZZ events can contain the same final state particles as ZH events. In most cases, ZZ events mimic ZH events when one Z decays to light leptons and the other Z decays to a tau pair. The ZZ process is also an irreducible background to the WH signal in cases where one of the final state particles does not pass selection criteria. For example, when one Z decays to light leptons and the other Z decays to a tau pair, this event can mimic either the $W(\to \ell\nu)H(\to \tau_\ell\tau_h)$ signal if one of the taus is lost, or the $W(\to \ell\nu)H(\to \tau_h\tau_h)$ signal if one of the light leptons is lost. The dominant ZZ backgrounds to the VH analysis are shown in Figure 4.7.

(a) ZZ s-channel   **(b)** ZZ t-channel
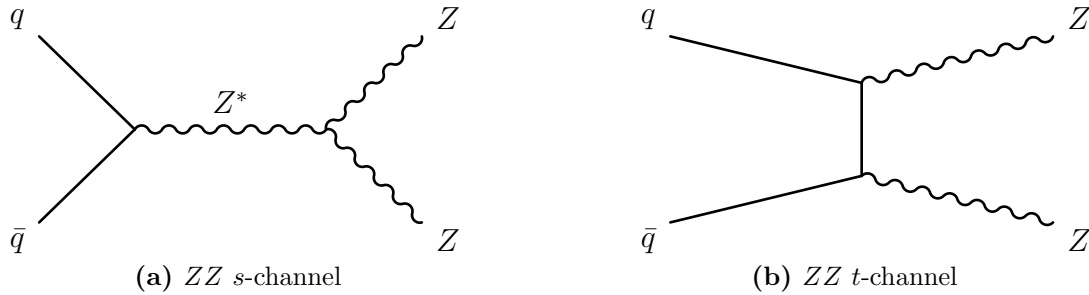
Figure 4.7: Example Feynman diagrams of the ZZ background.

4.4.8 $H \to WW^{(*)}$

Events containing Higgs decays to W bosons can be an irreducible background in the cases where the W bosons decay leptonically and the Higgs boson is produced via the VH production mode which also may produce up to two additional leptons from the leptonic decay of the associated vector boson. These events may contain up to four light leptons of any flavour, allowing for the possibility to mimic any of the $VH(\to \tau\tau)$ signal processes. Since the $H \to WW^{(*)}$ process has already been observed at ATLAS and CMS with a signal strength consistent with the SM prediction, it is treated as a background for the purposes of this analysis. Figure 4.8 shows the dominant $H \to WW^{(*)}$ backgrounds to the VH analysis.

(a) $W(\to \ell\nu)H(\to WW)$ **(b)** $Z(\to \ell\ell)H(\to WW)$
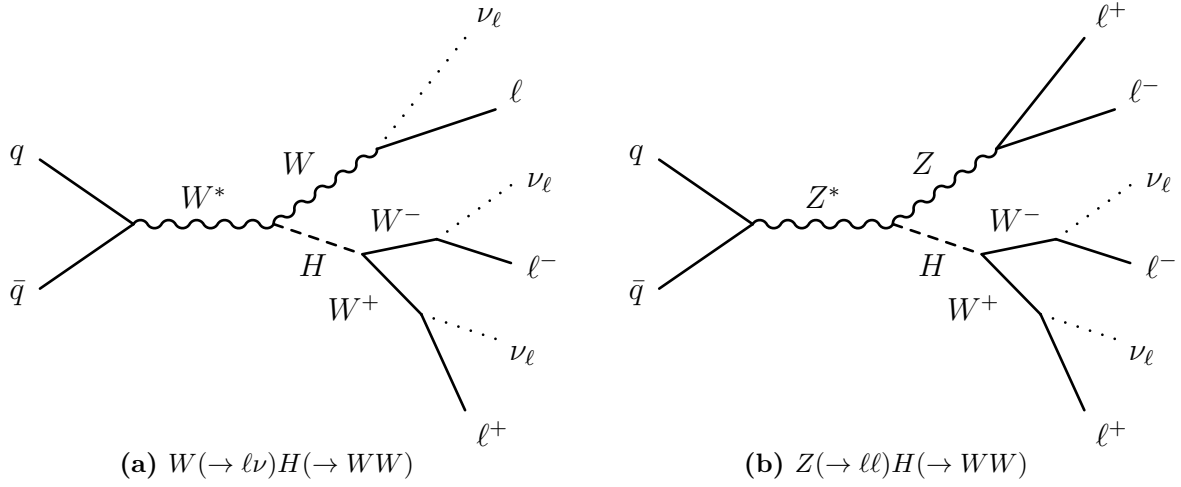
Figure 4.8: Example Feynman diagrams of the $H \to WW^{(*)}$ background.

(a) ggF $H(\to ZZ)$ **(b)** VBF $H(\to ZZ)$
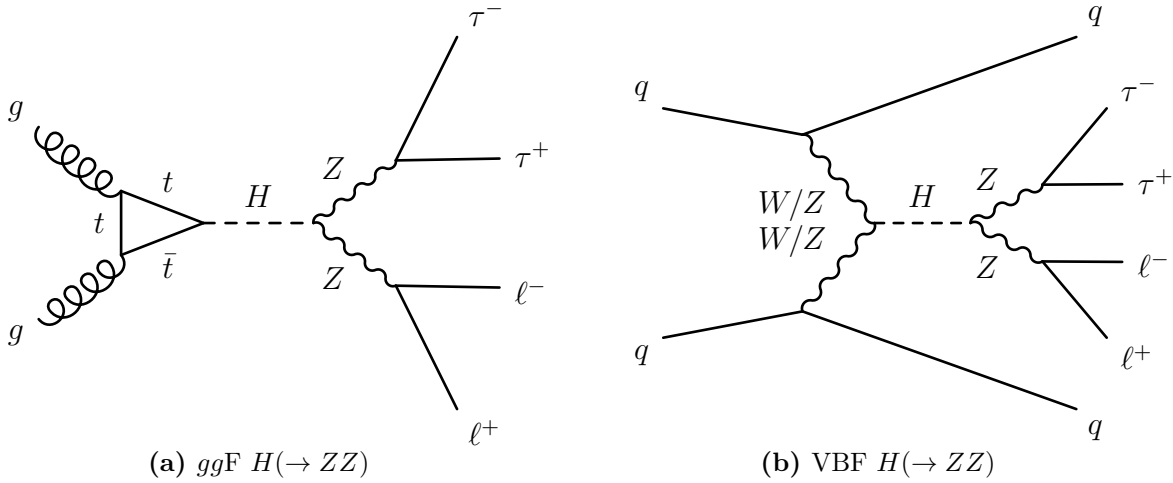
Figure 4.9: Example Feynman diagrams of the $H \to ZZ^{(*)}$ background.

4.4.9 $H \to ZZ^{(*)}$

Events containing Higgs decays to Z bosons can also be an irreducible background in the cases where both the Z bosons decay leptonically, producing four leptons. In addition, cases where one Z boson decays leptonically and the other decays hadronically may also mimic the $VH(\to \tau\tau)$ signal if the Higgs boson is produced via the VH production mode and the associated vector boson decays leptonically. This process is also treated as a background for the purposes of this analysis. Figure 4.9 shows the dominant $H \to ZZ^{(*)}$ backgrounds to the VH analysis.

4.4.10 Background Cross-sections

The relative magnitudes of the background cross-sections is shown in Figure 4.10. Also shown are the cross-sections of the different Higgs boson production modes including the VH signal. The cross-sections shown here are the total values, inclusive of all decay modes. In most cases, only the leptonic decay modes of the different processes contribute to the backgrounds in this analysis, however most of the backgrounds have cross-sections many orders of magnitude larger than the VH signal even after the leptonic branching fractions are accounted for.
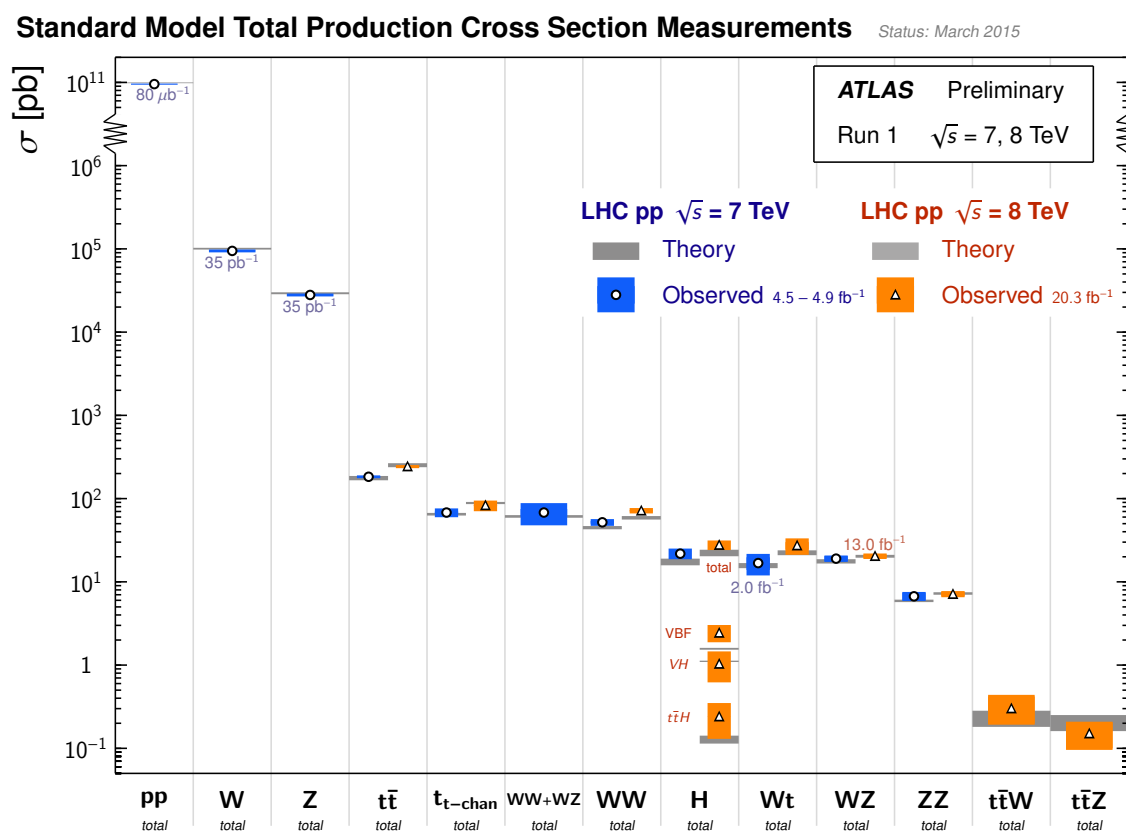
Figure 4.10: Summary of several Standard Model total production cross-section measurements, corrected for leptonic branching fractions, compared to the corresponding theoretical expectations. All theoretical expectations were calculated at Next-to-Leading Order or higher. The integrated luminosity used for each measurement is indicated close to the data point.

Chapter 5

Background Estimation

The backgrounds to the VH signal originate from the many different processes described in Section 4.4. Each of these processes is expected to mimic the signal in different ways. Some processes, such as WZ and ZZ, can match the final state signal topology exactly whereas others, such as $t\bar{t}$ and $Z \rightarrow \tau\tau$, are similar to the signal and can look signal-like when extra fake or non-prompt leptons are present in an event. Due to the signal's large number of final state particles, three for WH and four for ZH, estimating all of these backgrounds simultaneously is challenging using any one single method. It was determined early in the analysis that a pure MC-based background estimation method could not sufficiently describe all the backgrounds which contain fake and non-prompt leptons. For this reason, a hybrid method was developed for this analysis where the contributions of fake and non-prompt leptons are estimated from data and the contributions from real prompt leptons are estimated from MC. This is called the Fake Factor method and will be described in the following sections. It is however still useful to use a pure MC-based estimation method for additional background studies.

5.1 Monte-Carlo Background Estimation

MC simulated samples are used in this analysis to determine the expected background processes in each channel, as well as to study the features of the signal and background in order to determine the optimal signal selection requirements. These events are weighted by the cross-section of the given process to produce the number of events expected in $20.3\,\text{fb}^{-1}$ of data. In a pure MC-based background estimate, the properties of all final state reconstructed particles, real or fake, are determined from MC simulated samples.

70

5.1.1 Simulated Samples

The $VH(\to \tau\tau)$ signal MC samples used in this analysis are generated with Pythia using Leading Order (LO) QCD and electroweak contributions. The events are weighted to the cross-sections calculated with the more complete Next-to-Leading Order (NLO) electroweak and Next-to-Next-to-Leading Order (NNLO) QCD theoretical contributions using Hawk [60]. A separate sample is produced for each hypothesised Higgs mass value between 100 GeV and 150 GeV in 5 GeV increments.

Other Higgs production and decay channels with a similar final state to the $VH(\to \tau\tau)$ signal may contribute to this analysis. These include the decay channels: $H \to \tau\tau$ (ggF and VBF), $H \to ZZ^{(*)} \to 4\ell$, $H \to ZZ^{(*)} \to \ell\ell qq$, $H \to ZZ^{(*)} \to \ell\ell\nu\nu$, $H \to WW^{(*)} \to \ell\nu\ell\nu$, and $H \to WW^{(*)} \to \ell\nu qq$. The ggF and VBF production modes of these decay channels are generated with Powheg+Pythia, while the VH production modes are generated with Pythia. Each of these processes are treated as backgrounds and the samples are generated at the 125 GeV Higgs mass point.

The t-channel single top process is generated with AcerMC+Pythia. The s-channel and Wt-channel single top processes, as well as the $t\bar{t}$ processes are generated with MC@NLO+Jimmy. MC@NLO calculates the hard process with the full NLO corrections, up to order α_S^2, which gives a better description of top quark production observables. The WW, WZ, and ZZ processes are generated with Powheg+Pythia. The W+Jets and Z+Jets processes are generated with Alpgen+Pythia. The Alpgen generator employs the MLM matching scheme [61] to match up to five jets from the LO matrix-element with those from the parton shower to avoid double counting events with similar configurations.

After the event generation stage, the Tauola [62] and Photos [63] software packages are used to simulate the tau lepton decay and any additional photon radiation in this decay. As described in Section 3.3.2, all MC events are passed through Geant4 [51] to perform a complete ATLAS detector simulation before being passed to the event reconstruction stage.

5.2 Fake Factor Background Estimation

Backgrounds resulting from fakes, for example where a jet fakes a hadronic tau or an electron produced from a photon conversion fakes a prompt electron from a $W/Z/\tau/H$ decay, are the dominant backgrounds in all channels in the analysis. A data-driven estimation technique called the Fake Factor (FF) method has therefore been developed to model these cases. The FF method is a data driven extrapolation method for estimating the background contribution containing fake or non-prompt leptons. Events taken from a region adjacent to the signal region but enriched in objects which fail an identification criteria (see Section 5.3) are scaled by an extrapolation factor, called the fake factor. By means of this fake factor scaling, these events now represent the background events consisting of fake or non-prompt leptons that are predicted to appear in the signal region.

The fake rates (and therefore the fake factors) are measured in a FF measurement region, distinct from, but as close as possible to the signal region. Since the fake rates are sensitive to the underlying physics of the event, it is best to measure the fake factors in a region that will best represent the physics, e.g. kinematics and composition of fakes, that will be found in the signal region. Measurements of the fake rates for electrons and hadronic taus are detailed in the subsections to follow.

The FF method, in various forms, has been used previously in analyses involving hadronic tau decays, for example in the $H \to \tau\tau$ search in the VBF and ggF production modes [6]. The implementation of the method in these analyses has typically only been concerned with background events containing one tau being faked by a misidentified jet. Since the WH and ZH channels have a larger number of final state objects, the methods used by existing analysis are not directly applicable here. For this reason, a more general form of the FF method has been developed for this analysis. The general principle of the data-driven extrapolation is carried over, however it is performed at the more general *per-object* level rather than at the *per-event* level as has been done previously.

The rest of this discussion is dedicated to the derivation of the general fake background equation used in the analysis. Equations are worked out for the examples of signal regions containing one and two objects. However, it will be clear how to extrapolate to the n-object equation, and this will be stated after the derivation. The term *objects* is general, and can refer to an electron, muon, or hadronic tau.

(a) MC Background Estimate   **(b)** FF Background Estimate
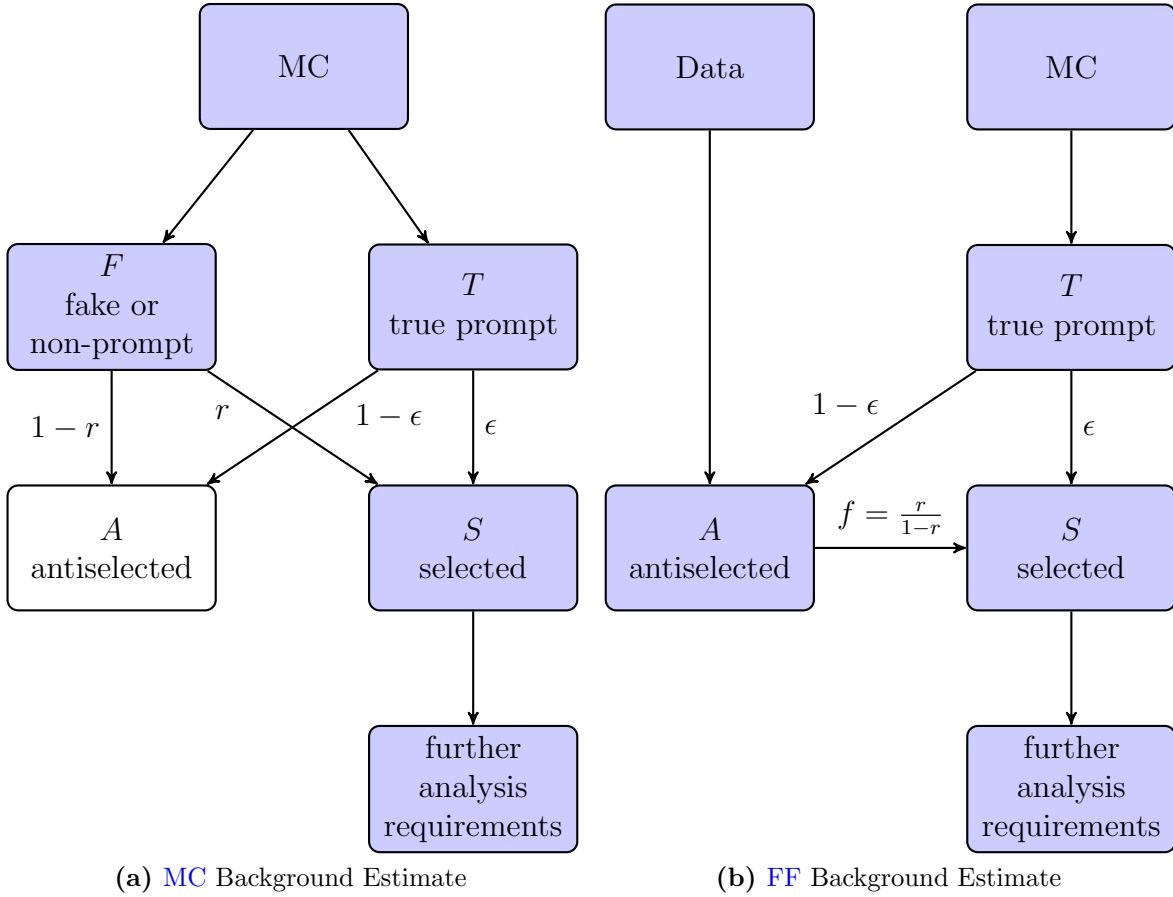
Figure 5.1: Flow diagram showing the MC (a) and FF (b) background estimation methods.

5.2.1 Method Derivation

In a purely MC-based background estimation method, MC for all processes with a final state similar to the signal process are considered. Figure 5.1a shows the flow diagram for objects considered in a purely MC-based background estimation. These processes can contain both true prompt objects (often called the irreducible background) and fake or non-prompt objects (the reducible background). True prompt objects, denoted T, have an efficiency, ϵ, of passing selection criteria. Fake and non-prompt objects, denoted F, may also pass selection criteria with an efficiency, r, called the *fake rate*.

Objects which pass selection criteria, denoted S, are then subject to further analysis requirements designed to extract the signal process. The number of *selected* objects (N_S) is simply the sum of the selected fake or non-prompt objects (N_{SF}) and the selected true

prompt objects (N_{S^T}).

$$N_S = N_{S^F} + N_{S^T} \tag{5.1}$$

$$= rN_F + \epsilon N_T \tag{5.2}$$

In this method, objects which fail selection criteria, called *antiselected*, denoted A, are no longer considered in the analysis. The region containing these antiselected objects is called the fake enriched region since it is composed mostly of fake and non-prompt backgrounds.

The FF method is designed to reduce the dependence on the MC modelling of the fake and non-prompt background by estimating these contributions from data. Figure 5.1b shows the flow diagram for objects in a FF background estimate. As in the MC method, the true prompt component of the background is estimated from MC, however the fake and non-prompt component is estimated from data. Objects in the fake enriched region which have failed selection criteria are extrapolated by the fake factor, f.

$$f = \frac{r}{1-r} \tag{5.3}$$

This extrapolation represents the number of fake or non-prompt objects expected to be selected. The total expected number of selected objects is the sum of three terms: the fake and non-prompt estimate from the fake factor extrapolation, a correction to the extrapolation to remove true prompt objects which may enter the fake enriched region, and the true prompt estimate taken from MC.

$$N_S = fN_A^{\text{data}} - f(1-\epsilon)N_T^{\text{MC}} + \epsilon N_T^{\text{MC}} \tag{5.4}$$

$$= fN_A^{\text{data}} - fN_{A^T}^{\text{MC}} + N_{S^T}^{\text{MC}} \tag{5.5}$$

In this method it is useful to distinguish objects which pass selection criteria from those which are extrapolated into the selected region. Objects which enter the signal region because they pass selection criteria are denoted S, as has been done up until this point. Objects which enter the signal region as a result of the fake factor extrapolation are denoted $\bar{S}$:

$$N_A \xrightarrow{\text{apply FF}} N_{\bar{S}} = fN_A \tag{5.6}$$

The FF estimate of the number of selected objects is then:

$$N_S = N_{\bar{S}}^{\text{data}} - N_{\bar{S}T}^{\text{MC}} + N_{ST}^{\text{MC}} \tag{5.7}$$

This expression represents the concept of the FF model, in the next sections the complete expression will be derived, starting with the simplest example case.

5.2.2 One Object Case

The simplest example is the case requiring exactly one selected object. In this section the one object case will be derived in its general form with the aid of an example analysis for context. Consider an analysis of the $W \to \tau_h \nu$ process, which has exactly one visible final state object, the τ_h. This analysis aims to find $W \to \tau_h \nu$ events by constructing event selection criteria to select only events with exactly one τ_h, and no other additional objects. Example backgrounds to this analysis may include $W \to e\nu$ events in the case where the electron is misidentified as a hadronic tau, or multi-jet events in the case where exactly one jet is misidentified as a hadronic tau.

In the general case of this example the aim is to estimate the background contribution where exactly one selected fake or non-prompt object appears in the final state. Background events may contain any number of fake or non-prompt objects, denoted F_i, which may either pass (S_i^F) or fail (A_i^F) selection criteria. The list of all possible combinations of selecting objects is:

$$F_1 \to S_1^F \text{ or } A_1^F \tag{5.8}$$

$$F_1 F_2 \to S_1^F S_2^F \text{ or } S_1^F A_2^F \text{ or } A_1^F S_2^F \text{ or } A_1^F A_2^F \tag{5.9}$$

$$F_1 F_2 F_3 \to S_1^F S_2^F S_3^F \text{ or } S_1^F S_2^F A_3^F \text{ or } S_1^F A_2^F S_3^F \text{ or } A_1^F S_2^F S_3^F \tag{5.10}$$

$$\text{or } S_1^F A_2^F A_3^F \text{ or } A_1^F S_2^F A_3^F \text{ or } A_1^F A_2^F S_3^F \text{ or } A_1^F A_2^F A_3^F \tag{5.11}$$

$$... \to ... \tag{5.12}$$

Returning to the specific $W \to \tau_h \nu$ example analysis, F_1 may represent the electron from the $W \to e\nu$ background which may be misidentified as a hadronic tau, and become S_1^F. $F_1 F_2$ and $F_1 F_2 F_3$ may represent di- and tri-jet events respectively, any of these jets may be misidentified as a hadronic tau, leading to many possible combinations of selecting these objects.

Events containing exactly one selected object fall into the signal region in this example, the probability of obtaining each combination is denoted by the weight in front of each term on the right hand side of the following:

$$N_{S_1^F} = r_1 N_{F_1} \tag{5.13}$$

$$N_{S_1^F A_2^F} = r_1(1 - r_2)N_{F_1 F_2} \tag{5.14}$$

$$N_{A_1^F S_2^F} = (1 - r_1)r_2 N_{F_1 F_2} \tag{5.15}$$

$$N_{S_1^F A_2^F A_3^F} = r_1(1 - r_2)(1 - r_3)N_{F_1 F_2 F_3} \tag{5.16}$$

$$N_{A_1^F S_2^F A_3^F} = (1 - r_1)r_2(1 - r_3)N_{F_1 F_2 F_3} \tag{5.17}$$

$$N_{A_1^F A_2^F S_3^F} = (1 - r_1)(1 - r_2)r_3 N_{F_1 F_2 F_3} \tag{5.18}$$

$$... = ... \tag{5.19}$$

The total contribution of fake and non-prompt backgrounds to this example signal region is the sum of all of these terms. In order to estimate these contributions, the terms: N_{F_1}, $N_{F_1 F_2}$, $N_{F_1 F_2 F_3}$, ... need to be determined. This is done by noting that these terms also show up in events entering the fake enriched region:

$$N_{A_1^F} = (1 - r_1)N_{F_1} \tag{5.20}$$

$$N_{A_1^F A_2^F} = (1 - r_1)(1 - r_2)N_{F_1 F_2} \tag{5.21}$$

$$N_{A_1^F A_2^F A_3^F} = (1 - r_1)(1 - r_2)(1 - r_3)N_{F_1 F_2 F_3} \tag{5.22}$$

$$... = ... \tag{5.23}$$

By inverting the above expressions and using equation (5.3), the estimate of background events entering into the signal region is the sum of the following terms:

$$N_{\bar{S}_1} = f_1 N_{A_1} \tag{5.24}$$

$$N_{\bar{S}_1 A_2} = f_1 N_{A_1 A_2} \tag{5.25}$$

$$N_{A_1 \bar{S}_2} = f_2 N_{A_1 A_2} \tag{5.26}$$

$$N_{\bar{S}_1 A_2 A_3} = f_1 N_{A_1 A_2 A_3} \tag{5.27}$$

$$N_{A_1 \bar{S}_2 A_3} = f_2 N_{A_1 A_2 A_3} \tag{5.28}$$

$$N_{A_1 A_2 \bar{S}_3} = f_3 N_{A_1 A_2 A_3} \tag{5.29}$$

$$... = ... \tag{5.30}$$

Input Event	Output Event(s)
A_1	$\bar{S}_1$
$A_1 A_2$	$\bar{S}_1,\ \bar{S}_2$
$A_1 A_2 A_3$	$\bar{S}_1,\ \bar{S}_2,\ \bar{S}_3$
...	...

Table 5.1: Input events in data and MC which fall into the fake enriched region are duplicated one or more times to extrapolate each combination of applying the fake factor. Output objects are then subject to further analysis requirements which treat the object in the same way as selected objects. The weight assigned to each event is the fake factor. In this scenario the signal region requires exactly one selected object.

Again returning to the $W \to \tau_h \nu$ example analysis, these equations describe how to estimate the contributions from different backgrounds. The electron in the $W \to e\nu$ background may sometimes be misidentified as a hadronic tau, but in most cases it will fail tau identification. The expression $N_{\bar{S}_1} = f_1 N_{A_1}$ describes how to estimate this misidentified electron contribution ($N_{\bar{S}_1}$) from events where the electron fails tau identification (N_{A_1}) using the $e \to \tau_h$ fake factor f_1. Likewise the terms involving two or three antiselected objects can be used to estimate the multi-jet background where exactly one of the jets is misidentified as a hadronic tau.

In practice, this infinite sum is evaluated by duplicating events in the fake enriched region multiple times, once for each combination of the fake factor application. This summation provides the expected yield of events containing fake objects based on observables (N_{A_1}, $N_{A_1 A_2}$, $N_{A_1 A_2 A_3}$, ...) instead of on knowledge about the types and rates of processes which contain fakes (N_{F_1}, $N_{F_1 F_2}$, $N_{F_1 F_2 F_3}$, ...). After application of the fake factor, any objects which fail selection criteria and have not been extrapolated into the signal region are no longer considered in the analysis. Table 5.1 shows the ways in which events from the fake enriched region are duplicated. This process is applied to data and MC events in the fake enriched region in order to produce the first two terms, respectively, on the right hand side of equation (5.7).

5.2.3 Two Object Case

The next simplest example is the case requiring exactly two selected objects. This example is slightly more complex than the one object case since there is a possibility of events containing combinations of true prompt and fake or non-prompt selected objects entering into the signal region. The list of all possible combinations of selecting objects is:

$$T_1 F_2 \rightarrow S_1^T S_2^F \text{ or } S_1^T A_2^F \text{ or } A_1^T S_2^F \text{ or } A_1^T A_2^F \tag{5.31}$$

$$T_1 F_2 F_3 \rightarrow S_1^T S_2^F A_3^F \text{ or } S_1^T A_2^F S_3^F \text{ or } S_1^T A_2^F A_3^F \text{ or } S_1^T S_2^F S_3^F \tag{5.32}$$

$$\text{or } A_1^T S_2^F A_3^F \text{ or } A_1^T A_2^F S_3^F \text{ or } A_1^T A_2^F A_3^F \text{ or } A_1^T S_2^F S_3^F \tag{5.33}$$

$$... \rightarrow ... \tag{5.34}$$

$$F_1 F_2 \rightarrow S_1^F S_2^F \text{ or } A_1^F A_2^F \text{ or } S_1^F A_2^F \text{ or } A_1^F S_2^F \tag{5.35}$$

$$F_1 F_2 F_3 \rightarrow S_1^F S_2^F S_3^F \text{ or } S_1^F S_2^F A_3^F \text{ or } S_1^F A_2^F S_3^F \text{ or } A_1^F S_2^F S_3^F \tag{5.36}$$

$$\text{or } S_1^F A_2^F A_3^F \text{ or } A_1^F S_2^F A_3^F \text{ or } A_1^F A_2^F S_3^F \text{ or } A_1^F A_2^F A_3^F \tag{5.37}$$

$$... \rightarrow ... \tag{5.38}$$

Consider an example analysis which aims to study the $H \rightarrow \tau_e \tau_h$ process, which requires exactly two final state objects, one electron and one hadronic tau. In this example, the $T_1 F_2$ term may represent the $W(\rightarrow e\nu)+$jets background where the electron (T_1) is real and an extra jet (F_2) is misidentified as a hadronic tau. The term $F_1 F_2$ may represent the di-jet background where one jet (F_1) is misidentified as an electron, and the other jet (F_2) is misidentified as a hadronic tau.

Events containing exactly two selected objects fall into the signal region in this example:

$$N_{S_1^T S_2^F} = \epsilon_1 r_2 N_{T_1 F_2} \tag{5.39}$$

$$N_{S_1^T S_2^F A_3^F} = \epsilon_1 r_2 (1 - r_3) N_{T_1 F_2 F_3} \tag{5.40}$$

$$N_{S_1^T A_2^F S_3^F} = \epsilon_1 (1 - r_2) r_3 N_{T_1 F_2 F_3} \tag{5.41}$$

$$N_{A_1^T S_2^F S_3^F} = (1 - \epsilon_1) r_2 r_3 N_{T_1 F_2 F_3} \tag{5.42}$$

$$... = ... \tag{5.43}$$

$$N_{S_1^F S_2^F} = r_1 r_2 N_{F_1 F_2} \tag{5.44}$$

$$N_{S_1^F S_2^F A_3^F} = r_1 r_2 (1 - r_3) N_{F_1 F_2 F_3} \tag{5.45}$$

$$N_{S_1^F A_2^F S_3^F} = r_1 (1 - r_2) r_3 N_{F_1 F_2 F_3} \tag{5.46}$$

$$N_{A_1^F S_2^F S_3^F} = (1 - r_1) r_2 r_3 N_{F_1 F_2 F_3} \tag{5.47}$$

$$... = ... \tag{5.48}$$

The terms on the right hand side of these equations can be determined by inverting the equations for the terms entering the fake enriched region:

$$N_{S_1^T A_2^F} = \epsilon_1(1 - r_2)N_{T_1 F_2} \tag{5.49}$$

$$N_{A_1^T S_2^F} = (1 - \epsilon_1)r_2 N_{T_1 F_2} \tag{5.50}$$

$$N_{A_1^T A_2^F} = (1 - \epsilon_1)(1 - r_2)N_{T_1 F_2} \tag{5.51}$$

$$N_{S_1^T A_2^F A_3^F} = \epsilon_1(1 - r_2)(1 - r_3)N_{T_1 F_2 F_3} \tag{5.52}$$

$$N_{A_1^T S_2^F A_3^F} = (1 - \epsilon_1)r_2(1 - r_3)N_{T_1 F_2 F_3} \tag{5.53}$$

$$N_{A_1^T A_2^F S_3^F} = (1 - \epsilon_1)(1 - r_2)r_3 N_{T_1 F_2 F_3} \tag{5.54}$$

$$N_{A_1^T A_2^F A_3^F} = (1 - \epsilon_1)(1 - r_2)(1 - r_3)N_{T_1 F_2 F_3} \tag{5.55}$$

$$... = ... \tag{5.56}$$

$$N_{S_1^F A_2^F} = r_1(1 - r_2)N_{F_1 F_2} \tag{5.57}$$

$$N_{A_1^F S_2^F} = (1 - r_1)r_2 N_{F_1 F_2} \tag{5.58}$$

$$N_{A_1^F A_2^F} = (1 - r_1)(1 - r_2)N_{F_1 F_2} \tag{5.59}$$

$$N_{S_1^F A_2^F A_3^F} = r_1(1 - r_2)(1 - r_3)N_{F_1 F_2 F_3} \tag{5.60}$$

$$N_{A_1^F S_2^F A_3^F} = (1 - r_1)r_2(1 - r_3)N_{F_1 F_2 F_3} \tag{5.61}$$

$$N_{A_1^F A_2^F S_3^F} = (1 - r_1)(1 - r_2)r_3 N_{F_1 F_2 F_3} \tag{5.62}$$

$$N_{A_1^F A_2^F A_3^F} = (1 - r_1)(1 - r_2)(1 - r_3)N_{F_1 F_2 F_3} \tag{5.63}$$

$$... = ... \tag{5.64}$$

The extra complexity of the two object case can be seen here, there are multiple ways in which an event can enter the fake enriched region with the same number of selected objects. Up until this point, indices have been used on objects to assist in mapping initial to final states, however since objects in an event are inherently unordered when evaluating total yields ($N_{T_1 F_2} = N_{F_1 T_2}$), indices will be dropped for the remainder of the derivation. The solutions to the equations requiring two selected objects can be found by using the expressions for events entering the fake enriched region. This is done by grouping terms with the same number of objects, for example, the contribution from processes containing exactly two objects is:

$$N_{SS}^{\text{two objects}} = N_{S^T S^F} + N_{S^F S^F} \tag{5.65}$$

$$= \epsilon r N_{TF} + rr N_{FF} \tag{5.66}$$

The contributions to the fake enriched region from processes containing exactly two objects are:

$$N_{SA}^{\text{two objects}} = N_{S^T A^F} + N_{A^T S^F} + N_{S^F A^F} + N_{A^F S^F} \tag{5.67}$$

$$= \epsilon(1-r)N_{TF} + (1-\epsilon)rN_{TF} + r(1-r)N_{FF} + (1-r)rN_{FF} \tag{5.68}$$

and:

$$N_{AA}^{\text{two objects}} = N_{A^T A^F} + N_{A^F A^F} \tag{5.69}$$

$$= (1-\epsilon)(1-r)N_{TF} + (1-r)(1-r)N_{FF} \tag{5.70}$$

Inverting equation (5.68) gives:

$$\epsilon(1-r)N_{TF} = N_{SA} - (1-\epsilon)rN_{TF} - r(1-r)N_{FF} - (1-r)rN_{FF} \tag{5.71}$$

Multiplying both sides by f gives:

$$\epsilon r N_{TF} = fN_{SA} - f(1-\epsilon)rN_{TF} - fr(1-r)N_{FF} - f(1-r)rN_{FF} \tag{5.72}$$

$$= fN_{SA} - f(1-\epsilon)rN_{TF} - rrN_{FF} - rrN_{FF} \tag{5.73}$$

This gives the expression for the first term in equation (5.66), giving:

$$N_{SS}^{\text{two objects}} = \epsilon r N_{TF} + rrN_{FF} \tag{5.74}$$

$$= fN_{SA} - f(1-\epsilon)rN_{TF} - rrN_{FF} \tag{5.75}$$

Inverting equation (5.70) gives:

$$(1-r)(1-r)N_{FF} = N_{AA} - (1-\epsilon)(1-r)N_{TF} \tag{5.76}$$

Multiplying both sides by f^2 gives:

$$rrN_{FF} = ffN_{AA} - ff(1-\epsilon)(1-r)N_{TF} \tag{5.77}$$

$$= ffN_{AA} - f(1-\epsilon)rN_{TF} \tag{5.78}$$

Putting this result back into equation (5.75) gives the final expression for two objects:

$$N_{SS}^{\text{two objects}} = fN_{SA} - ffN_{AA} \tag{5.79}$$

Input Event	Output Event(s)
$S_1 A_2$	$+S_1 \bar{S}_2$
$S_1 A_2 A_3$	$+S_1 \bar{S}_2,\ +S_1 \bar{S}_3$
...	...
$A_1 A_2$	$-\bar{S}_1 \bar{S}_2$
$A_1 A_2 A_3$	$-\bar{S}_1 \bar{S}_2,\ -\bar{S}_1 \bar{S}_3,\ -\bar{S}_2 \bar{S}_3$
...	...

Table 5.2: Input events in data and MC which fall into the fake enriched region are duplicated one or more times to extrapolate each combination of applying the fake factor. Output objects are then subject to further analysis requirements which treat the object in the same way as selected objects. The weight assigned to each event is the fake factor. In this scenario the signal region requires exactly two selected objects.

This expresses the contribution of the fake or non-prompt background to the two object signal region as the application of the fake factor to each antiselected object in the event. The sign of the term is positive when one fake factor is applied and negative when two fake factors are applied. The expressions for the contributions from terms containing exactly three objects ($N_{T_1 F_2 F_3}$ and $N_{F_1 F_2 F_3}$) are determined using the same procedure, the only difference being that there are then multiple ways to apply fake factors to events with three or more objects. Table 5.2 shows the ways in which events from the fake enriched region are duplicated, indices have been restored to show the different combinations of applying the fake factor.

5.2.4 Three and Four Object Cases

The VH signal region requires three (WH) or four (ZH) objects in the final state. The expression for the fake and non-prompt contribution to these signal regions is an extension of the previous results. The general form of the expression is to apply the fake factor to each available combination of antiselected objects in the fake enriched region. The sign of each term is positive if the number of fake factor applications is odd, and negative if it's even. The contribution of fake and non-prompt objects to the WH and ZH signal regions are the sum of the output events in Table 5.3 and Table 5.4 respectively.

Input Event	Output Event(s)
$S_1 S_2 A_3$	$+S_1 S_2 \bar{S}_3$
$S_1 S_2 A_3 A_4$	$+S_1 S_2 \bar{S}_3, +S_1 S_2 \bar{S}_4$
$S_1 S_2 A_3 A_4 A_5$	$+S_1 S_2 \bar{S}_3, +S_1 S_2 \bar{S}_4, +S_1 S_2 \bar{S}_5$
...	...
$S_1 A_2 A_3$	$-S_1 \bar{S}_2 \bar{S}_3$
$S_1 A_2 A_3 A_4$	$-S_1 \bar{S}_2 \bar{S}_3, -S_1 \bar{S}_2 \bar{S}_4, -S_1 \bar{S}_3 \bar{S}_4$
...	...
$A_1 A_2 A_3$	$+\bar{S}_1 \bar{S}_2 \bar{S}_3$
$A_1 A_2 A_3 A_4$	$+\bar{S}_1 \bar{S}_2 \bar{S}_3, +\bar{S}_1 \bar{S}_2 \bar{S}_4, +\bar{S}_1 \bar{S}_3 \bar{S}_4, +\bar{S}_2 \bar{S}_3 \bar{S}_4$
...	...

Table 5.3: Input events in data and MC which fall into the fake enriched region are duplicated one or more times to extrapolate each combination of applying the fake factor. Output objects are then subject to further analysis requirements which treat the object in the same way as selected objects. The weight assigned to each event is the fake factor. In this scenario the signal region requires exactly three selected objects, as is the case for the WH signal.

5.3 Fake and Non-Prompt Candidate Requirements

The requirements imposed on antiselected objects must be orthogonal to those for selected objects, however the antiselected objects must still appear similar to selected objects in order for the fake factor extrapolation to meaningfully represent the fake and non-prompt background.

5.3.1 Electrons

Antiselected electrons are required to satisfy all criteria in Section 4.3.2 with the exception that they are required to fail `loose++` identification (see Section 3.4.1). This definition is used in Section 5.4 and is found to adequately allow for the fake factor extrapolation to estimate the fake and non-prompt electron background.

Input Event	Output Event(s)
$S_1 S_2 S_3 A_4$	$+S_1 S_2 S_3 \bar{S}_4$
$S_1 S_2 S_3 A_4 A_5$	$+S_1 S_2 S_3 \bar{S}_4, \ +S_1 S_2 S_3 \bar{S}_5$
...	...
$S_1 S_2 A_3 A_4$	$-S_1 S_2 \bar{S}_3 \bar{S}_4$
$S_1 S_2 A_3 A_4 A_5$	$-S_1 S_2 \bar{S}_3 \bar{S}_4, \ -S_1 S_2 \bar{S}_3 \bar{S}_5, \ -S_1 S_2 \bar{S}_4 \bar{S}_5$
...	...
$S_1 A_2 A_3 A_4$	$+S_1 \bar{S}_2 \bar{S}_3 \bar{S}_4$
$S_1 A_2 A_3 A_4 A_5$	$+S_1 \bar{S}_2 \bar{S}_3 \bar{S}_4, \ +S_1 \bar{S}_2 \bar{S}_3 \bar{S}_5, \ +S_1 \bar{S}_2 \bar{S}_4 \bar{S}_5$
...	...
$A_1 A_2 A_3 A_4$	$-\bar{S}_1 \bar{S}_2 \bar{S}_3 \bar{S}_4$
...	...

Table 5.4: Input events in data and MC which fall into the fake enriched region are duplicated one or more times to extrapolate each combination of applying the fake factor. Output objects are then subject to further analysis requirements which treat the object in the same way as selected objects. The weight assigned to each event is the fake factor. In this scenario the signal region requires exactly four selected objects, as is the case for the ZH signal.

5.3.2 Hadronic Taus

Antiselected taus are required to satisfy all criteria in Section 4.3.2 with the exception that they are required to fail medium BDT identification. Antiselected taus must also pass BDT identification with a BDT score of at least 70% of the loose identification threshold. This definition is used in Section 5.5 where it is found to adequately describe the fake tau background expected in the VH signal regions.

5.3.3 Overlap Removal

The procedure described in Section 4.3.3 is extended to handle antiselected candidates. The order of priority becomes: selected muons, selected electrons, selected hadronic taus, antiselected hadronic taus, antiselected electrons.

(a) $Z(\rightarrow \mu\mu) + \text{jet}$ **(b)** $Z \rightarrow \mu\mu\gamma$
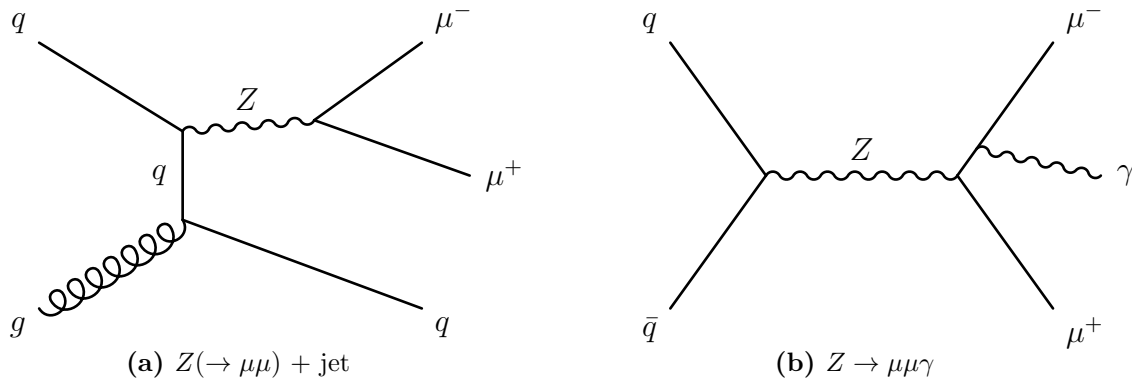
Figure 5.2: Example Feynman diagrams of the $Z \rightarrow \mu\mu$ process containing additional objects which may fake electron identification or produce non-prompt electrons.

5.4 Electron Fake Factor Measurement

Electrons considered in the fake background originate from multiple sources. Jets may be misidentified as electrons. Photons passing through material can pair create real non-prompt electrons and positrons, either may pass object selection. Jets may contain real electrons from non-prompt decays of light mesons or heavy flavour hadrons. From here onward, the reducible fake background collectively refers to all three of these fake and non-prompt sources.

Measurement of the electron fake factor is performed in a process with similar kinematics and fake and non-prompt electron composition to the VH signal region. This is a requirement as it is known that fake factor measurements are strongly dependent on the kinematics and composition, for example photon conversions occur more frequently at high η as they pass through more material. The remainder of this chapter will be as follows: first the fake factor measurement region will be defined, followed by the separate fake factor measurements performed for the WH and ZH channels.

5.4.1 Measurement Region

The electron fake factor is measured in a $Z \rightarrow \mu\mu$ enriched region. This process was chosen as it can occur with additional jets (Figure 5.2a) or photons (Figure 5.2b). These additional objects form a similar composition to the expected background of fake and non-prompt electrons in the VH signal regions.
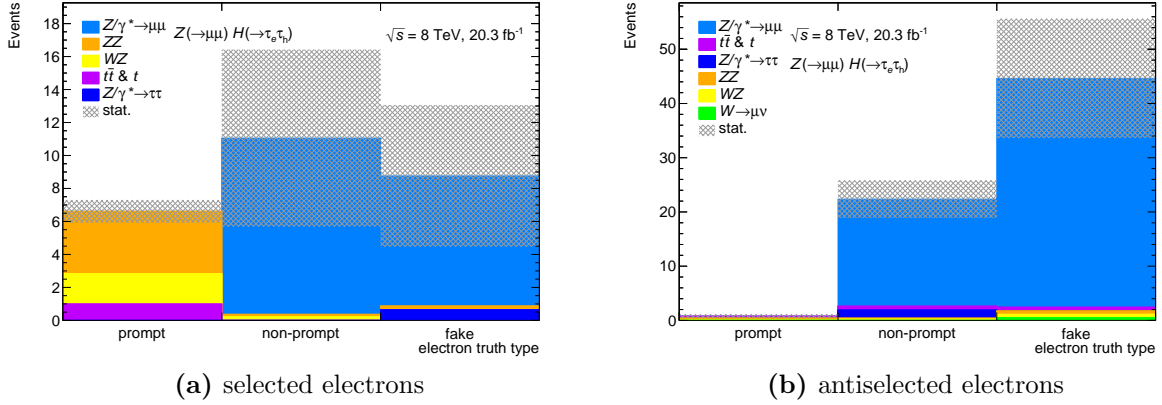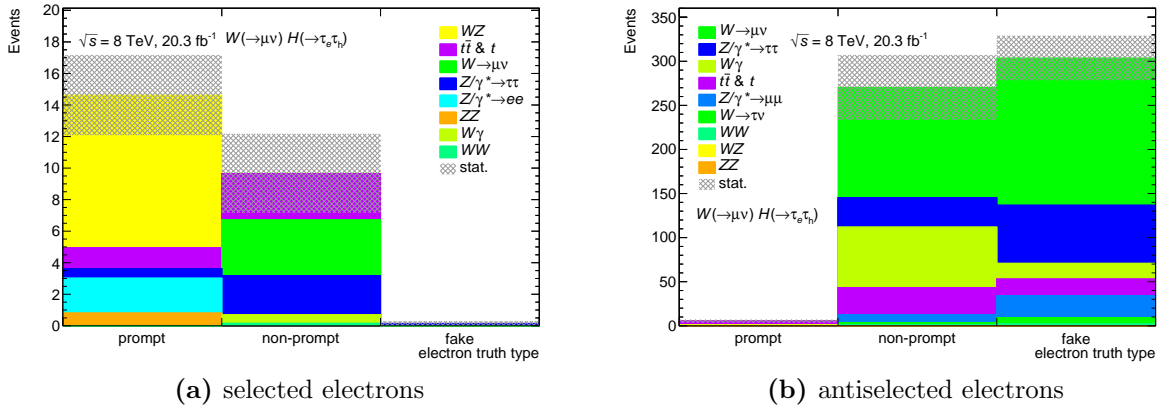
Figure 5.3: Composition of electrons in the $Z(\to \mu\mu)H(\to \tau_e\tau_h)$ channel. The grey cross-hatched region gives the statistical error on the sum of the backgrounds.

The events are required to be triggered by either the `EF_mu24i_tight` or `EF_mu36_tight` trigger, contain exactly two opposite sign muons, and contain no b-tagged jets. The events are required to contain exactly one probe electron which passes all electron object and quality criteria with the exception that no identification requirement is imposed. Probe electrons which pass `tight++` identification are referred to as *selected electrons*, those which fail `loose++` identification are referred to as *antiselected electrons*.

Two separate fake factor measurements are performed, targeted at the WH and ZH categories as they contain a significantly different composition of fake electrons, these measurements will be outlined in the following sections.

5.4.2 Measurement for the *ZH* Channel

The MC estimate of the electron composition in the ZH signal region, shown in Figure 5.3a, contains roughly equal portions of jet fakes and photon conversions. The sideband, shown in Figure 5.3b, contains significant contributions from both sources but is dominated by jet fakes. Electron identification strongly suppresses jet fakes. Photon conversions produce real non-prompt electrons which more closely match the signature of real prompt electrons. The suppression of photon conversions is less strong than for fake jets, leading to a higher fake factor. This compositional dependence is accounted for by performing the fake factor measurement in a subset of the $Z \to \mu\mu$ enriched region which most closely matches the expected composition in the ZH categories. This is achieved by requiring a tight cut on the di-muon mass: $|M_{\mu\mu} - M_Z| < 10\,\text{GeV}$, shown
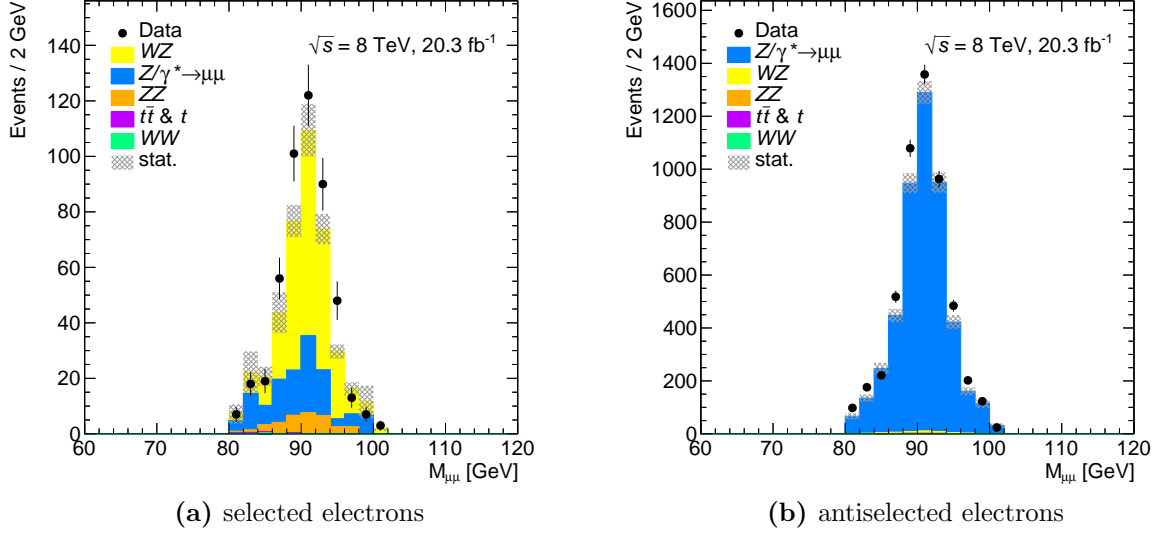
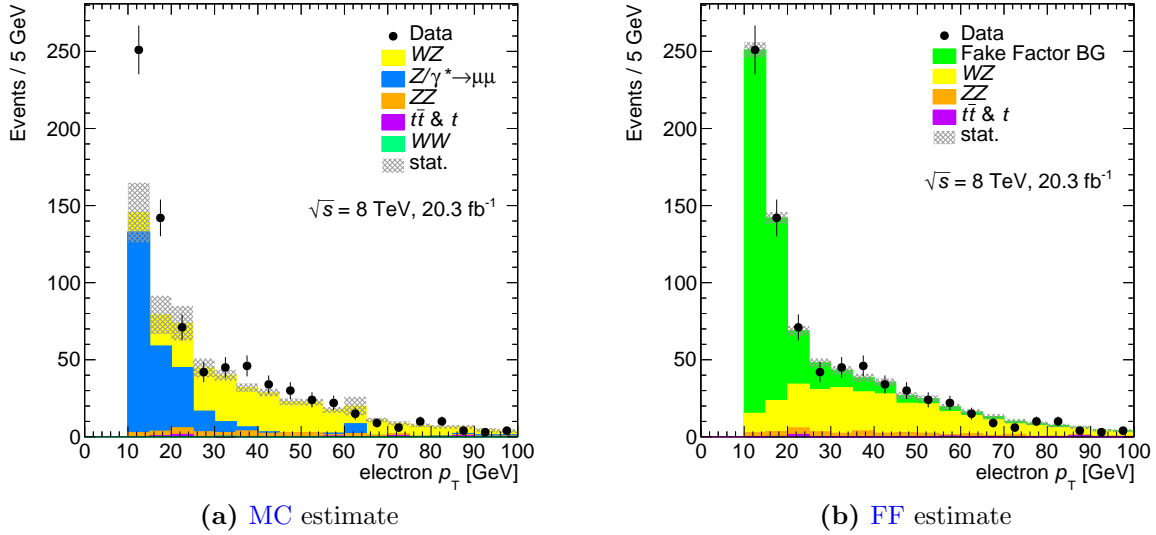**Figure 5.4:** The mass window used for the ZH category fake factor measurement. The error bars on the data (filled black circles) are statistical, whilst the grey cross-hatched region gives the statistical error on the sum of the backgrounds.
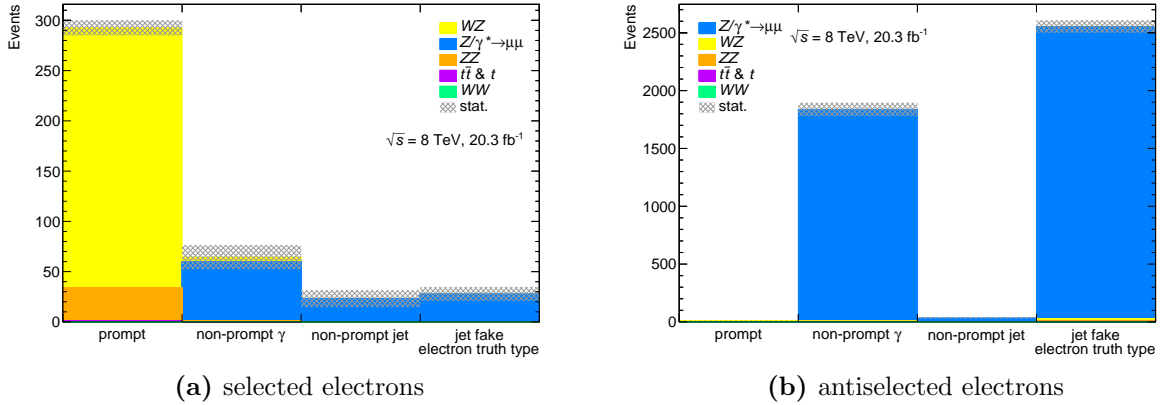
Figure 5.5: Composition of electrons in the $Z \rightarrow \mu\mu$ measurement region with the requirement that $|M_{\mu\mu} - M_Z| < 10\,\text{GeV}$. The grey cross-hatched region gives the statistical error on the sum of the backgrounds.

in Figure 5.4. This requirement ensures that the $Z \rightarrow \mu\mu$ decay produces a minimal amount of final state radiation, which would increase the non-prompt photon contribution. After this requirement, the composition of selected and antiselected electrons is shown in Figure 5.5a and Figure 5.5b respectively.

(a) electron p_T **(b)** electron η
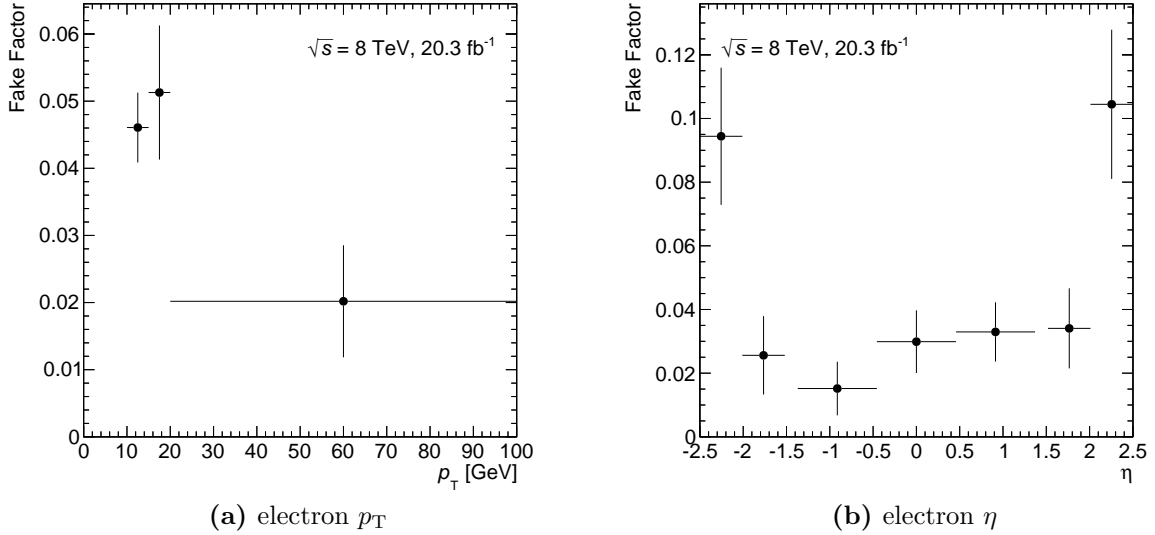
Figure 5.6: Measured fake factor for the ZH category in the two separate projections of the measurement. The error bars on the data (filled black circles) are statistical.

The fake factor measured in the $Z \to \mu\mu$ enriched region is defined as:

$$f(p_{\mathrm{T}}, \ \eta) = \frac{N_{\mathrm{selected}}^{\mathrm{data}}(p_{\mathrm{T}}, \ \eta) - N_{\mathrm{selected}}^{\mathrm{prompt\ MC}}(p_{\mathrm{T}}, \ \eta)}{N_{\mathrm{antiselected}}^{\mathrm{data}}(p_{\mathrm{T}}, \ \eta) - N_{\mathrm{antiselected}}^{\mathrm{prompt\ MC}}(p_{\mathrm{T}}, \ \eta)} \tag{5.80}$$

The fake factor is measured in the 2D phase-space of electron p_{T} and η since these are the variables which the fake factor is most strongly dependent on. Seven η bins and three p_{T} bins are chosen for the measurement as this best describes the observed dependence given the available statistics. Figure 5.6b shows the measured fake factor projected onto the η axis, there are two evenly spaced bins in each end cap region ($1.52 < |\eta| < 2.5$) and three evenly spaced bins in the barrel region ($|\eta| < 1.37$). As mentioned in Section 4.3.2, electron candidates falling in the crack region, $1.37 < |\eta| < 1.52$, are ignored as there is insufficient calorimeter information. Figure 5.6a shows p_{T} dependence, measured in three bins chosen to give a roughly consistent statistical error. Figure 5.7 and Table 5.5 show the measured fake factor for the ZH category as a function of both p_{T} and η.

5.4.3 Closure Test for the ZH Channel Measurement

To determine how well the chosen FF binning is capable of modelling the fake electrons, a closure test is performed whereby the fake factor is applied back to the $Z \to \mu\mu$
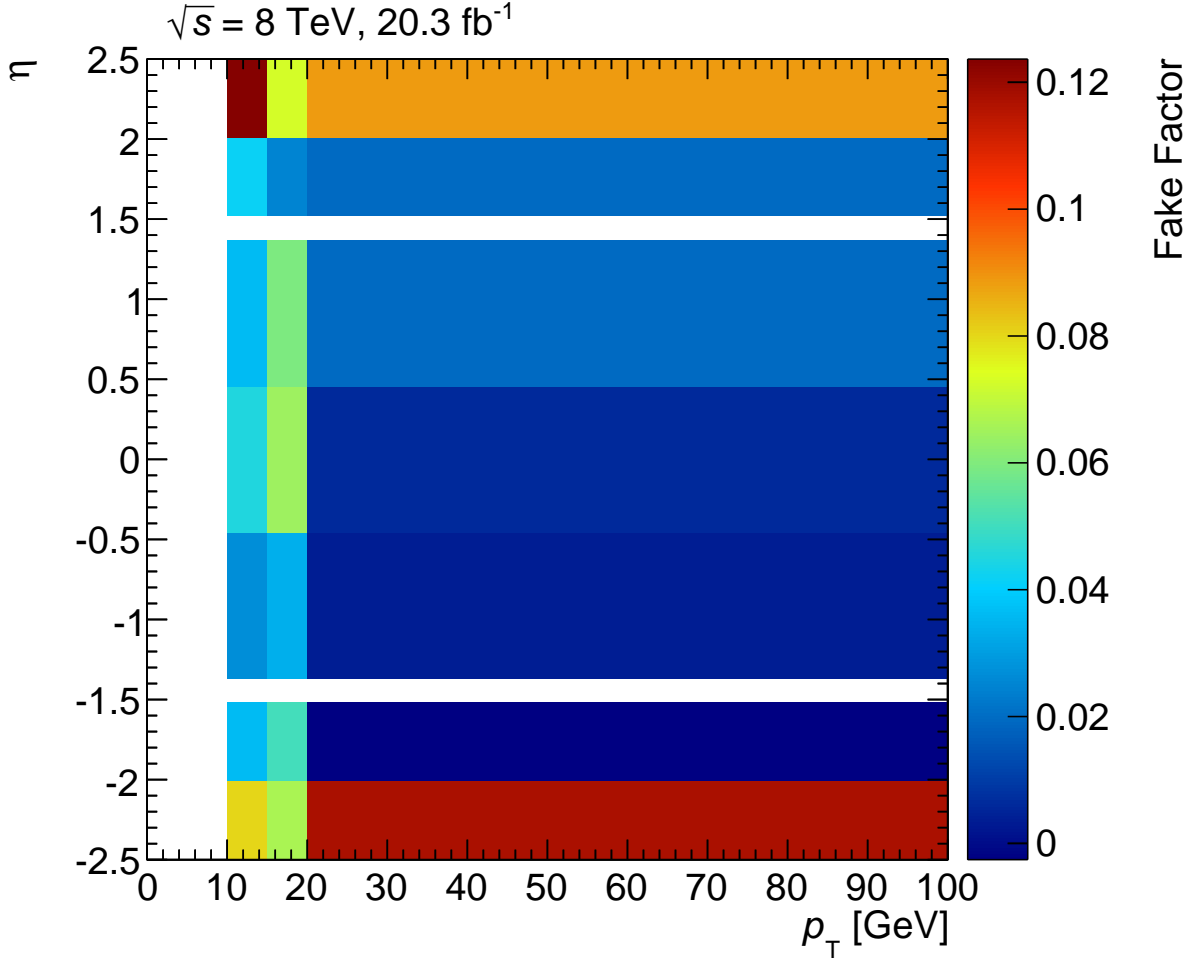
Figure 5.7: Measured fake factor for the ZH category.

η vs. p_T [GeV]	$10 < p_T < 15$	$15 < p_T < 20$	$p_T > 20$
$-2.5 < \eta < -2.01$	0.124 ± 0.032	0.073 ± 0.043	0.089 ± 0.043
$-2.01 < \eta < -1.52$	0.042 ± 0.014	0.025 ± 0.025	0.018 ± 0.025
$-1.37 < \eta < -0.46$	0.036 ± 0.010	0.059 ± 0.021	0.020 ± 0.017
$-0.46 < \eta < 0.46$	0.045 ± 0.012	0.064 ± 0.025	0.006 ± 0.017
$0.46 < \eta < 1.37$	0.027 ± 0.009	0.034 ± 0.019	0.002 ± 0.016
$1.52 < \eta < 2.01$	0.036 ± 0.014	0.051 ± 0.030	-0.003 ± 0.022
$2.01 < \eta < 2.5$	0.080 ± 0.024	0.066 ± 0.040	0.117 ± 0.048

Table 5.5: Measured fake factor for the ZH category. Uncertainties shown are due to statistics.

(a) MC estimate   **(b)** FF estimate
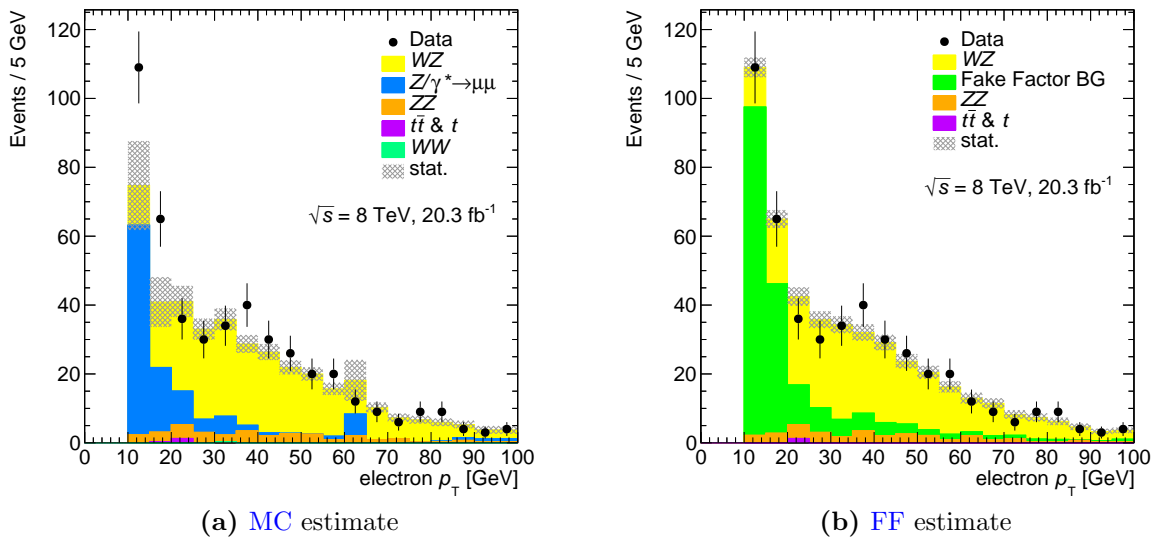
Figure 5.8: *ZH* category measurement closure test. The error bars on the data (filled black circles) are statistical, whilst the grey cross-hatched region gives the statistical error on the sum of the backgrounds.

measurement region. The result of this closure test is compared with the original MC estimate in the measurement signal region. Figure 5.8 shows this comparison for the electron p_{T}, the MC significantly underestimates the fake component at low p_{T} whereas the FF based estimate more closely describes data through the whole range. Figure 5.9 shows the same comparison for the electron η.

5.4.4 Measurement for the *WH* Channel

The composition of selected electrons in the *WH* categories, shown in Figure 5.10a, is dominated by non-prompt photon conversions from initial/final state radiation. The composition of antiselected electrons in the *WH* categories, shown in Figure 5.10b, contains both non-prompt photon conversion and jet fakes. This composition is accounted for in the fake factor measurement by selecting a subset of the $Z \rightarrow \mu\mu$ enriched region which is enriched with electrons from photon conversions. This subset is obtained by allowing a wide range for the di-muon invariant mass, chosen to be $|M_{\mu\mu} - M_Z| < 30\,\mathrm{GeV}$, shown in Figure 5.11. This increased mass window range contains a larger amount of final state photon conversion than the *ZH* category mass range. Approximately 15% of $Z \rightarrow \mu\mu$ decays contain a final state radiation photon with energy greater than $1\,\mathrm{GeV}$ [63]. The low di-muon mass range, between 60 and

(a) MC estimate **(b)** FF estimate
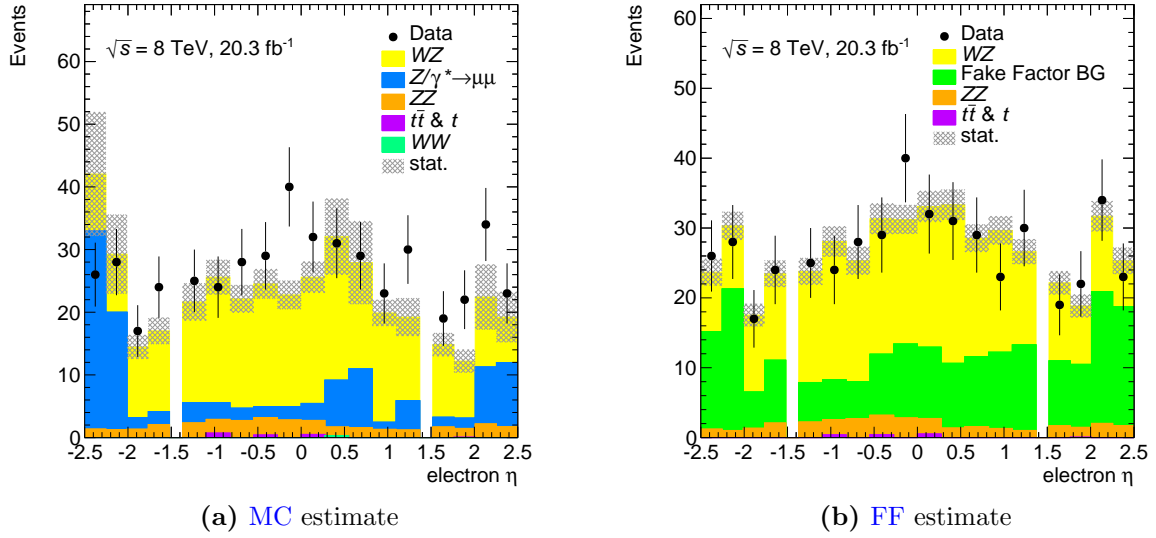
Figure 5.9: *ZH* category measurement closure test. The error bars on the data (filled black circles) are statistical, whilst the grey cross-hatched region gives the statistical error on the sum of the backgrounds.

(a) selected electrons **(b)** antiselected electrons

Figure 5.10: Composition of electrons in the $W(\to \mu\nu)H(\to \tau_e\tau_h)$ channel. The grey cross-hatched region gives the statistical error on the sum of the backgrounds.

(a) selected electrons   **(b)** antiselected electrons
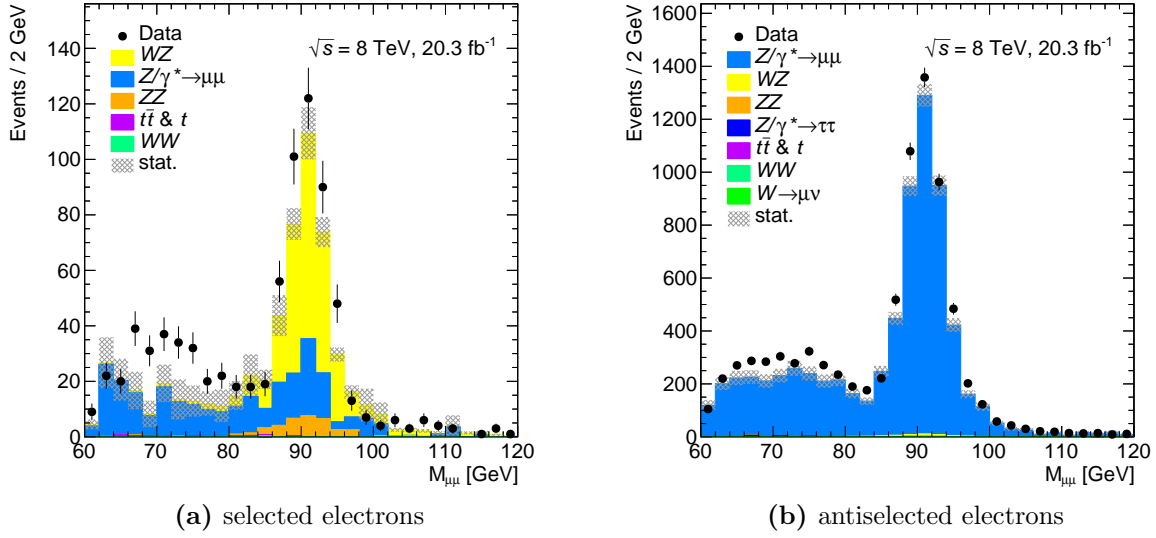
Figure 5.11: The mass window used for the WH category fake factor measurement. The error bars on the data (filled black circles) are statistical, whilst the grey cross-hatched region gives the statistical error on the sum of the backgrounds.

(a) selected electrons   **(b)** antiselected electrons
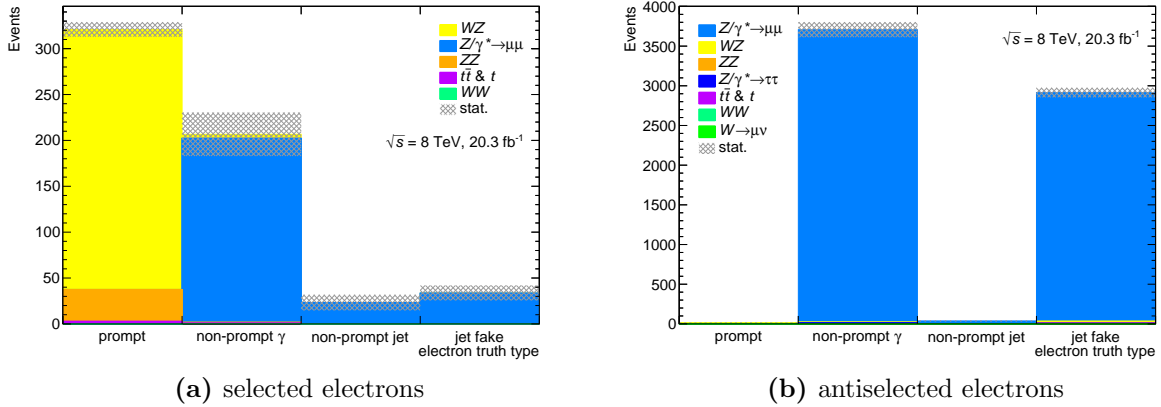
Figure 5.12: Composition of electrons in the $Z \rightarrow \mu\mu$ measurement region with the requirement that $|M_{\mu\mu} - M_Z| < 30\,\mathrm{GeV}$. The grey cross-hatched region gives the statistical error on the sum of the backgrounds.

80 GeV, isolates these events where the final state radiation photon converts into a non-prompt electron. Since there is a $p_\mathrm{T} > 10\,\mathrm{GeV}$ requirement on the electron, these events are isolated to the region $M_{\mu\mu} < M_Z - 10\,\mathrm{GeV}$. The composition of electrons in this di-muon mass range, shown in Figure 5.12, provides a better representation of the expected composition in the WH category.

(a) electron p_{T}

(b) electron η
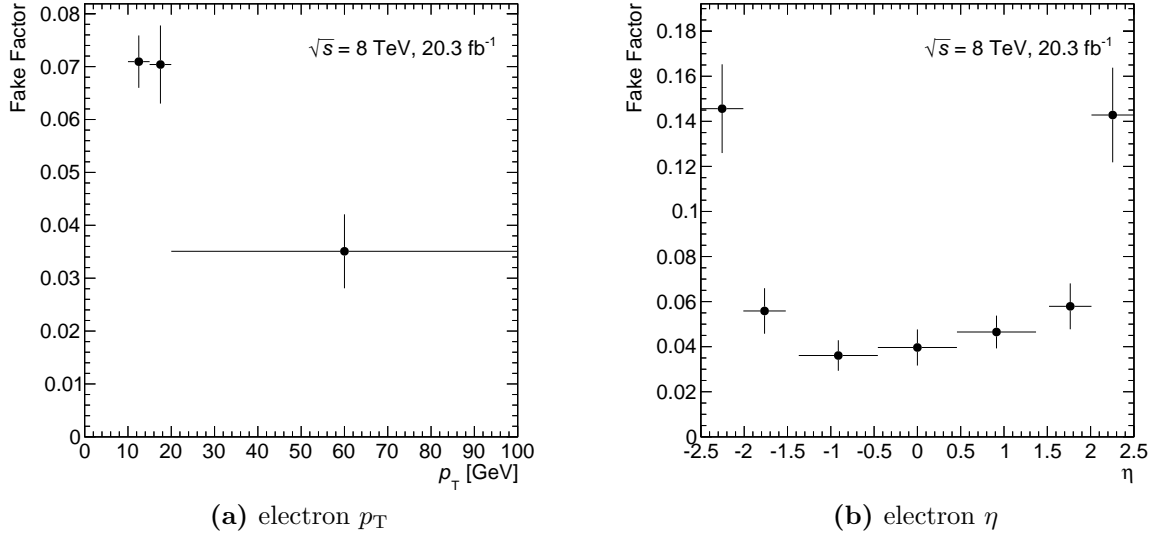
Figure 5.13: Measured fake factor for the WH category in the two separate projections of the measurement. The error bars on the data (filled black circles) are statistical.

η vs. p_{T} [GeV]	$10 < p_{\text{T}} < 15$	$15 < p_{\text{T}} < 20$	$p_{\text{T}} > 20$
$-2.5 < \eta < -2.01$	0.171 ± 0.032	0.128 ± 0.040	0.105 ± 0.038
$-2.01 < \eta < -1.52$	0.062 ± 0.013	0.058 ± 0.020	0.046 ± 0.021
$-1.37 < \eta < -0.46$	0.055 ± 0.010	0.049 ± 0.013	0.037 ± 0.015
$-0.46 < \eta < 0.46$	0.056 ± 0.010	0.070 ± 0.017	0.008 ± 0.015
$0.46 < \eta < 1.37$	0.047 ± 0.008	0.055 ± 0.015	0.017 ± 0.013
$1.52 < \eta < 2.01$	0.071 ± 0.014	0.082 ± 0.021	0.017 ± 0.018
$2.01 < \eta < 2.5$	0.156 ± 0.027	0.136 ± 0.039	0.129 ± 0.039

Table 5.6: Measured fake factor for the WH category. Uncertainties shown are due to statistics.

The WH fake factor measurement uses the same binning as the ZH fake factor measurement. Figure 5.13 shows the two projections of the measurement, Figure 5.14 and Table 5.6 show the measured fake factor for the WH category as a function of both p_{T} and η.
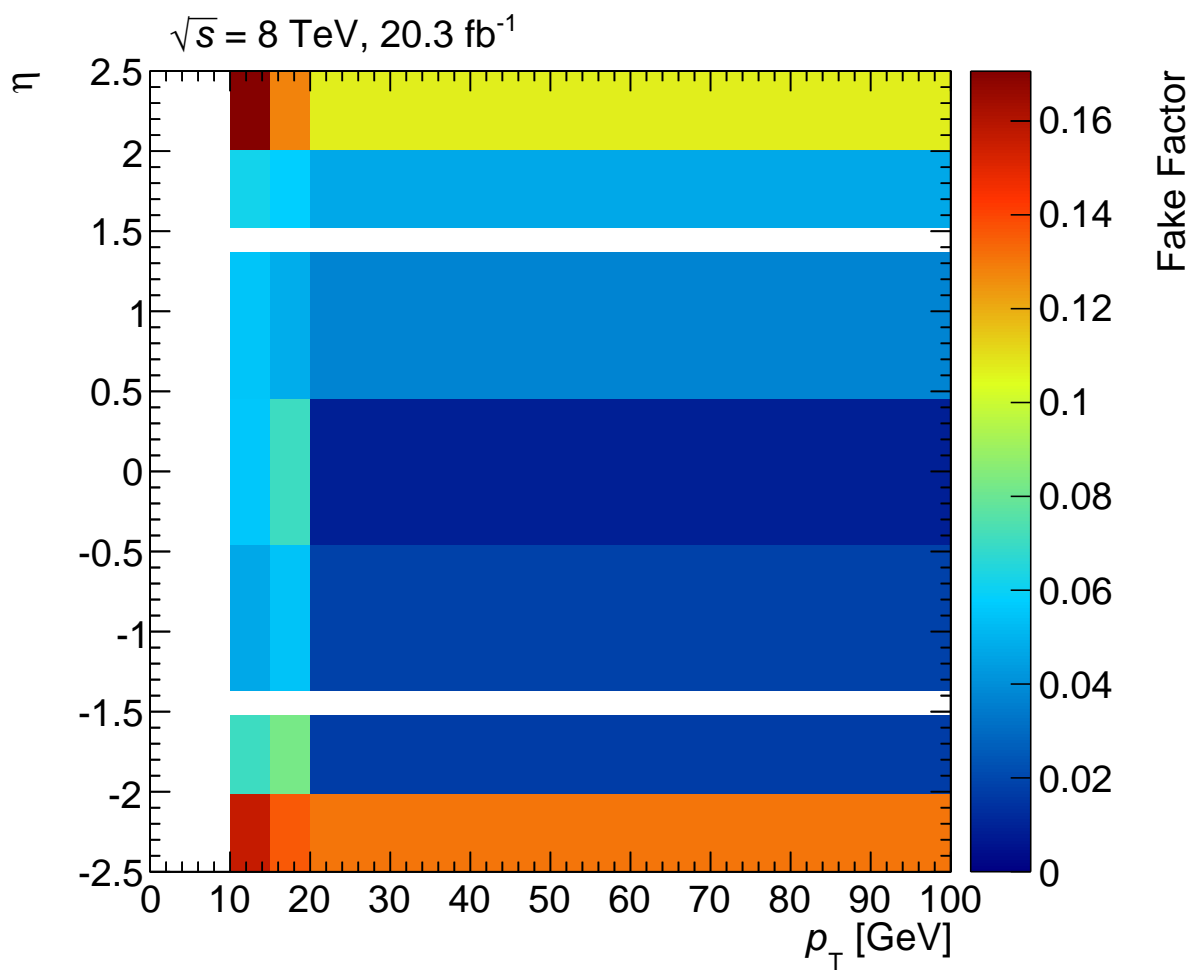
Figure 5.14: Measured fake factor for the WH category.

(a) MC estimate   **(b)** FF estimate

Figure 5.15: WH category measurement closure test. The error bars on the data (filled black circles) are statistical, whilst the grey cross-hatched region gives the statistical error on the sum of the backgrounds.

5.4.5 Closure Test for the WH Channel Measurement

As was done for the ZH category measurement, a closure test is performed by applying the measured WH category fake factor back to the $Z \to \mu\mu$ measurement region in the range $|M_{\mu\mu} - M_Z| < 30 \, \text{GeV}$. The results of this test, shown in Figure 5.15 and Figure 5.16, show that the fake factor estimate more accurately describes the data than the MC estimate.

5.5 Tau Fake Factor Measurement

Taus considered in the fake background originate primarily from misidentified hadronic jets. The tau fake factors are measured using a similar method to that for electrons. The events are required to be triggered by either the `EF_mu24i_tight` or `EF_mu36_tight` trigger, contain exactly two opposite-sign muons, and contain no b-tagged jets. The di-muon invariant mass is required to be in a window around the Z mass: $|M_{\mu\mu} - M_Z| < 20 \, \text{GeV}$. The events are required to contain exactly one probe tau which passes all object and quality criteria with the exception that no identification requirement is imposed. Probe taus which pass `medium` identification are referred to as *selected taus*, those

(a) MC estimate   **(b)** FF estimate
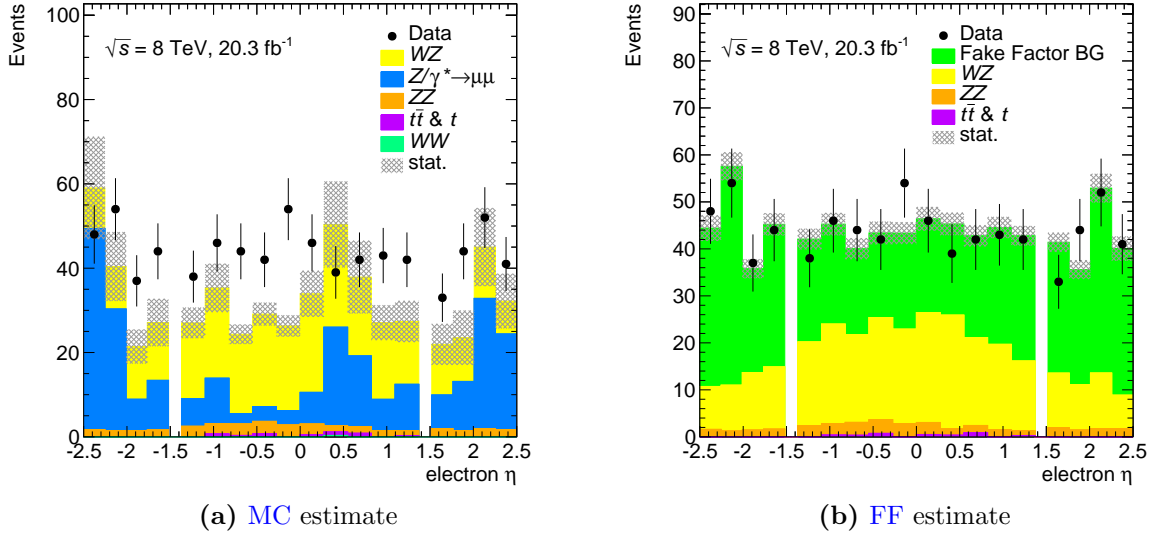
Figure 5.16: WH category measurement closure test. The error bars on the data (filled black circles) are statistical, whilst the grey cross-hatched region gives the statistical error on the sum of the backgrounds.

which fail `medium` but have an identification score above 70% of the `loose` identification threshold are referred to as *antiselected taus*. The fake rate is given by the ratio of the number of selected taus to the total number of selected and antiselected taus.

This lower bound of 70% of the `loose` threshold is imposed to ensure the composition of antiselected taus matches the expected fake background. Hadronic tau candidates with an identification score below 70% of the `loose` threshold have been found to appear too different in composition to the expected fake background. This requirement ensures the quark-initiated vs. gluon-initiated jet ratio more closely matches the VH signal region. Figure 5.17 shows the composition of fake taus as a function of the BDT identification score as found in $Z \rightarrow \mu\mu$ MC events in the tau fake factor measurement region. The yellow, orange, red, and purple lines show the 70% of `loose`, `loose`, `medium`, and `tight` identification thresholds respectively. The lower bound of 70% of the `loose` threshold removes a large portion of gluon-initiated jets and brings the measurement in line with the mostly quark-initiated jet composition expected in the VH signal region.

The calculation of E_T^{miss} is sensitive to the presence, and composition, of jets in an event. The WH category generally has larger E_T^{miss} than the ZH category due neutrino from the W decay. The rate of jets faking taus is expected to be higher for 1-prong taus. For these reasons, the fake rates are measured separately for the WH and ZH
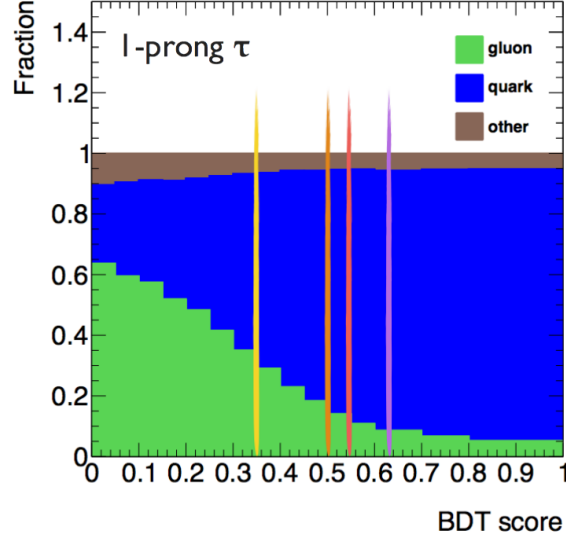
Figure 5.17: The composition of 1-prong fake tau candidates as a function of the BDT identification score as found in $Z \to \mu\mu$ MC events in the tau fake factor measurement region. The thresholds for the identification working points are shown by the vertical lines, from left to right they are: 70% of `loose` (yellow), `loose` (orange), `medium` (red), and `tight` (purple).

categories and for both 1- and 3-prong tau candidates. The measurement for the WH category requires events to satisfy $E_{\mathrm{T}}^{\mathrm{miss}} > 20\,\mathrm{GeV}$. No such requirement is imposed for the ZH category measurement. Each measurement is performed in bins of p_{T} and $|\eta|$. The fake rates were found to be symmetrical in η within statistical error, for this reason the measurement is performed in bins of $|\eta|$ rather than η to increase statistics in each bin. The measured fake rates are shown in: Table 5.7 for 1-prong taus in the WH category, Table 5.8 for 3-prong taus in the WH category, Table 5.9 for 1-prong taus in the ZH category, and Table 5.10 for 3-prong taus in the ZH category. The fake factors are computed from these fake rates using equation (5.3).

p_{T} [GeV] vs. η	$|\eta| < 0.8$	$0.8 < |\eta| < 1.37$	$1.37 < |\eta| < 2.5$
$20 < p_{\mathrm{T}} < 25$	0.075 ± 0.002	0.079 ± 0.003	0.096 ± 0.003
$25 < p_{\mathrm{T}} < 30$	0.077 ± 0.003	0.080 ± 0.005	0.088 ± 0.005
$30 < p_{\mathrm{T}} < 35$	0.067 ± 0.004	0.068 ± 0.006	0.073 ± 0.005
$35 < p_{\mathrm{T}} < 40$	0.076 ± 0.006	0.069 ± 0.007	0.076 ± 0.007
$40 < p_{\mathrm{T}} < 60$	0.064 ± 0.004	0.064 ± 0.005	0.061 ± 0.005
$p_{\mathrm{T}} > 60$	0.062 ± 0.007	0.060 ± 0.009	0.076 ± 0.010

Table 5.7: Fake rate of 1-prong τ_h for the WH category. Uncertainties shown are due to statistics.

p_{T} [GeV] vs. η	$|\eta| < 0.8$	$0.8 < |\eta| < 1.37$	$1.37 < |\eta| < 2.5$
$20 < p_{\mathrm{T}} < 25$	0.029 ± 0.001	0.036 ± 0.002	0.030 ± 0.002
$25 < p_{\mathrm{T}} < 30$	0.021 ± 0.001	0.023 ± 0.002	0.018 ± 0.002
$30 < p_{\mathrm{T}} < 35$	0.017 ± 0.001	0.015 ± 0.002	0.015 ± 0.002
$35 < p_{\mathrm{T}} < 40$	0.013 ± 0.001	0.017 ± 0.002	0.014 ± 0.002
$40 < p_{\mathrm{T}} < 60$	0.011 ± 0.001	0.009 ± 0.001	0.010 ± 0.001
$p_{\mathrm{T}} > 60$	0.006 ± 0.001	0.006 ± 0.002	0.009 ± 0.002

Table 5.8: Fake rate of 3-prong τ_h for the WH category. Uncertainties shown as due to statistics.

p_{T} [GeV] vs. η	$|\eta| < 0.8$	$0.8 < |\eta| < 1.37$	$1.37 < |\eta| < 2.5$
$20 < p_{\mathrm{T}} < 25$	0.085 ± 0.002	0.090 ± 0.002	0.102 ± 0.002
$25 < p_{\mathrm{T}} < 30$	0.082 ± 0.002	0.082 ± 0.003	0.094 ± 0.003
$30 < p_{\mathrm{T}} < 35$	0.076 ± 0.003	0.075 ± 0.004	0.079 ± 0.004
$35 < p_{\mathrm{T}} < 40$	0.076 ± 0.004	0.072 ± 0.005	0.077 ± 0.005
$40 < p_{\mathrm{T}} < 60$	0.070 ± 0.003	0.067 ± 0.004	0.067 ± 0.003
$p_{\mathrm{T}} > 60$	0.069 ± 0.005	0.073 ± 0.007	0.077 ± 0.007

Table 5.9: Fake rate of 1-prong τ_h for the ZH category. Uncertainties shown are due to statistics.

p_{T} [GeV] vs. η	$|\eta| < 0.8$	$0.8 < |\eta| < 1.37$	$1.37 < |\eta| < 2.5$
$20 < p_{\mathrm{T}} < 25$	0.031 ± 0.001	0.037 ± 0.001	0.032 ± 0.001
$25 < p_{\mathrm{T}} < 30$	0.022 ± 0.001	0.022 ± 0.001	0.019 ± 0.001
$30 < p_{\mathrm{T}} < 35$	0.017 ± 0.001	0.017 ± 0.001	0.017 ± 0.001
$35 < p_{\mathrm{T}} < 40$	0.013 ± 0.001	0.016 ± 0.001	0.014 ± 0.001
$40 < p_{\mathrm{T}} < 60$	0.011 ± 0.001	0.010 ± 0.001	0.011 ± 0.001
$p_{\mathrm{T}} > 60$	0.007 ± 0.001	0.006 ± 0.001	0.007 ± 0.001

Table 5.10: Fake rate of 3-prong τ_h for the ZH category. Uncertainties shown are due to statistics.

5.6 Fake Factor Method for the $VH(\to \tau\tau)$ Channels

In the $W(\to \ell\nu)H(\to \tau_\ell\tau_h)$ channel, fake hadronic taus contribute significantly to the background, as do fake and non-prompt electrons to a smaller but still significant extent. Fake and non-prompt muons are expected to exist but are however difficult to include in the FF method as antiselected muons, defined by inverting muon identification, do not adequately represent the expected background, making the fake factor extrapolation for muons unreliable and difficult to validate. For this reason, the FF background estimate used in the $W(\to \ell\nu)H(\to \tau_\ell\tau_h)$ channel estimates fake and non-prompt electrons and hadronic taus from data, and uses MC for the background of fake and non-prompt muons.

In the remaining channels it was found that using a FF method with only fake taus adequately describes the backgrounds. This was checked by comparing the expected background distributions of the main kinematic variables with the two background models: fake electron and fake tau, and fake tau only. Due to the small component of fake electrons in these channels, no significant difference was observed between the two models. Since the use of the electron fake factor carries with it a large systematic uncertainty, and the fake and non-prompt electron background is expected to be small compared to the fake tau background in these channels, the remaining channels estimate fake hadronic taus from data, and use MC for the background of fake and non-prompt electrons and muons. As such, the electron fake factor measurement for the ZH channels is not used for the final results in this analysis. It was however used throughout the development of the FF method to test the performance of the method with many fake

objects. It was also used to determine that the fake and non-prompt electron background in these channels is small and adequately modelled by MC, this provided confidence in the tau-only background estimate.

5.7 Method Validation in the $W(\to \ell\nu)H(\to \tau_\ell\tau_h)$ Channel

The FF method is validated in each of the analysis channels by comparing the data to the background prediction in many different regions constructed to test the method's performance under different background compositions. The loosened signal region validation is a superset of the final signal selection, while the $t\bar{t}$ and $Z \to \tau\tau$ validation regions are orthogonal to the final signal region designed to test different background compositions.

5.7.1 Loosened Signal Selection Validation Region

The loosened signal selection validation region is constructed to contain a composition of fake and non-prompt leptons similar to that in final tighter signal region, described in Section 6.2. This region contains many, but not all, of the requirements for the final signal region and remains loose enough to allow the inclusion of a large amount of background events in order to compare the data and prediction with large statistics.

The loosened signal selection validation region contains all events categorised as $W(\to \ell\nu)H(\to \tau_\ell\tau_h)$ from Section 4.3 with the additional requirements as follows. The two light leptons in the event are required to be of different flavour, that is, one electron and one muon. Electrons are required to be identified as `tight++`. Isolation criteria are imposed on both light leptons. Track isolation requires the sum of the p_T of additional tracks in a cone of $\Delta R < 0.4$ around the lepton to be less than 8% of the lepton p_T. Calorimeter isolation requires the sum of energies of additional calorimeter clusters in a cone of $\Delta R < 0.2$ around the lepton to be less than 8% of the lepton p_T. The sum of the electric charges of the electron, muon, and hadronic tau must equal ± 1. Hadronic taus are required to have $p_T > 25 \, \text{GeV}$. Figure 5.18 shows the main kinematic variables of the $W(\to \ell\nu)H(\to \tau_\ell\tau_h)$ channel in the loosened signal selection validation region.
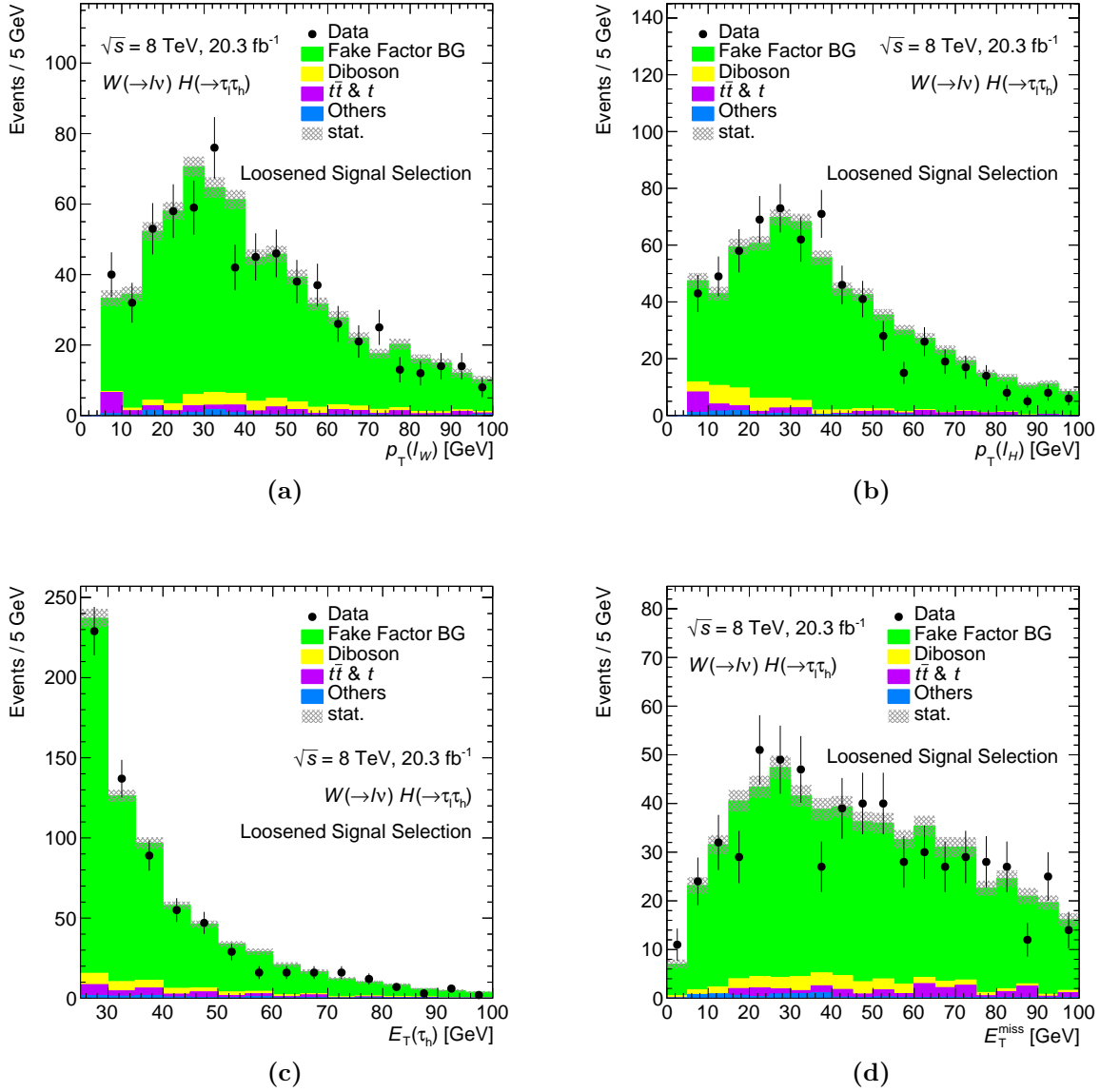
Figure 5.18: The main kinematic variables in the loosened signal selection validation region of the $W(\to \ell\nu)H(\to \tau_\ell\tau_h)$ category: (a) the transverse momentum of the lepton assigned to the W, (b) the transverse momentum of the lepton assigned to the H, (c) the transverse energy of the hadronic tau assigned to the H, (d) the missing transverse energy. The error bars on the data (filled black circles) are statistical, whilst the grey cross-hatched region gives the statistical error on the sum of the backgrounds.

5.7.2 $t\bar{t}$ Validation Region

The $t\bar{t}$ validation region is constructed to select fully leptonic $t\bar{t}$ events with an additional jet being misidentified as a hadronic tau.

The requirements of the $t\bar{t}$ validation are the same as the loosened signal selection region with two additional requirements. The electron and muon must have opposite electric charge. The event is required to have at least one b-tagged jet with $p_{\mathrm{T}} > 30\,\mathrm{GeV}$. Figure 5.19 shows the main kinematic variables of the $W(\to \ell\nu)H(\to \tau_\ell\tau_h)$ channel in the $t\bar{t}$ validation region.

5.7.3 $Z \to \tau\tau$ Validation Region

The $Z \to \tau\tau$ validation region is constructed to select $Z \to \tau_e\tau_\mu$ events with an additional jet being misidentified as a hadronic tau.

The requirements of the $Z \to \tau\tau$ validation are the same as the loosened signal selection region with three additional requirements. The electron and muon must have opposite electric charge. Events containing b-tagged jets with $p_{\mathrm{T}} > 30\,\mathrm{GeV}$ are vetoed to reduce the background of $t\bar{t}$ events. To select events where the electron and muon come from tau decays from a Z boson decay, the collinear mass (see Section 6.1.1) of the electron and muon is required to be within 30 GeV of the Z mass, that is between 60 GeV and 120 GeV. Figure 5.20 shows the main kinematic variables of the $W(\to \ell\nu)H(\to \tau_\ell\tau_h)$ channel in the $Z \to \tau\tau$ validation region.

5.7.4 Summary of Validation Regions

The three validation regions demonstrate the FF method's performance under different compositions of background processes and types of fake an non-prompt leptons. Each of the validation regions shows good agreement between between data and expectation for the main kinematic variables which are used to define the signal-sensitive regions in the next chapter.
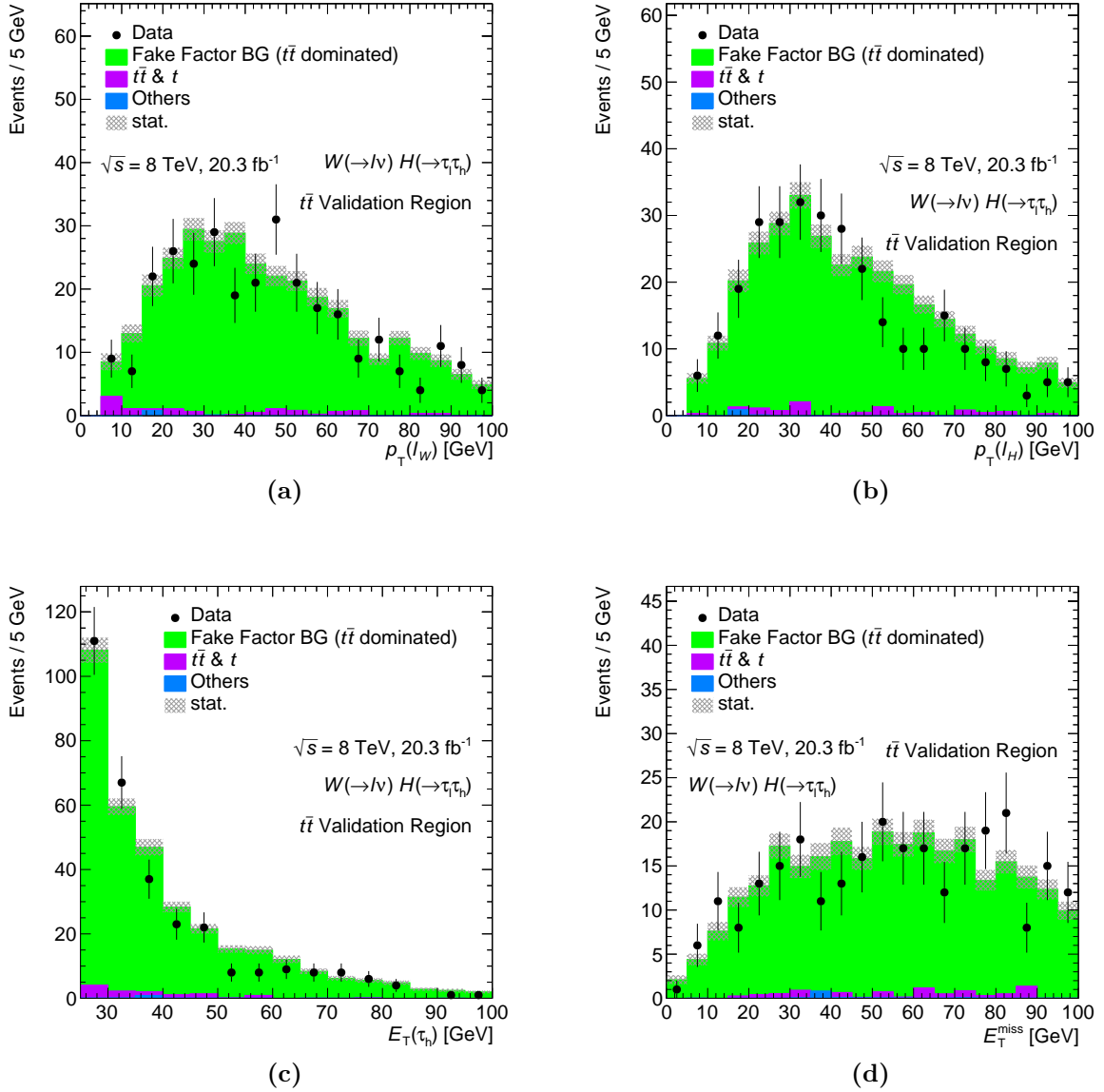
Figure 5.19: The main kinematic variables in the $t\bar{t}$ validation region of the $W(\to \ell\nu)H(\to \tau_\ell\tau_h)$ category: (a) the transverse momentum of the lepton assigned to the W, (b) the transverse momentum of the lepton assigned to the H, (c) the transverse energy of the hadronic tau assigned to the H, (d) the missing transverse energy. The error bars on the data (filled black circles) are statistical, whilst the grey cross-hatched region gives the statistical error on the sum of the backgrounds.
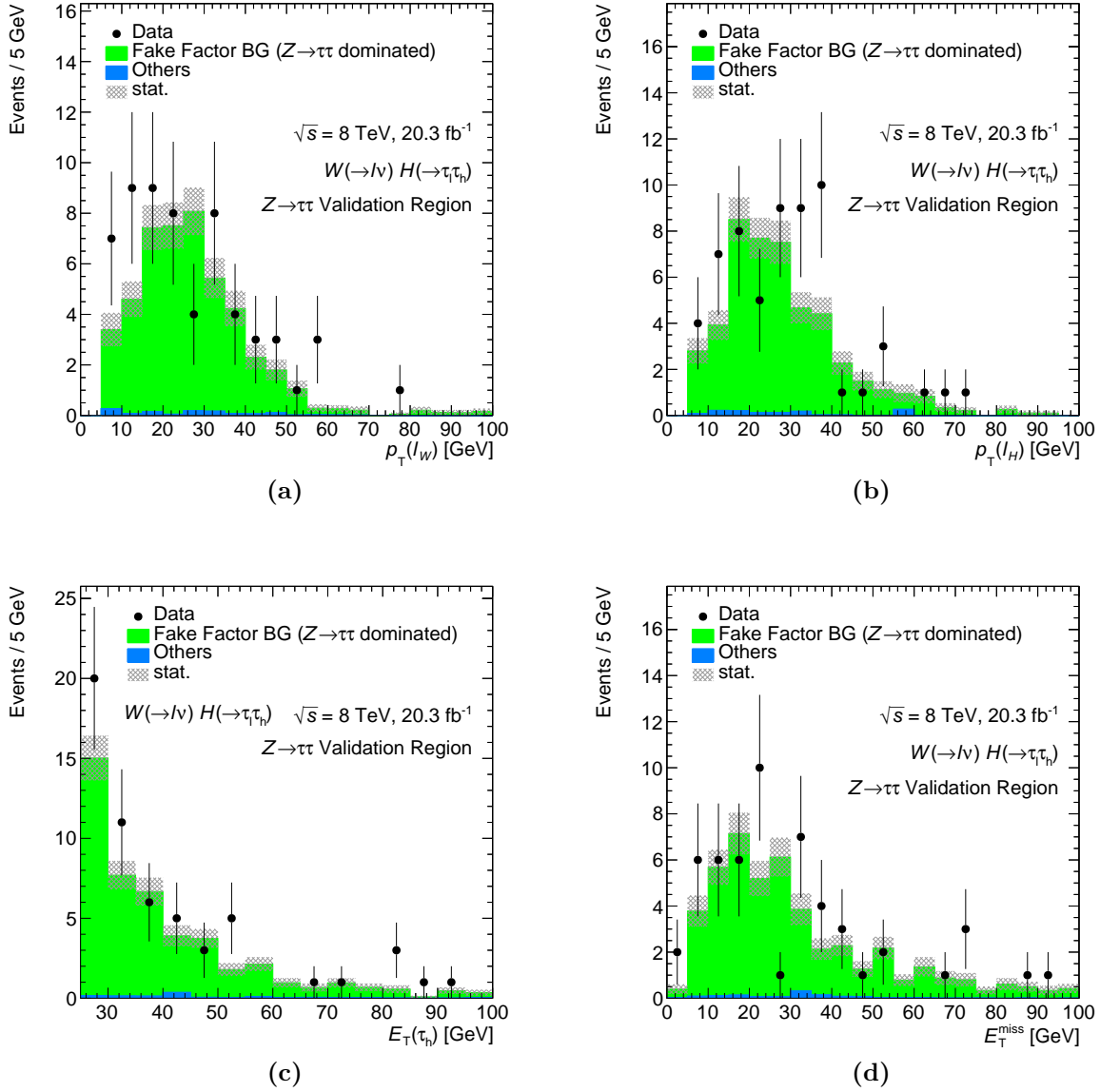
Figure 5.20: The main kinematic variables in the $Z \rightarrow \tau\tau$ validation region of the $W(\rightarrow \ell\nu)H(\rightarrow \tau_\ell\tau_h)$ category: (a) the transverse momentum of the lepton assigned to the W, (b) the transverse momentum of the lepton assigned to the H, (c) the transverse energy of the hadronic tau assigned to the H, (d) the missing transverse energy. The error bars on the data (filled black circles) are statistical, whilst the grey cross-hatched region gives the statistical error on the sum of the backgrounds.

5.8 Summary of the Background Estimation Method

A general form of the FF method has been developed for this analysis where the data-driven extrapolation from the fake-enriched region occurs at the per-object level. The method's ability to handle different types of fake objects, such as electrons and hadronic taus, simultaneously makes it especially suited to the $VH(\rightarrow \tau\tau)$ analysis which has many different final state particles. In addition, the measurements of the electron and tau fake factors have demonstrated to be robust against the different compositions of fake and non-prompt lepton backgrounds. The method as described here is used in the following chapter to estimate the expected background of fake and non-prompt leptons in the signal-sensitive regions used to extract the final results of the search.

Chapter 6

Analysis of the $VH(\to \tau\tau)$ Channels

Each of the VH channels has a unique final state topology. The event selection and categorisation process described in Section 4.3 separates events to match the final state of each of these channels. After this procedure, each channel contains different compositions of background processes. For these reasons, each channel requires further, individually optimised, selection criteria to reduce the backgrounds and isolate the signal events. These final event selection requirements define the signal-enriched region for each channel. In each channel a fit is performed on a kinematic variable which discriminates the signal from background events.

The following section describes the process of reconstructing mass-sensitive variables to be used in the fitting procedure. Following this, in Sections 6.2 to 6.5, the final event selection criteria for each channel are defined. The systematic uncertainties which affect the mass distributions are described in Section 6.6. In Section 6.7, the fitting procedure is described, along with the statistical tests used to produce the final results which are presented in Section 6.8.

6.1 Mass Reconstruction

The final result is extracted using fits to distributions of variables, reconstructed from the visible decay products of the tau pair, which are sensitive to the Higgs boson mass. The mass is reconstructed using one of two methods, depending on the signal category.

In the ZH category, the Higgs boson mass is calculated using the Missing Mass Calculator (MMC) method [64]. This method assumes that the observed $E_\mathrm{T}^\mathrm{miss}$ is due solely to the neutrinos from tau decays. This calculation requires solving an under-constrained system of equations for the unknown components of the momentum carried by the neutrinos. A probabilistic approach is used to determine the most likely solutions for the neutrinos' momenta by performing a scan over the unknown variables. Each scan point is weighted by its probability based on the observed $E_\mathrm{T}^\mathrm{miss}$ and visible tau decay products. The MMC estimate of the di-tau mass is the most probable value of the scan points. The algorithm provides a solution for approximately 99% of $H \rightarrow \tau\tau$ events [6].

In the WH category, the presence of the additional neutrino from the W decay makes mass reconstruction techniques such as MMC or collinear mass unreliable. Variables such as the visible mass of the Higgs decay products can be used, however they don't include complete knowledge of the event topology which may provide an increase in discriminating power. A set of techniques to constrain mass variables built from known topologies was proposed in reference [65]. In particular, the so-called *late-projected* transverse mass (M_2T) was chosen. In this analysis the M_2T variable is constructed to incorporate two features of the WH event topology. The collinear mass estimation method is used to incorporate the Higgs decay products and the W mass is used to incorporate the W decay products. The remainder of this section will be structured as follows: first the collinear mass will be outlined, followed by the kinematics of W decays. Lastly the construction of the M_2T variable will be described.

6.1.1 The Collinear Approximation

The collinear approximation was first proposed to reconstruct the $\tau\tau$ invariant mass from decays of Higgs bosons produced in association with an energetic jet [66]. This approximation relies on two assumptions. Firstly, it assumes that the neutrinos from tau decays are approximately collinear with the visible tau decay products. This assumption improves with large tau momentum, as is typically the case for $H \rightarrow \tau\tau$ decays since $m_\tau \ll m_H$. In detector coordinates this implies $\phi_\nu \approx \phi_\mathrm{vis}$ and $\theta_\nu \approx \theta_\mathrm{vis}$. This assumption allows the neutrino three-momentum, $\vec{p}_\nu$, to be expressed in terms of the three-momentum of the visible decay products, $\vec{p}_\mathrm{vis}$, as

$$\vec{p}_\nu = \left(\frac{1}{x} - 1 \right) \vec{p}_\mathrm{vis} \tag{6.1}$$

where x is the fraction, in the range (0, 1), of the momentum of the tau taken by the visible decay products, given by

$$x = \frac{|\vec{p}_{\text{vis}}|}{|\vec{p}_{\text{vis}}| + |\vec{p}_\nu|} \tag{6.2}$$

The second assumption is that the missing momentum of the event is due solely to the neutrinos from the tau decays. With this assumption, the transverse components of missing momentum in an event with two tau decays is given by

$$p_x^{\text{miss}} = p_x^{\nu_1} + p_x^{\nu_2} \tag{6.3}$$

$$= \left(\frac{1}{x_1} - 1\right) p_x^{\text{vis}_1} + \left(\frac{1}{x_2} - 1\right) p_x^{\text{vis}_2} \tag{6.4}$$

$$p_y^{\text{miss}} = p_y^{\nu_1} + p_y^{\nu_2} \tag{6.5}$$

$$= \left(\frac{1}{x_1} - 1\right) p_y^{\text{vis}_1} + \left(\frac{1}{x_2} - 1\right) p_y^{\text{vis}_2} \tag{6.6}$$

These two equations can solve this system entirely, yielding solutions for the two unknowns, x_1 and x_2. With these solutions the tau four-vector, P_τ, can be reconstructed from the four-vectors of the visible, P_{vis}, and invisible, P_ν, decay products as

$$P_\tau = P_{\text{vis}} + P_\nu \tag{6.7}$$

$$= (E_{\text{vis}}, \ \vec{p}_{\text{vis}}) + (E_\nu, \ \vec{p}_\nu) \tag{6.8}$$

$$= (E_{\text{vis}} + E_\nu, \ \vec{p}_{\text{vis}} + \vec{p}_\nu) \tag{6.9}$$

$$= \left(E_{\text{vis}} + |\vec{p}_\nu|, \ \vec{p}_{\text{vis}} + \left(\frac{1}{x} - 1\right)\vec{p}_{\text{vis}}\right) \tag{6.10}$$

$$= \left(E_{\text{vis}} + \left(\frac{1}{x} - 1\right)|\vec{p}_{\text{vis}}|, \ \frac{1}{x}\vec{p}_{\text{vis}}\right) \tag{6.11}$$

Using one final approximation that the tau is massless (i.e. $E_\tau = |\vec{p}_\tau|$), which is reasonable since $m_\tau \ll m_H$, gives

$$P_\tau = \left(\frac{1}{x}E_{\text{vis}}, \ \frac{1}{x}\vec{p}_{\text{vis}}\right) \tag{6.12}$$

$$= \frac{1}{x}P_{\text{vis}} \tag{6.13}$$

The collinear mass of the tau pair can then be calculated as

$$M^2_{\tau\tau} = (P_{\tau_1})_\mu (P_{\tau_2})^\mu \tag{6.14}$$

$$= \left(\frac{1}{x_1} P_{\text{vis}_1}\right)_\mu \left(\frac{1}{x_2} P_{\text{vis}_2}\right)^\mu \tag{6.15}$$

$$= \frac{M^2_{\text{vis}}}{x_1 x_2} \tag{6.16}$$

where M_{vis} is the invariant mass of the visible tau decay products.

6.1.2 W Decay Kinematics

Consider the decay of a W boson into a lepton, ℓ, and neutrino, ν. If the four-vector of the lepton can be fully reconstructed, this gives four known quantities

$$p_{x,\ell} \tag{6.17}$$

$$p_{y,\ell} \tag{6.18}$$

$$p_{z,\ell} \tag{6.19}$$

$$E_\ell = \sqrt{|\vec{p}_\ell|^2 + m^2_\ell} \tag{6.20}$$

where $\vec{p}_\ell = (p_{x,\ell},\ p_{y,\ell},\ p_{z,\ell})$ is the three-momentum of the lepton. Additionally, if the transverse momentum of the neutrino can be reconstructed from $E_{\text{T}}^{\text{miss}}$, this gives two more quantities

$$p_{x,\nu} \tag{6.21}$$

$$p_{y,\nu} \tag{6.22}$$

The only unknown variable of this system is the longitudinal momentum of the neutrino, $p_{z,\nu}$. The invariant mass of the two-particle system is

$$M^2_{\ell\nu} = (P_\ell + P_\nu)_\mu (P_\ell + P_\nu)^\mu \tag{6.23}$$

$$= (E_\ell + E_\nu)^2 - |\vec{p}_\ell + \vec{p}_\nu|^2 \tag{6.24}$$

where P_ℓ and P_ν are the four-vectors of the lepton and neutrino respectively. Assuming the W is produced on-shell, the mass of this system is m_W, giving

$$m_W^2 = (E_\ell + E_\nu)^2 - |\vec{p}_\ell + \vec{p}_\nu|^2 \tag{6.25}$$

$$= (E_\ell + E_\nu)^2 - (p_{x,\ell} + p_{x,\nu})^2 - (p_{y,\ell} + p_{y,\nu})^2 - (p_{z,\ell} + p_{z,\nu})^2 \tag{6.26}$$

Expanding out all the terms gives

$$m_W^2 = E_\ell^2 + E_\nu^2 + 2E_\ell E_\nu \tag{6.27}$$

$$- p_{x,\ell}^2 - p_{x,\nu}^2 - 2p_{x,\ell}p_{x,\nu} \tag{6.28}$$

$$- p_{y,\ell}^2 - p_{y,\nu}^2 - 2p_{y,\ell}p_{y,\nu} \tag{6.29}$$

$$- p_{z,\ell}^2 - p_{z,\nu}^2 - 2p_{z,\ell}p_{z,\nu} \tag{6.30}$$

Noting that $m_\ell^2 = E_\ell^2 - p_{x,\ell}^2 - p_{y,\ell}^2 - p_{z,\ell}^2$ and $m_\nu^2 = E_\nu^2 - p_{x,\nu}^2 - p_{y,\nu}^2 - p_{z,\nu}^2$ gives:

$$m_W^2 = m_\ell^2 + m_\nu^2 + 2E_\ell E_\nu - 2p_{x,\ell}p_{x,\nu} - 2p_{y,\ell}p_{y,\nu} - 2p_{z,\ell}p_{z,\nu} \tag{6.31}$$

Assuming massless neutrinos, $m_\nu = 0$, implying $E_\nu = \sqrt{p_{x,\nu}^2 + p_{y,\nu}^2 + p_{z,\nu}^2}$, gives:

$$m_W^2 = m_\ell^2 + 2E_\ell \sqrt{p_{x,\nu}^2 + p_{y,\nu}^2 + p_{z,\nu}^2} - 2p_{x,\ell}p_{x,\nu} - 2p_{y,\ell}p_{y,\nu} - 2p_{z,\ell}p_{z,\nu} \tag{6.32}$$

Solving this quadratic for $p_{z,\nu}$ gives the two solutions

$$p_{z,\nu} = \frac{p_{z,\ell}\left(\frac{m_W^2 - m_\ell^2}{2} - p_{x,\ell}p_{x,\nu} - p_{y,\ell}p_{y,\nu}\right)}{E_\ell^2 - p_{z,\ell}^2}$$

$$\pm \frac{E_\ell \sqrt{\left(\frac{m_W^2 - m_\ell^2}{2} - p_{x,\ell}p_{x,\nu} - p_{y,\ell}p_{y,\nu}\right)^2 - (p_{x,\nu}^2 + p_{y,\nu}^2)(E_\ell^2 - p_{z,\ell}^2)}}{E_\ell^2 - p_{z,\ell}^2} \tag{6.33}$$

Two real solutions exist provided:

$$\left(\frac{m_W^2 - m_\ell^2}{2} - p_{x,\ell}p_{x,\nu} - p_{y,\ell}p_{y,\nu}\right)^2 - (p_{x,\nu}^2 + p_{y,\nu}^2)(E_\ell^2 - p_{z,\ell}^2) \geq 0 \tag{6.34}$$

which is the case for W bosons produced on-shell. For the case of off-shell W bosons, i.e., $m_W^2 \to m_W^2 + \delta m^2$, the solutions can become imaginary. Thus, if no real solutions exist, the W boson can be assumed to be off-shell by an amount δm^2, the value of δm^2 which gives an invariant mass closest to the W pole mass is found by making the substitution

$m_W^2 \to m_W^2 + \delta m^2$ into equation (6.34), giving

$$m_W^2 \to m_W^2 + \delta m^2 = 2\sqrt{(p_{x,\nu}^2 + p_{y,\nu}^2)(E_\ell^2 - p_{z,\ell}^2)} + 2(p_{x,\ell}p_{x,\nu} + p_{y,\ell}p_{y,\nu}) + m_\ell^2 \quad (6.35)$$

The solution for $p_{z,\nu}$ in the case where the W boson is produced minimally off-shell (smallest $|\delta m^2|$) is then found by substituting this result into equation (6.33), giving

$$p_{z,\nu} = p_{z,\ell}\sqrt{\frac{p_{x,\nu}^2 + p_{y,\nu}^2}{E_\ell^2 - p_{z,\ell}^2}} \quad (6.36)$$

6.1.3 $M_{2\mathrm{T}}$

The $M_{2\mathrm{T}}$ variable [65] is constructed to provide an event-by-event lower bound on the transverse mass of the heaviest parent particle, the Higgs, in this topology. The $M_{2\mathrm{T}}$ distribution is bounded from above (within detector resolution) by the invariant mass of the Higgs.

The principle of the procedure is that of a minimisation over the allowed phase-space of possible momenta of all invisible particles in the event. Before introducing the final constructed variable, the notation of the transverse projections used and the process of particle partitioning must be discussed. Throughout this section, the index i is used to label individual final state particles, while a is used for parent particles and the corresponding collections of final state particles. The three-momentum of the ith visible (invisible) final state particle is denoted $\vec{p}_i$ ($\vec{q}_i$). Each final state particle is assigned to a parent in the topology, the set of parent particles (denoted $\mathcal{P}$) in the WH category is:

$$\mathcal{P} = \{W, H\} \quad (6.37)$$

Within each parent partition, particles are further partitioned into the set of visible ($\mathcal{V}_a$) or invisible ($\mathcal{I}_a$) particles originating from the ath parent. The partitioning of the children from a leptonic W decay is simple:

$$\mathcal{V}_W = \{\ell\} \quad (6.38)$$

$$\mathcal{I}_W = \{\nu_\ell\} \quad (6.39)$$

Partitioning of the visible children from the Higgs decay depends on the WH sub-channel:

$$
\mathcal{V}_H = \begin{cases} \{\ell, \ell\} & W(\to \ell\nu)H(\to \tau_\ell\tau_\ell) \\ \{\ell, \tau_h\} & W(\to \ell\nu)H(\to \tau_\ell\tau_h) \\ \{\tau_h, \tau_h\} & W(\to \ell\nu)H(\to \tau_h\tau_h) \end{cases} \tag{6.40}
$$

Partitioning of the invisible children from the Higgs decay uses the collinear approximation to reduce the phase-space minimised over. In this approximation, each tau decay is considered to have only one final state neutrino. For the hadronic decays ($\tau \to \tau_h\nu_\tau$) this is already true, for the leptonic decays ($\tau \to \ell\nu_\ell\nu_\tau$) the collinear approximation treats the sum of both neutrino momenta as belonging to only one neutrino, thus the partitioning of the invisible children from the Higgs decay is always:

$$
\mathcal{I}_H = \{\nu_\tau, \nu_\tau\} \tag{6.41}
$$

After the final state particles are partitioned, the transverse projection of each partition is determined. The 2 dimensional transverse momentum vector of the set of visible particles from the ath parent is given by:

$$
\vec{p}_{a\mathrm{T}} = \sum_{i \in \mathcal{V}_a} \vec{p}_{i\mathrm{T}} \tag{6.42}
$$

Likewise for the set of invisible particles:

$$
\vec{q}_{a\mathrm{T}} = \sum_{i \in \mathcal{I}_a} \vec{q}_{i\mathrm{T}} \tag{6.43}
$$

The time-like component of the transverse projection (the transverse energy) of the set of visible particles from the ath parent is given by:

$$
e_{a\mathrm{T}} = \sqrt{\left(\sum_{i \in \mathcal{V}_a} E_i\right)^2 - \left(\sum_{i \in \mathcal{V}_a} p_{iz}\right)^2} \tag{6.44}
$$

Likewise for the set of invisible particles:

$$
\tilde{e}_{a\mathrm{T}} = \sqrt{\left(\sum_{i \in \mathcal{I}_a} E_i\right)^2 - \left(\sum_{i \in \mathcal{I}_a} p_{iz}\right)^2} \tag{6.45}
$$

These definitions allow for the construction of the 1+2 dimensional transverse energy-momentum vectors of the visible ($p_{a\mathrm{T}}^\alpha$) and invisible ($q_{a\mathrm{T}}^\alpha$) components of the ath parent particle, given by:

$$p_{a\mathrm{T}}^\alpha = (e_{a\mathrm{T}}, \vec{p}_{a\mathrm{T}}) \tag{6.46}$$

and:

$$q_{a\mathrm{T}}^\alpha = (\tilde{e}_{a\mathrm{T}}, \vec{q}_{a\mathrm{T}}) \tag{6.47}$$

where α is the index of the 1+2 dimensional Minkowski space-time components $\{0, 1, 2\}$. The late-projected transverse mass of the ath parent particle is given by:

$$\mathcal{M}_{a\mathrm{T}} = \sqrt{g_{\alpha\beta}(p_{a\mathrm{T}}^\alpha + q_{a\mathrm{T}}^\alpha)(p_{a\mathrm{T}}^\beta + q_{a\mathrm{T}}^\beta)} \tag{6.48}$$

where $g_{\alpha\beta} = \mathrm{diag}(1, -1, -1)$ is the 1+2 dimensional metric. The final step is to consider the largest parent mass ($\max_a [\mathcal{M}_{a\mathrm{T}}]$) and minimise this value over all possible values of the invisible particles' momenta, expressed as:

$$M_{2\mathrm{T}} = \min_{\sum \vec{q}_{i\mathrm{T}} = \vec{p}_{\mathrm{T}}^{\mathrm{miss}}} \left[\max_a [\mathcal{M}_{a\mathrm{T}}] \right] \tag{6.49}$$

In the general case, the only constraint on the phase-space is that the sum of the transverse momenta of all invisible particles ($\sum \vec{q}_{i\mathrm{T}}$) equals the observed missing transverse momentum ($\vec{p}_{\mathrm{T}}^{\mathrm{miss}}$) of the event, however, the authors of reference [65] intend implementers to add any additional reliable information which will constrain the phase-space. In the WH event topology, the additional constraint which is imposed is that the invariant mass of the lepton and neutrino ($M_{\ell\nu}$) assigned to the W be equal to (on-shell), or as close as possible to (minimally off-shell), the mass of the W (m_W).

The full phase-space of the minimisation in the general case would be 12 dimensional in the $W(\to \ell\nu)H(\to \tau_\ell\tau_h)$ channel (3 momentum components of 4 neutrinos) and 9 dimensional in the $W(\to \ell\nu)H(\to \tau_h\tau_h)$ channel (3 momentum components of 3 neutrinos). The W mass constraint reduces the dimensionality of the minimisation by one as the neutrino p_z can be expressed in terms of other variables as outlined in Section 6.1.2. The collinear approximation is used to reduce the number of neutrinos considered in the $W(\to \ell\nu)H(\to \tau_\ell\tau_h)$ channel. This approximation reduces the six unknowns of the momenta of the two neutrinos from tau decays into two variables: x_1 and x_2, as outlined in Section 6.1.1, thus reducing the dimensionality of the minimisation

(a) $W(\to \ell\nu)H(\to \tau_\ell\tau_h)$ **(b)** $W(\to \ell\nu)H(\to \tau_h\tau_h)$
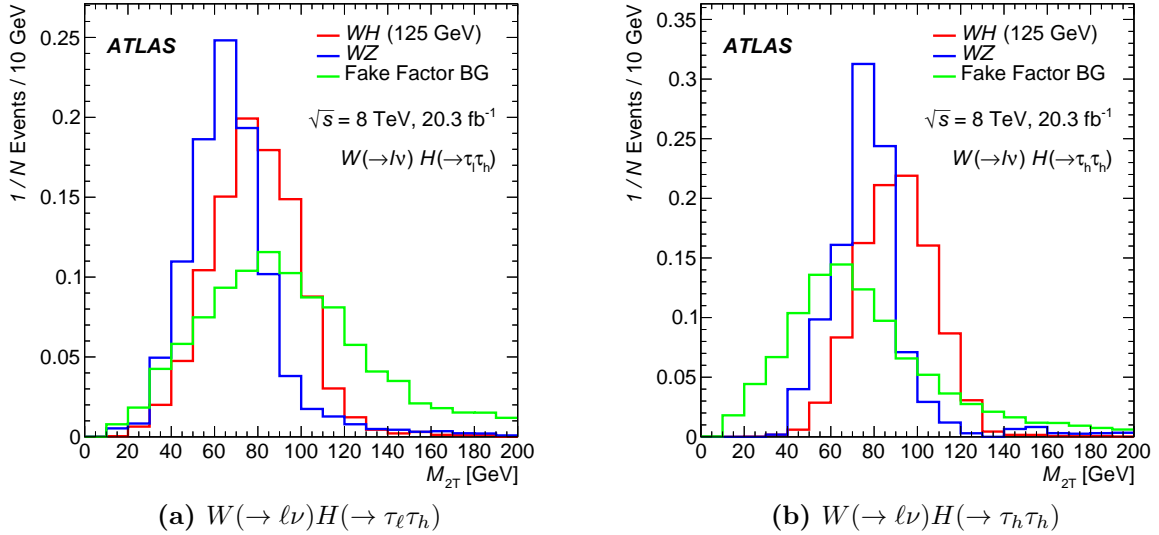
Figure 6.1: $M_{2\mathrm{T}}$ after event categorisation cuts in the WH channels. The 125 GeV signal mass point, the WZ background, and the fake background are each separately normalised to unit area.

by four. The requirement stated above that $\sum \vec{q}_{i\mathrm{T}} = \vec{p}_{\mathrm{T}}^{\mathrm{miss}}$ reduces the dimensionality of the minimisation by two. The final minimisation then becomes a two dimensional scan in the $x_1 - x_2$ phase space.

Figure 6.1 shows the $M_{2\mathrm{T}}$ distribution after WH event categorisation requirements. The 125 GeV signal mass points is shown as well as the main irreducible background, WZ, and the main reducible background, fakes. Each of these are normalised separately to unit area to compare shape differences. The variable discriminates signal from the fake and non-prompt lepton background due to the fact that these background events usually do not contain a real W boson decay. This causes the distribution of the fake background to have a long tail compared to the localised peak of the signal distribution.

6.2 The $W(\to \ell\nu)H(\to \tau_\ell\tau_h)$ Channel

After events are categorised as $W(\to \ell\nu)H(\to \tau_\ell\tau_h)$ candidates (see Section 4.3.4) further requirements are imposed to increase the signal-to-background ratio. The two light leptons in the event are required to be of different flavour, that is, one electron and one muon. Electrons are required to be identified as `tight++`. To reduce the background

contributions of non-prompt leptons, isolation criteria are imposed on both light leptons. Track isolation requires the sum of the p_{T} of additional tracks in a cone of $\Delta R < 0.4$ around the lepton to be less than 8% of the lepton p_{T}. Calorimeter isolation requires the sum of energies of additional calorimeter clusters in a cone of $\Delta R < 0.2$ around the lepton to be less than 8% of the lepton p_{T}. To reduce the background contributions from $Z \to \tau\tau$ and $t\bar{t}$ events, the electron and muon are required to have the same sign electric charge. To reduce the background of jets being misidentified as hadronic taus, they are required to have $p_{\mathrm{T}} > 25\,\mathrm{GeV}$ and to have opposite electric charge to both light leptons. Events containing b-tagged jets with $p_{\mathrm{T}} > 30\,\mathrm{GeV}$ are vetoed to further reduce the background of $t\bar{t}$ events. To further reduce the multi-jet and Z/γ^*+jets events, the scalar sum of the p_{T} of the electron, muon, and hadronic tau must be greater than $80\,\mathrm{GeV}$. To further reduce the background of jets being misidentified as hadronic taus, the angle between the hadronic tau and the lepton associated to the Higgs boson is required to satisfy $\Delta R(\tau_h,\ \ell) < 3.2$. Figure 6.2 shows the $M_{2\mathrm{T}}$ distribution in the $W(\to \ell\nu)H(\to \tau_\ell\tau_h)$ channel after these selection criteria are imposed.

6.3 The $W(\to \ell\nu)H(\to \tau_h\tau_h)$ Channel

In addition to the $W(\to \ell\nu)H(\to \tau_h\tau_h)$ categorisation requirements described in Section 4.3, further criteria are imposed to define the signal-sensitive region. Electrons are required to be identified as `tight++`. The two hadronic tau candidates are required to have opposite charge. Events containing b-tagged jets with $p_{\mathrm{T}} > 30\,\mathrm{GeV}$ are vetoed to further reduce the background of $t\bar{t}$ events. The scalar sum of the p_{T} of the lepton and two hadronic tau candidates must be greater than $100\,\mathrm{GeV}$ in order to reduce the background from multi-jet events. The transverse mass[1] of the light lepton and $\vec{E}_{\mathrm{T}}^{\mathrm{miss}}$ must be greater than $20\,\mathrm{GeV}$. To further reduce the background of jets being misidentified as hadronic taus, the angle between the two hadronic taus is required to satisfy $0.8 < \Delta R(\tau_h^1,\ \tau_h^2) < 2.8$. Figure 6.3 shows the $M_{2\mathrm{T}}$ distribution in the $W(\to \ell\nu)H(\to \tau_h\tau_h)$ channel after these selection criteria are imposed.

---

[1]The transverse mass is defined as $m_{\mathrm{T}} = \sqrt{2p_{\mathrm{T}}^\ell E_{\mathrm{T}}^{\mathrm{miss}}(1 - \cos\Delta\phi)}$ where $\Delta\phi$ is the azimuthal angular separation between the lepton and direction of $E_{\mathrm{T}}^{\mathrm{miss}}$.
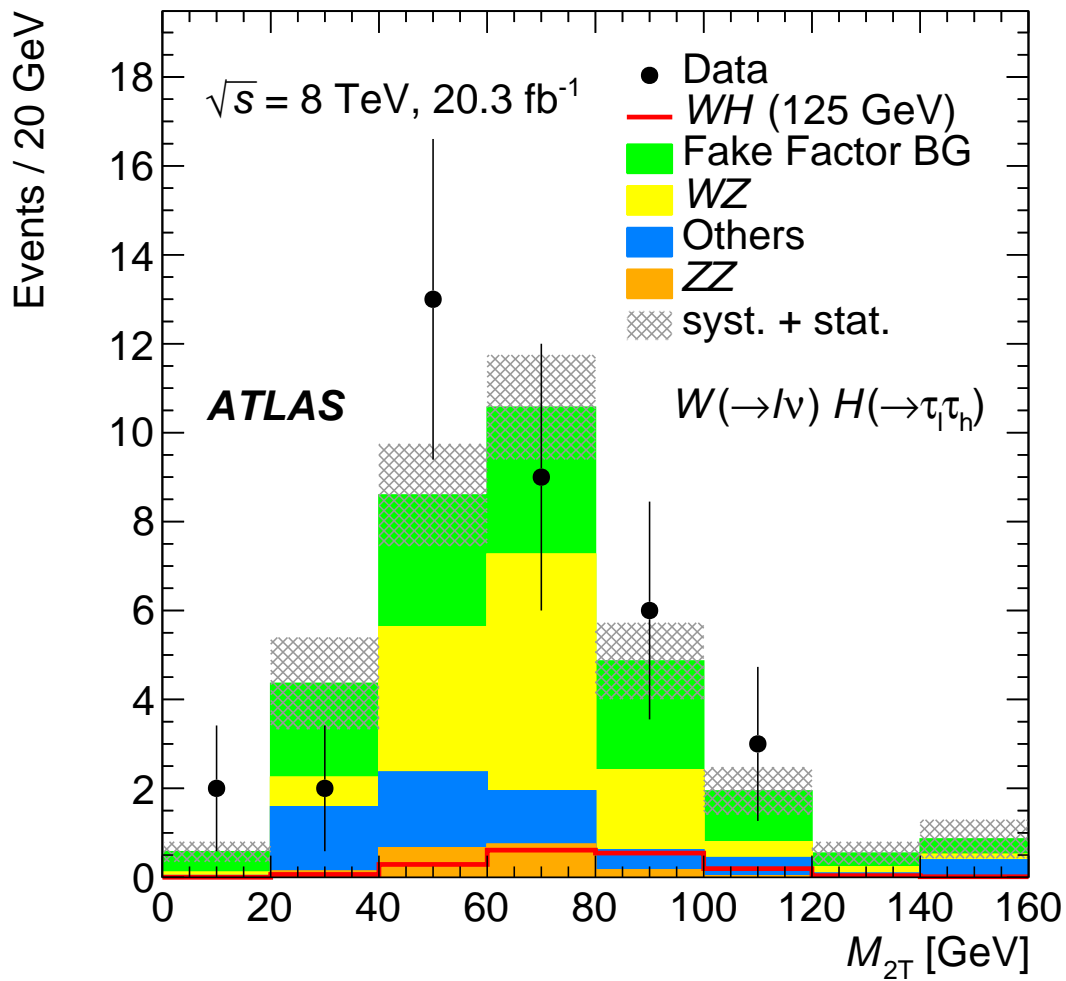
Figure 6.2: $M_{2\mathrm{T}}$ mass distribution in the signal-sensitive region of the $W(\to \ell\nu)H(\to \tau_\ell\tau_h)$ channel. The error bars on the data (filled black circles) are statistical, whilst the grey cross-hatched region gives the total error (statistical and systematic) on the sum of the backgrounds.
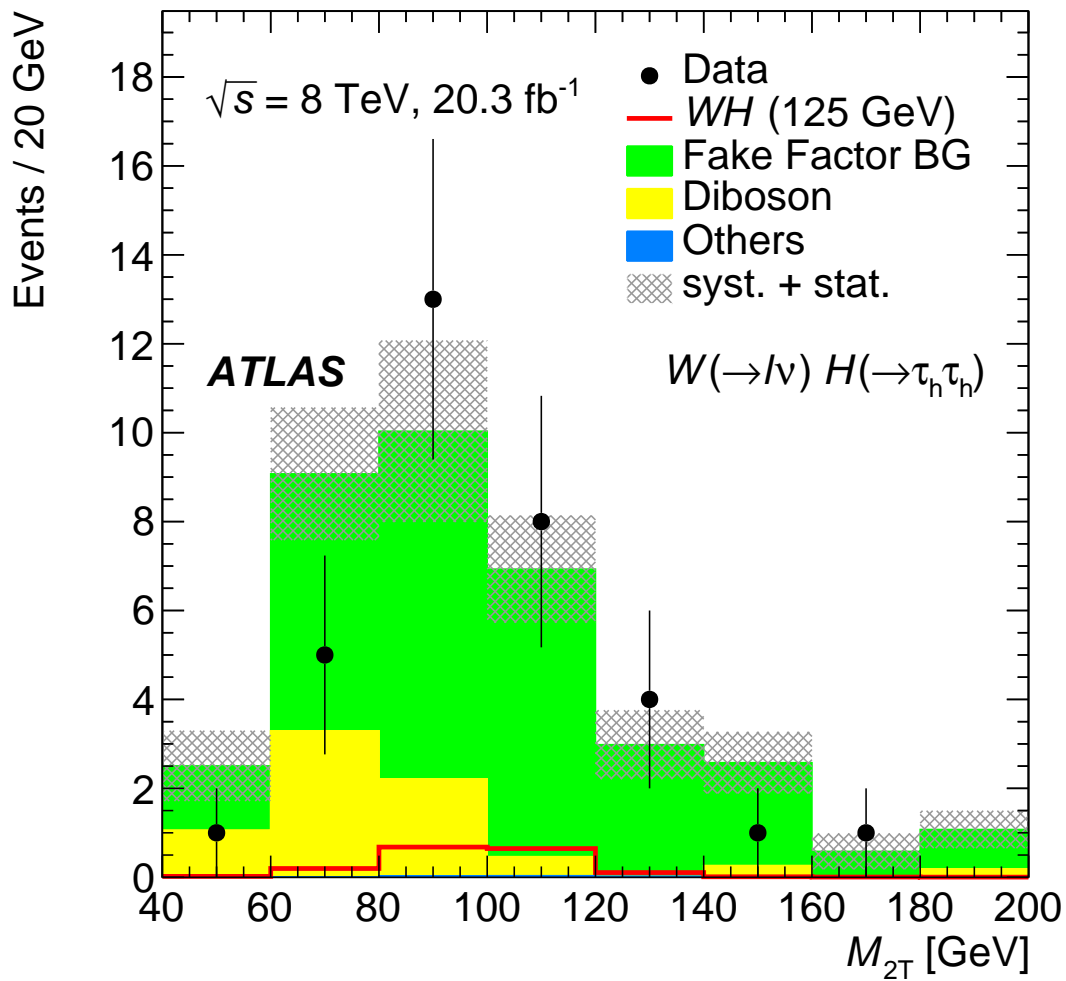
Figure 6.3: $M_{2\mathrm{T}}$ mass distribution in the signal-sensitive region of the $W(\to \ell\nu)H(\to \tau_h\tau_h)$ channel. The error bars on the data (filled black circles) are statistical, whilst the grey cross-hatched region gives the total error (statistical and systematic) on the sum of the backgrounds.

6.4 The $Z(\rightarrow \ell\ell)H(\rightarrow \tau_\ell\tau_h)$ Channel

In addition to the $Z(\rightarrow \ell\ell)H(\rightarrow \tau_\ell\tau_h)$ categorisation requirements described in Section 4.3, further criteria are imposed to define the signal-sensitive region. The two light leptons associated to the Z are required to have an invariant mass between 80 GeV and 100 GeV. The remaining light lepton is required to have opposite electric charge to the hadronic tau. The scalar sum of the p_T of the light lepton and hadronic tau associated to the Higgs boson must be greater than 60 GeV. Figure 6.4 shows the M_MMC distribution in the $Z(\rightarrow \ell\ell)H(\rightarrow \tau_\ell\tau_h)$ channel after these selection criteria are imposed.

6.5 The $Z(\rightarrow \ell\ell)H(\rightarrow \tau_h\tau_h)$ Channel

In addition to the $Z(\rightarrow \ell\ell)H(\rightarrow \tau_h\tau_h)$ categorisation requirements described in Section 4.3, further criteria are imposed to define the signal-sensitive region. The two light leptons associated to the Z boson are required to be the same flavour, have opposite electric charge, and have an invariant mass between 60 GeV and 120 GeV. The two hadronic taus are required to have opposite electric charge and the scalar sum of their p_T must be greater than 88 GeV. Figure 6.5 shows the M_MMC distribution in the $Z(\rightarrow \ell\ell)H(\rightarrow \tau_h\tau_h)$ channel after these selection criteria are imposed.

6.6 Systematic Uncertainties

The main source of uncertainty in each of the analysis channels is due statistical limitations. However this analysis is affected by a number of systematic uncertainties, both theoretical and experimental. This section describes all sources of systematic uncertainty which affect the analysis.

Each of these systematic uncertainties will be accounted for in the final results. This is done through the use of *nuisance parameters* which account for the additional variation in the model due to the uncertainty. Each systematic is represented as a nuisance parameter in the likelihood fit which is described fully in Section 6.7. The name of each nuisance parameter is specified in the discussion of each systematic below as a reference to be used when the final fit is later performed.
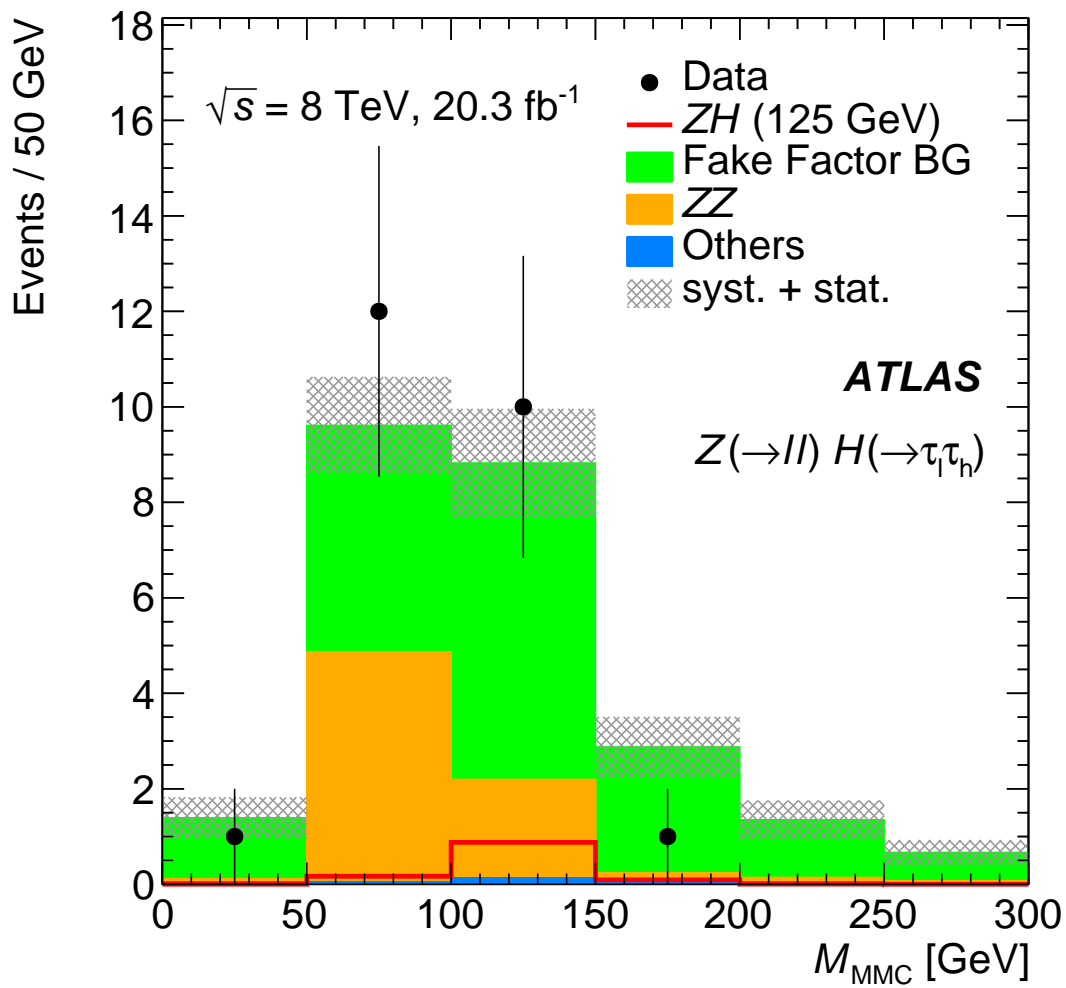
Figure 6.4: M_{MMC} mass distribution in the signal-sensitive region of the $Z(\to \ell\ell)H(\to \tau_\ell\tau_h)$ channel. The error bars on the data (filled black circles) are statistical, whilst the grey cross-hatched region gives the total error (statistical and systematic) on the sum of the backgrounds.
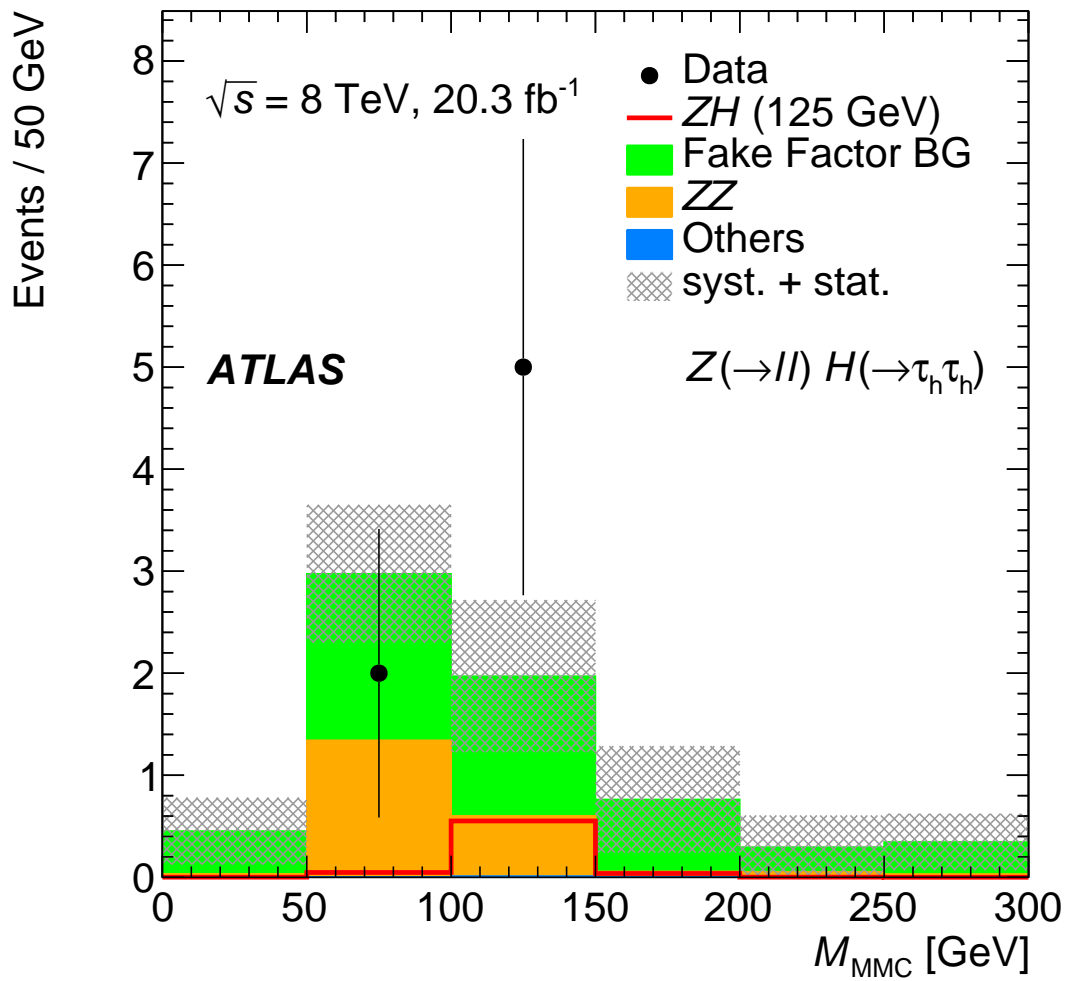
Figure 6.5: M_{MMC} mass distribution in the signal-sensitive region of the $Z(\to \ell\ell)H(\to \tau_h\tau_h)$ channel. The error bars on the data (filled black circles) are statistical, whilst the grey cross-hatched region gives the total error (statistical and systematic) on the sum of the backgrounds.

6.6.1 $H \to \tau\tau$ Branching Fraction Uncertainty

There is an uncertainty on the theoretical calculation of the Higgs decay branching fractions. These uncertainties are provided by the Higgs cross-section working group [20]. They are attributed primarily to missing higher-order electroweak and QCD corrections used in the calculation of the partial widths of the different decay modes. Table 6.1 shows the uncertainties for each Higgs mass point used in this analysis. The nuisance parameter for this uncertainty is named `ATLAS_BR_tautau` and is included in the fit for all signal $H \to \tau\tau$ MC samples.

Higgs Mass [GeV]	Variation [%]
100	$+6.87$ -6.73
105	$+6.79$ -6.65
110	$+6.64$ -6.51
115	$+6.42$ -6.31
120	$+6.13$ -6.01
125	$+5.71$ -5.67
130	$+5.26$ -5.22
135	$+4.75$ -4.75
140	$+4.26$ -4.26
145	$+3.80$ -3.81
150	$+3.37$ -3.43

Table 6.1: The theoretical uncertainty on the $H \to \tau\tau$ branching fraction for each Higgs mass hypothesis used in this analysis.

6.6.2 QCD Scale Uncertainties

The QCD scale uncertainties on the signal production cross-sections are provided by the Higgs cross-section working group [20]. These account for missing higher-order QCD corrections and are estimated by varying the factorisation and renormalisation scales up and down by a factor of two around the nominal value. The values of these uncertainties are shown in Table 6.2 for each signal production process. Scale uncertainties are larger for the ZH production mode due to the one-loop-induced $gg \to ZH$ contribution to the

cross-section. This uncertainty also applies to background processes estimated from MC. For the WW, WZ, and ZZ processes this uncertainty is 5% and is included in the fit with the nuisance parameter QCDscale_VV. This uncertainty is considered negligible for other background processes estimated from MC due to their small contributions in the signal region.

Process	WH	ZH	VBF	ggF
Nuisance Parameter	QCDscale_WH	QCDscale_ZH	QCDscale_qqH	QCDscale_ggH
Higgs Mass [GeV]	Variation [%]	Variation [%]	Variation [%]	Variation [%]
100	± 1.0	± 2.4	± 0.2	$^{+7.9}_{-8.4}$
105	± 1.0	± 2.5	$^{+0.3}_{-0.2}$	$^{+7.8}_{-8.3}$
110	± 1.0	± 2.7	± 0.2	$^{+7.6}_{-8.2}$
115	± 1.0	± 2.8	± 0.2	$^{+7.4}_{-8.1}$
120	± 1.0	± 3.0	± 0.2	$^{+7.3}_{-7.9}$
125	± 1.0	± 3.1	± 0.2	$^{+7.2}_{-7.8}$
130	± 1.0	± 3.3	± 0.2	$^{+7.1}_{-7.7}$
135	± 1.0	± 3.5	± 0.2	$^{+7.0}_{-7.7}$
140	± 1.0	± 3.6	± 0.2	$^{+6.9}_{-7.6}$
145	± 1.0	± 3.8	$^{+0.3}_{-0.1}$	$^{+6.8}_{-7.5}$
150	± 1.0	± 3.9	$^{+0.3}_{-0.2}$	$^{+6.7}_{-7.4}$

Table 6.2: QCD scale uncertainties on the signal production cross-sections for each Higgs mass hypothesis used in this analysis.

In addition to the overall uncertainty on the cross-section, the effect of the QCD scale uncertainty on the signal acceptance is also evaluated. MC samples for the $VH(\rightarrow \tau\tau)$ signal processes were generated with the factorisation and renormalisation scales varied up and down by a factor of two. These truth level MC samples were passed through event selection criteria which emulate the full analysis requirements. The largest change in the signal acceptance across all channels is 1%. This uncertainty is included in the fit for all $VH(\rightarrow \tau\tau)$ signal processes with the nuisance parameter QCDscale_VH_ACCEPTANCE.

6.6.3 PDF Uncertainties

The PDF uncertainties on the signal production cross-sections are provided by the Higgs cross-section working group [20]. PDF uncertainties are obtained by comparing the cross-sections obtained from the MCFM [67] generator with different PDF sets: CT10 [68], NNPDF2.3 [69], and MSTW2008 [70]. CT10 is used as the nominal set, the differences between the nominal set and the variation sets is combined in quadrature to give the uncertainty on the inclusive cross-section. Table 6.3 shows the measured uncertainty for the signal processes and the main irreducible background processes.

Process	Nuisance Parameter	Variation [%]
$WW/WZ/ZZ$	pdf_qq	± 4
$WH/ZH/$VBF	pdf_Higgs_qq	± 3
ggF	pdf_Higgs_gg	$^{+8}_{-7}$

Table 6.3: PDF uncertainties on the production cross-sections of the signal and the main irreducible background processes.

In addition to the overall uncertainty on the cross-section, the effect of the PDF uncertainty on the signal acceptance is also evaluated. MC samples for the $VH(\rightarrow \tau\tau)$ signal processes were generated with the PDF sets: CT10, NNPDF2.3, and MSTW2008. These truth level MC samples were passed through event selection criteria which emulate the full analysis requirements. The largest change in the signal acceptance between different PDF sets is 1%. This uncertainty is included in the fit for all $VH(\rightarrow \tau\tau)$ signal processes with the nuisance parameter pdf_VH_ACCEPTANCE.

6.6.4 Underlying Event Uncertainties

Uncertainties in the soft QCD interactions in the underlying event result in uncertainties on the reconstruction observables such as the Higgs boson p_{T}. This can translate into an uncertainty on the signal selection acceptance. To estimate this uncertainty, signal samples were generated with POWHEG and showered with both PYTHIA and HERWIG/JIMMY. These events are passed through emulated selection requirements on the truth level particles for each signal category. The difference in signal acceptance between the PYTHIA and JIMMY samples due to the different underlying event modelling

is taken as the overall uncertainty on the underlying event. The results are shown in Table 6.4 and are given the nuisance parameter name `ATLAS_VH_UE`.

Process	Variation [%]
$W(\to \ell\nu)H(\to \tau_\ell\tau_h)$	± 2.4
$W(\to \ell\nu)H(\to \tau_h\tau_h)$	± 1.0
$Z(\to \ell\ell)H(\to \tau_\ell\tau_h)$	± 4.1
$Z(\to \ell\ell)H(\to \tau_h\tau_h)$	± 2.1

Table 6.4: Uncertainties on the signal acceptance due to the underlying event model for each signal category.

6.6.5 Electroweak Correction Uncertainty

The signal MC samples were generated with LO QCD and LO electroweak Pythia. The cross-sections of the signal processes are computed with NNLO QCD and NLO electroweak using Hawk [60]. These higher-order corrections to the cross-sections are primarily dependent on the Higgs p_T and are accounted for by weighting the signal MC events accordingly. This weighting procedure has an associated uncertainty of 2% which is applied to both VH processes in the fit using the nuisance parameter `ATLAS_VH_EWK`.

6.6.6 Luminosity Measurement Uncertainty

The bulk of the sample composition in the signal region comes from the data-driven fake factor method, but there is some small contribution estimated from the simulation. In order to account for the systematic uncertainty on the integrated luminosity, the analysis is performed with the simulation prediction shifted up and down by 2.8%. This shift is derived using the method described in [71] using beam-separation scans. The nuisance parameter name for this systematic is `ATLAS_LUMI_2012` which enters the fit for all MC samples.

6.6.7 Pileup Uncertainty

The LHC running conditions change over the duration of data collection as the beam parameters are being improved. The distribution of the number of collisions per bunch crossing, shown in Figure 3.8, is therefore only known at the time of data collection. MC samples are usually generated before experiment operation and are generated with pileup configurations which attempt to match the expected distribution. After data has been collected, the MC is weighted to match the observed running conditions. The uncertainty on this procedure typically about 1% and is treated as a nuisance parameter called `ATLAS_PU_RESCALE_2012` which enters the fit for all MC samples.

6.6.8 Electron Reconstruction Uncertainties

There are three sources of electron reconstruction uncertainty: selection efficiency, energy scale, and energy resolution. The selection efficiency uncertainty is the combination of the uncertainties on electron identification, isolation requirements, and trigger selection. These three efficiency uncertainties each separately have a small effect on the overall normalisation, for this reason they are treated as correlated and combined into one nuisance parameter called `ATLAS_EL_EFF_2012` which is typically less than 2%. The electron energy scale calibration has an associated uncertainty which is typically 1-3%, called `ATLAS_EL_SCALE_2012`. In addition, there is also an uncertainty on the energy resolution which is about 1-4%, called `ATLAS_EL_RES_2012`. These nuisance parameters enter the fit for all MC samples with simulated electrons. All of these electron uncertainty measurements are provided by the ATLAS electron performance group [72].

6.6.9 Muon Reconstruction Uncertainties

Similar to electrons, muon reconstruction has uncertainties on selection efficiency and momentum scale. The selection efficiency uncertainty is the combination of the uncertainties on muon identification, isolation requirements, and trigger selection. These three efficiency uncertainties are treated as correlated and combined into one nuisance parameter called `ATLAS_MU_EFF_2012` which is typically about 1%. The muon momentum scale calibration has an associated uncertainty which is typically less than 1%, the nuisance parameter is called `ATLAS_MU_SCALE_2012`. These nuisance parameters enter the fit for

all MC samples with simulated muons. All of these muon uncertainty measurements are provided by the ATLAS muon performance group [53].

6.6.10 Tau Reconstruction Uncertainties

Hadronic tau reconstruction has multiple sources of uncertainty. The uncertainty on the energy scale calibration for true taus is 2-4% and is treated as the nuisance parameter `ATLAS_TES_TRUE_2012`. The efficiency of hadronic tau identification has been measured in data and provided as two separate components. The systematic uncertainty on the efficiency is treated as the nuisance parameter `ATLAS_TAU_ID_2012`. There is an associated statistical uncertainty on the measurement of the efficiency uncertainty which is treated as the nuisance parameter `ATLAS_TAU_ID_STAT_2012`. The total uncertainty on the tau identification efficiency is 2.5% for 1-prong taus and 4% for 3-prong taus. These nuisance parameters enter the fit for all MC samples with simulated hadronic taus. All of these hadronic tau uncertainty measurements are provided by the ATLAS tau performance group [73].

6.6.11 b-tagging Uncertainties

The efficiency of b-tagging jets has an uncertainty which depends on the type of jet. Jets initiated by b-quarks and c-quarks have different efficiency uncertainties which are given the nuisance parameter names `ATLAS_BTag_BEFF` and `ATLAS_BTag_CEFF` respectively. These nuisance parameters enter the fit for all MC samples with jets that pass the b-jet veto in the WH channels. These efficiency uncertainties have been measured in data using $t\bar{t}$ events to be about 2%, and are provided by the ATLAS b-tagging performance group [74].

6.6.12 Fake and Non-Prompt Background Estimation Uncertainties

The total systematic uncertainty on the fake background estimation is separated into terms for each type of fake lepton. The systematic uncertainties on the fake factor for each type of fake lepton are evaluated and treated as uncorrelated with all other uncertainties. The total systematic uncertainty on the fake background estimate is

evaluated by performing the analysis with the fake factors for each fake lepton type shifted up and down by their respective uncertainties.

Fake and Non-Prompt Electrons

For the fake electron background, the systematic uncertainty on the electron fake factor is further separated into two terms. The first takes into account the error on the measurement of the electron fake factor, this is taken to be the statistical uncertainty on the fake factor in each bin of the measurement. The nuisance parameter name for this systematic is `ATLAS_EL_FF_STATISTICAL`. The second takes into account the uncertainty of the expected composition of the fake electrons in the signal region. The measurement of the electron fake factor was separated into two measurements, targeting the expected composition of fakes electrons in the WH and ZH signal regions. In the ZH channels, the expected composition of fake electrons is roughly equal parts jet fakes and photon conversions (Figure 5.3a). The WH channels contain a larger contribution from photon conversions (Figure 5.10a). This difference in composition required two measurements of the electron fake factor, one targeted to each channel. The uncertainty on the fake factor due to compositional changes in the fake background is taken to be the difference in these two measured fake factors. This uncertainty is evaluated by performing the two fake factor measurements again without binning in p_T or η. These measurements are performed un-binned to remove statistical fluctuations already accounted for in the measurement uncertainty term. The difference in these two measurements is due to compositional changes and was measured to be 0.22, this corresponds to a 38% and 61% relative uncertainty on the electron fake factor for the WH and ZH channels respectively. The nuisance parameter name for this systematic is `ATLAS_EL_FF_COMPOSITION`.

Fake Hadronic Taus

For the fake tau background, the systematic uncertainty on the tau fake factor is further separated into two terms. The first takes into account the error on the measurement of the tau fake factor, this is taken to be the statistical uncertainty on the fake factor in each bin of the measurement. The nuisance parameter name for this systematic is `ATLAS_TAU_FF_STAT`. The second takes into account the uncertainty of the expected composition of jets faking taus in the signal region. Quark-initiated jets pass tau reconstruction at a different rate than gluon initiated jets. The FF measurement was

repeated with different requirements on $E_{\mathrm{T}}^{\mathrm{miss}}$, this produced a different composition of jets faking tau reconstruction as observed in MC. The difference in the measured FF is due to composition, the variation from the nominal is treated as the uncertainty, shown in Table 6.5. The nuisance parameter name for this systematic is `ATLAS_TAU_FF_MODEL`.

Tau Prongs	Down [%]	Up [%]
One	+6.7	-13.4
Three	-14.1	+28.2

Table 6.5: Systematic uncertainties on the tau FF due to the variation in the composition of quark- vs. gluon-initiated jets passing tau identification. The variations apply to the measured fake rates for 1-prong (Tables 5.7 and 5.9) and 3-prong (Tables 5.8 and 5.10) taus.

6.7 Statistical Tests

The results of this search are derived by testing the level of agreement of the observed data with two exclusive hypotheses. The scenario where the Higgs boson does not decay to taus is called the *background-only* hypothesis H_0. The *signal-plus-background* hypothesis H_μ describes the scenario where the Higgs boson decays to taus with the frequency predicted by the SM. The *signal strength* parameter $\mu = \frac{\sigma}{\sigma_{\mathrm{SM}}}$ accommodates deviations from the SM prediction, this allows for the testing of the signal-plus-background hypothesis without assuming the signal frequency. These hypotheses will be tested by answering two questions:

1. Assuming H_μ represents reality: What is the largest signal strength that can exist given the observed data?

2. Assuming H_0 represents reality: What is the probability that an excess of observed events comes from background fluctuations?

This section reviews the statistical approach adopted by ATLAS as outlined in full in reference [75]. Firstly, the construction of the fitting procedure in general is described, followed by the specific techniques used to answer the previous two questions.

6.7.1 The Profile Likelihood Ratio

Given a histogram of any particular kinematic variable, the prediction for the number of expected events in the i-th bin is given by

$$p_i(\mu) = b_i + \mu s_i \tag{6.50}$$

where b_i and s_i are the respective background and signal predictions. This expression yields the background-only hypothesis for the case where $\mu = 0$, and the nominal signal-plus-background hypothesis for the case where $\mu = 1$. This prediction is compared to the observed number of events in data d_i, the level of agreement L_i is measured with a Poisson probability given by

$$L_i = \frac{p_i^{d_i}}{d_i!} e^{-p_i} \tag{6.51}$$

The overall agreement across all N bins of the distribution is tested with a likelihood function defined as the product of the Poisson probabilities for each bin, given by

$$L = \prod_i^N L_i \tag{6.52}$$

This expression is a somewhat simplified measure of goodness of fit. In reality, information regarding systematic uncertainties must be included in the fit model. This is done though the use of *nuisance parameters*, which allow the model to handle how any given uncertainty affects the predictions of b_i or s_i. The set of nuisance parameters which affect the prediction p_i is referred to as θ, the expression for the prediction is now

$$p_i(\mu, \theta) = b_i(\theta) + \mu s_i(\theta) \tag{6.53}$$

The likelihood function in equation (6.52) can now be written out explicitly as

$$L(\mu, \theta) = \prod_i^N \frac{(b_i(\theta) + \mu s_i(\theta))^{d_i}}{d_i!} e^{-(b_i(\theta) + \mu s_i(\theta))} \tag{6.54}$$

The values of μ and θ which maximise L are $\hat{\mu}$ and $\hat{\theta}$ respectively.

$$(\hat{\mu}, \hat{\theta}) = \arg \max_{\mu,\,\theta} L(\mu, \theta) \tag{6.55}$$

Therefore, $L(\hat{\mu}, \hat{\theta})$ represents the best possible fit and is known as the *unconditional maximum likelihood*. $\hat{\mu}$ represents the best fit value of the signal strength and is called the observed signal strength. For any given value of μ, the set of nuisance parameters which maximise L is $\tilde{\theta}$.

$$\tilde{\theta} = \arg\max_{\theta} L(\mu, \theta) \tag{6.56}$$

Therefore, $L(\mu, \tilde{\theta})$ represents the best possible fit for the given value of μ, this is called the *conditional maximum likelihood*. The *profile likelihood ratio* $\lambda(\mu)$ is constructed from the ratio of these two maximum likelihoods, given by

$$\lambda(\mu) = \frac{L(\mu, \tilde{\theta})}{L(\hat{\mu}, \hat{\theta})} \tag{6.57}$$

By construction this value occupies the range $0 \le \lambda \le 1$, with values close to 1 indicating good agreement between data and the hypothesised value of μ.

Statistical hypothesis testing requires the construction of a *test statistic*. A test statistic is a number which quantifies the level of agreement between data and a given hypothesis. For convenience, it is desirable for the test statistic to take larger values for increasing level of incompatibility between data and the given hypothesis. A test statistic t_μ can be constructed from the likelihood ratio as

$$t_\mu = -2 \ln \lambda(\mu) \tag{6.58}$$

This construction will be used to provide answers to the two questions posed in the previous section.

6.7.2 Exclusion Limit

To answer question 1, the upper limit is placed on the signal strength given the observed data. The test statistic q_μ is constructed as

$$q_\mu = \begin{cases} -2 \ln \lambda(\mu) & \text{if } \hat{\mu} \le \mu \\ 0 & \text{if } \hat{\mu} > \mu \end{cases} \tag{6.59}$$

This test statistic is constructed from two related statistical tests. The test statistic $q_\mu = t_\mu$ is used in the region $\hat{\mu} \le \mu$ where the observed signal strength is smaller than

the hypothesised signal strength, which is considered to be incompatible with H_μ. The region $\hat{\mu} > \mu$ where the observed signal strength is larger than expected is not taken to represent incompatibility with H_μ, therefore $q_\mu = 0$ in this region. The probability that a value at least as large as as $\hat{\mu}$ is observed, assuming H_μ, is given by a p-value

$$p_\mu = \int_{q_{\hat{\mu}}}^{\infty} f(q_\mu|\mu)dq_\mu \tag{6.60}$$

Here $f(q_\mu|\mu)$ is the probability density function of q_μ assuming H_μ. An upper limit on the signal strength can be placed by finding the largest value of μ excluded by data at a given confidence level. It is common practice to determine the upper limit at the 95% confidence level, this is done by finding the value of μ for which $p_\mu = 0.05$. This can be interpreted as there being only a 5% chance of missing a signal this large, and a smaller chance of missing a larger signal.

6.7.3 Statistical Significance

To answer question 2, the test statistic q_0 is constructed as

$$q_0 = \begin{cases} -2\ln\lambda(0) & \text{if } \hat{\mu} \geq 0 \\ 0 & \text{if } \hat{\mu} < 0 \end{cases} \tag{6.61}$$

The test statistic t_μ is used in the region $\hat{\mu} \geq 0$ where any positive observed signal strength is considered incompatible with H_0. The region $\hat{\mu} < 0$ may be seen as evidence against H_0. However, in searches where the signal can only be seen as a positive excess in data, an observed signal strength in this region does not show that the data contain signal events, but rather points to a systematic error in the background modelling. For this reason, a downward fluctuation in $\hat{\mu}$ is considered consistent with observing no signal, thus setting $q_0 = 0$. The probability that the observed signal strength takes a value this large, assuming H_0, is given by

$$p_0 = \int_{q_{\hat{\mu}}}^{\infty} f(q_0|0)dq_0 \tag{6.62}$$

Here $f(q_0|0)$ is the probability density function of q_0 assuming H_0. The interpretation of p_0 is the probability of background fluctuations being large enough to produce the observed signal strength. It is convenient to convert this p-value to an equivalent statistical

significance, Z, given by

$$Z = \Phi^{-1}(1 - p) \tag{6.63}$$

Here Φ^{-1} is the quantile of the the standard Gaussian. The significance is the number of standard deviations (σ) $\hat{\mu}$ is from $\mu = 0$, which represents the statistical significance of a signal-like excess above the background.

6.7.4 Expected Limits and Significances

To evaluate the sensitivity of either the exclusion limit or statistical significance, it is not sufficient to look at the observed values of a given data set, but rather to look at the expected sensitivity. When optimising an analysis, the expected sensitivity gives a good metric for comparison. The expected sensitivity is also important for blinded analyses which are unable to look at data until the analysis is finalised, this includes validation of the fitting model and statistical tests. The expected limits and significances can be found by substituting a pseudo data set in place of the real observed data in equation (6.51). This pseudo data is called *Asimov data* [75]. The Asimov data is constructed from the signal and background predictions in each bin, given by

$$d_i^A(\mu) = b_i + \mu s_i \tag{6.64}$$

This expression is independent of the set of nuisance parameters as it is constructed from the nominal values of the predictions. This expression is a function of the hypothesised signal strength, however when constructing the expected limits and significances only two values of μ are used, specifically $\mu = 0$ and $\mu = 1$ respectively. To calculate the expected limit, the data d_i in equation (6.51) is substituted with $d_i^A(0)$. This sets the data to look like the background-only expectation which means the profile likelihood ratio is now dominantly dependent on how well the set of nuisance parameters can be constrained in the fit. This gives the nominal value of the most tightly constrained exclusion limit which can be obtained with the given background model. To calculate the expected significance, the data d_i in equation (6.51) is substituted with $d_i^A(1)$. This sets the data to look like the nominal signal-plus-background expectation. The expected significance is then interpreted as how large a nominal signal excess is above the background compared to the size of the systematic uncertainties obtained from the constrained values of the nuisance parameters in the fit.

Overall	Overall + Shape
ATLAS_LUMI_2012	ATLAS_BTag_BEFF
pdf_qq	ATLAS_BTag_CEFF
QCDscale_VV	ATLAS_EL_RES_2012
ATLAS_BR_tautau	ATLAS_EL_SCALE_2012
pdf_Higgs_qq	ATLAS_EL_EFF_2012
pdf_Higgs_gg	ATLAS_MU_SCALE_2012
QCDscale_ggH	ATLAS_MU_EFF_2012
QCDscale_qqH	ATLAS_TES_TRUE_2012
QCDscale_WH	ATLAS_TAU_ID_2012
QCDscale_ZH	ATLAS_TAU_ID_STAT_2012
ATLAS_EL_FF_COMPOSITION	ATLAS_PU_RESCALE_2012
ATLAS_TAU_FF_MODEL	ATLAS_EL_FF_STATISTICAL
pdf_VH_ACCEPTANCE	ATLAS_TAU_FF_STAT
QCDscale_VH_ACCEPTANCE	ATLAS_VH_UE
	ATLAS_VH_EWK

Table 6.6: Summary of all systematic uncertainties considered in this analysis. The left column lists systematics which affect the overall normalisation of a process. The right column lists systematics which affect both the shape and normalisation of a process. The meaning of the various systematic uncertainties is discussed in Section 6.6.

6.7.5 Nuisance Parameter Pruning

Some systematics described in the previous section only affect the overall normalisation of a process. Other systematics can affect the shape of a distribution as well as the overall normalisation. Table 6.6 lists all the systematic uncertainties considered in this analysis.

All systematics which enter the fit must first pass through multiple stages of pruning. This procedure filters the full list of systematics to remove any which are expected to have a negligible affect on any given process. After the pruning is performed, the fit is performed on the subset of systematics which are expected to have an observable impact. This is done to ensure fit stability as well as to remove any statistical fluctuations in

distributions which may bias the fit. For each signal and background process, each nuisance parameter is separately tested.

Firstly, shape systematics must pass a χ^2 test. In this test, each of the $\pm 1\sigma$ variations and nominal shape are separately normalised to unit area. If the shapes of either of the $\pm 1\sigma$ variations differs from the nominal shape with $\chi^2 < 0.95$, the nuisance parameter is included in the fit as is. If the shape systematic fails this test, the yields of the $\pm 1\sigma$ variations are converted to overall uncertainties which are applied to the nominal shape in the fit. This is done to remove the possibility of a nuisance parameter having shape variations which are due to statistical fluctuations.

Secondly, for background processes only, a nuisance parameter will be pruned if the difference between the $+1\sigma$ and -1σ yield in all bins of the distribution is less than 10% of the total background statistical error of that bin.

Lastly, overall systematics with $\pm 1\sigma$ variations that differ from the nominal by less than 0.5% are pruned. The only exception to this last step is the treatment of theory systematics, these are always kept in the fit even if they have a small overall effect.

6.7.6 The Fit Model

The fit is performed on the distributions of the sensitive mass variable for each channel: M_{2T} in the WH channels, and M_{MMC} in the ZH channels. These distributions are shown in Figure 6.2 for the $W(\to \ell\nu)H(\to \tau_\ell\tau_h)$ channel, Figure 6.3 for the $W(\to \ell\nu)H(\to \tau_h\tau_h)$ channel, Figure 6.4 for the $Z(\to \ell\ell)H(\to \tau_\ell\tau_h)$ channel, and Figure 6.5 for the $Z(\to \ell\ell)H(\to \tau_h\tau_h)$ channel. The nominal distribution for each signal and background is included in the fit. For the purpose of fitting, all four Higgs production modes (ggF, VBF, WH, and ZH) of $H \to \tau\tau$ are classified as signal, all other processes are classified as backgrounds. To assist the stability of the fit, all the small background contributions (such as $t\bar{t}$, $Z \to \tau\tau$, $H \to WW^{(*)}$, and $H \to ZZ^{(*)}$) are grouped into one background called *others*.

Overall systematics are included in the fit by specifying the size of the variation that would apply to the nominal shape. Shape systematics are included in the fit by specifying a separate histogram for each of the $\pm 1\sigma$ shapes. The different nuisance parameters provided to the fit are assumed to be fully uncorrelated.

The event yields and their uncertainties for each signal and background process which enters the fit are shown for each channel: $W(\to \ell\nu)H(\to \tau_\ell\tau_h)$ in Table 6.7, $W(\to \ell\nu)H(\to \tau_h\tau_h)$ in Table 6.8, $Z(\to \ell\ell)H(\to \tau_\ell\tau_h)$ in Table 6.9, and $Z(\to \ell\ell)H(\to \tau_h\tau_h)$ in Table 6.10. Uncertainties which are not shown for any given nuisance parameter either do not apply to the given process or have failed the pruning process and so are considered negligible.

The fit allows each nuisance parameter, as well as the statistical uncertainties of each bin of the distributions, to vary independently to maximise the likelihood and find the best fit value of the signal strength $\hat{\mu}$.

The implementation of these statistical tools is provided by packages integrated into ROOT [76]. The implementation of the likelihood function is provided by RooStats [77], and the fitting procedure to maximise the likelihood is provided by RooFit [78].

	$H \to \tau\tau$ Signals				Backgrounds			
	ggF	VBF	WH	ZH	WZ	ZZ	Others	Fakes
NOMINAL	0.023	0.0046	1.75	0.184	11.76	1.779	5.7	13.1
STATISTICAL	±0.013	±0.0018	±0.045	±0.011	±0.34	±0.073	±1.4	±1.3
ATLAS_TAU_FF_STAT								$^{+1.5}_{-1.4}$
QCDscale_VV					$^{+0.59}_{-0.59}$	$^{+0.089}_{-0.089}$		
ATLAS_LUMI_2012	$^{+0.00064}_{-0.00064}$	$^{+0.00013}_{-0.00013}$	$^{+0.049}_{-0.049}$	$^{+0.0051}_{-0.0051}$	$^{+0.33}_{-0.33}$	$^{+0.05}_{-0.05}$	$^{+0.16}_{-0.16}$	
ATLAS_TAU_ID_2012	$^{+0.00067}_{-0.00067}$	$^{+0.00012}_{-0.00012}$	$^{+0.047}_{-0.047}$	$^{+0.005}_{-0.005}$	$^{+0.31}_{-0.31}$	$^{+0.048}_{-0.048}$	$^{+0.14}_{-0.14}$	
pdf_qq					$^{+0.47}_{-0.47}$	$^{+0.071}_{-0.071}$		
ATLAS_BTag_CEFF	$^{-0.00083}_{+0.00085}$	$^{-0.00017}_{+0.00017}$	$^{-0.044}_{+0.045}$	$^{-0.005}_{+0.005}$	$^{-0.27}_{+0.28}$	$^{-0.043}_{+0.043}$	$^{-0.15}_{+0.15}$	
ATLAS_EL_EFF_2012	$^{+0.00044}_{-0.00044}$	$^{+0.00008}_{-0.00008}$	$^{+0.033}_{-0.033}$	$^{+0.0037}_{-0.0037}$	$^{+0.24}_{-0.24}$	$^{+0.036}_{-0.036}$	$^{+0.097}_{-0.097}$	
ATLAS_TES_TRUE_2012	$^{+0.0064}_{-0.0064}$	$^{+0.0054}_{-0.0054}$	$^{+0.024}_{-0.031}$	$^{+0.0027}_{-0.0047}$	$^{+0.25}_{-0.24}$	$^{+0.047}_{-0.052}$		
ATLAS_TAU_ID_STAT_2012	$^{+0.00043}_{-0.00043}$	$^{+0.00007}_{-0.00007}$	$^{+0.028}_{-0.028}$	$^{+0.003}_{-0.003}$	$^{+0.19}_{-0.19}$	$^{+0.028}_{-0.028}$	$^{+0.08}_{-0.08}$	
ATLAS_TAU_FF_MODEL								$^{-0.38}_{+0.19}$
ATLAS_MU_EFF_2012	$^{+0.00033}_{-0.00033}$	$^{+0.00007}_{-0.00007}$	$^{+0.024}_{-0.024}$	$^{+0.0024}_{-0.0024}$	$^{+0.14}_{-0.14}$	$^{+0.021}_{-0.021}$	$^{+0.055}_{-0.055}$	
ATLAS_BR_tautau	$^{+0.0013}_{-0.0013}$	$^{+0.00026}_{-0.00026}$	$^{+0.1}_{-0.1}$	$^{+0.01}_{-0.01}$				
ATLAS_EL_FF_STATISTICAL								$^{+0.1}_{-0.1}$
ATLAS_BTag_BEFF	$^{-0.00075}_{+0.00075}$						$^{-0.12}_{+0.12}$	
ATLAS_PU_RESCALE_2012	$^{-0.00014}_{+0.00037}$	$^{+0.00009}_{-0.00009}$		$^{-0.0013}_{+0.0007}$	$^{+0.09}_{-0.11}$			
pdf_Higgs_qq		$^{+0.00014}_{-0.00014}$	$^{+0.053}_{-0.053}$	$^{+0.0055}_{-0.0055}$			$^{+0.0082}_{-0.0082}$	
ATLAS_VH_UE			$^{+0.042}_{-0.042}$	$^{+0.0072}_{-0.0072}$				
ATLAS_VH_EWK			$^{+0.035}_{-0.035}$	$^{+0.0037}_{-0.0037}$				
ATLAS_EL_SCALE_2012		$^{+0.0024}_{+0.0024}$	$^{-0.043}_{-0.053}$		$^{+0.22}_{+0.13}$			
QCDscale_WH			$^{+0.018}_{-0.018}$				$^{+0.0021}_{-0.0021}$	
QCDscale_ggH	$^{+0.0016}_{-0.0018}$						$^{+0.002}_{-0.002}$	
QCDscale_ZH				$^{+0.0057}_{-0.0057}$			$^{+0.0019}_{-0.0019}$	
QCDscale_qqH		$^{+0.00001}_{-0.00001}$					$^{+0.00001}_{-0.00001}$	

Table 6.7: Yields and their uncertainties in the $W(\to \ell\nu)H(\to \tau_\ell\tau_h)$ signal region. The signal yields are shown for a Higgs mass of 125 GeV. The nuisance parameters are ordered by decreasing size of the post-fit impact on $\hat{\mu}$.

	$H \to \tau\tau$ Signals				Backgrounds	
	ggF	VBF	WH	ZH	Diboson	Fakes
NOMINAL	0.0085	0.0108	1.668	0.1494	7.4	28.1
STATISTICAL	±0.0085	±0.0024	±0.042	±0.0095	±1.2	±2.4
ATLAS_TAU_FF_STAT						$^{+0.6}_{-1.6}$
ATLAS_TAU_ID_2012	$^{+0.00021}_{-0.00021}$	$^{+0.00043}_{-0.00042}$	$^{+0.092}_{-0.089}$	$^{+0.0081}_{-0.0079}$	$^{+0.4}_{-0.4}$	
ATLAS_TES_TRUE_2012		$^{+0.0013}_{-0.0013}$	$^{+0.1}_{-0.1}$	$^{+0.015}_{-0.011}$	$^{+1.2}_{-0.1}$	
ATLAS_BTag_CEFF	$^{-0.00018}_{+0.00018}$	$^{-0.00035}_{+0.00036}$	$^{-0.065}_{+0.066}$	$^{-0.0062}_{+0.0063}$	$^{-0.28}_{+0.29}$	
ATLAS_TAU_ID_STAT_2012	$^{+0.00011}_{-0.00011}$	$^{+0.00027}_{-0.00027}$	$^{+0.055}_{-0.054}$	$^{+0.0049}_{-0.0048}$	$^{+0.24}_{-0.23}$	
ATLAS_TAU_FF_MODEL						$^{-0.16}_{+0.05}$
ATLAS_LUMI_2012	$^{+0.00024}_{-0.00024}$	$^{+0.0003}_{-0.0003}$	$^{+0.047}_{-0.047}$	$^{+0.0042}_{-0.0042}$	$^{+0.21}_{-0.21}$	
ATLAS_BR_tautau	$^{+0.00048}_{-0.00048}$	$^{+0.00062}_{-0.00061}$	$^{+0.095}_{-0.095}$	$^{+0.0085}_{-0.0085}$		
ATLAS_MU_SCALE_2012		$^{+0.00041}_{-0.00041}$				
pdf_Higgs_gg	$^{+0.00068}_{-0.00059}$					
QCDscale_ggH	$^{+0.00061}_{-0.00066}$					
QCDscale_ZH				$^{+0.0046}_{-0.0046}$		
ATLAS_VH_EWK			$^{+0.033}_{-0.033}$	$^{+0.003}_{-0.003}$		
ATLAS_EL_EFF_2012		$^{+0.00015}_{-0.00015}$	$^{+0.013}_{-0.013}$	$^{+0.0013}_{-0.0013}$	$^{+0.038}_{-0.038}$	
ATLAS_PU_RESCALE_2012	$^{+0.00019}_{-0.00005}$	$^{-0.00012}_{+0.00011}$				
QCDscale_qqH		$^{+0.00002}_{-0.00002}$				
QCDscale_WH			$^{+0.017}_{-0.017}$			
pdf_Higgs_qq		$^{+0.00032}_{-0.00032}$	$^{+0.05}_{-0.05}$	$^{+0.0045}_{-0.0045}$		
ATLAS_VH_UE			$^{+0.017}_{-0.017}$	$^{+0.0035}_{-0.0035}$		
QCDscale_VV					$^{+0.37}_{-0.37}$	
ATLAS_MU_EFF_2012	$^{+0.00015}_{-0.00015}$		$^{+0.019}_{-0.019}$	$^{+0.0014}_{-0.0014}$	$^{+0.11}_{-0.11}$	
pdf_qq					$^{+0.3}_{-0.3}$	
ATLAS_EL_RES_2012		$^{-0.00032}_{-0.00012}$			$^{+0.12}_{+0.12}$	
ATLAS_EL_SCALE_2012		$^{-0.00071}_{-0.00071}$		$^{-0.0015}_{-0.0009}$	$^{+0.46}_{+0.46}$	

Table 6.8: Yields and their uncertainties in the $W(\to \ell\nu)H(\to \tau_h\tau_h)$ signal region. The signal yields are shown for a Higgs mass of 125 GeV. The nuisance parameters are ordered by decreasing size of the post-fit impact on $\hat{\mu}$.

	$H \to \tau\tau$ Signals			Backgrounds		
	VBF	WH	ZH	ZZ	Others	Fakes
NOMINAL	0.00054	0.0008	1.143	7.28	0.198	17.1
STATISTICAL	±0.00054	±0.00046	±0.027	±0.16	±0.013	±1.5
ATLAS_TAU_FF_STAT						$^{+1.3}_{-1.2}$
ATLAS_TES_TRUE_2012			$^{+0.02}_{-0.03}$	$^{+0.36}_{-0.28}$	$^{+0.005}_{-0.005}$	
ATLAS_TAU_FF_MODEL						$^{-0.56}_{+0.28}$
QCDscale_VV				$^{+0.36}_{-0.36}$		
pdf_qq				$^{+0.29}_{-0.29}$		
ATLAS_LUMI_2012	$^{+0.00002}_{-0.00002}$	$^{+0.00002}_{-0.00002}$	$^{+0.032}_{-0.032}$	$^{+0.2}_{-0.2}$	$^{+0.0056}_{-0.0056}$	
ATLAS_TAU_ID_2012	$^{+0.00002}_{-0.00002}$		$^{+0.032}_{-0.032}$	$^{+0.19}_{-0.19}$	$^{+0.0055}_{-0.0055}$	
ATLAS_EL_EFF_2012	$^{+0.00003}_{-0.00003}$	$^{+0.00002}_{-0.00002}$	$^{+0.024}_{-0.023}$	$^{+0.16}_{-0.16}$	$^{+0.0038}_{-0.0038}$	
ATLAS_TAU_ID_STAT_2012	$^{+0.00001}_{-0.00001}$		$^{+0.02}_{-0.02}$	$^{+0.12}_{-0.12}$	$^{+0.0033}_{-0.0033}$	
ATLAS_BR_tautau	$^{+0.00003}_{-0.00003}$	$^{+0.00005}_{-0.00005}$	$^{+0.065}_{-0.065}$			
ATLAS_MU_EFF_2012		$^{+0.00001}_{-0.00001}$	$^{+0.012}_{-0.012}$	$^{+0.069}_{-0.069}$	$^{+0.0022}_{-0.0022}$	
ATLAS_VH_UE			$^{+0.045}_{-0.045}$			
QCDscale_ZH			$^{+0.035}_{-0.035}$			
pdf_Higgs_qq	$^{+0.00002}_{-0.00002}$	$^{+0.00002}_{-0.00002}$	$^{+0.034}_{-0.034}$			
ATLAS_VH_EWK		$^{+0.00002}_{-0.00002}$	$^{+0.023}_{-0.023}$			
ATLAS_EL_SCALE_2012			$^{+0.011}_{+0.004}$	$^{+0.06}_{-0.06}$		
QCDscale_qqH	$^{+0.0000011}_{-0.0000011}$					
QCDscale_WH		$^{+0.000008}_{-0.000008}$				
ATLAS_PU_RESCALE_2012	$^{+0.0000077}_{-0.0000077}$	$^{+0.00002}_{-0.00002}$			$^{+0.0021}_{-0.0022}$	
ATLAS_EL_RES_2012					$^{-0.0024}_{+0.0001}$	
ATLAS_MU_SCALE_2012					$^{-0.0023}_{-0.0029}$	

Table 6.9: Yields and their uncertainties in the $Z(\to \ell\ell)H(\to \tau_\ell\tau_h)$ signal region. The signal yields are shown for a Higgs mass of 125 GeV. The nuisance parameters are ordered by decreasing size of the post-fit impact on $\hat{\mu}$.

	$H \to \tau\tau$ Signal	Backgrounds		
	ZH	ZZ	Others	Fakes
NOMINAL	0.64	2.09	0.0123	4.7
STATISTICAL	±0.02	±0.089	±0.0031	±1.2
ATLAS_TES_TRUE_2012	$^{+0.03}_{-0.03}$	$^{+0.2}_{-0.2}$		$^{-0.024}_{+0.018}$
ATLAS_TAU_ID_2012	$^{+0.036}_{-0.035}$	$^{+0.11}_{-0.11}$	$^{+0.00074}_{-0.00072}$	
ATLAS_BR_tautau	$^{+0.036}_{-0.036}$			
ATLAS_TAU_ID_STAT_2012	$^{+0.022}_{-0.021}$	$^{+0.067}_{-0.066}$	$^{+0.00046}_{-0.00045}$	
ATLAS_LUMI_2012	$^{+0.018}_{-0.018}$	$^{+0.059}_{-0.059}$	$^{+0.00035}_{-0.00035}$	
QCDscale_ZH	$^{+0.02}_{-0.02}$			
pdf_Higgs_qq	$^{+0.019}_{-0.019}$			
ATLAS_TAU_FF_MODEL				$^{+0.28}_{-0.14}$
ATLAS_TAU_FF_STAT				$^{-0.24}_{+0.12}$
ATLAS_VH_UE	$^{+0.014}_{-0.014}$			
ATLAS_VH_EWK	$^{+0.013}_{-0.013}$			
ATLAS_PU_RESCALE_2012	$^{+0.0026}_{-0.0036}$		$^{-0.00031}_{+0.00047}$	
pdf_qq		$^{+0.084}_{-0.084}$		
QCDscale_WH				
ATLAS_MU_SCALE_2012			$^{-0.000081}_{+0.00081}$	
QCDscale_VV		$^{+0.1}_{-0.1}$		
ATLAS_MU_EFF_2012	$^{+0.0048}_{-0.0048}$	$^{+0.014}_{-0.014}$	$^{+0.00007}_{-0.00007}$	
ATLAS_EL_RES_2012				
ATLAS_EL_EFF_2012	$^{+0.0077}_{-0.0077}$	$^{+0.027}_{-0.027}$	$^{+0.00023}_{-0.00022}$	
ATLAS_EL_SCALE_2012	$^{+0.0074}_{+0.0061}$	$^{+0.012}_{+0.014}$		

Table 6.10: Yields and their uncertainties in the $Z(\to \ell\ell)H(\to \tau_h\tau_h)$ signal region. The signal yields are shown for a Higgs mass of 125 GeV. The nuisance parameters are ordered by decreasing size of the post-fit impact on $\hat{\mu}$.

6.7.7 Fit Model Validation

A number of tests have been performed to test the stability of the likelihood fit and the robustness of the background modelling. Some of these tests were performed before the analysis was unblinded, the results of these tests provided grounds for confidence in the method before the approval was given to unblind. These tests were also performed on the unblinded data as a final check.

The reliability of the background modelling and understanding of the systematic uncertainties can be tested by examining the post-fit values of the nuisance parameters. It is common practice to compute the *pull* of a nuisance parameter to test the agreement between the post-fit ($\hat{\theta}$) value and the pre-fit (central) value (θ_0) compared to the size of the uncertainty ($\Delta\theta$).

$$\text{pull} = \frac{\hat{\theta} - \theta_0}{\Delta\theta} \tag{6.65}$$

One requirement of the test for good background and systematic modelling is for the nuisance parameter pulls to be consistent with zero. Large outliers can indicate under-estimation of the size of the systematic uncertainties as well as over- or under-estimation of the expected background.

The second test checks the influence of each nuisance parameter on the fitted signal strength. The fit is repeated for each nuisance parameter with its value fixed to its $\pm 1\sigma$ variations, the change in the fitted signal strength is the post-fit impact $\Delta\hat{\mu}$.

The nuisance parameter pulls and their impact on the fitted signal strength are shown for each channel: $W(\to \ell\nu)H(\to \tau_\ell\tau_h)$ in Figure 6.6, $W(\to \ell\nu)H(\to \tau_h\tau_h)$ in Figure 6.7, $Z(\to \ell\ell)H(\to \tau_\ell\tau_h)$ in Figure 6.8, $Z(\to \ell\ell)H(\to \tau_h\tau_h)$ in Figure 6.9, as well as the combination of all $VH(\to \tau\tau)$ channels in Figure 6.10.

A few nuisance parameters in some channels show asymmetric behaviour on the post-fit impact on the fitted signal strength. It is important to understand the source of this behaviour, especially for nuisance parameters which have a large impact. In the $W(\to \ell\nu)H(\to \tau_h\tau_h)$ channel the highest ranked nuisance parameter, the statistical uncertainty on the measured tau fake factor (`ATLAS_TAU_FF_STAT`), shows a larger impact for the -1σ deviation than for the $+1\sigma$ deviation. Likewise in the $Z(\to \ell\ell)H(\to \tau_\ell\tau_h)$ channel, the quark- vs. gluon-initiated jet composition uncertainty on the measured tau fake factor (`ATLAS_TAU_FF_MODEL`) has a larger impact for the $+1\sigma$ deviation than
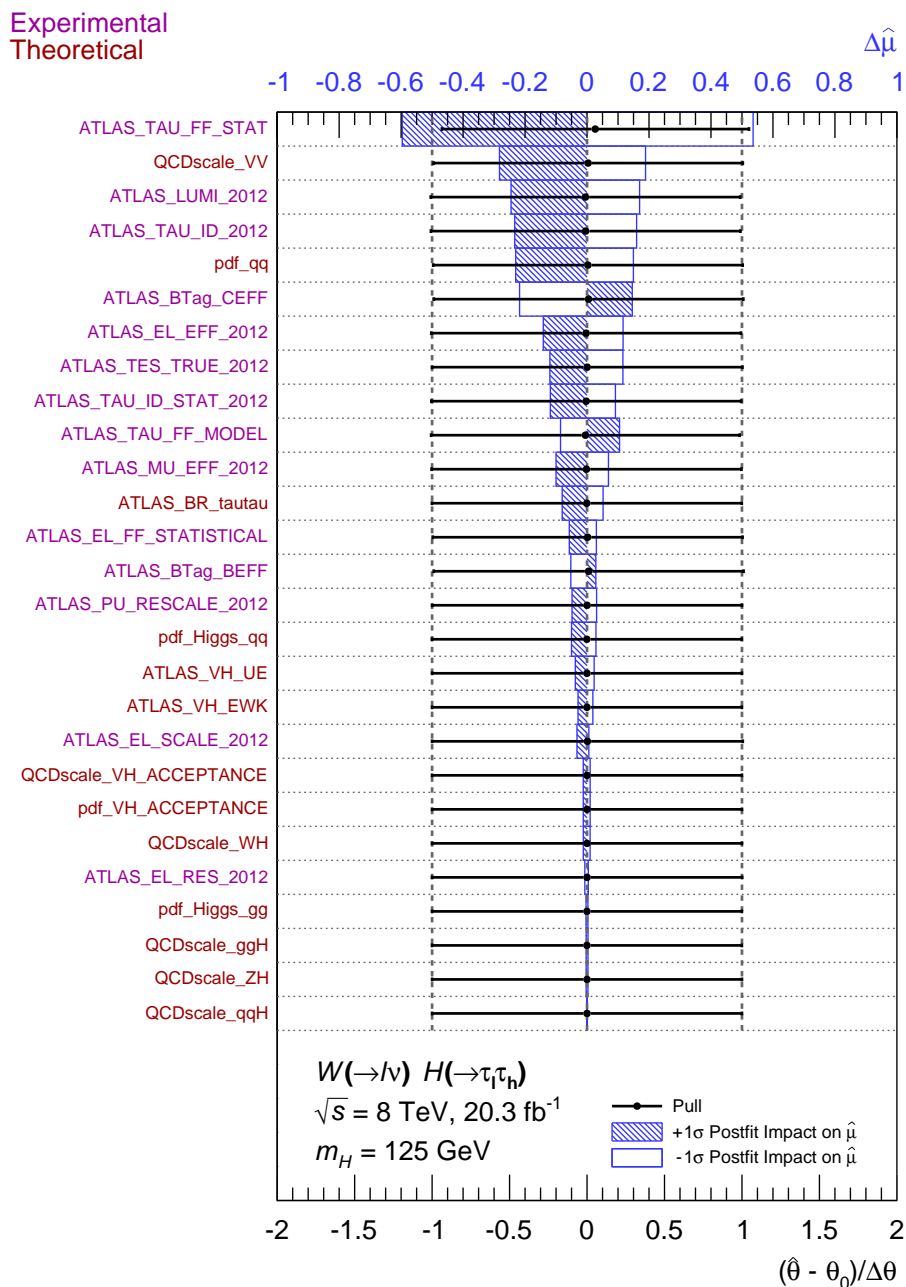
Figure 6.6: Nuisance parameter check for the $W(\rightarrow \ell\nu)H(\rightarrow \tau_\ell\tau_h)$ category. The black marker shows the fitted value $\hat{\theta}$ of each nuisance parameter which maximises the likelihood ratio, to be compared to the nominal value θ_0 relative to the width of the $\pm 1\sigma$ variations indicated by the error bars. The blue band shows the impact of uncertainties on the fitted signal-strength parameter $\hat{\mu}$. These are the variations of $\hat{\mu}$ when fixing the corresponding individual nuisance parameter to its post-fit value modified upwards (hatched) or downwards (open) by its post-fit uncertainty, and repeating the fit. The nuisance parameters are ordered by decreasing size of the post-fit impact on $\hat{\mu}$.

Figure 6.7: Nuisance parameter check for the $W(\to \ell\nu)H(\to \tau_h\tau_h)$ category. The black marker shows the fitted value $\hat{\theta}$ of each nuisance parameter which maximises the likelihood ratio, to be compared to the nominal value θ_0 relative to the width of the $\pm 1\sigma$ variations indicated by the error bars. The blue band shows the impact of uncertainties on the fitted signal-strength parameter $\hat{\mu}$. These are the variations of $\hat{\mu}$ when fixing the corresponding individual nuisance parameter to its post-fit value modified upwards (hatched) or downwards (open) by its post-fit uncertainty, and repeating the fit. The nuisance parameters are ordered by decreasing size of the post-fit impact on $\hat{\mu}$.

Figure 6.8: Nuisance parameter check for the $Z(\to \ell\ell)H(\to \tau_\ell\tau_h)$ category. The black marker shows the fitted value $\hat{\theta}$ of each nuisance parameter which maximises the likelihood ratio, to be compared to the nominal value θ_0 relative to the width of the $\pm 1\sigma$ variations indicated by the error bars. The blue band shows the impact of uncertainties on the fitted signal-strength parameter $\hat{\mu}$. These are the variations of $\hat{\mu}$ when fixing the corresponding individual nuisance parameter to its post-fit value modified upwards (hatched) or downwards (open) by its post-fit uncertainty, and repeating the fit. The nuisance parameters are ordered by decreasing size of the post-fit impact on $\hat{\mu}$.

Figure 6.9: Nuisance parameter check for the $Z(\to \ell\ell)H(\to \tau_h\tau_h)$ category. The black marker shows the fitted value $\hat{\theta}$ of each nuisance parameter which maximises the likelihood ratio, to be compared to the nominal value θ_0 relative to the width of the $\pm 1\sigma$ variations indicated by the error bars. The blue band shows the impact of uncertainties on the fitted signal-strength parameter $\hat{\mu}$. These are the variations of $\hat{\mu}$ when fixing the corresponding individual nuisance parameter to its post-fit value modified upwards (hatched) or downwards (open) by its post-fit uncertainty, and repeating the fit. The nuisance parameters are ordered by decreasing size of the post-fit impact on $\hat{\mu}$.

Figure 6.10: Nuisance parameter check for the combination of all $VH(\to \tau\tau)$ analysis categories. The black marker shows the fitted value $\hat{\theta}$ of each nuisance parameter which maximises the likelihood ratio, to be compared to the nominal value θ_0 relative to the width of the $\pm 1\sigma$ variations indicated by the error bars. The blue band shows the impact of uncertainties on the fitted signal-strength parameter $\hat{\mu}$. These are the variations of $\hat{\mu}$ when fixing the corresponding individual nuisance parameter to its post-fit value modified upwards (hatched) or downwards (open) by its post-fit uncertainty, and repeating the fit. The nuisance parameters are ordered by decreasing size of the post-fit impact on $\hat{\mu}$.

the -1σ deviation. In both of these cases the asymmetry is due to the construction of the systematic uncertainty. The `ATLAS_TAU_FF_MODEL` nuisance parameter itself is asymmetric, due to the change in composition of the quark- vs. gluon-initiated jet fakes, shown in Table 6.5. The `ATLAS_TAU_FF_STAT` nuisance parameter itself is symmetric, however in the $\tau_h\tau_h$ channels the background is composed of a mixture of events with either one or two fake hadronic taus. Background events with one fake tau will receive a weight of f_τ, events with two fake taus will receive a weight of $-f_\tau^2$. Due to the construction of the FF model, the background event yield is then proportional to $f_\tau N_A - f_\tau^2 N_{AA}$, this will be asymmetric under the substitution $f_\tau \to f_\tau \pm \Delta f_\tau$. The result of this is that in both cases, the overall up/down event yields will be asymmetric compared to the nominal. The sizes of the $\pm 1\sigma$ deviations are asymmetric, which manifests in the post-fit impact distributions for these nuisance parameters.

All nuisance parameters have pulls consistent with zero, indicating that the fit is converging around the nominal value of each nuisance parameter in each channel. This provides confidence in the fitting procedure and the background modelling.

6.8 Search Results

The results for each channel are produced from events selected with the optimised reconstruction and categorisation procedure described in Section 4.3 with additional requirements, optimised for each channel individually, as described in: Section 6.2 for the $W(\to \ell\nu)H(\to \tau_\ell\tau_h)$ channel, Section 6.3 for the $W(\to \ell\nu)H(\to \tau_h\tau_h)$ channel, Section 6.4 for the $Z(\to \ell\ell)H(\to \tau_\ell\tau_h)$ channel, and Section 6.5 for the $Z(\to \ell\ell)H(\to \tau_h\tau_h)$ channel. The backgrounds are estimated using the FF method described in Chapter 5, developed for this analysis to adequately model the fake and non-prompt lepton backgrounds. The fit is performed on the sensitive mass distributions (Section 6.1) for each channel. The results of this analysis are presented in the form of an exclusion limit (Section 6.7.2) and statistical significance (Section 6.7.3) for each channel separately, and for the combination of all channels using the fitting procedure described in Section 6.7.6. The fit is performed separately for signal MC samples with hypothesis Higgs mass values in the range between 100 GeV and 150 GeV in 5 GeV increments.

The results for the $W(\to \ell\nu)H(\to \tau_\ell\tau_h)$ channel are shown in Figure 6.11. The expected limit (Figure 6.11a) represents the 95% confidence level upper limit on the signal cross-section (normalised to the SM prediction) in the absence of a signal. This can
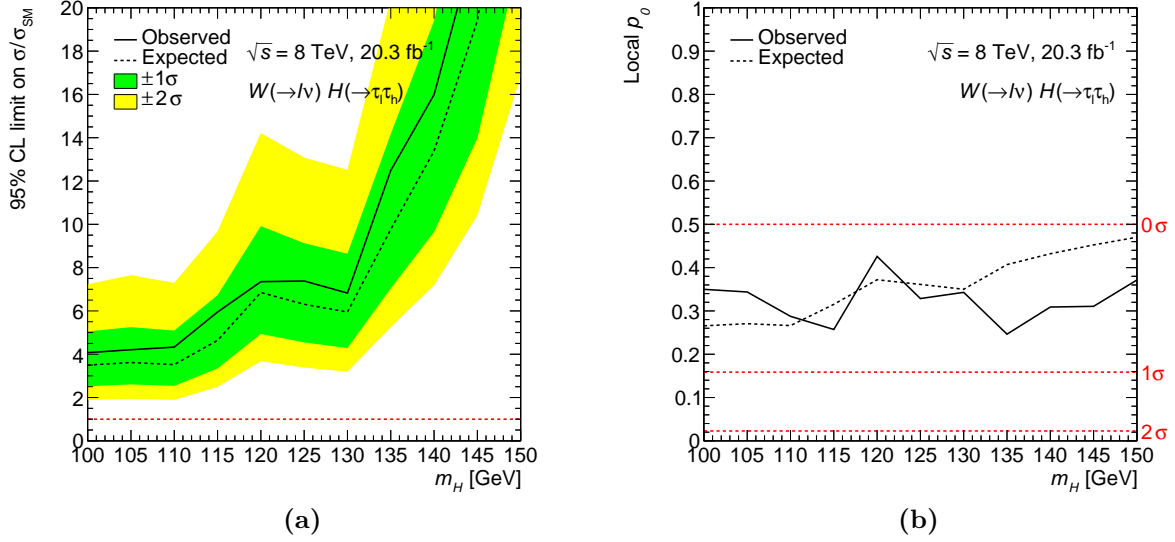
Figure 6.11: Expected and observed results in the $W(\to \ell\nu)H(\to \tau_\ell\tau_h)$ category as a function of the Higgs boson mass hypothesis. (a) shows the 95% confidence level upper limits, normalised to the SM Higgs boson production cross-section. The green and yellow bands represent the 1σ and 2σ ranges of the expectation in the absence of a signal. (b) shows the signal significance.

be used as an indication of the sensitivity of the channel. Smaller expected limits indicate higher sensitivity to the signal, with values below unity (the dashed red line) indicating a level of sensitivity comparable to the SM prediction. The uncertainties on the expectation represent the variation in the limit due to the statistical and systematic uncertainties on the background modelling. The expected signal significance (Figure 6.11b) represents the size of the nominal signal compared to the size of the total uncertainty on the background modelling. Due to the good agreement between data and prediction in Figure 6.2, the observed limit tracks the expected limit behaviour within 1σ across the full Higgs mass range tested. At the $120\,\text{GeV}$ mass point there is an upward spike in the limit. The signal MC samples generated at this mass point contain a smaller number of events than all other mass points in this channel. This causes the signal $M_{2\text{T}}$ mass distribution to contain larger relative statistical uncertainties, resulting in lower sensitivity.

The results for the $W(\to \ell\nu)H(\to \tau_h\tau_h)$ channel are shown in Figure 6.12. In this channel there is a fluctuation in the results at the $115\,\text{GeV}$ Higgs mass point. This is also due to reduced MC signal sample size generated at this mass point. No deviation larger than 1σ is found between the observed and expected limits.
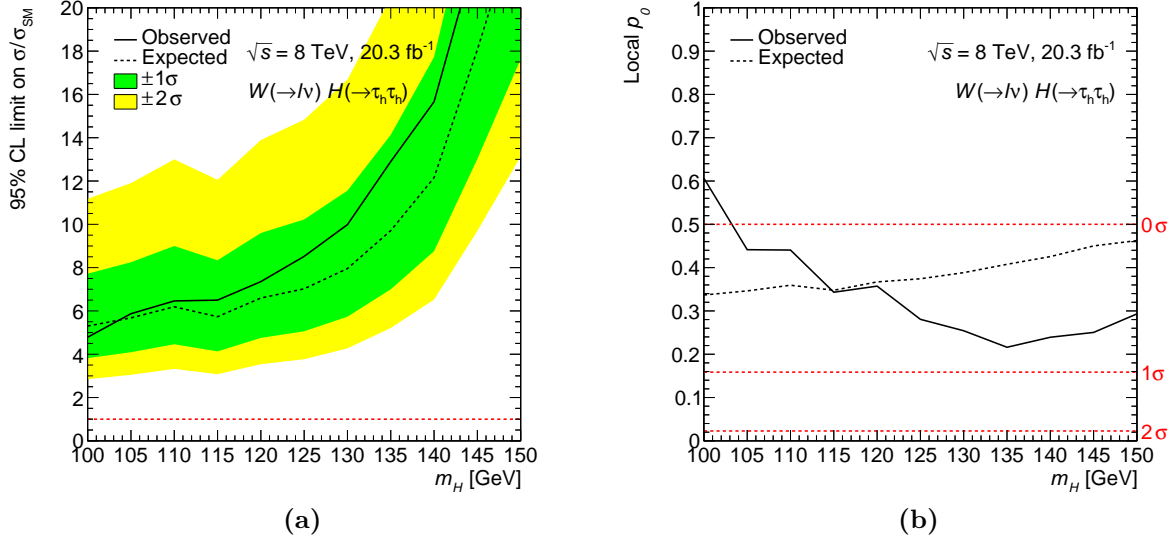
Figure 6.12: Expected and observed results in the $W(\to \ell\nu)H(\to \tau_h\tau_h)$ category as a function of the Higgs boson mass hypothesis. (a) shows the 95% confidence level upper limits, normalised to the SM Higgs boson production cross-section. The green and yellow bands represent the 1σ and 2σ ranges of the expectation in the absence of a signal. (b) shows the signal significance.

The results for the $Z(\to \ell\ell)H(\to \tau_\ell\tau_h)$ channel are shown in Figure 6.13. Again, no deviation larger than 1σ is found between the observed and expected limits.

The results for the $Z(\to \ell\ell)H(\to \tau_h\tau_h)$ channel are shown in Figure 6.14. The spike in the limit at the 115 GeV mass point is again due to the limited MC sample size used. In general, the observed results are 1σ larger than expected, this is due to the excess of observed events in the $100 - 150$ GeV bin in Figure 6.5 which is sensitive to signal events in the full mass range.

The fit is performed on all channels simultaneously to produce the final combined result of the analysis. The observed result tracks the $+1\sigma$ expectation due to the observed excess of events in signal sensitive bins of the mass distributions in some channels. In general the sensitivity decreases at higher masses, this is due to the decrease in the $H \to \tau\tau$ branching fraction as shown in Figure 2.15. Since the Higgs boson has been discovered in other channels, of particular interest is the result at the 125 GeV Higgs mass point. The results of the exclusion limit at this mass point are shown in Figure 6.16 which also includes the breakdown of results for the different channels. The signal significance results for each channel and the combination are shown in Table 6.11. The fitted value of the signal strength parameter $\hat{\mu}$ is also determined for each channel and
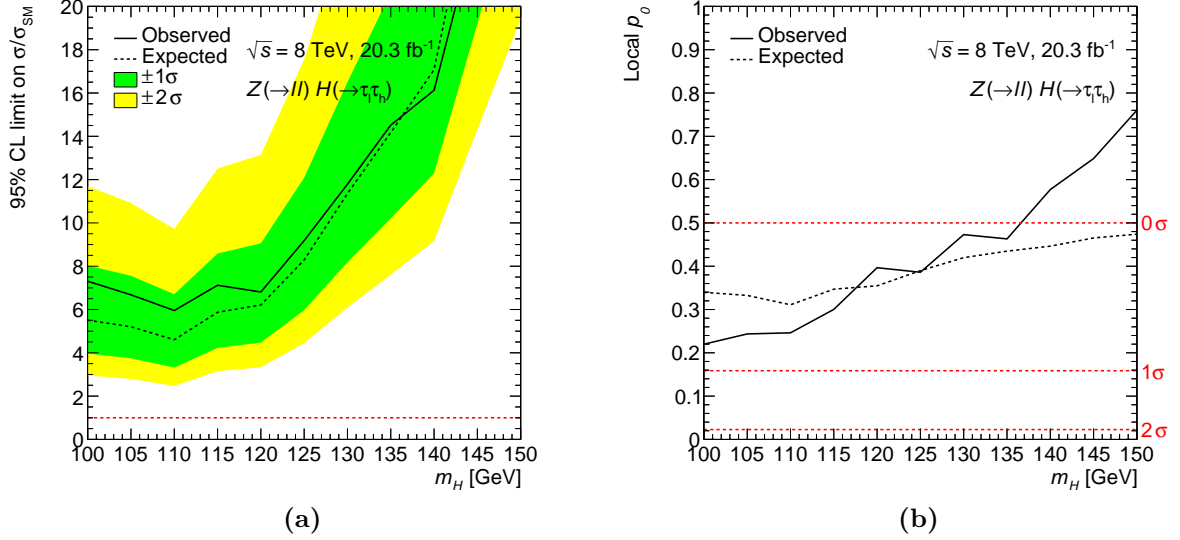
Figure 6.13: Expected and observed results in the $Z(\to \ell\ell)H(\to \tau_\ell\tau_h)$ category as a function of the Higgs boson mass hypothesis. (a) shows the 95% confidence level upper limits, normalised to the SM Higgs boson production cross-section. The green and yellow bands represent the 1σ and 2σ ranges of the expectation in the absence of a signal. (b) shows the signal significance.
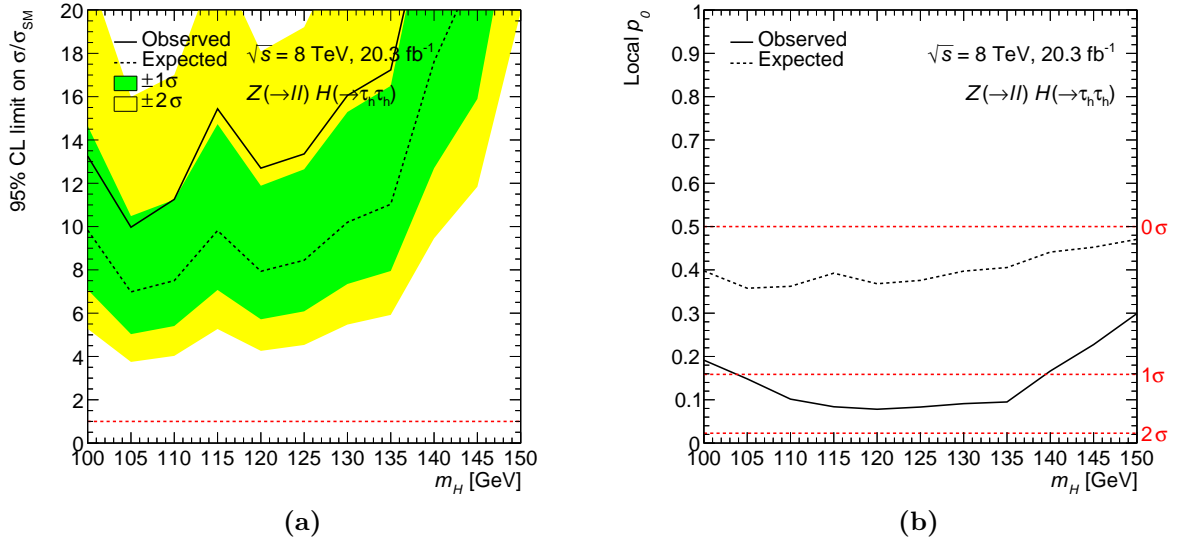
Figure 6.14: Expected and observed results in the $Z(\to \ell\ell)H(\to \tau_h\tau_h)$ category as a function of the Higgs boson mass hypothesis. (a) shows the 95% confidence level upper limits, normalised to the SM Higgs boson production cross-section. The green and yellow bands represent the 1σ and 2σ ranges of the expectation in the absence of a signal. (b) shows the signal significance.
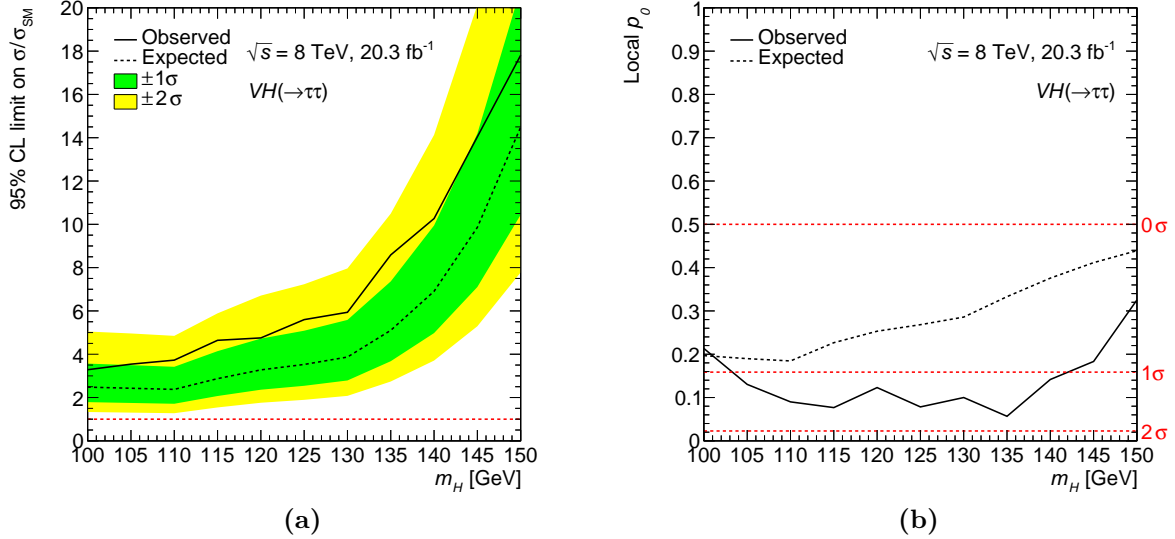
Figure 6.15: Expected and observed results for the combination of all analysis categories as a function of the Higgs boson mass hypothesis. (a) shows the 95% confidence level upper limits, normalised to the SM Higgs boson production cross-section. The green and yellow bands represent the 1σ and 2σ ranges of the expectation in the absence of a signal. (b) shows the signal significance.

for the combination of all channels, shown in Figure 6.17. The combined result of $\hat{\mu} = 2.3 \pm 1.6$ is consistent with the signal-plus-background hypothesis of $\mu = 1$ within 1σ, and the background-only hypothesis of $\mu = 0$ within 2σ. The $W(\to \ell\nu)H(\to \tau_\ell\tau_h)$, $W(\to \ell\nu)H(\to \tau_h\tau_h)$, and $Z(\to \ell\ell)H(\to \tau_\ell\tau_h)$ channels are each consistent with both hypotheses within 1σ. The excess of events in the $100 - 150$ GeV bin in Figure 6.5 results in a larger fitted signal strength in the $Z(\to \ell\ell)H(\to \tau_h\tau_h)$ channel.

Due to the higher cross-section of the WH process compared to the ZH process, the WH channels generally contain larger signal yields leading to higher sensitivities in these channels. The ZH channels however are aided by the additional light lepton in the events, these selection criteria increase the signal-to-background ratio to the point where the sensitivities are comparable to the WH channels. Although the sensitivity of the combined result does not reach a level comparable to the expected signal size, the results are consistent with the SM prediction.
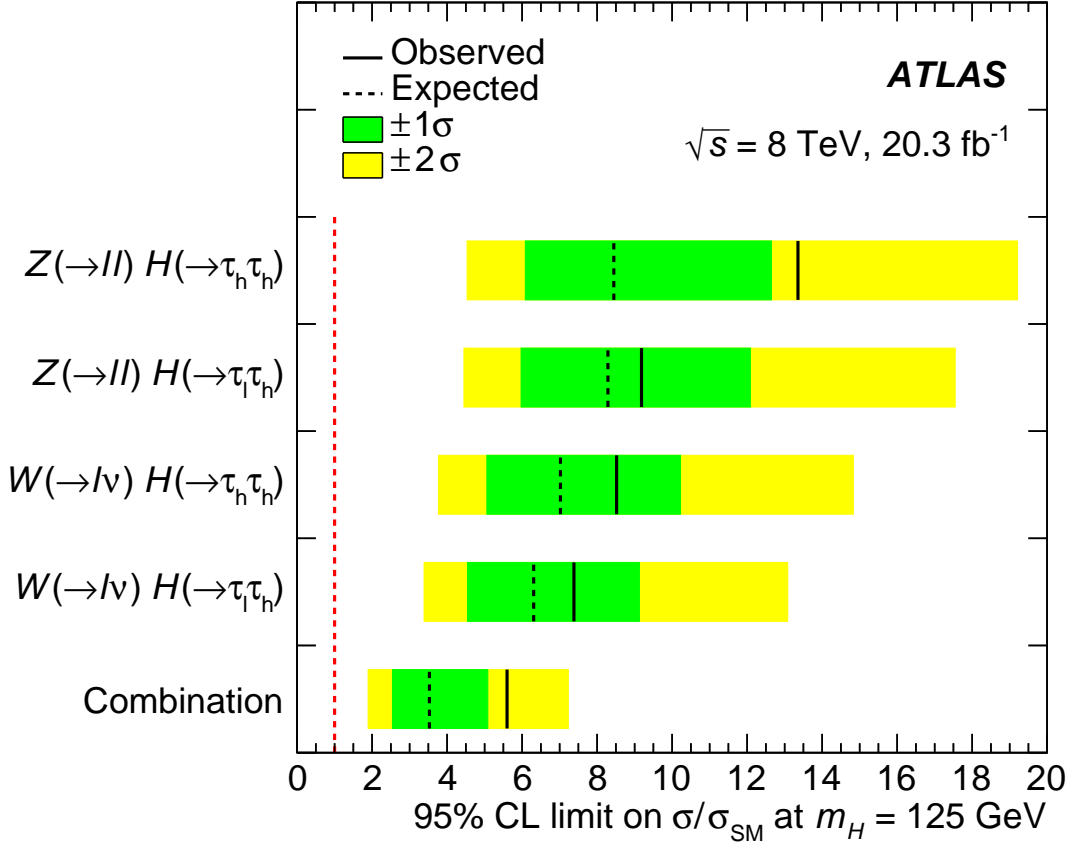
Figure 6.16: Expected and observed 95% confidence level upper limit for each channel and the combination for a Higgs mass hypothesis of 125 GeV. The green and yellow bands represent the 1σ and 2σ ranges of the expectation in the absence of a signal.

Channel	Expected Significance	Observed Significance
$W(\to \ell\nu)H(\to \tau_\ell\tau_h)$	0.36σ	0.44σ
$W(\to \ell\nu)H(\to \tau_h\tau_h)$	0.32σ	0.58σ
$Z(\to \ell\ell)H(\to \tau_\ell\tau_h)$	0.28σ	0.29σ
$Z(\to \ell\ell)H(\to \tau_h\tau_h)$	0.32σ	1.38σ
Combination	0.62σ	1.42σ

Table 6.11: Expected and observed signal significances for each channel and the combination for a Higgs mass hypothesis of 125 GeV.
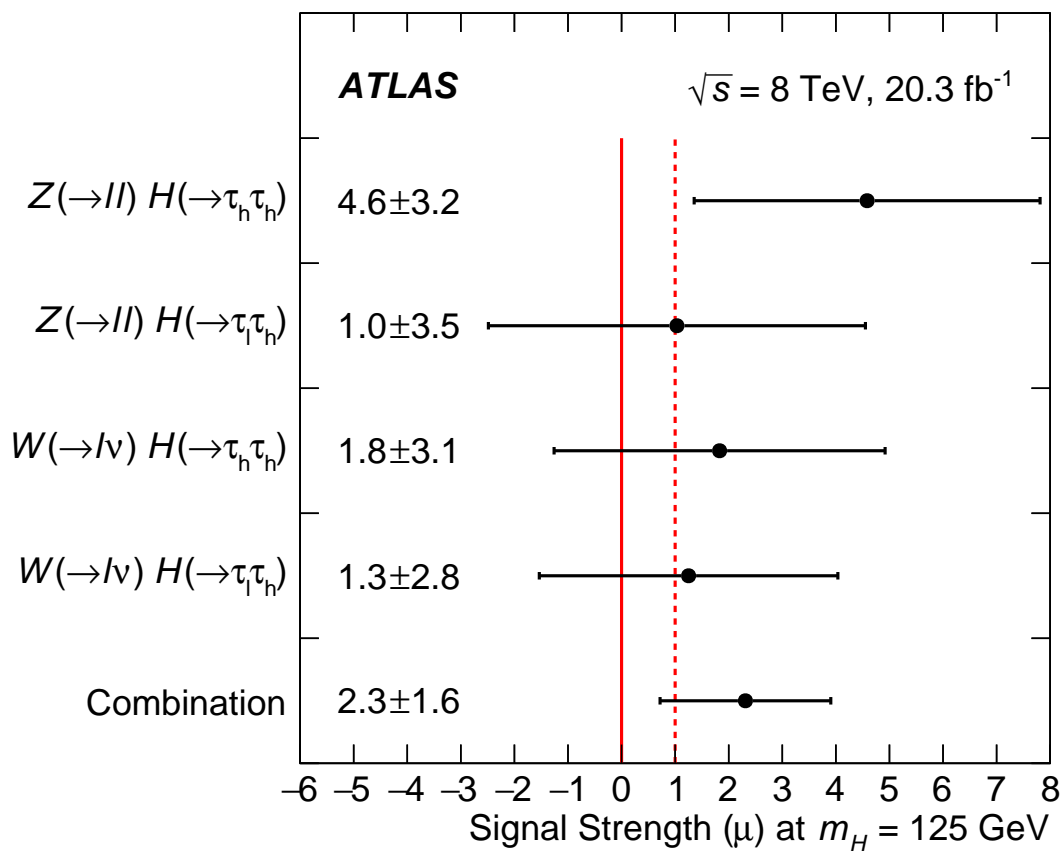
Figure 6.17: Best fit value of the signal strength $\hat{\mu}$ for each channel and the combination with a Higgs mass hypothesis of 125 GeV. The solid red line represents the background-only hypothesis. The dashed red line represents the nominal signal-plus-background hypothesis predicted by the SM.

Chapter 7

Conclusions

Run 1 of the LHC has proved to be incredibly successful. Most notable is the discovery of the Higgs boson, by the ATLAS and CMS experiments in 2012, which confirms the existence of the Higgs mechanism. Subsequent analysis of the properties of the Higgs boson have strengthened the confidence that this particle is indeed the SM Higgs boson. Of interest still is Higgs boson decays to fermionic final states, in particular the $H \rightarrow \tau\tau$ decay mode provides one of the most promising opportunities to provide such evidence. The analysis of the $H \rightarrow \tau\tau$ decay channel in the VBF and ggF production modes provides strong evidence for the existence of fermionic couplings, however additional studies are needed in the other production modes to potentially increase sensitivity.

This thesis presents the first dedicated search, with the ATLAS detector, for the associated production of the SM Higgs boson with a vector boson where the Higgs boson decays to a pair of tau leptons. The analysis is performed on $20.3\,\mathrm{fb}^{-1}$ of proton-proton collisions recorded in 2012 at $\sqrt{s} = 8\,\mathrm{TeV}$ centre-of-mass energy. No significant excess of events is observed. For a Higgs boson mass of $m_H = 125\,\mathrm{GeV}$, the 95% confidence level upper limit on the observed cross-section is 5.6 times the SM prediction. The measured signal strength, normalized to the SM expectation, is $\hat{\mu} = 2.3 \pm 1.6$. This excess corresponds to a 1.4σ upward fluctuation of the background-only expectation but is consistent with the SM expectation.

These results are made possible by the development of a data-driven background estimation method. The FF method provides a robust background estimation across all channels simultaneously. It provides a more reliable background estimate than pure MC as it combines the MC estimate of the irreducible backgrounds with a data-driven estimate of the fake and non-prompt backgrounds. This data-driven component is able to account for the different types of fake and non-prompt reconstructed particles as the

measurements of the fake rates are performed in regions suitably similar to the analysis signal regions.

The LHC started Run 2 in 2015, colliding proton beams at an unprecedented $\sqrt{s} = 13\,\mathrm{GeV}$ centre-of-mass energy and is expected to deliver hundreds of fb^{-1} of integrated luminosity in the coming years. As the dominant uncertainty in each of the VH channels is due to statistical limitations, the larger dataset expected in Run 2 will allow future continuations of this search to potentially reach higher sensitivity. In addition, the background estimation method presented here, which relies on a data-driven estimate of the reducible backgrounds, may be particularly suited to Run 2 conditions due to its flexibility in handling different compositions of fake and non-prompt lepton backgrounds.

Bibliography

[1] ATLAS Collaboration, "Search for the standard model Higgs boson produced in association with a vector boson and decaying into a tau pair in pp collisions at $\sqrt{s} = 8$ TeV with the ATLAS detector," *Phys. Rev. D* **93** (May, 2016) 092005, `arXiv:1511.08352 [hep-ex]`. Cited on page iv.

[2] ATLAS Collaboration, "Observation of a new particle in the search for the Standard Model Higgs boson with the ATLAS detector at the LHC," *Phys. Lett. B* **716** no. 1, (2012) 1 – 29. Cited on pages 1, 21, 23, 24, and 164.

[3] CMS Collaboration, "Observation of a new boson at a mass of 125 GeV with the CMS experiment at the LHC," *Phys. Lett. B* **716** no. 1, (2012) 30 – 61. Cited on pages 1 and 21.

[4] ATLAS Collaboration, "Measurements of the Higgs boson production and decay rates and coupling strengths using pp collision data at $\sqrt{s} = 7$ and 8 TeV in the ATLAS experiment," 2015. ATLAS-CONF-2015-007. Cited on pages 1, 24, 25, 26, 27, and 164.

[5] ATLAS Collaboration, "Evidence for the spin-0 nature of the Higgs boson using ATLAS data," *Phys.Lett.* **B726** (2013) 120–144, `arXiv:1307.1432 [hep-ex]`. Cited on pages 1 and 25.

[6] ATLAS Collaboration, "Evidence for the Higgs-boson Yukawa coupling to tau leptons with the ATLAS detector," `arXiv:1501.04943 [hep-ex]`. Cited on pages 2, 27, 29, 72, 107, and 165.

[7] Particle Data Group Collaboration, "Review of Particle Physics," *Chin. Phys.* **C38** (2014) 090001. Cited on pages 5, 52, 63, 64, and 172.

[8] E. Noether, "Invariante variationsprobleme," *Nachr. D. König. Gesellsch. D. Wiss. Zu Göttingen, Math-phys. Klasse* (1918) 235 257. Cited on page 6.

[9] D. J. Gross and F. Wilczek, "Ultraviolet behavior of non-abelian gauge theories," *Phys. Rev. Lett.* **30** (Jun, 1973) 1343–1346. Cited on page 9.

[10] H. D. Politzer, "Reliable perturbative results for strong interactions?," *Phys. Rev. Lett.* **30** (Jun, 1973) 1346–1349. Cited on page 9.

[11] S. L. Glashow, "Partial Symmetries of Weak Interactions," *Nucl. Phys.* **22** (1961) 579–588. Cited on page 12.

[12] S. Weinberg, "A Model of Leptons," *Phys. Rev. Lett.* **19** (1967) 1264–1266. Cited on page 12.

[13] A. Salam and J. Ward, "Electromagnetic and weak interactions," *Physics Letters* **13** no. 2, (1964) 168 – 171. Cited on page 12.

[14] F. Englert and R. Brout, "Broken Symmetry and the Mass of Gauge Vector Mesons," *Phys. Rev. Lett.* **13** (Aug, 1964) 321 – 323. Cited on page 13.

[15] P. W. Higgs, "Broken symmetries, massless particles and gauge fields," *Physics Letters* **12** no. 2, (1964) 132 – 133. Cited on page 13.

[16] P. W. Higgs, "Broken Symmetries and the Masses of Gauge Bosons," *Phys. Rev. Lett.* **13** (Oct, 1964) 508 – 509. Cited on page 13.

[17] G. S. Guralnik and C. R. Hagen and T. W. B. Kibble, "Global Conservation Laws and Massless Particles," *Phys. Rev. Lett.* **13** (Nov, 1964) 585 – 587. Cited on page 13.

[18] P. W. Higgs, "Spontaneous Symmetry Breakdown without Massless Bosons," *Phys. Rev.* **145** (May, 1966) 1156 – 1163. Cited on page 13.

[19] T. W. B. Kibble, "Symmetry Breaking in Non-Abelian Gauge Theories," *Phys. Rev.* **155** (Mar, 1967) 1554 – 1561. Cited on page 13.

[20] LHC Higgs Cross Section Working Group Collaboration, S. Heinemeyer *et al.*, "Handbook of LHC Higgs Cross Sections: 3. Higgs Properties," `arXiv:1307.1347 [hep-ph]`. Cited on pages 18, 22, 30, 32, 121, 123, 163, 165, and 172.

[21] LEP Working Group for Higgs boson searches, ALEPH Collaboration, DELPHI Collaboration, L3 Collaboration, OPAL Collaboration Collaboration, R. Barate *et al.*, "Search for the standard model Higgs boson at LEP," *Phys. Lett. B* **B565** (2003) 61–75, `arXiv:hep-ex/0306033 [hep-ex]`. Cited on pages 19 and 163.

[22] CDF Collaboration, "The CDF Detector: An Overview," *Nucl.Instrum.Meth.* **A271** (1988) 387–403. Cited on page 19.

[23] D0 Collaboration, "The D0 Detector," *Nucl.Instrum.Meth.* **A338** (1994) 185–253. Cited on page 19.

[24] Tevatron New Physics Higgs Working Group, CDF Collaboration, D0 Collaboration Collaboration, "Updated Combination of CDF and D0 Searches for Standard Model Higgs Boson Production with up to 10.0 fb^{-1} of Data," `arXiv:1207.0449 [hep-ex]`. Cited on pages 21 and 163.

[25] ATLAS Collaboration, "Measurement of Higgs boson production in the diphoton decay channel in pp collisions at center-of-mass energies of 7 and 8 TeV with the ATLAS detector," *Phys.Rev.* **D90** no. 11, (2014) 112015, `arXiv:1408.7084 [hep-ex]`. Cited on page 23.

[26] ATLAS Collaboration, "Measurements of Higgs boson production and couplings in the four-lepton channel in pp collisions at center-of-mass energies of 7 and 8 TeV with the ATLAS detector," *Phys.Rev.* **D91** no. 1, (2015) 012006, `arXiv:1408.5191 [hep-ex]`. Cited on page 23.

[27] ATLAS Collaboration, "Observation and measurement of Higgs boson decays to WW^* with the ATLAS detector," `arXiv:1412.2641 [hep-ex]`. Cited on page 23.

[28] ATLAS, CMS Collaboration, "Combined Measurement of the Higgs Boson Mass in pp Collisions at $\sqrt{s} = 7$ and 8 TeV with the ATLAS and CMS Experiments," `arXiv:1503.07589 [hep-ex]`. Cited on pages 23, 24, 25, and 164.

[29] L. Landau, "On the angular momentum of a two-photon system," *Dokl.Akad.Nauk Ser.Fiz.* **60** (1948) 207–209. Cited on page 25.

[30] C. N. Yang, "Selection Rules for the Dematerialization of a Particle into Two Photons," *Phys. Rev.* **77** (Jan, 1950) 242–245. Cited on page 25.

[31] CMS Collaboration, "Search for the standard model Higgs boson decaying to tau pairs produced in association with a W or Z boson," 2013. CMS-PAS-HIG-12-053. Cited on page 28.

[32] ATLAS Collaboration, "The ATLAS Experiment at the CERN Large Hadron Collider," *JINST* **3** (2008) S08003. Cited on pages 33 and 36.

[33] CMS Collaboration, "The CMS experiment at the CERN LHC," *JINST* **3** (2008)

S08004. Cited on page 33.

[34] LHCb Collaboration, "The LHCb Detector at the LHC," *JINST* **3** (2008) S08005.
Cited on page 33.

[35] ALICE Collaboration, "The ALICE experiment at the CERN LHC," *JINST* **3**
(2008) S08002. Cited on page 33.

[36] ATLAS Collaboration, "ATLAS Collaboration Photo Gallery.".
http://www.atlas.ch/photos/. Cited on pages 34, 37, 39, 41, 43, 44, 49, and 165.

[37] ATLAS Collaboration, "Luminosity Public Results.". https:
//twiki.cern.ch/twiki/bin/view/AtlasPublic/LuminosityPublicResults.
Cited on pages 36, 47, and 165.

[38] ATLAS Collaboration, "ATLAS pixel detector electronics and sensors," *JINST* **3**
no. 07, (2008) P07007. Cited on page 38.

[39] Y. Unno, "ATLAS silicon microstrip detector system (SCT)," *Nuclear Instruments
and Methods in Physics Research Section A: Accelerators, Spectrometers, Detectors
and Associated Equipment* **511** no. 1, (2003) 58–63. Cited on page 39.

[40] ATLAS TRT Collaboration, "The ATLAS TRT Barrel Detector," *JINST* **3** no. 02,
(2008) P02014. Cited on page 40.

[41] ATLAS TRT Collaboration, "The ATLAS TRT end-cap detectors," *JINST* **3**
no. 10, (2008) P10003. Cited on page 40.

[42] W. Lampl, S. Laplace, D. Lelas, P. Loch, H. Ma, S. Menke, S. Rajagopalan,
D. Rousseau, S. Snyder, and G. Unal, "Calorimeter Clustering Algorithms:
Description and Performance," Apr, 2008. ATL-LARG-PUB-2008-002. Cited on
pages 43 and 48.

[43] T. Sjostrand, S. Mrenna, and P. Z. Skands, "A Brief Introduction to PYTHIA 8.1,"
Comput.Phys.Commun. **178** (2008) 852–867, arXiv:0710.3820 [hep-ph]. Cited
on page 47.

[44] M. Bahr, S. Gieseke, M. Gigg, D. Grellscheid, K. Hamilton, *et al.*, "Herwig++
Physics and Manual," *Eur.Phys.J.* **C58** (2008) 639–707, arXiv:0803.0883
[hep-ph]. Cited on page 47.

[45] J. Butterworth, J. R. Forshaw, and M. Seymour, "Multiparton interactions in

photoproduction at HERA," *Z.Phys.* **C72** (1996) 637–646, `arXiv:9601371 [hep-ph]`. Cited on page 47.

[46] S. Alioli, P. Nason, C. Oleari, and E. Re, "A general framework for implementing NLO calculations in shower Monte Carlo programs: the POWHEG BOX," *JHEP* **1006** (2010) 043, `arXiv:1002.2581 [hep-ph]`. Cited on page 47.

[47] M. L. Mangano, M. Moretti, F. Piccinini, R. Pittau, and A. D. Polosa, "ALPGEN, a generator for hard multiparton processes in hadronic collisions," *JHEP* **0307** (2003) 001, `arXiv:hep-ph/0206293`. Cited on page 47.

[48] S. Frixione, F. Stoeckli, P. Torrielli, B. R. Webber, and C. D. White, "The MC@NLO 4.0 Event Generator," `arXiv:1010.0819 [hep-ph]`. Cited on page 47.

[49] B. P. Kersevan and E. Richter-Was, "The Monte Carlo event generator AcerMC versions 2.0 to 3.8 with interfaces to PYTHIA 6.4, HERWIG 6.5 and ARIADNE 4.1," *Comput.Phys.Commun.* **184** (2013) 919–985, `arXiv:0405247 [hep-ph]`. Cited on page 47.

[50] ATLAS Collaboration, "The ATLAS Simulation Infrastructure," *The European Physical Journal C* **70** no. 3, (2010) 823–874. Cited on page 47.

[51] GEANT4 Collaboration, S. Agostinelli *et al.*, "GEANT4: A simulation toolkit," *Nucl. Instrum. Meth. A* **506** (2003) 250. Cited on pages 47 and 71.

[52] ATLAS Collaboration, "Electron reconstruction and identification efficiency measurements with the ATLAS detector using the 2011 LHC proton-proton collision data," *Eur.Phys.J.* **C74** no. 7, (2014) 2941, `arXiv:1404.2240 [hep-ex]`. Cited on page 48.

[53] ATLAS Collaboration, "Measurement of the muon reconstruction performance of the ATLAS detector using 2011 and 2012 LHC proton-proton collision data," *Eur.Phys.J.* **C74** no. 11, (2014) 3130, `arXiv:1407.3935 [hep-ex]`. Cited on pages 49 and 126.

[54] M. Cacciari, G. P. Salam, and G. Soyez, "The Anti-k(t) jet clustering algorithm," *JHEP* **0804** (2008) 063, `arXiv:0802.1189 [hep-ph]`. Cited on page 50.

[55] ATLAS Collaboration, "Pile-up subtraction and suppression for jets in ATLAS," Aug, 2013. ATLAS-CONF-2013-083. Cited on page 51.

[56] ATLAS Collaboration, "Commissioning of the ATLAS high-performance *b*-tagging

algorithms in the 7 TeV collision data," Jul, 2011. ATLAS-CONF-2011-102. Cited on page 51.

[57] ATLAS Collaboration, "Identification of the Hadronic Decays of Tau Leptons in 2012 Data with the ATLAS Detector," Jul, 2013. ATLAS-CONF-2013-064. Cited on page 52.

[58] ATLAS Collaboration, "Performance of Missing Transverse Momentum Reconstruction in ATLAS studied in Proton-Proton Collisions recorded in 2012 at 8 TeV," Aug, 2013. ATLAS-CONF-2013-082. Cited on page 55.

[59] L. Fiorini, "Top-Quark Physics Results From LHC," arXiv:1201.5844 [hep-ex]. Cited on pages 65 and 166.

[60] A. Denner, S. Dittmaier, S. Kallweit, and A. Mück, "HAWK 2.0: A Monte Carlo program for Higgs production in vector-boson fusion and Higgs strahlung at hadron colliders," arXiv:1412.5390 [hep-ph]. Cited on pages 71 and 124.

[61] M. L. Mangano, M. Moretti, and R. Pittau, "Multijet matrix elements and shower evolution in hadronic collisions: $Wb\bar{b} + n$ jets as a case study," *Nucl. Phys.* **B632** (2002) 343–362, arXiv:hep-ph/0108069 [hep-ph]. Cited on page 71.

[62] N. Davidson, G. Nanava, T. Przedzinski, E. Richter-Was, and Z. Was, "Universal Interface of TAUOLA Technical and Physics Documentation," *Comput.Phys.Commun.* **183** (2012) 821–843, arXiv:1002.0543 [hep-ph]. Cited on page 71.

[63] N. Davidson, T. Przedzinski, and Z. Was, "PHOTOS Interface in C++: Technical and Physics Documentation," arXiv:1011.0937 [hep-ph]. Cited on pages 71 and 90.

[64] A. Elagin, P. Murat, A. Pranko, and A. Safonov, "A New Mass Reconstruction Technique for Resonances Decaying to di-tau," *Nucl. Instrum. Meth.* **A654** (2011) 481–489, arXiv:1012.4686 [hep-ex]. Cited on page 107.

[65] A. Barr, T. Khoo, P. Konar, K. Kong, C. Lester, *et al.*, "Guide to transverse projections and mass-constraining variables," *Phys. Rev. D* **84** (2011) 095031, arXiv:1105.2977 [hep-ph]. Cited on pages 107, 111, and 113.

[66] R.K. Ellis and I. Hinchliffe and M. Soldate and J.J. Van Der Bij, "Higgs decay to $\tau^+\tau^-$: A possible signature of intermediate mass Higgs bosons at high energy

hadron colliders," *Nucl. Phys. B* **297** no. 2, (1988) 221 – 243. Cited on page 107.

[67] J. M. Campbell and R. K. Ellis, "An Update on vector boson pair production at hadron colliders," *Phys.Rev.* **D60** (1999) 113006, `arXiv:hep-ph/9905386 [hep-ph]`. Cited on page 123.

[68] H.-L. Lai, M. Guzzi, J. Huston, Z. Li, P. M. Nadolsky, *et al.*, "New parton distributions for collider physics," *Phys. Rev. D* **82** (2010) 074024, `arXiv:1007.2241 [hep-ph]`. Cited on page 123.

[69] R. D. Ball, V. Bertone, S. Carrazza, C. S. Deans, L. Del Debbio, *et al.*, "Parton distributions with LHC data," *Nucl.Phys.* **B867** (2013) 244–289, `arXiv:1207.1303 [hep-ph]`. Cited on page 123.

[70] A. Martin, W. Stirling, R. Thorne, and G. Watt, "Parton distributions for the LHC," *Eur.Phys.J.* **C63** (2009) 189–285, `arXiv:0901.0002 [hep-ph]`. Cited on page 123.

[71] ATLAS Collaboration, "Improved luminosity determination in pp collisions at $\sqrt{s}$ = 7 TeV using the ATLAS detector at the LHC," *Eur. Phys. J. C* **73** (Feb, 2013) 2518. 40 p. CERN-PH-EP-2013-026. Cited on page 124.

[72] ATLAS Collaboration, "Electron efficiency measurements with the ATLAS detector using the 2012 LHC proton-proton collision data," Jun, 2014. ATLAS-CONF-2014-032. Cited on page 125.

[73] ATLAS Collaboration, "Identification and energy calibration of hadronically decaying tau leptons with the ATLAS experiment in *pp* collisions at $\sqrt{s}$=8 TeV," `arXiv:1412.7086 [hep-ex]`. Cited on page 126.

[74] ATLAS Collaboration, "Calibration of the performance of *b*-tagging for *c* and light-flavour jets in the 2012 ATLAS data," Jul, 2014. ATLAS-CONF-2014-046. Cited on page 126.

[75] G. Cowan, K. Cranmer, E. Gross, and O. Vitells, "Asymptotic formulae for likelihood-based tests of new physics," *European Physical Journal C* **71** (Feb., 2011) 1554, `arXiv:1007.1727 [physics.data-an]`. Cited on pages 128 and 132.

[76] R. Brun and F. Rademakers, "ROOT - An object oriented data analysis framework," *Nuclear Instruments and Methods in Physics Research Section A: Accelerators, Spectrometers, Detectors and Associated Equipment* **389** no. 12, (1997) 81 – 86. New Computing Techniques in Physics Research V. Cited on page 135.

[77] L. Moneta, K. Cranmer, G. Schott, and W. Verkerke, "The RooStats project," in *Proceedings of the 13th International Workshop on Advanced Computing and Analysis Techniques in Physics Research.*, p. 57. 2010. `arXiv:1009.1003 [physics.data-an]`. Cited on page 135.

[78] W. Verkerke and D. Kirkby, "The RooFit toolkit for data modeling," `arXiv:0306116 [physics.data-an]`. Cited on page 135.

List of Figures

List of Tables

List of Acronyms

ALICE A Large Ion Collider Experiment. 33, 34

ATLAS A Toroidal LHC Apparatus. ii, iv, 1, 2, 20, 22–29, 33, 34, 36–39, 41–44, 46, 47, 49, 52, 57, 59, 67, 71, 125, 126, 128, 153

BDT Boosted Decision Tree. 53, 60, 84, 96, 97

CERN European Organisation for Nuclear Research. 17, 20, 33

CMS Compact Muon Solenoid. 1, 20, 22, 23, 25, 28, 33, 34, 67, 153

CTP Central Trigger Processor. 43

ECAL Electromagnetic Calorimeter. 40, 41, 48, 50, 54, 60

EF Event Filter. 45, 58, 59

FCAL Forward Calorimeter. 42

FF Fake Factor. 70, 72–75, 88, 90, 91, 95, 96, 99, 100, 102, 105, 127, 128, 146, 153

GRL Good Run List. 57

HCAL Hadronic Calorimeter. 41, 42, 45, 50, 54, 60

HEC Hadronic End Cap. 42

ID Inner Detector. 38, 40, 44, 48–50, 52–54, 60

JVF Jet Vertex Fraction. 51, 52, 60

L1 Level 1. 42, 43, 45

L2 Level 2. 43, 44

LEP Large Electron Positron Collider. 17–20, 33

LHC Large Hadron Collider. ii, iv, 1, 2, 17, 20–22, 33–37, 42, 56, 65, 125, 153, 154

LO Leading Order. 71, 124

MC Monte-Carlo. ii, 2, 46, 58, 70, 71, 73, 74, 77, 82–84, 86, 90, 91, 95–97, 99, 100, 121–126, 128, 146–148, 153

MMC Missing Mass Calculator. 107

MS Muon Spectrometer. 42, 49, 54, 60

NLO Next-to-Leading Order. 69, 71, 124

NNLO Next-to-Next-to-Leading Order. 71, 124

PD Pixel Detector. 38, 39, 48, 50, 53

PDF Parton Distribution Function. 46, 123

PV Primary Vertex. 51

QCD Quantum Chromodynamics. 9, 53, 54, 71, 121–124

RoI Region of Interest. 43, 44

SCT Semiconductor Tracker. 39, 40, 50, 53

SM Standard Model. ii, 1, 2, 4–7, 10, 13, 16, 17, 19–25, 27, 33, 67, 69, 128, 146–150, 152, 153

TRT Transition Radiation Tracker. 40, 50, 53